ERDC/CHL TR-02-24

Coastal and Hydraulics Laboratory

US Army Corps
of Engineers®
Engineer Research and
Development Center

Coastal Inlets Research Program

Eastcoast 2001, A Tidal Constituent Database for Western North Atlantic, Gulf of Mexico, and Caribbean Sea

A. Y. Mukai, J. J. Westerink, R. A. Luettich, Jr., and D. Mark

September 2002

The contents of this report are not to be used for advertising, publication, or promotional purposes. Citation of trade names does not constitute an official endorsement or approval of the use of such commercial products.

The findings of this report are not to be construed as an official Department of the Army position, unless so designated by other authorized documents.

PRINTED ON RECYCLED PAPER

Coastal Inlets Research Program

ERDC/CHL TR-02-24
September 2002

Eastcoast 2001, A Tidal Constituent Database for the Western North Atlantic, Gulf of Mexico, and Caribbean Sea

by A. Y. Mukai, J. J. Westerink

Department of Civil Engineering and Geological Sciences
University of Notre Dame
Notre Dame, IN 46556

R. A. Luettich, Jr.

University of North Carolina at Chapel Hill
Institute of Marine Sciences
Morehead City, NC 28557

D. Mark

Coastal and Hydraulics Laboratory
U.S. Army Engineer Research and Development Center
3909 Halls Ferry Road
Vicksburg, MS 39180-6199

Final report

Prepared for U.S. Army Corps of Engineers
Washington, DC 20314-1000

Contents

Preface

This report describes a tidal constituent database developed for the Western North Atlantic Ocean, Gulf of Mexico, and Caribbean Sea, referred to as the *Eastcoast 2001* database. The work was performed as an activity of the Inlet Modeling System (IMS) Work Unit, Coastal Inlets Research Program (CIRP), of Headquarters, U.S. Army Corps of Engineers (HQUSACE). This IMS research and development product was conducted under contract DACW 42-00-C-0006 with the U.S. Army Research and Development Center (ERDC), Coastal and Hydraulics Laboratory (CHL), Vicksburg, MS. CIRP HQUSACE Program Monitors are Messrs. Charles B. Chesnutt and Barry W. Holliday.

Computations were performed on IBM Power3 SMP and Cray T3E computers at the ERDC Major Shared Resource Center (MSRC) Information Technology Laboratory (ITL), Vicksburg, MS. Professors Mary Wheeler and Clint Dawson and Dr. Victor Parr of the University of Texas at Austin developed the domain decomposition-based parallel version of the ADvanced CIRCulation model (ADCIRC) for the computations. Messrs. John Atkinson and Jesse Feyen of the University of Notre Dame provided technical assistance during the course of this project.

Dr. Adele Militello, formerly of the Coastal Hydraulics Branch (CHB), CHL, was IMS Work Unit Principal Investigator (PI) through the course of this project, and Ms. Mary A. Cialone, Coastal Processes Branch was PI during report publication. Work within CHB was performed under the supervision of Dr. Zeki Demirbilek, Acting Chief, CHB. Dr. Nicholas C. Kraus, CHL, was CIRP Program Manager, and Dr. William H. McAnally, CHL, was Technical Director for Navigation. Word Processing and formatting were completed by Ms. J. Holley Messing, CHL. This project was performed under the administrative supervision of Mr. Thomas W. Richardson, Director, CHL.

At the time of publication of this report, Dr. James R. Houston was Director of ERDC, and COL John W. Morris III, EN, was Commander and Executive Director.

Summary

This report describes the development of the *Eastcoast 2001* database of computed tidal elevation and velocity constituents within the Western North Atlantic Tidal (WNAT) domain. The WNAT domain encompasses the Western North Atlantic Ocean, Gulf of Mexico, and Caribbean Sea. The computations are based on a strategically designed finite element grid and the coastal hydrodynamic circulation model, ADCIRC. The resulting *Eastcoast 2001* database defines the computed elevation and velocity amplitude and phase for the O_1, K_1, Q_1, M_2, S_2, N_2, and K_2 tidal constituents.

The *Eastcoast 2001* database is significantly more accurate than the previous *Eastcoast 1995* and *Eastcoast 1991* databases based on the following feature improvements: (a) a new grid generation technique with better node placement and distribution, (b) a significantly greater number of total nodes, (c) a more accurate coastal boundary, and (d) inclusion of more reliable bathymetric databases. The new grid generation technique is the combination of two a priori mesh criteria: (a) the wavelength to grid size ratio and (b) the topographic length scale criteria. This combination optimally and more accurately places grid nodes in areas where high resolution is needed. Error analysis of computed versus measured elevation amplitude and phase at 101 stations in addition to an assessment of measured data errors globally and locally quantifies the level of reliability of the computed constituents.

1 Introduction and Objectives

Coastal ocean tidal models are used to define navigable depths and currents in nearshore regions, to assess pollutant and/or sediment movement on the continental shelf, and to evaluate coastal inundation. The hydrodynamics of coastal tides are difficult to predict due to various complexities including irregular coastlines, intricacies of the ocean floor, and the interaction of astronomical tides and numerous nonlinearly generated overtides and compound tides. Since the tidal problem cannot be directly solved analytically, numerical models have been developed to evaluate sea surface elevations and currents.

To obtain accurate tidal predictions, computer models depend on various interrelated factors including: (a) the governing equations accurately representing the actual flow processes and phenomena, (b) the representation of the water body and boundary forcing functions being sufficiently accurate for the given problem, (c) the scope of the computational domain being appropriately sized, (d) the numerical algorithms being accurate and robust, and (e) the temporal and spatial scales being adequately and if possible optimally discretized.

A successful strategy to enhance the accuracy of coastal ocean circulation models has been the use of increasingly larger computational domains such as the Western North Atlantic Tidal (WNAT) domain (Westerink, Luettich, and Scheffner 1993; Westerink, Luettich, and Muccino 1994; Westerink, Luettich, and Pourtaheri 2000; Blain, Westerink, and Luettich 1994, 1998). The WNAT domain encompasses the Western North Atlantic Ocean, Gulf of Mexico, and the Caribbean Sea. The domain has an eastern open ocean boundary along the 60°W meridian, which is placed such that an accurate set of boundary conditions can be specified. The 60°W meridian is geometrically simple and does not lie within a resonant basin such as the Gulf of Mexico. Furthermore, the boundary is mostly in the deep Atlantic where tides vary more gradually than on the shelf and nonlinear tidal species are minimal. However, large domains add complications to the process of computational node placement, since they require strategic placement of nodes in order to maintain acceptable levels of local and global accuracy for a given computational cost.

Grids for large domains should be unstructured and nonuniform. A uniformly discretized grid would require a high level of resolution throughout the domain due to resolution constraints imposed by regions with shallow depths

and/or rapidly varying flow. However, since the deep ocean, which comprises the majority of the WNAT domain, is a vast region with very deep bathymetry and a slowly spatially varying tidal response, which only require a relatively coarse mesh, a high resolution uniformly graded grid would overdiscretize large areas unnecessarily and only add to the computational cost. In general, tidal wave propagation speeds and wavelengths decrease with decreasing depths. Therefore, unstructured grid size should decrease along with bathymetry to continue describing the flow at the same level of accuracy. In addition, variations in geometry and bathymetry impose gradients on the localized tidal elevation and especially velocity responses, particularly in shallow waters. This requires that additional localized grid refinement be imposed in regions with high bathymetric gradients. Thus, regions such as the continental shelf break and the continental slope require higher grid resolution (Hagen, Westerink, and Kolar 2000; Hagen et al. 2001). Other areas needing local refinement include regions exhibiting two-dimensional (2-D) response structures associated with complex shorelines, 2-D topography and amphidromic points.

Several studies on grid generation techniques have been made in recent years to provide a strategy for the methodical and optimal placement of nodes in variable graded grids for large computational domains (Hagen, Westerink, and Kolar 2000; Hannah and Wright 1995). Various techniques have been implemented and studied over the years, but no technique has been proven to independently work accurately enough to implement the appropriate grid spacing based on the physical characteristics of the domain while being computationally economical. The most widely used technique remains the wavelength to grid size ($\lambda/\Delta x$) criterion that is based on computing an estimated wavelength using one-dimensional linear constant depth long wave theory. However, this technique does not recognize gradients in response associated with changing bathymetry, 2-D structure in boundaries and/or response. The topographic length scale (TLS) criterion keys grid resolution to the rate of change in topography (Kashiyama and Okada 1992; Hannah and Wright 1995). However, in and of itself this criterion does not properly resolve constant depth or slowly varying depth waters or account for 2-D response structures. A recent technique based on localized truncation error analysis (LTEA) formally computes truncation error and controls this by adjusting grid size (Hagen, Westerink, and Kolar 2000; Hagen et al. 2001). Although the LTEA grid generation technique has been successful in creating computationally more accurate and economical grids, the process involved is long and tedious. However, a combination of the wavelength to grid size ratio and the TLS criteria yields grids that are similar in performance to LTEA based grids.

The WNAT domain has been used as a basis for unstructured graded grid tidal computations since 1991. Westerink, Luettich, and Scheffner (1993) and Westerink, Luettich, and Muccino (1994) developed *Eastcoast 1991*, a tidal database of surface-water elevations and currents in the WNAT domain. The *Eastcoast 1991* grid, as shown in Figure 1, consists of 19,858 nodes and 36,653 elements with element sizes varying from 7 km at the coastline to approximately 140 km in the deep ocean, shown in Figure 2. This grid was generated using the wavelength to grid-size ratio criterion and specifying a maximum element size equal to 140 km. The *Eastcoast 1991* bathymetry was constructed from the Earth

Topography 5 min gridded resolution (ETOPO5)[1] bathymetric database which defines bathymetry on a coarse resolution 5' x 5' grid and extends over all the world oceans.

An updated WNAT tidal database, *Eastcoast 1995*, was developed in 1995. The *Eastcoast 1995* grid, shown in Figure 3, consists of 31,435 nodes and 58,369 elements, and was considered a large finely variable graded grid at the time it was generated. This grid was also generated under the guidance of the wavelength to grid-size ratio criterion. Element sizes vary from 5 to 15 km at the coastline, to about 100 km in the deep ocean as shown in Figure 4. The bathymetry for this tidal constituent database, shown in Figure 5, was significantly improved by using both the ETOPO5 database and the NOS sounding bathymetric database (National Ocean Service (NOS) 1997).[2] The NOS bathymetric database represents the raw sounding tracks from surveys and typically extends only to the continental shelf break in U.S. coastal waters.

ADvanced CIRCulation (ADCIRC) was the hydrodynamic numerical model used to compute the *Eastcoast 1991* and *Eastcoast 1995* tidal databases. The *Eastcoast 1991* in its time provided invaluable results, until *Eastcoast 1995* database superceded it with improved values. *Eastcoast 1991* had average tidal constituent errors in amplitude between 18.2 and 45.3 percent, and average errors in phase between 8.3 and 27.5 deg for predictive WNAT tidal computations driven by the K_1, O_1, Q_1, M_2, S_2, N_2, and K_2 constituents. *Eastcoast 1995* had average errors in amplitude between 9.4 and 29.0 deg, and average errors in phase between 7.1 and 15.0 deg for similar computations. Further improvements in local and global accuracy of tidal constituents were desired for the WNAT domain.

In this report, the development of the latest and most accurate tidal database for the WNAT domain is described. The most significant improvements include a more refined and strategically laid out unstructured grid of the WNAT domain as well as significant improvements in the definition of bathymetry in select regions. Specifically, a 254,629-node unstructured finite element grid was developed using the combined wavelength to grid size and TLS criteria with a defined minimum resolution equal to 1 to 2 km in most areas and a maximum resolution equal to 25 km. Furthermore, improved resolution allowed for better precision in the placement of coastal boundaries as well as the addition of important islands. An updated WNAT bathymetry created from the ETOPO5, NOS and DNC (U.S. Department of Defense 1999) databases was also implemented. The open boundary was forced with the most current Le Provost et al. (1998) tidal database, FES95.2, which incorporates assimilated satellite altimetry based sea surface data. Finally, data from elevation recording stations scattered throughout the WNAT domain were updated and were used for more extensive model validation.

---

[1] Data obtained from National Geophysical Data Center, National Oceanic and Atmospheric Administration, Boulder, CO, 80303-3328, 1988, World Wide Web page accessed on 2 May 2001, http://edcwww.cr.usgs.gov/glis/hyper/guide/etopo5.

[2] Additional information available on the World Wide Web at http://www.ngdc.noaa.gov/mgg/fliers/97mgg02.html).

2 Governing Equations and 2-D Modeling

This chapter briefly describes the ADCIRC hydrodynamic computer model as well as model parameter values and the boundary and interior domain forcing functions utilized to attain the results used to build the tidal database.

Hydrodynamic Model Description

The hydrodynamic numerical model used in the *Eastcoast 2001* tidal database computations is ADCIRC-2DDI, the depth-integrated option of the 2-D and 3-D fully nonlinear hydrodynamic code ADCIRC (Luettic, Westerink, and Scheffner 1992[1]; Westerink, Luettich, and Kolar 1996). ADCIRC-2DDI uses the depth-integrated equations of mass and momentum subject to the incompressibility, Boussinesq, and hydrostatic pressure approximations. Baroclinic processes were neglected, including any expansion and contraction due to radiational heating. The governing continuity and momentum equations are written in primitive form as:

$$\frac{\partial \xi}{\partial t}+\frac{1}{R\cos\phi}\left[\frac{\partial UH}{\partial \lambda}+\frac{\partial (VH\cos\phi)}{\partial \phi}\right]=0 \tag{1}$$

$$\begin{aligned}\frac{\partial U}{\partial t}+\frac{1}{R\cos\phi}U\frac{\partial U}{\partial \lambda}+\frac{V}{R}\frac{\partial U}{\partial \phi}-\left(\frac{\tan\phi}{R}U+f\right)V = \\ -\frac{1}{R\cos\phi}\frac{\partial}{\partial \lambda}\left[\frac{p_s}{\rho_0}+g(\xi-\alpha\eta)\right]+\frac{\tau_{s\lambda}}{\rho_0 H}-\tau_* U\end{aligned} \tag{2}$$

[1] Additional information available on the World Wide Web at http://www.marine.unc.edu/C_CATS/adcirc/adcirc.htm).

$$\frac{\partial V}{\partial t}+\frac{1}{R\cos\phi}U\frac{\partial V}{\partial \lambda}+\frac{V}{R}\frac{\partial V}{\partial \phi}+\left(\frac{\tan\phi}{R}U+f\right)U= -\frac{1}{R}\frac{\partial}{\partial \phi}\left[\frac{p_s}{\rho_0}+g(\xi-\alpha\eta)\right]+\frac{\tau_{s\phi}}{\rho_0 H}-\tau_* V \quad (3)$$

Equation 1 is the primitive continuity equation, and Equations 2 and 3 are the λ (degrees longitude) and ϕ (degrees latitude) direction primitive momentum equations in nonconservative form. The variables are defined as: ξ = free-surface elevation relative to the geoid; U, V = depth-averaged horizontal velocities; $H = \xi + h$ = total water column; h = bathymetric depth relative to the geoid; $f = 2\Omega \sin\phi$ = Coriolis parameter; Ω = angular speed of the Earth; p_s = atmospheric pressure at the free surface; g = acceleration due to gravity; η = Newtonian equilibrium tide potential; α = effective Earth elasticity factor; ρ_0 = reference density of water; $\tau_{s\lambda}$, $\tau_{s\phi}$ = applied free-surface stress; $\tau_* = C_f(U^2 + V^2)^{1/2}/H$, and C_f = bottom friction coefficient. For this application, a hybrid form of the standard quadratic parameterization for bottom stress is used that provides a friction factor that increases as the depth decreases in shallow water, similar to a Manning relationship. A practical expression for the Newtonian equilibrium tide potential is given by Reid (1990).

Prior to the application of the numerical discretization, Equations 1-3 are extensively rearranged for reasons of convenience and improved numerical properties. First in order to facilitate a Finite Element solution, these equations are mapped from spherical form into a rectilinear coordinate system using a Carte Parallelogrammatique projection. Furthermore the equations are cast into the Generalized Wave Continuity Equation (GWCE) form instead of their primitive form. The GWCE is derived by substituting the rearranged, spatially differentiated primitive conservative momentum equations into the time-differentiated primitive continuity equation. Then the primitive continuity equation multiplied by the GWCE weighting parameter, τ_0, is added and the advective terms are transformed to nonconservative form. It is noted that it is important to formulate the advective terms in the GWCE in nonconservative form to obtain a consistent solution with good local mass conservation properties (Kolar et al. 1994a). The GWCE weighting parameter, τ_0, is a purely numerical constant that sets the balance between the wave equation and primitive continuity equations. An appropriate choice of the weighting parameter τ_0 is essential for the GWCE to perform well. A large value of τ_0 leads to artificial spurious modes associated with a folded dispersion relationship, a small value of τ_0 leads to poor localized mass conservation properties. When τ_0 is properly chosen, the solution exhibits a solution free of spurious numerical oscillations while maintaining minimal local and global mass balance errors. Our past experience indicates the optimal value of τ_0 is two to 10 times that of τ_* (Kolar et al. 1994a). However, since τ_* varies linearly with the flow speed and friction factor, C_f, and varies inversely with the total depth, H, it can vary dramatically throughout a domain. It is therefore difficult to select a single GWCE weighting parameter value for a domain that has large regions of both deep and shallow water. To address this problem ADCIRC-2DDI has been implemented to permit a spatially varying τ_0. The change in ADCIRC to a nodally varying weighting parameter τ_0 allows for

appropriate local selection of the parameter. Therefore, regardless of flow depth, a locally consistent τ_0 is chosen.

The details of ADCIRC, our implementation of the GWCE based shallow water equations, accuracy tests, and basic algorithm analysis are provided in a series of reports and papers (Luettich and Westerink 1991; Luettich, Hu, and Westerink 1994; Kolar et al. 1994a, 1994b; Kolar, Gray, and Westerink 1996; Westerink et al. 1992, 1994). Additional information available on the World Wide Web at http://www.marine.unc.edu/C_CATS/adcirc/adcirc.htm). As with most GWCE based solutions, ADCIRC applies three node triangles for surface elevation, velocity, and depth. Time-stepping for all linear terms is based on a three-level implicit scheme for the GWCE and a two-level Crank-Nicholson scheme for the momentum equations. Nonlinear terms are treated explicitly, which imposes a Courant-based stability constraint. The decoupling of the time and space discrete form of the GWCE and momentum equations, time independent and/or tridiagonal system matrices, elimination of spatial integration procedures during time-stepping, and full vectorization of all major loops result in a highly efficient code.

ADCIRC has also been implemented in parallel using domain decomposition, a conjugate gradient solver and MPI (Message Passing Interface) based message passing. When a low ratio of interface to processor partition nodes is maintained, linear or even superlinear speedups are achieved. Thus, the wall clock time is reduced by a factor equal to or greater than the number of processors that the code is being run on. Superlinear speedups are possible since the problem sizes are reduced such that the portion of the simulation being run on each processor can take advantage of the on chip caching available on Random Instruction Set Computer (RISC) RISC-based chips used in parallel computers. Benchmarks have been run on a variety of platforms with up to 128 processors.

ADCIRC also includes a wide range of additional hydrodynamic features including wetting/drying of elements based on water-surface elevations and gradients (Luettich and Westerink 1995a, 1995b, 1999).

Model Input Parameters

The *Eastcoast 2001* tidal database was derived from a 90-day simulation run with the O_1, K_1 and Q_1 diurnal and the M_2, N_2, S_2, and K_2 semidiurnal astronomical tidal constituents forced on the open ocean boundary and within the interior domain. A smooth hyperbolic tangent time ramp function, which acts over 20 days, is applied to both the boundary forcing functions and the tidal potential forcing functions. Computed time-histories were calculated and then harmonically analyzed at all of the nodes in the domain, as well as at 101 tidal elevation stations where measured tidal constituent data are available. The harmonic analysis was based on the last 45 days of record using time-history values recorded every 5 min. Since harmonic constituents are allowed to fully interact through various nonlinear terms in the shallow-water equations, nonlinear overtides and compound tides are generated as well. Therefore, the harmonic analysis included the seven forcing constituents as well as the M_4, M_6,

M_8, and M_{10} overtides and the MN, SM, MNS_2, $2MS_2$, $2MN_2$, $2SM_2$, MN_4 MS_4, $2MN_6$, and MSN_6 compound tides. The resulting ADCIRC computed harmonic constituents were used as the basis of comparison to measured harmonically decomposed field data at the 101 defined elevation recording stations.

A time-step of 5 sec was used yielding a maximum Courant number based on wave celerity of approximately one for the *Eastcoast 2001* grid. This requirement on the Courant number is associated with the explicit treatment of the nonlinear terms. It is noted that Courant number is less than 0.4 over most of the domain, between 0.4 and 0.5 in the Bahamas, around Cuba, north of Jamaica, and north of the Dominican Republic, and between 0.5 and 0.8 in the Bahamas and in a small region south of Cuba. Elsewhere the Courant number is significantly smaller. The time weighting factors for the three-level implicit scheme in the GWCE equation are 0.35, 0.30, and 0.35 for the future, present and past time levels respectively. A two-level Crank-Nicholson scheme is used for the momentum equations.

The nonlinear finite amplitude option, which determines how the finite amplitude component of the total depth is considered, was utilized with wetting and drying enabled. The hybrid fully nonlinear bottom friction option was used. This option defines a Darcy-Weisbach type friction law for water column depths greater than the break depth, h_{break}, and modifies the friction factor for water column depths below the break depth to:

$$C_{f_{applied}} = C_f \left[1 + \left(\frac{h_{break}}{H} \right)^{\theta} \right]^{\frac{\gamma}{\theta}} \tag{4}$$

This increases bottom friction for shallow waters in order to accommodate a realistic wetting/drying front. The bottom friction parameters were specified as $C_f = 0.0025$, $h_{break} = 1.0$ m, $\theta = 10.0$, and $\gamma = 0.3333$ throughout the domain. The lateral eddy diffusion/dispersion coefficient was set equal to 5 sq m/sec. Finally, due to the locally high Courant number, the advective terms were turned off.

Boundary and Interior Forcing

The domain was forced on the 60°W meridian open boundary with O_1, K_1, Q_1, M_2, N_2, S_2, and K_2 tidal amplitudes and phases interpolated onto the open ocean boundary nodes using data from Le Provost 1995 global model (Le Provost et al. 1998). Le Provost created a worldwide ocean tidal database from a finite element hydrodynamic model in 1994, designated FES94.1 (Le Provost, Bennett, and Cartwright 1995). In 1995, Le Provost revised FES94.1 by assimilating a satellite altimeter-derived data set, thus creating FES95.2. FES95.2 has better accuracy than FES94.1 because of corrections to major constituents by TOPEX/POSEIDON mission data assimilation and because of the increase in the number of constituents in the model. A comparison study of both FES94.1 and FES95.2 on the *Eastcoast 2001* grid has shown that FES95.2 provided better results, and thus was used to force the open ocean

boundary. It is noted that Le Provost's database values had to be extrapolated for portions of the *Eastcoast 2001* open ocean boundary lying on the continental shelf in the vicinity of Nova Scotia and Venezuela since Le Provost's databases do not provide complete coverage in these areas. Simply applying the nearest available FES95.2 value across the stretches of the continental shelf not covered by FES95.2 led to the formation of unphysical and unstable eddies on the shelf off Venezuela. Zero normal flow specified boundary conditions were applied to all coastal and island boundaries.

Tidal potential amplitudes and the associated effective Earth elasticity factors for the seven forcing constituents are listed in Table 1. Earth elasticity factors (which reduces the magnitude of the tidal potential forcing due to Earth tides) ranging between 0.693 to 0.736 were used instead of the theoretical value of 0.69 (Schwiderski 1979; Hendershott 1981).

3 *Eastcoast 2001* Grid Development

The domain used to develop the *Eastcoast 2001* tidal database remains essentially the same as for the *Eastcoast 1991* and *Eastcoast 1995* databases. The land boundary definition has been improved due to increased grid resolution near the coast. The grid has been improved by increasing the total number of nodes by a factor of four and by placing these nodes in a more strategic manner due to the use of both the wavelength to grid size ratio and the topographic length scale (TLS) criteria. Further significant improvements were derived from the use of an additional bathymetric database, which drastically redefined depths in critical regions.

Domain Definition

The WNAT domain used in these computations covers the deep Atlantic Ocean westward from the 60°W meridian and encompasses the western North Atlantic Ocean, the Gulf of Mexico, and the Caribbean Sea. The 60°W meridian open-ocean boundary runs from the vicinity of Glace Bay in Nova Scotia, Canada, to the vicinity of Corocora Island in eastern Venezuela. This boundary lies almost entirely in the deep Atlantic Ocean and has the following advantages: (a) It is geometrically simple and includes no corners, (b) the tidal signal generally varies slowly in space since the boundary includes only a small portion of the continental shelf and is positioned well away from any amphidromes, and (c) nonlinear tidal constituents are not significant in the deep ocean, since they are generated on the continental shelf and are largely trapped there due to the out-of-phase reflective character of the continental slope.

An updated land boundary for the WNAT domain, shown in Figure 6, was necessary to improve the accuracy of its placement and inclusion of details neglected in the prior WNAT grids. Grid size at the shoreline was targeted to be half the size of that in the *Eastcoast 1995* grid or less. The Defense Mapping Agency's (DMA) World Vector Shoreline (WVS) coastal database was utilized for updating the land boundaries (Soluri and Woodson 1990).[1] The WVS yields data points approximately every 100 m and has a stated accuracy that 90 percent of the points are within 500 m of the actual feature. The *Eastcoast 2001*

[1] Data obtained from National Geophysical Data Center, World Wide Web page accessed on 25 February 2000, http://rimmer.ngdc.noaa.gov/coast.

boundary was implemented with a land boundary resolution ranging from 1 km to 7 km depending on location. Along the Atlantic coastline element sizes were 2 km, along the Gulf of Mexico coastline resolution was 2-4 km, with the exception of 1 km along southern Louisiana, 2-5 km along the northern South American coastline, and 1-4 km in the Caribbean Sea with the exception of Haiti/Dominican Republic with 4-7 km. Improved grid resolution also allowed the inclusion of islands previously neglected in the *Eastcoast 1995* grid due to the relative size of the island to the element size. Many of these islands have been added in the vicinity of the Bahamas as well as in the Caribbean basin and will be expected to have a significant impact in directing the path of the tidal flow through these areas and into the Caribbean Sea and the Gulf of Mexico. The islands added include Aruba, Curacao, Bonaire, Isla Margarita, Trinidad and Tobago, St. Vincent and the Grenadines, Saint Lucia, and the Cayman Islands in the Caribbean; Turks and Caicos Islands in the West Indies; and the Exuma Cays in the Bahamas.

Grid Development

A systematic methodology to discretize the WNAT domain is necessary to create a more accurate and computationally efficient mesh. Grid refinement is desired in four fundamental areas: (a) shallow waters, (b) coastline, (c) continental slope, especially at the shelf break, and (d) in regions with significant 2-D response structures (including resonant basins). Fine resolution is necessary in shallow waters to correctly resolve tidal waves while additional resolution is necessary near the coastline to represent its changing geometry with sufficient accuracy. In the deep ocean, since the hydrodynamic response is small and slowly varying and the wavelengths are large, larger element sizes can be used. As the waves approach the shelf, the change in bathymetry forces the wavelengths to shorten. To accurately capture this effect, a sufficient density of nodes is required on the continental slope, and especially at the continental shelf break (Hagen, Westerink, and Kolar 2000; Hagen et al. 2001). In resonant basins, such as the Gulf of Mexico and the Caribbean Sea, long-term stability problems which are related to resolution can occur over the course of time, thus requiring additional resolution in deeper waters within these basins as well (Hagen 1998; Roe 1998).

In the development of the previous *Eastcoast 1991* and *Eastcoast 1995* databases, a wavelength to grid size ratio ($\lambda/\Delta x$) criterion with a defined minimum and maximum grid size was applied to construct the mesh. Extensive numerical analysis and experimentation has demonstrated a need for additional resolution in regions where bathymetric gradients are significant (Hagen, Westerink, and Kolar 2000; Hagen et al. 2001). This can be easily accomplished by considering the TLS criterion in combination with the wavelength to grid-size ratio criterion.

The wavelength to grid-size ratio is a scalar parameter, which serves as a criterion for one-dimensional, linear, frictionless, constant bathymetry flow and is defined as:

$$\frac{\lambda}{\Delta x} = \frac{\sqrt{gh}}{\Delta x} T \tag{5}$$

where λ is the wavelength, Δx is the grid size, g is the gravitational constant, h is the water depth, and T is the tidal period of interest. The $\lambda/\Delta x$ ratio is generally set at a constant value to create a graded variable mesh. This implies that the element size should decrease with decreasing bathymetry along with decreasing wavelength to maintain the constant ratio value.

The $\lambda/\Delta x$ ratio does not call for increased resolution in the vicinity of steep topographic gradients such as the continental shelf break and slope and rise. Nonetheless it has been demonstrated that increased resolution is necessary to correctly capture the changes occurring in these regions. The topographic length scale is another grid generation technique that has been developed in recent years (Hannah and Wright 1995). This one-dimensional criterion calculates the grid size as:

$$\Delta x \leq \frac{\alpha h}{h_{,x}} \tag{6}$$

where Δx is the grid size, h is the water depth, $h_{,x}$ is the bathymetric gradient, and α is the mesh generation criterion set to a constant value of $\Delta h/h \leq \alpha$ over any element. This ratio creates a relationship that will incorporate both the bathymetry and the change of bathymetry relative to the grid size. TLS indicates the need for resolution in areas with steep topographic gradients, such as at the continental shelf break and slope, which the wavelength to grid-size ratio would tend to underresolve. Unfortunately the TLS criterion will fail as $h_{,x}$ becomes small requiring that the wavelength to grid-size ratio criterion be applied as well.

The combination of the wavelength to grid-size ratio and the TLS criteria can be shown to create grids similar to more sophisticated grid development techniques based on localized truncation error analysis (Hagen, Westerink, and Kolar 2000; Hagen et al. 2001). The *Eastcoast 2001* grid, as shown in Figure 7, was developed with these criteria. The wavelength to grid-size ratio was targeted to 100 or more, and the TLS criterion was aimed at 1.00. The *Eastcoast 2001* grid has a defined minimum element size generally ranging from 1 to 4 km along the land boundaries and a defined maximum element size equal to 25 km in the deep ocean. The maximum element size of 25 km in the deep ocean was defined to ensure that the computations did not have long-term stability problems (Roe 1998). Once these minimum and maximum mesh sizes were set, the combined $\lambda/\Delta x$ and TLS grid generating criteria were used to develop the rest of the grid. The wavelength to grid-size ratio was implemented first, indicating much needed resolution near the coastline and areas of shallow depths. The TLS criterion was implemented next, which necessitated additional resolution in the vicinity of the shelf break and slope. The resulting grid-size distribution throughout the domain is shown in Figure 8 while the $\lambda/\Delta x$ and TLS values are shown in Figures 9 and 10, respectively. Along the coastline, the wavelength to grid-size ratio ($\lambda/\Delta x$) ranges between 100 to 500 wherever waters are shallow. In the deep ocean, the $\lambda/\Delta x$ ranges between 200 and 1,000. Although the targeted $\lambda/\Delta x$ was 100 or

greater, some areas such as the Bahamas, Nicaragua Rise, Cuba, and Florida have values as low as 70 and were not further resolved in order to maintain the minimum element size of 1 km. The majority of the TLS values equal 0.25 or less, however, along the continental shelf break and other areas with steep bathymetric gradients the TLS values were closer to the set target of 1.0. The final *Eastcoast 2001* grid contains 254,629 nodes and 492,182 elements.

Bathymetry

It is essential that bathymetry be accurately represented to ensure accurate results. In fact, bathymetry controls physical processes ranging from wave propagation, reflection and refraction, the 2-D structure of the waves as well as dissipation. Bathymetry for the *Eastcoast 1991* computations was based on the ETOPO5 database while bathymetry for the *Eastcoast 1995* computations was based on the ETOPO5 and NOS (National Ocean Service) databases.

ETOPO5, shown in Figure 11, is a 5-min gridded Earth topography database, which was put together by the U.S. Naval Oceanographic Office in 1985 and revised again in 1987. The ETOPO5 database, which has been widely used in the past, provides values throughout the entire WNAT domain. However, the ETOPO5 database is somewhat limited in resolution and in some areas can be unreliable, particularly on the continental shelves. Nonetheless, ETOPO5 is the best and sometimes the only general database to which nonmilitary applications have access.

The NOS bathymetric data values, Figure 12, are derived from the NOS' raw sounding database (National Oceanic and Atmospheric Administration (NOAA) Digital U.S. Coastal Hydrography Sounding Database). NOS' sounding database includes bathymetric values on most of the U.S. continental shelf, from the shoreline and within selected estuaries to the continental shelf break. Since the data is in raw sounding track values form, the NOS bathymetric data values are filtered onto the *Eastcoast 2001* grid using an element-based gathering/averaging procedure instead of a direct interpolation procedure. The gathering/averaging procedure searches for all available sounding/topographic survey values within the cluster of elements connected to one specific node, averages these values and assigns the average value as the depth/topographic elevation to that node. This gathering/averaging procedure essentially implements grid scale filtering to the bathymetric/topographic data and ensures that bathymetry/topography is consistent with the scale of the grid. The NOS database has significant higher density to represent critical features and is also more reliable than the ETOPO5 database. Therefore, NOS' values are used instead of the ETOPO5's where possible.

Recently the Digital Nautical Charts (DNC) bathymetric database, shown in Figure 13, by the National Imagery and Mapping Agency has been made available. This database provides bathymetry throughout most of the WNAT domain with significantly more precision than the ETOPO5 database. In some regions within the WNAT domain, such as in parts of the Atlantic Ocean and the northern coast of South America, an insufficient number of data points were

available for reliable bathymetric interpolation. In such areas, DNC data points were manually removed to maintain a sufficient level of accuracy in the bathymetry.

There are many significant differences between the DNC and ETOPO5 databases. Significant differences between the two databases often lie along the continental slopes and in certain shallow regions such as the vicinity of the Bahamas. Figure 14 is a representation of the fractional differences between the DNC and the ETOPO5 databases. This comparison indicates that ETOPO5 depths in many regions are extremely inaccurate, with percentage differences ranging from 20 to 5,000 percent or greater. The Great Bahama Bank, a shallow region located west of the Andros Islands, extends as far down as the Exuma Islands in the DNC database. However, the older ETOPO5 database does not capture this feature. Depths in this region in the ETOPO5 database are on the order of hundreds of meters, whereas the depths given by the DNC database are on the order of meters. This updated bathymetry is expected to dramatically impact the tidal computations since these new features impede the tidal exchange between the Atlantic Ocean and the Gulf of Mexico, forcing the water to travel predominantly through much narrower channels between Florida and the Great Bahama Bank and between Cuba and the Great Bahama Bank. Adding islands and redefining the bathymetry of the sea mounds located on the eastern edge of the Caribbean Sea also restricts the forcing flow at the 60°W meridian to enter the Caribbean basin, altering the dynamics of the tides in the Caribbean and in turn, also affecting the Gulf-Caribbean exchange.

Figure 15 shows fractional differences between the NOS and DNC bathymetric databases. The majority of the common areas that both databases cover have a difference of less than 10 percent, with 10 to 30 percent differences scattered along the continental shelf break. Therefore the DNC database supports the accuracy of the bathymetric values in the NOS database along the United States continental shelf.

The DNC database is used in conjunction with the NOS and ETOPO5 databases to create a new composite bathymetry set for the *Eastcoast 2001* grid, Figure 16. This new bathymetry is based on a priority/availability system. In areas where NOS values, which use a gathering/averaging procedure, are available, they are used. The secondary database used is the DNC, and the third is ETOPO5 if no other sources are available, both of which are interpolated databases. Bathymetry for the southern Louisiana area is provided by regional bathymetric surveys from the U.S. Army Engineer District, New Orleans (Westerink, Luettich, and Pourtaheri 2000).

4 Description and Error Analysis of Field Data

One-hundred-and-one measurement tidal elevation stations with high quality observational data in harmonic constituent form were selected for model validation. These stations are scattered mostly along the coastline and continental shelf as is shown in Figure 17. These 101 stations are used to validate the *Eastcoast 2001* harmonic tidal database values by comparing simulated harmonically decomposed tidal elevation constituents with measured harmonically analyzed published field data. Published measured elevation harmonic constituent data is derived from long-term records of sea surface elevation. The measured station data are obtained from several sources: International Hydrographic Organization Tidal Constituent Bank (IHO) 1991, U.S. Geological Survey 1984, Reid and Whitaker 1981; the NOS Survey,[1] and the NOAA. Stations are listed in Table 2. Stations 1-34 lie along the Atlantic coastline; stas 35-60 and 82 are located in the Gulf of Mexico; stas 61-71, 73, 75, 76, 78, 79, 81, and 88 lie in the Caribbean Sea; and stas 72, 74 , 77, 80, 83-87, and 89-101 are scattered in the deep Atlantic Ocean or near small islands in the Atlantic.

Most of these recording stations are located in open waters or in areas accessible to the adjacent open ocean. A careful study of each station's location was conducted to ensure that the stations closely represent the open-water conditions simulated in the computation. Table 2 provides an overview of the location of each station by indicating if it is in the open ocean with no obstructions or the degree of constriction to the adjacent open waters. If the stations have flow partially impeded, the width of the opening and length of the path between open water and the recording station are noted. Since small inlets were typically not included in the computational domain and grid, it is important that all stations do not lie too far away from open water and/or lie behind highly dissipative lateral or vertical constrictions. All stations selected attempt to represent as closely as possible the adjacent open-water tidal elevation values.

An intercomparison of the harmonic constituent values at stations with multiple published measured values was performed to establish an estimate of the reliability of the data itself. Twenty-one of the 101 stations have two sources of published measured recorded harmonic data, one being the newest release from NOS (2001) and the other being either IHO or a NOAA source, as listed in

[1] Data obtained from National Ocean Service World Wide Web page accessed on 2 May 2001, http://co-ops.nos.noaa.gov/data_retrieve.shtml?input_code=100201001har\.

Table 2. Note that the IHO data originate from older NOS analyses. A comparison study between the latest NOS and IHO/NOAA data was completed over multiple stations.

Measured harmonic constituent amplitude values are compared by calculating a proportional standard deviation per harmonic constituents over all 21 stations throughout the domain and defined regions as shown in the following equations.

$$E^{m}_{j-amp} = \left\{ \frac{\sum_{l=1}^{L} \left[\hat{\eta}_j^{\text{IHO/NOAA}}(x_l, y_l) - \hat{\eta}_j^{\text{NOS}}(x_l, y_l) \right]^2}{\sum_{l=1}^{L} \left[\hat{\eta}_j^{\text{NOS}}(x_l, y_l) \right]^2} \right\}^{1/2} \tag{7}$$

where

L = the total number of elevation stations within a given region

(x_l, y_l) = the location of an elevation station

$\hat{\eta}_j^{\text{IHO/NOAA}}(x_l, y_l)$ = the IHO/NOAA elevation amplitude for constituent *j* at station coordinates (x_l, y_l)

$\hat{\eta}_j^{\text{NOS}}(x_l, y_l)$ = the NOS elevation amplitude for constituent *j* at station coordinates (x_l, y_l)

Measured phase values are compared for each constituent j by computing an absolute average difference defined over a region as:

$$E^{m}_{j-phase} = \frac{1}{L} \sum_{l=1}^{L} \left| \varphi_j^{\text{IHO/NOAA}}(x_l, y_l) - \varphi_j^{\text{NOS}}(x_l, y_l) \right| \tag{8}$$

where

$\varphi_j^{\text{IHO/NOAA}}(x_l, y_l)$ = the IHO/NOAA elevation phase for constituent *j* at measurement location (x_l, y_l)

$\varphi_j^{\text{NOS}}(x_l, y_l)$ = the NOS elevation phase for constituent *j* at measurement location (x_l, y_l)

E^{m}_{j-amp} and $E^{m}_{j-phase}$ are used as best estimates of the error in the measured harmonic amplitude and phase of the published constituent data. The estimated measured data error values for each tidal constituent at all 21 stations with dual measured values in each subregion are listed in Table 3 for the O_1, K_1, Q_1, M_2, N_2, S_2, and

K_2 tidal constituents. Overall the percent errors in amplitudes range between 3.1 and 16.1 percent, the phase differences range between 2.0 and 6.2 deg.

Differences in values of tidal data between the NOS and IHO/NOAA databases can be explained by the constantly shifting bathymetry of coastal regions and of the geometry of the coasts themselves as well as by the occurrences of nontidal events. Over the course of a few years, the geometry and bathymetry of an estuary can change dramatically due to the natural transport of sediments or through dredging operations, thus altering the hydrodynamics of the flow in the area. If an elevation recording station is located in an area where the localized geography is in a perpetual state of change, there may be differences in measured harmonic values depending on when the information was collected. Nontidal events including wind-driven events, such as hurricanes and tropical storms, radiational heating cycles of the surface waters, and other natural disturbances can also perturb observed tidal constituent values from analysis to analysis. The simple intercomparison of the constituent data is only an estimate of the long-term reliability of this data. It is also related to the reliability of shoreline and near coastline bathymetric values. However, these estimates of measurement error for each constituent should be taken into consideration when comparing simulated results to the available measured data.

5 Model Results

Results for the *Eastcoast 2001* tidal database are presented in harmonic constituent form, both globally and locally. Coamplitude and cotidal charts are presented for each of the seven forcing constituents. Comparison plots between computed and measured tidal elevations at each of the 101 tidal elevation measurement stations allow the computations to be validated. Computed to measured harmonic constituent error analysis evaluates the overall performance for each tidal constituent. The measured field data error estimates from the previous chapter are examined to allow a realistic assessment of model performance. Finally, computed-measurement errors for the *Eastcoast 1991* and *Eastcoast 1995* databases are also examined.

Coamplitude and cotidal charts for *Eastcoast 2001* computations are presented for the three diurnal (K_1, O_1, Q_1) and four semidiurnal (M_2, S_2, N_2, K_2) constituents in Figures 18-31. The three diurnal constituents and four semidiurnal constituents respectively exhibit very similar structure within each group. The diurnal tides tend to increase in amplitude within the Gulf of Mexico. The K_1 constituent exhibits an amphidrome or degenerate amphidrome northwest of the Bahamas and north of Cuba as well as off Cancun, Mexico. The O_1 and Q_1 constituents display amphidromes or degenerate amphidromes off Nova Scotia, Canada, northwest of the Bahamas and north of central Cuba as well as off northern Nicaragua. Semidiurnal tides dominate in the Atlantic, and taper in the Gulf of Mexico and the Caribbean Sea. The M_2 constituent shows an amphidrome or degenerate amphidrome off Nantucket Island in the Atlantic, off Puerto Rico in the Caribbean and off Merida, Mexico, in the south central Gulf of Mexico. The S_2 and N_2 constituents also display a degenerate amphidrome off the Island of Grand Bahamas in the Atlantic. Finally, the K_2 constituent only exhibits an amphidrome or degenerate amphidrome off Cancun, Mexico, and the Island of Grand Bahamas.

The reliability of the *Eastcoast 2001* tidal values was evaluated by comparing computed values at the 101 measurement stations for the seven astronomical constituents to available measured elevation field data. Figures 32-132 present the computed versus measured amplitude and phase for the O_1, K_1, Q_1, M_2, S_2, N_2, and K_2 constituents. Each of the seven tidal constituents has a corresponding symbol found in the legend to the right of the plots. Some stations have two sets of constituent symbols. The red set is found on every plot and represents the basic set of IHO, NOAA, and older NOS values. The blue set of symbols shows the updated NOS field measurement data. Each graph has a solid diagonal line with a one-to-one ratio which represents the no error line, and two

sets of dashed lines corresponding either to 5 and 10 percent amplitude error or 10- and 20-deg phase difference.

Ideally when the tidal symbols are plotted, they will fall on the one-to-one ratio line, indicating that the simulated values exactly match the field values. If they fall below the one-to-one line the *Eastcoast 2001* computations under-predicted and if they fall above the line the *Eastcoast 2001* computations over-predicted. The majority of the results fall at least within the 10 percent amplitude and 20-deg phase error range or better, and most of the dominant tidal constituent in each region can be found within the 5 percent amplitude and 10-deg phase error range. Note that phase errors for some of the smaller tidal constituents such as the Q_1 and K_2 can be very large at some stations such as sta 66 at the Curacao Antilles, and sta 68 at Cumana, Venezuela. However, the corresponding amplitudes are extremely small, which could account for its large phasing errors since smaller waves are more susceptible to phase misalignment in the harmonic decomposition of the measurement data.

For each harmonic constituent, plots of amplitude and phase errors are provided at each station throughout the domain in Figures 132-145. The symbols at each station location signify which error range it belongs in; the red color indicates overprediction, whereas the blue color indicates underprediction.

The accuracy of the simulated tides was further quantified by comparing the amplitude and phases of the seven astronomical constituents simulated at the 101 elevation recording stations to the measured field data. The measured data used the most up to date values when multiple values were available at the station. The computed to measured amplitude error for each constituent j was calculated for the entire domain, Atlantic coast, Gulf of Mexico, Caribbean Sea, and the remote stations in the Atlantic Ocean, as a proportional standard deviation as:

$$E_{j-amp}^{c-m} = \left\{ \frac{\sum_{l=1}^{L} \left[\hat{\eta}_j^{computed}(x_l, y_l) - \hat{\eta}_j^{meas}(x_l, y_l) \right]^2}{\sum_{l=1}^{L} \left[\hat{\eta}_j^{meas}(x_l, y_l) \right]^2} \right\}^{1/2} \tag{9}$$

where

L = the total number of elevation stations within a given region

(x_l, y_l) = the location of an elevation station

$\hat{\eta}_j^{computed}(x_l, y_l)$ = the computed model elevation amplitude for constituent j at station coordinates (x_l, y_l)

$\hat{\eta}_j^{meas}(x_l, y_l)$ = the measured elevation amplitude for constituent j at station coordinates (x_l, y_l)

The computed to measured phase error for each constituent j was calculated as an absolute average error defined over a region as:

$$E_{j-phase}^{c-m} = \frac{1}{L}\sum_{l=1}^{L}\left|\varphi_j^{computed}(x_l, y_l) - \varphi_j^{meas}(x_l, y_l)\right| \tag{10}$$

where

$\varphi_j^{computed}(x_l, y_l)$ = the computed model elevation phase for constituent *j* at measurement location (x_l, y_l)

$\varphi_j^{meas}(x_l, y_l)$ = the measured elevation phase for constituent *j* at measurement location (x_l, y_l)

Note that $E_{j-phase}^{c-m}$ excludes stations with phase differences larger than 50 deg associated with very small corresponding amplitudes and highly unreliable measurement data.

Table 4 provides the computed to measured amplitude and phase errors for each of the seven astronomical constituent in each defined portion of the domain. The constituents in Eastcoast 2001 are predicted with proportional standard deviation amplitude errors ranging between 6.2 and 14.1 percent and absolute average phase errors between 8.1 and 12.9 percent. Generally, the amplitude errors for the larger constituents, K_1, O_1, M_2, S_2, and N_2 tides, are smaller than the errors of the Q_1 and K_2 constituents. In regions dominated by diurnal constituents, the diurnal amplitude errors are smaller than the semidiurnal errors, and vice versa for regions dictated by semidiurnal tides. As noted previously, along the Atlantic coast the M_2 tide dominates, whereas the O_1 and K_1 diurnal constituents govern in the Gulf of Mexico.

A comparison of Eastcoast 2001 error levels to that of previous databases as well as the estimated measured field data errors is useful in ascertaining the improvements derived from the additional grid resolution and enhanced bathymetry. For the Eastcoast 1991 database, error levels were obtained from a previous study (Westerink, Luettich, and Scheffner 1993; Westerink, Luettich, and Muccino 1994). For the Eastcoast 1995 database, the average computed to measured data constituent errors was calculated in a similar manner as the errors for Eastcoast 2001 using the updated 101 stations. Errors were calculated as computed to measured data proportional standard deviation over the entire domain as well as the defined regions. Amplitude and phase errors for each tidal database are given in Tables 5-9 globally and by defined regions, and are graphed in Figures 147-151. Each figure corresponds to a defined region and is composed of two bar charts; the top compares amplitude errors (E_{j-amp}^{c-m} for each of the Eastcoast databases and E_{j-amp}^{m} for the measured data) whereas the bottom compares phase errors ($E_{j-phase}^{c-m}$ for each of the Eastcoast databases and $E_{j-phase}^{m}$ for the measured data). In each chart, the x-axis corresponds to the tidal constituent simulated and the y-axis represents the magnitude of the error.

Overall the *Eastcoast 2001* tidal database has significant improvements in amplitude errors for all seven harmonic constituents compared to previous *Eastcoast* databases. Within each subregion, the dominant tide(s) achieved the greatest improvement. Along the Atlantic coastline, error in the dominant tidal constituent, M_2, reduced from 9.3 percent in the *Eastcoast 1995* to 5.6 percent in *Eastcoast 2001*. As expected in the Gulf of Mexico, errors in the dominant astronomical constituents, K_1 and O_1, reduced by over half. This tremendous decrease in amplitude errors within the Gulf is partly due to the updated bathymetry of the Great Bahama Bank. In the Caribbean Sea, most of the errors stayed about the same except for the S_2 constituent for which errors were reduced by half. At the remote stations, there were no significant improvements from *Eastcoast 1995* to *Eastcoast 2001*, indicating that the extra resolution added to the deep Atlantic Ocean was most likely not necessary for accuracy reasons in these tidal simulations. The phase error improvements were more modest than the amplitude error gain. Nonetheless the semidiurnal constituents phases improved significantly in the Atlantic.

Estimated errors for measured field data, from Chapter 3, were also included in the bar charts, Figures 147-151. The errors in the measured field data itself will affect the error analysis between the computed and measured data. In the figures, the measured data error estimates are roughly half the computed to measured data's error values. This indicates that a significant proportion of the errors estimated for *Eastcoast 2001* can be attributed to the uncertainty of the measured field data, and not to the inaccuracy of the numerical computations.

Eastcoast 2001 tidal database simulations were computed on 128 IBM Power3 SMP machines at the U.S. Army Engineer Research and Development Center, Major Shared Resource Center (ERDC, MSRC) in Vicksburg, MS. A 90-day simulation took 58 wall clock hours on 128 processors.

6 Discussion and Conclusions

The *Eastcoast 2001* is the new and improved tidal database for the WNAT domain. The computed harmonic constituents compare very well with measured data throughout the domain. Computed harmonic constituents compare to measured amplitude data to within 6 to 13 percent and to measured phase data to within 7 to 13 deg on a globally averaged basis. In general, comparisons to measured data are the best in the Atlantic Ocean and the worst in the Caribbean Sea. This is not entirely surprising since the bathymetric data is least accurate in the Caribbean Basin, particularly on the continental shelves and near the Lesser Antilles Ridge, which controls the Atlantic-Caribbean coupling. In general, the dominant tidal constituent in a given basin is the most accurately modeled constituent. Thus, on average the M_2, N_2, and S_2 constituents compare to measured amplitude data to within 6 to 7 percent and to measured phase data to within 4 to 8 deg in the Atlantic. The K_1 and O_1 constituents on average compare to measured amplitude data to within 10 to 11 percent and measured phase data to within 6 to 9 deg in the Gulf of Mexico. Considering potential measurement data error estimates puts the computed to measured data agreement into perspective. Typically, measured data error estimates are half of the computed to measured data errors. Since the computed to measured data errors include the uncertainty in the measured data, it is clear that a substantial portion of the reported computed to measured data errors originate from the errors in the measured data.

Improvements made to the *Eastcoast 2001* tidal database stem from a highly detailed grid, updating the coastline boundary with greater detail and precision and applying an improved bathymetric database. The *Eastcoast 2001* database computations applied a 254,629-node grid based on a combination of the widely used wavelength to grid-size ratio and the topographic length scale criteria. Together these criteria produced a state-of-the-art grid to accurately capture the change in the wavelength's energy as it travels from the deep ocean over the shelf break onto the continental shelf and to the shore. Maximum grid resolution was defined as 25 km, and minimum resolution was defined as 1 to 4 km. Although it appears that elements in deep waters can be larger than 25 km from an accuracy perspective, potential long-term stability problems led to the use of this level resolution in all deeper waters.

The coastline boundaries were updated with the World Vector Shoreline database. Significant islands could be added in the Bahamas as well as in the

Caribbean due to the improved grid resolution. Bathymetry for the *Eastcoast 2001* grid was derived from three different bathymetric sources, NOS, DNC, and ETOPO5. The accuracy and reliability of these databases dictated a priority/ availability system with NOS data being used where available, then DNC and finally ETOPO5. Le Provost's (1998) worldwide tidal database, FES95.2, was used to force the open-ocean boundary.

Further improvements to the WNAT model will be possible with more accurately defined bathymetry. This is especially true in the non-U.S. waters, namely the southern portion of the Gulf of Mexico and the Caribbean Sea. In particular, in the vicinity of the Lesser Antilles, often the bathymetry does not match the placement of islands, thus raising questions to the reliability of the topography. A higher level of bathymetric detail in this area could make significant improvements in the computed response in the Caribbean since this underwater range of mounds controls the tidal exchange between the Atlantic and the Caribbean. Better response in the Caribbean will also affect the responses in the Gulf of Mexico due to the exchange between these two basins.

Finally, in addition to improving the global bathymetry, increasing grid and bathymetric refinement in select bays and inlets with measurement data stations will allow for further improvements in the match between computations and measurements at these stations which do not lie in open water.

References

Blain, C. A., Westerink, J. J., and Luettich, R. A., Jr. (1994). "The influence of domain size on the response characteristics of a hurricane storm surge model," *Journal of Geophysical Research* 99(C9), 18,467-18,479.

Blain, C. A., Westerink, J. J., and Luettich, R. A., Jr. (1998). "Grid convergence studies for the prediction of hurricane storm surge," *International Journal for Numerical Methods in Fluids* 26, 369-401.

Hagen, S. C. (1998). "Finite element grids based on a localized truncation error analysis," Ph.D. diss., Department of Civil Engineering and Geological Science, University of Notre Dame, IN.

Hagen, S. C., Westerink, J. J., and Kolar, R. L. (2000). "One-dimensional finite element grids based on a localized truncation error analysis," *International Journal for Numerical Methods in Fluids* 32, 241-261.

Hagen, S. C., Westerink, J. J., Kolar, R. L., and Horstmann, O. (2001). "Two-dimensional, unstructured mesh generation for tidal models," *International Journal for Numerical Methods in Fluids* 35, 669-686.

Hannah C. G., and Wright, D. G. (1995). "Depth dependent analytical and numerical solutions for wind-driven flow in the coastal ocean," *Quantitative Skill Assessment for Coastal Ocean Models*. D. R. Lynch and A. M. Davies, ed., A.G.U. 47, 125-152 (1995).

Hendershott, M. C. (1981). "Long waves and ocean tides," *Evolution of Physical Oceanography*. B. A. Warren and C. Wunsch, ed., MIT Press, Cambridge, MA, 292-341.

Kashiyama, K. and Okada, T. (1992). "Automatic mesh generation method for shallow water flow analysis," *International Journal for Numerical Methods in Fluids* 15, 1,037-1,057.

Kolar, R. L., Westerink, J. J., Cantekin, M. E., and Blain, C. A. (1994a). "Aspects of nonlinear simulations using shallow water models based on the wave continuity equation," *Computers and Fluids* 23, 3, 523-538.

Kolar, R. L., Gray, W. G., Westerink, J. J., and Luettich, R.A. (1994b). "Shallow water modeling in spherical coordinates: Equations formulation, numerical implementation and application," *Journal of Hydraulic Research* 32(1), 3-24.

Kolar, R. L., Gray, W.G., and Westerink, J. J. (1996). "Boundary conditions in shallow water models—an alternative implementation for finite element codes," *International Journal for Numerical Methods in Fluids* 22, 603-618.

Le Provost, C., Bennett, A. F., and Cartwright, D. E. (1995). "Ocean tides for and from TOPEX/POSEIDON," *Science* 267, 639-642.

Le Provost, C., Lyard, F., Molines, J. M., Genco, M. L., and Rabilloud, F. (1998). "A hydrodynamic ocean tide model improved by assimilating a satellite altimeter-derived data set," *Journal of Geophysical Research* 103, 5,513-5,529.

Luettich, R. A., and Westerink, J. J. (1991). "A solution for the vertical variation of stress, rather than velocity, in a three-dimensional circulation model," *International Journal for Numerical Methods in Fluids* 12, 911-928.

Luettich, R. A., Westerink, J. J., and Scheffner, N. W. (1992). "ADCIRC: An advanced three-dimensional circulation model for shelves, coasts, and estuaries, Report 1: Theory and methodology of ADCIRC-2DDI and ADCIRC-3DL," Technical Report DRP-92-6, U.S. Army Engineer Waterways Experiment Station, Coastal and Hydraulics Laboratory, Vicksburg, MS.

Luettich, R. A., Hu, S., and Westerink, J. J. (1994). "Development of the direct stress solution technique for three dimensional hydrodynamic models using finite elements," *International Journal for Numerical Methods in Fluids* 19, 295-319.

Luettich, R. A., and Westerink, J. J. (1995a). "Continental shelf scale convergence studies with a barotropic model," *Quantitative skill assessment for coastal ocean models*. D. R. Lynch and A. M. Davies, ed., American Geophysical Union.

Luettich, R. A., and Westerink, J. J. (1995b). "An assessment of flooding and drying techniques for use in the ADCIRC hydrodynamic model: Implementation and performance in one-dimensional flows," Contract Report prepared for the U.S. Army Engineer District, Vicksburg, MS.

Luettich, R. A., and Westerink, J. J. (1999). "Elemental wetting and drying in the ADCIRC hydrodynamic model: Upgrades and documentation for ADCIRC Version 34.XX," Contract Report prepared for the Department of the Army, U.S. Army Engineer Waterways Experiment Station, Vicksburg, MS.

National Ocean Service. (1997). Hydrographic Survey Digital Database, CD-ROM set, 1 Vol, version 3.3.

Reid, R. O., and Whitaker, R. E. (1981). "Numerical model for astronomical tides in the Gulf of Mexico," Technical Report for the U.S. Army Engineer Waterways Experiment Station, Department of Oceanography, Texas A&M University.

Reid, R. O. (1990). "Water level changes," *Handbook of Coastal and Ocean Engineering*. J. Herbich, ed., Gulf Publishing, Houston, TX.

Roe, M. J. (1998). "Achieving a dynamic steady state in the western North Atlantic/Gulf of Mexico/Caribbean using graded finite element grids," Master's thesis, Department of Civil Engineering and Geological Science, University of Notre Dame.

Schwiderski, E. W. (1979). "Global ocean tides; Part II: The semidiurnal principal lunar tide (M_2)," *Atlas of tidal charts and maps*, MSWC TR 79-414.

Soluri, E. A., and Woodson, V. A. (1990). *1990* "World vector shoreline," *International Hydrographic Review*, LXVII(1).

U.S. Department of Defense. (1999). National Imagery Mapping Agency, Digital Nautical Chart, Washington, DC.

Westerink, J. J., Luettich, R. A., Jr., Blain, C. A., and Scheffner, N. W. (1992). "ADCIRC: An advanced three-dimensional circulation model for shelves, coasts, and estuaries, Report 2: Users manual for ADCIRC-2DDI," Technical Report DRP 92-6, Coastal and Hydraulics Laboratory, U.S. Army Engineer Research and Development Center, Vicksburg, MS.

Westerink, J. J., Luettich, R. A., Jr., and Scheffner, N. W. (1993). "ADCIRC: An advanced three-dimensional circulation model for shelves, coasts, and estuaries, Report 3: Development of a tidal constituent database for the western north Atlantic and Gulf of Mexico," Technical Report DRP 92-6, U.S. Army Engineer Research and Development Center, Coastal and Hydraulics Laboratory, Vicksburg, MS.

Westerink, J. J., Luettich, R. A., Jr., and Muccino, J. C. (1994). "Modeling tides in the western North Atlantic using unstructured graded grids," *Tellus* 46A, 178-199.

Westerink, J. J., Luettich, R. A., Jr., Wu, J. K., and Kolar, R. L. (1994). "The influence of normal flow boundary conditions on spurious modes in finite element solutions to the shallow water equations," *International Journal for Numerical Methods in Fluids* 18, 1,021-1,060.

Westerink, J. J., Luettich, R. A., Jr., and Kolar, R. L. (1996). "Advances in finite element modeling of coastal ocean hydrodynamics," *Comp. Methods in Water Resources XI* 2. A. A. Aldama et al., ed., 313-322.

Westerink, J. J., Luettich, R. A., Jr., and Pourtaheri, H. (2000). "Hurricane simulations within the Lake Pontchartrain – Gulf of Mexico system; Historical hindcasts and design storms," prepared for the Technical Review Board, U.S. Army Engineer District, New Orleans.

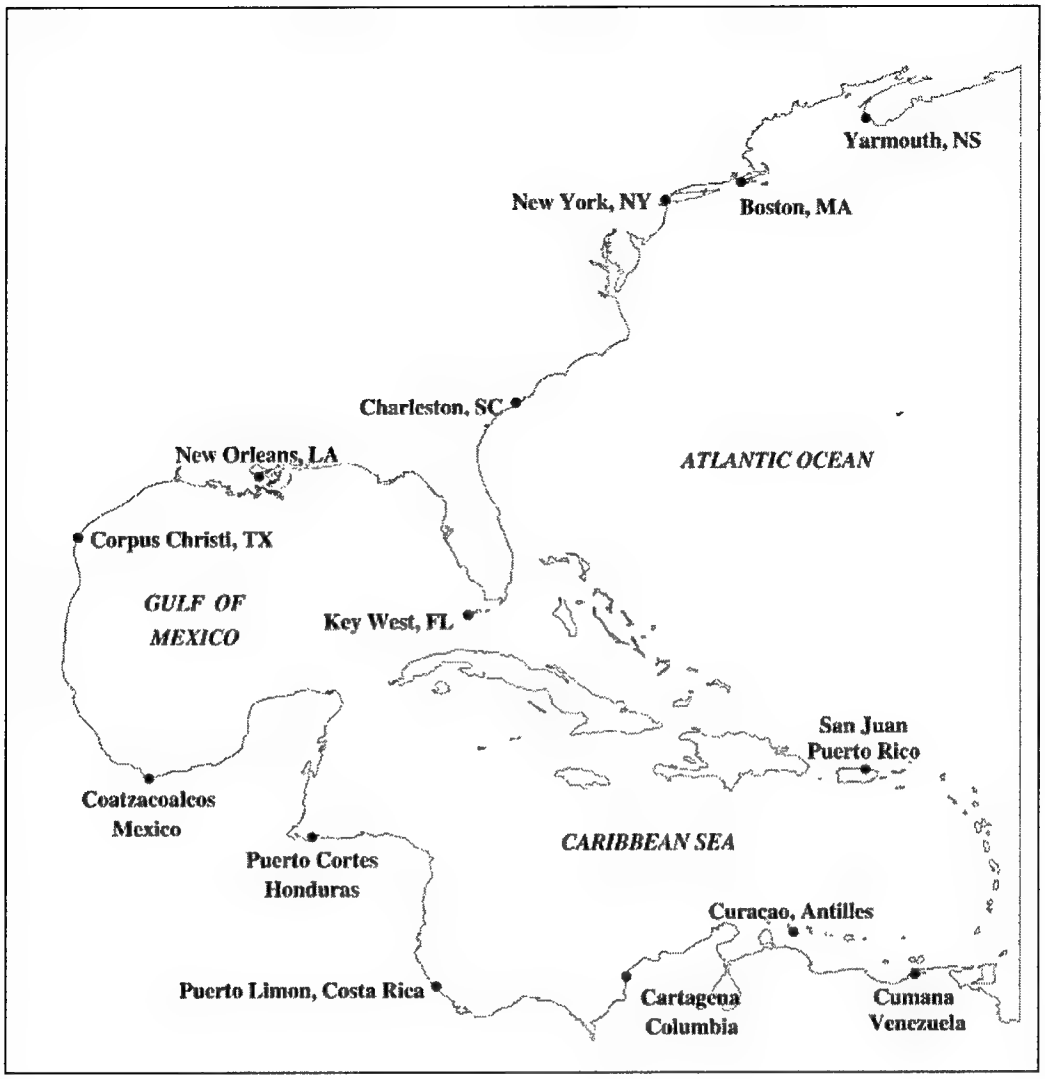

Figure 1. *Eastcoast 2001* domain boundary

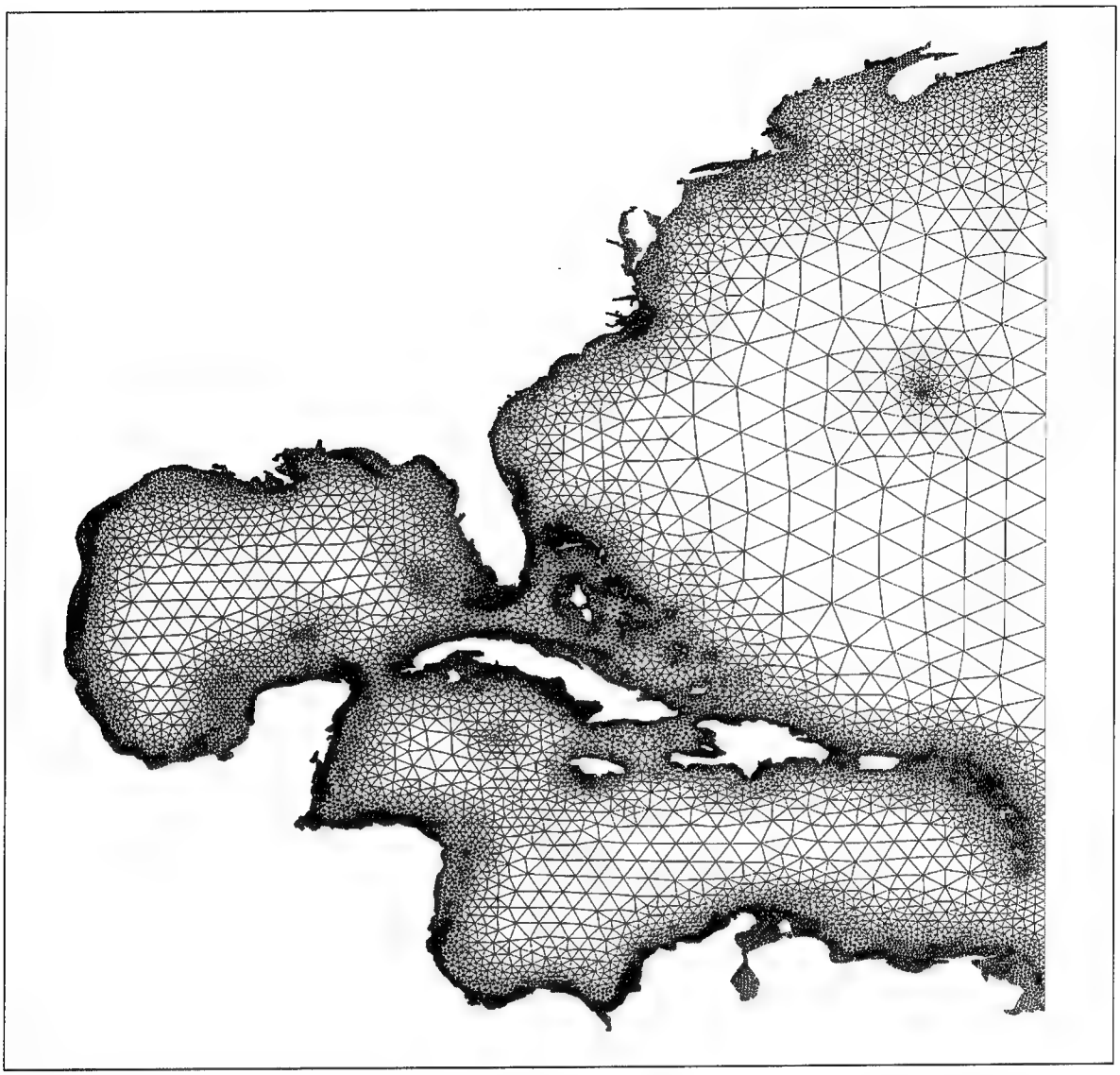

Figure 2. *Eastcoast 1991* finite element grid

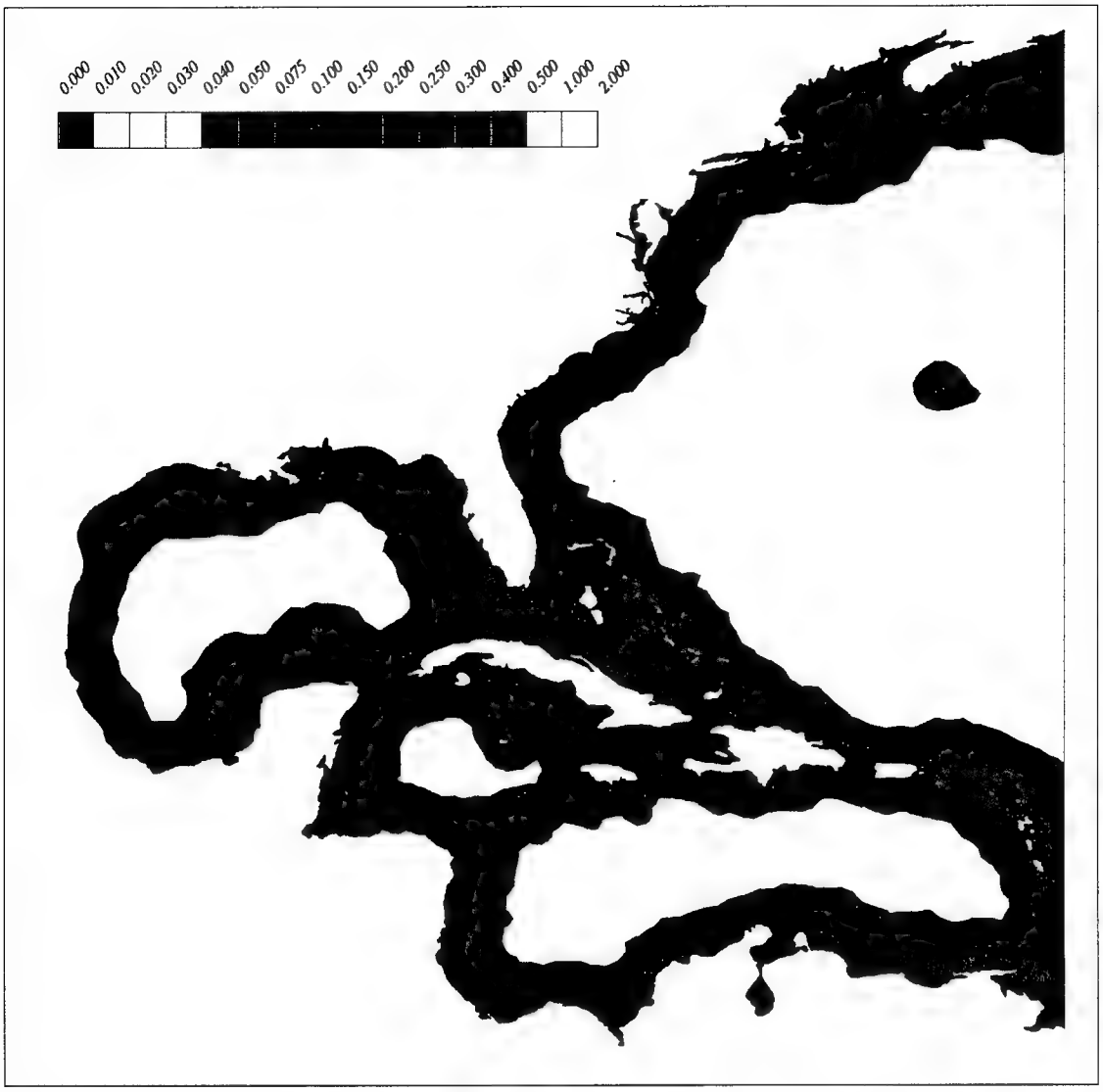

Figure 3. *Eastcoast 1991* grid size (in degrees). Approximate grid size in kilometers is obtained by multiplying legend values by 100

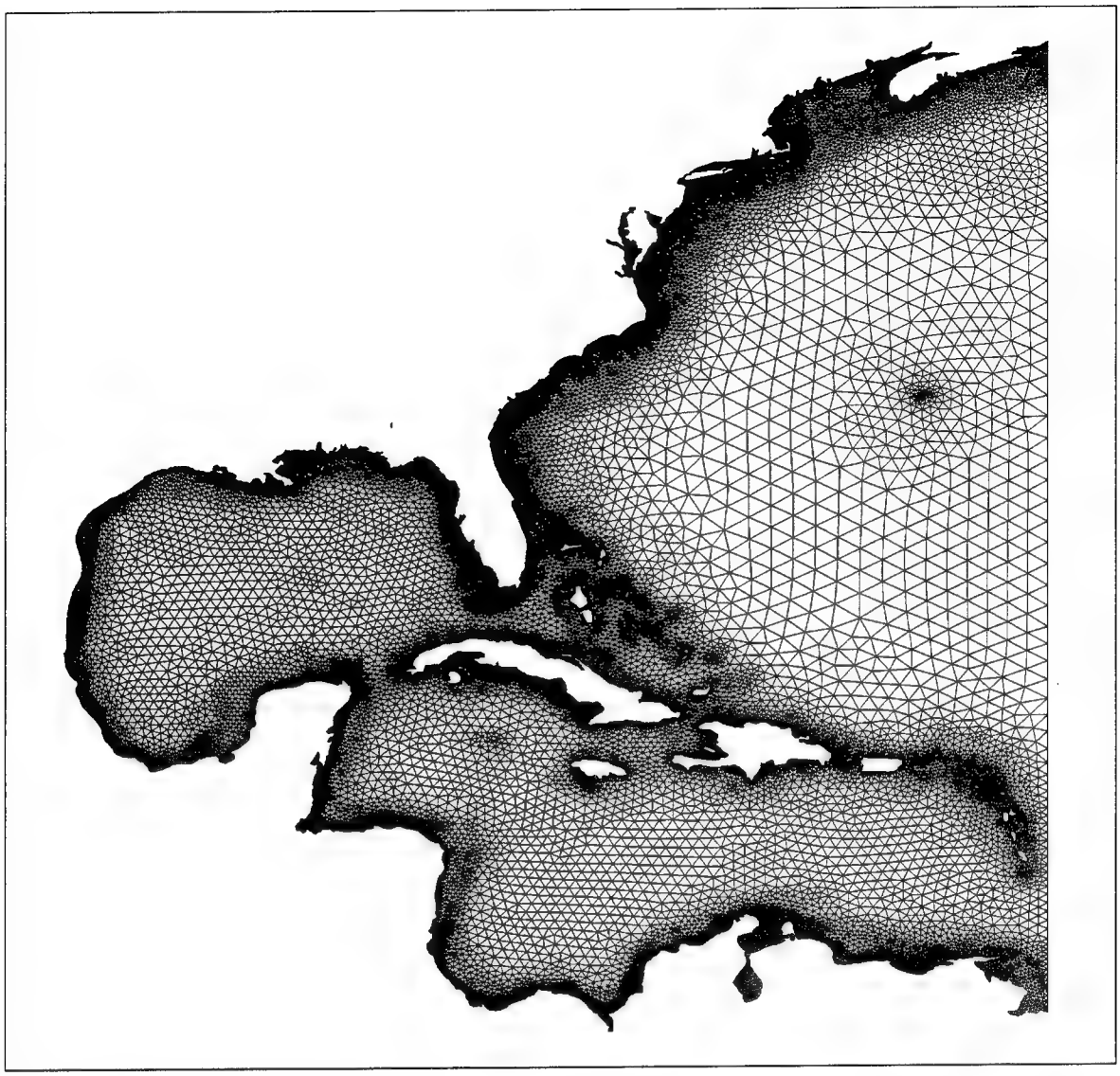

Figure 4. *Eastcoast 1995* finite element grid

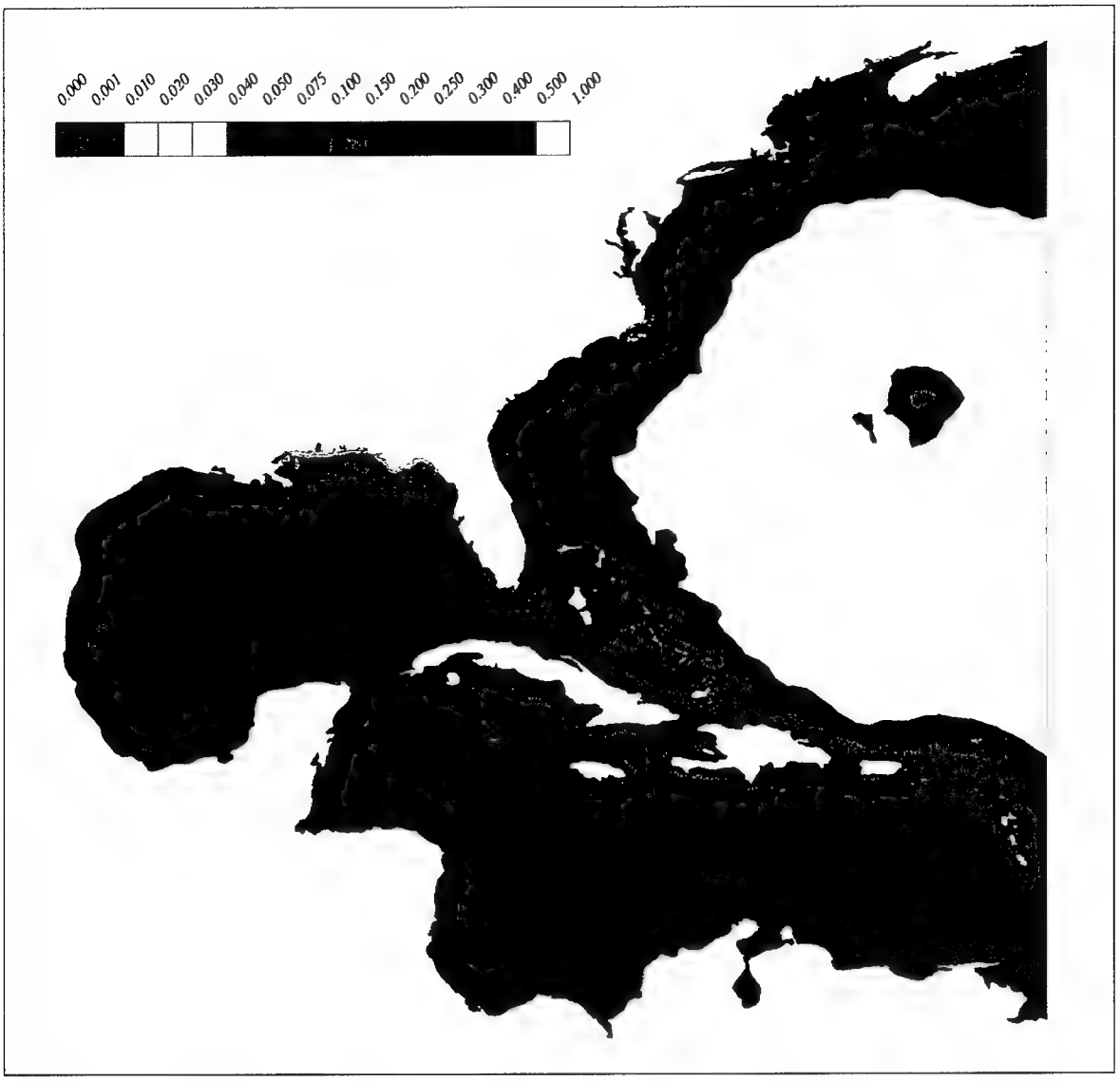

Figure 5. *Eastcoast 1995* grid size (in degrees). Approximate grid size in kilometers is obtained by multiplying legend values by 100

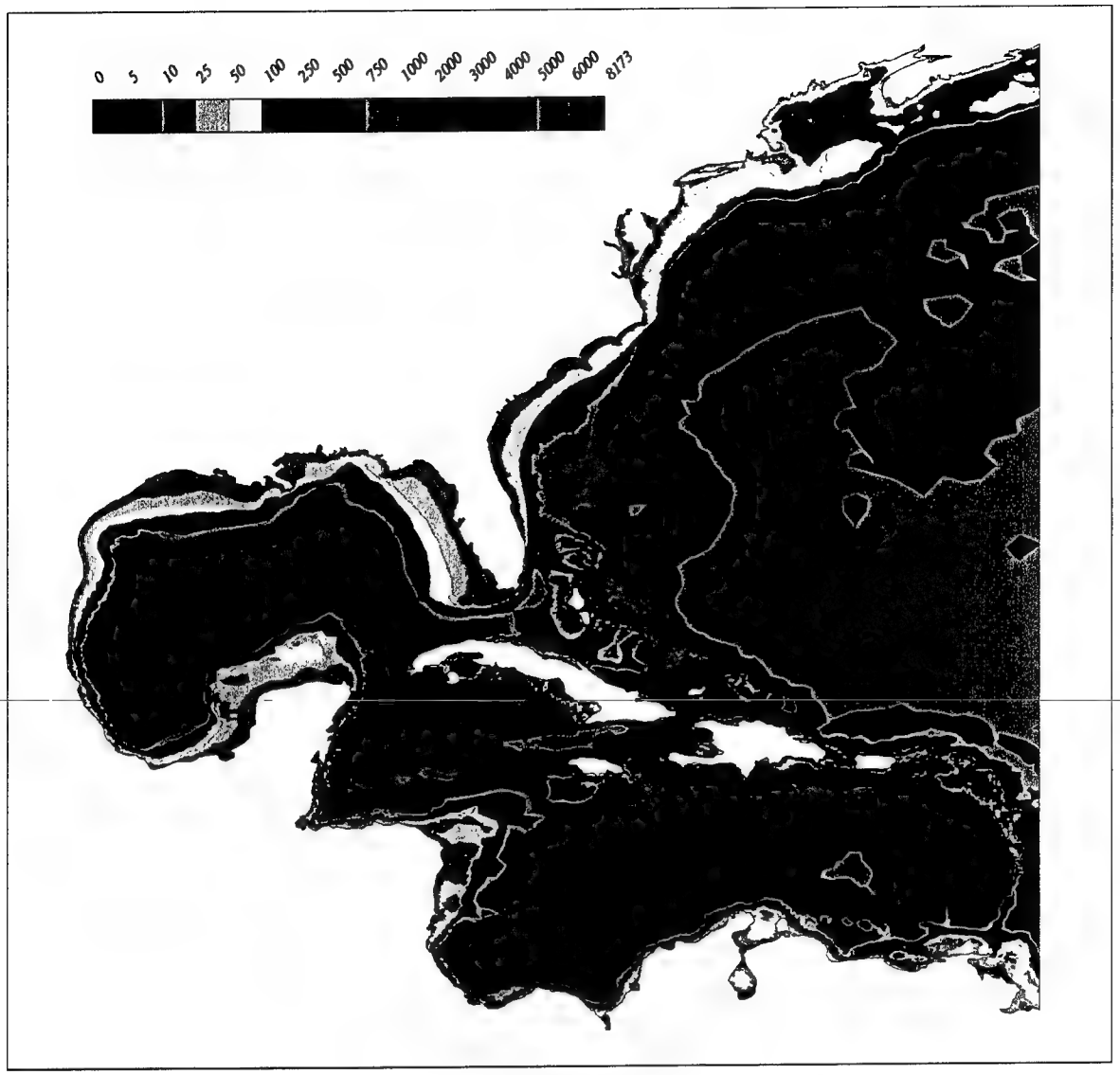

Figure 6. *Eastcoast 1995* bathymetry in meters relative to geoid

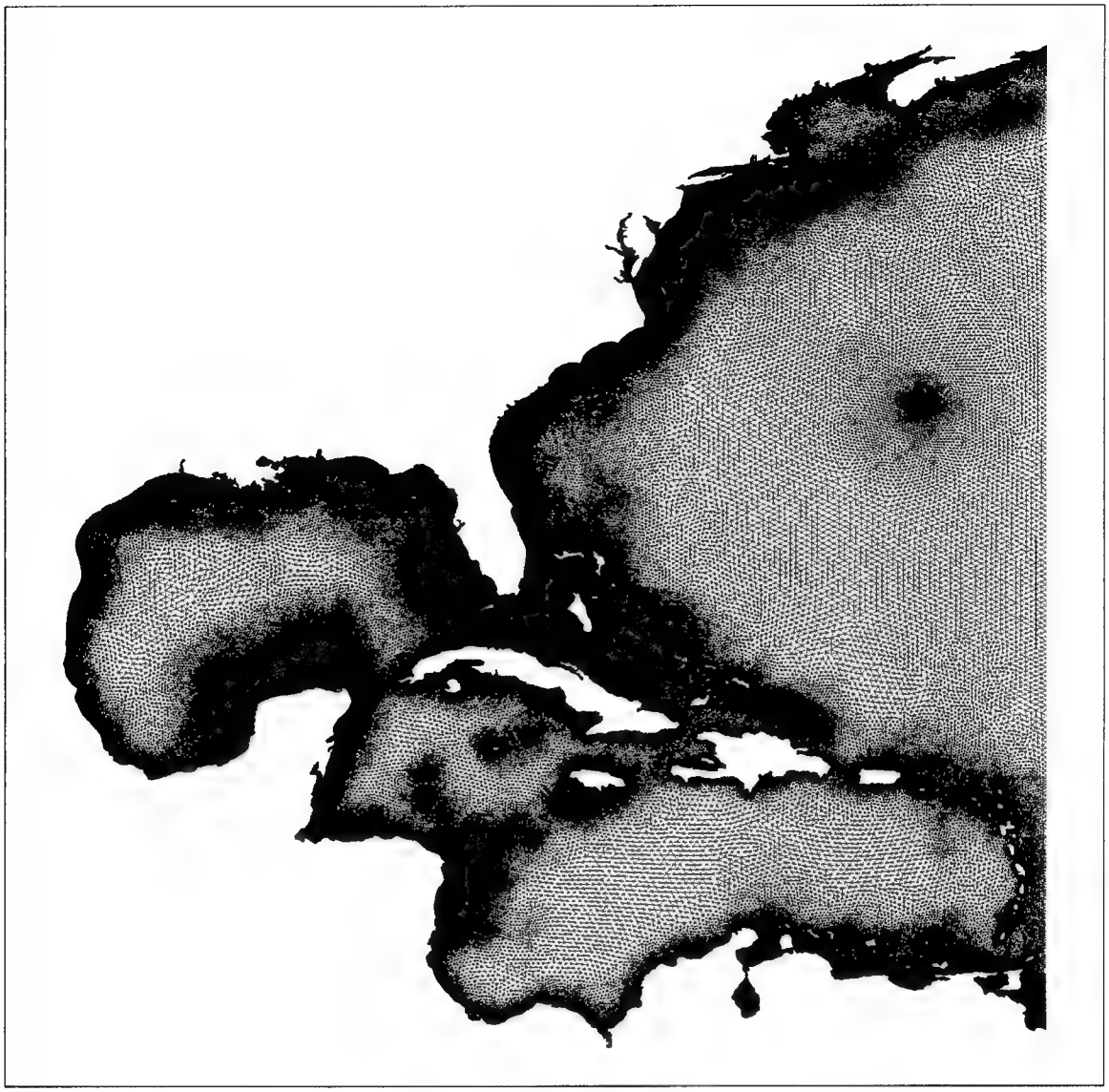

Figure 7. *Eastcoast 2001* finite element grid

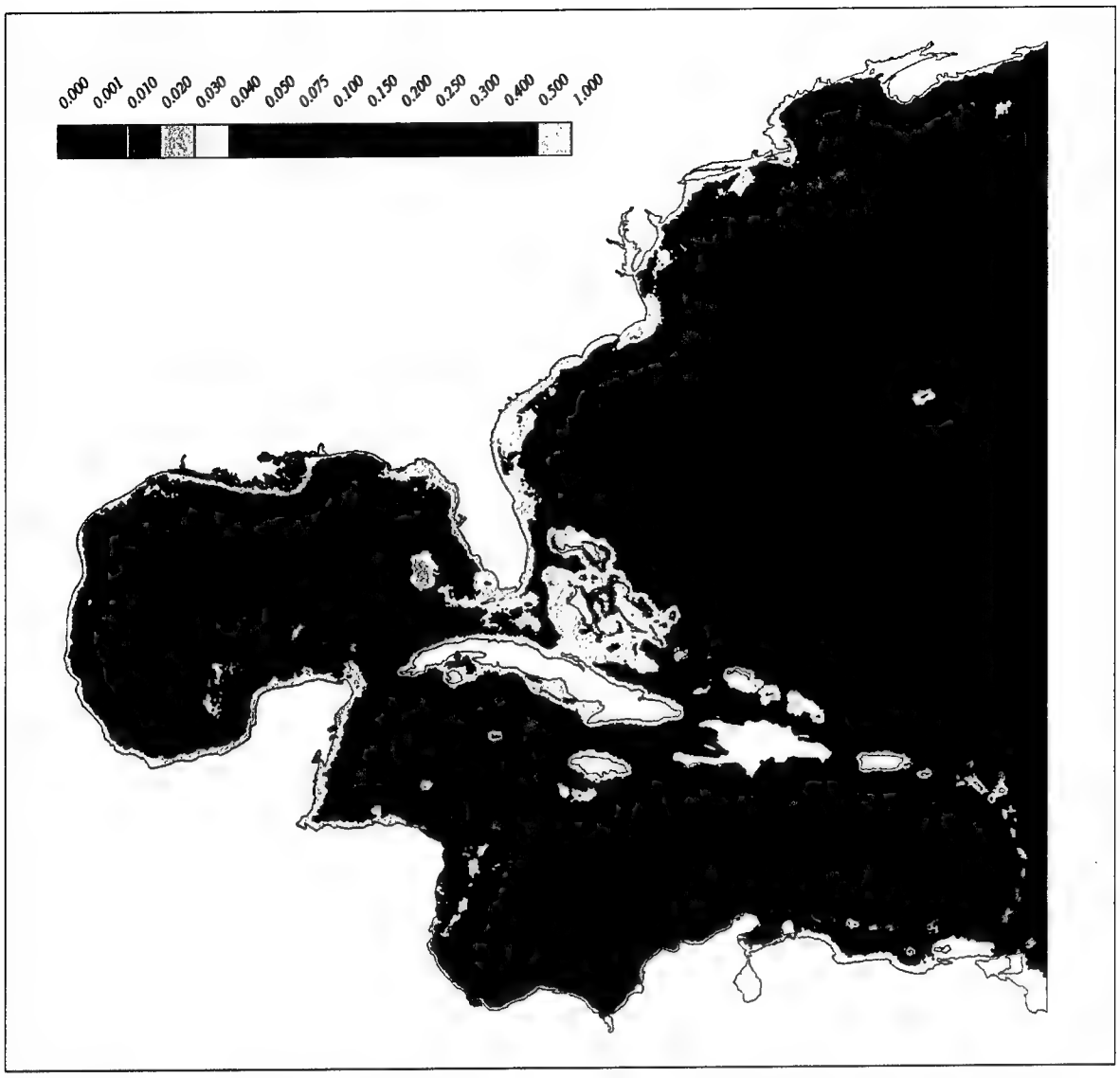

Figure 8. *Eastcoast 2001* grid size in degrees. Approximate grid size in kilometers is obtained by multiplying legend values by 100

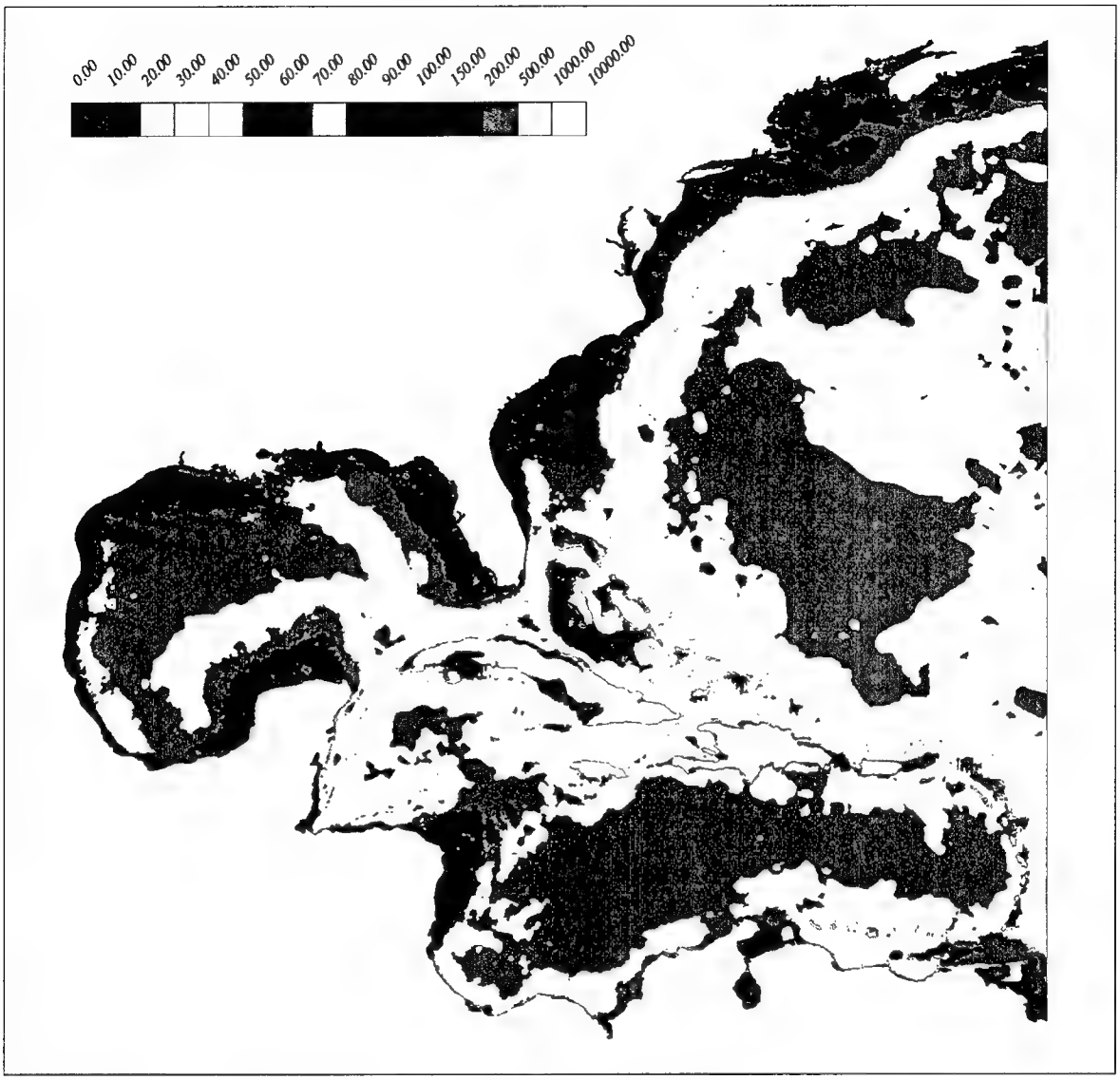

Figure 9. *Eastcoast 2001* wavelength to grid size ratio

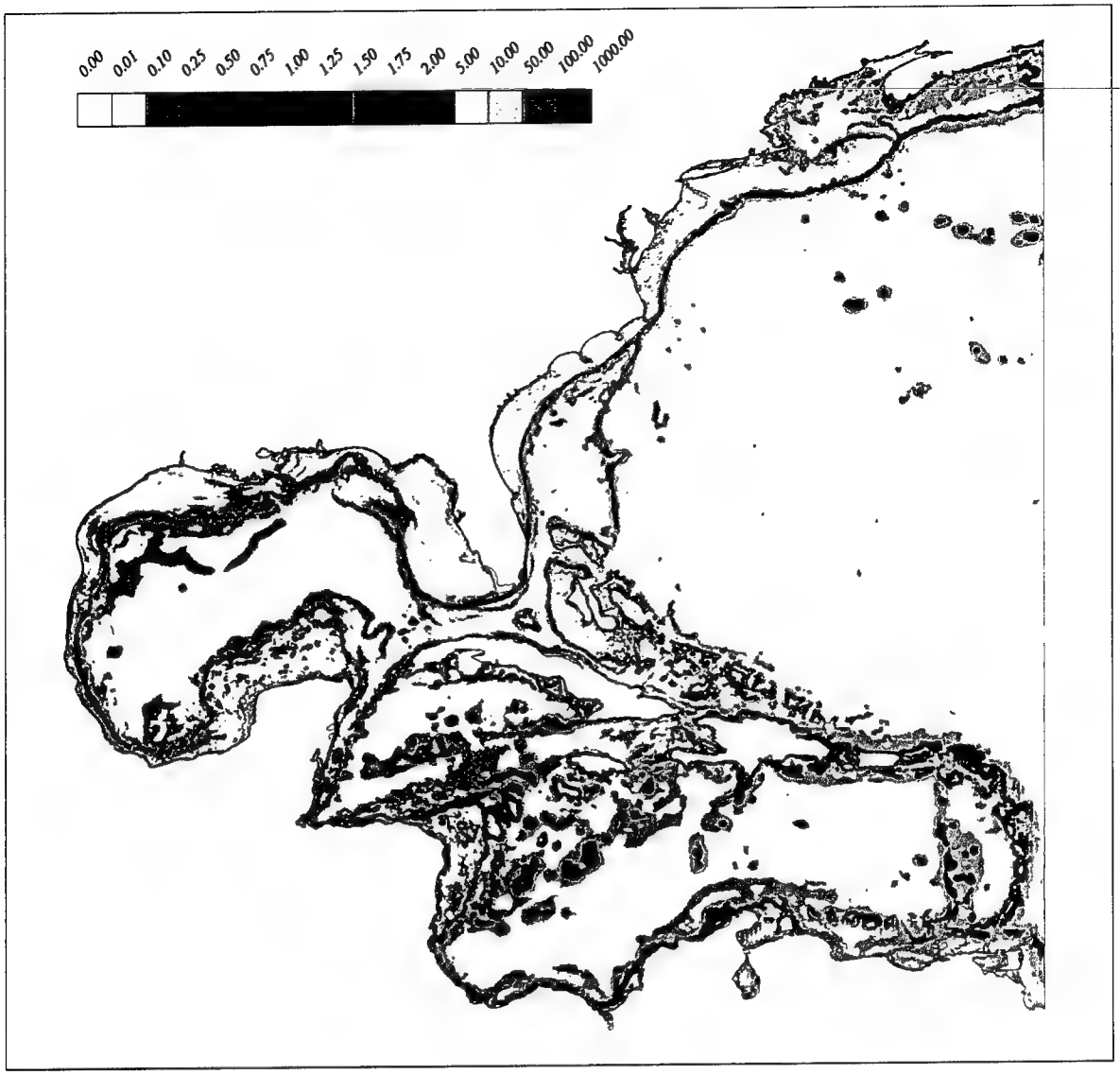

Figure 10. *Eastcoast 2001* topographic length scale (parameter value α)

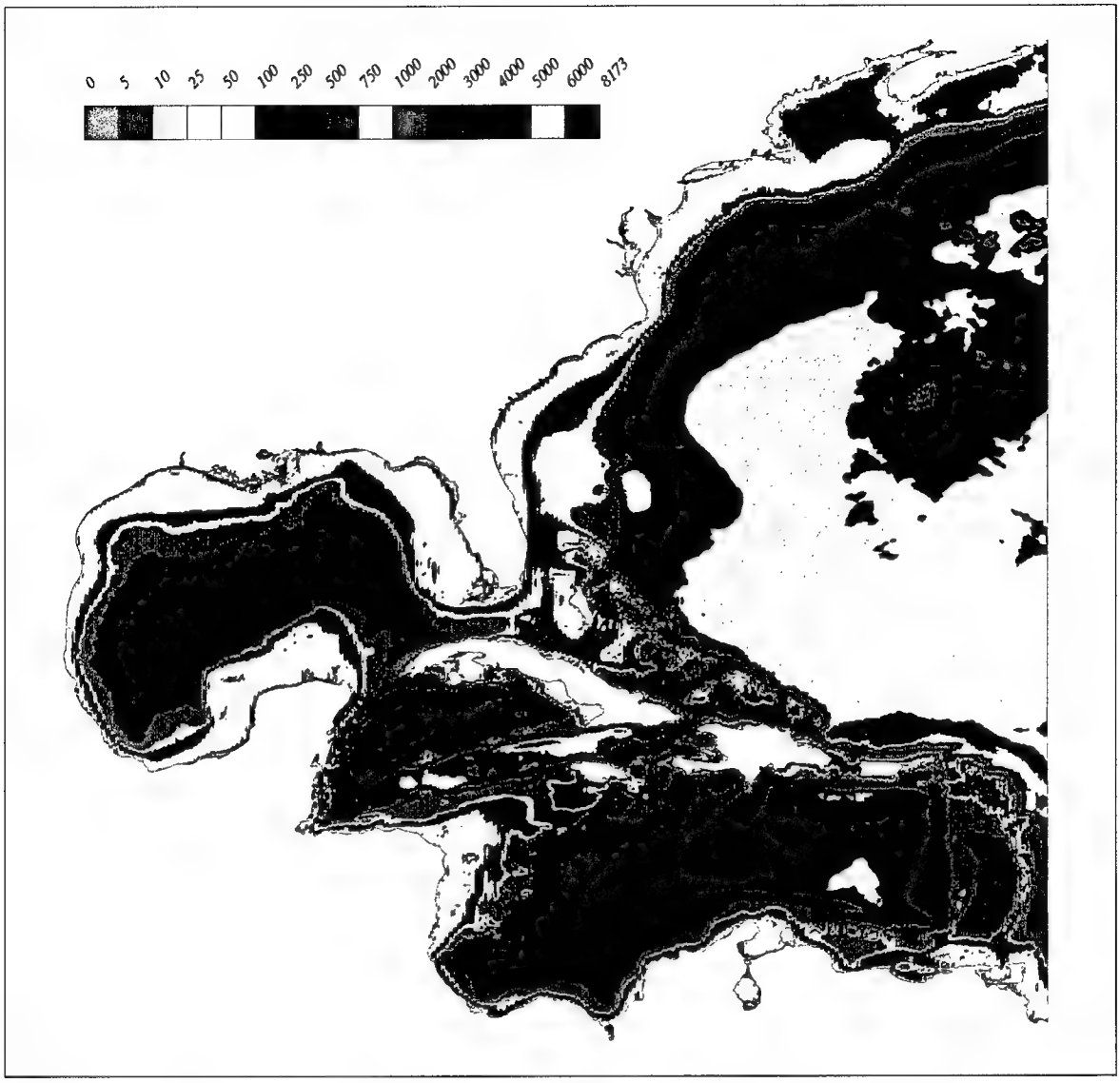

Figure 11. ETOPO5 bathymetric database (depths in meters relative to geoid)

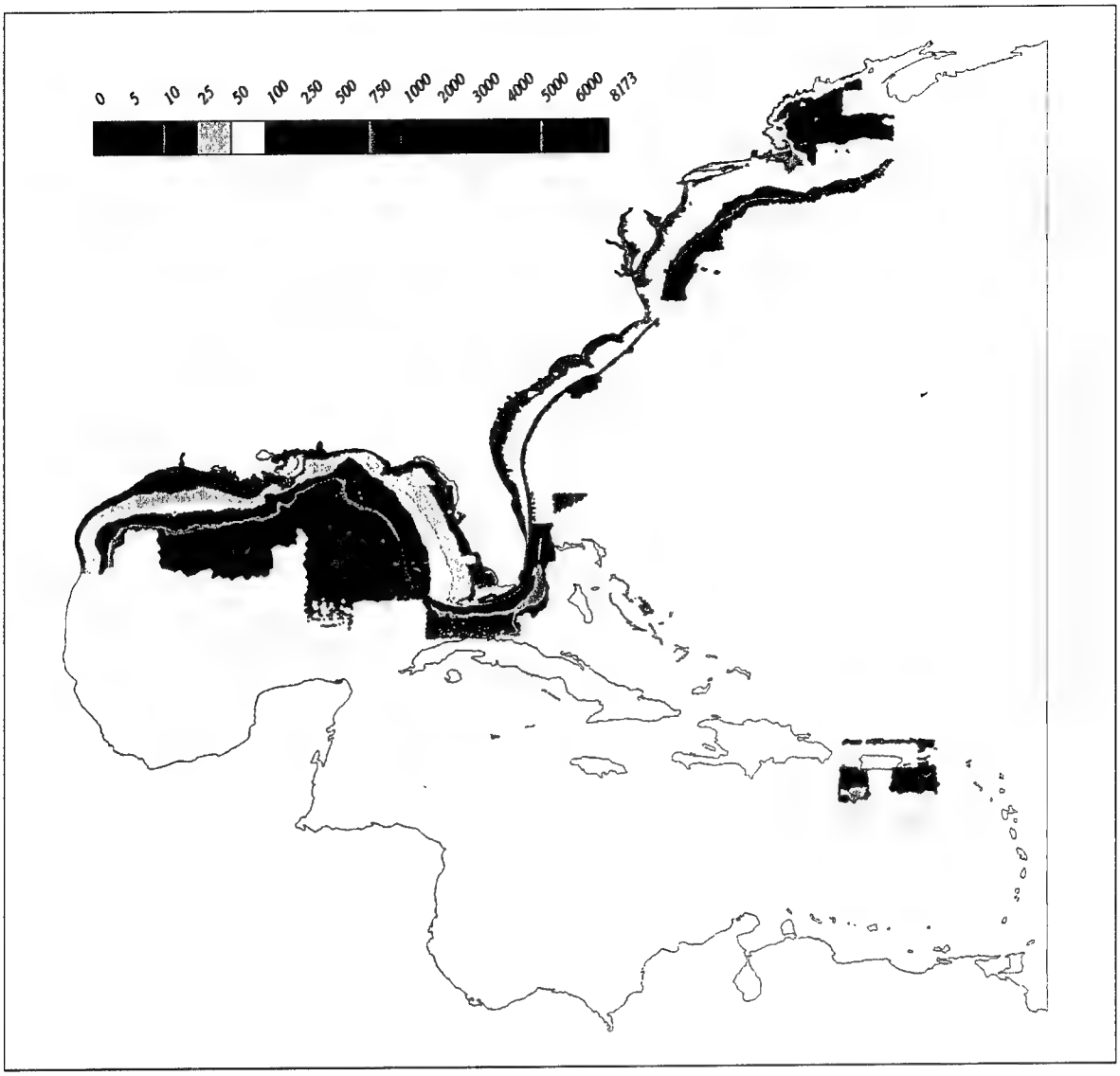

Figure 12. NOS bathymetric database (depths in meters relative to geoid)

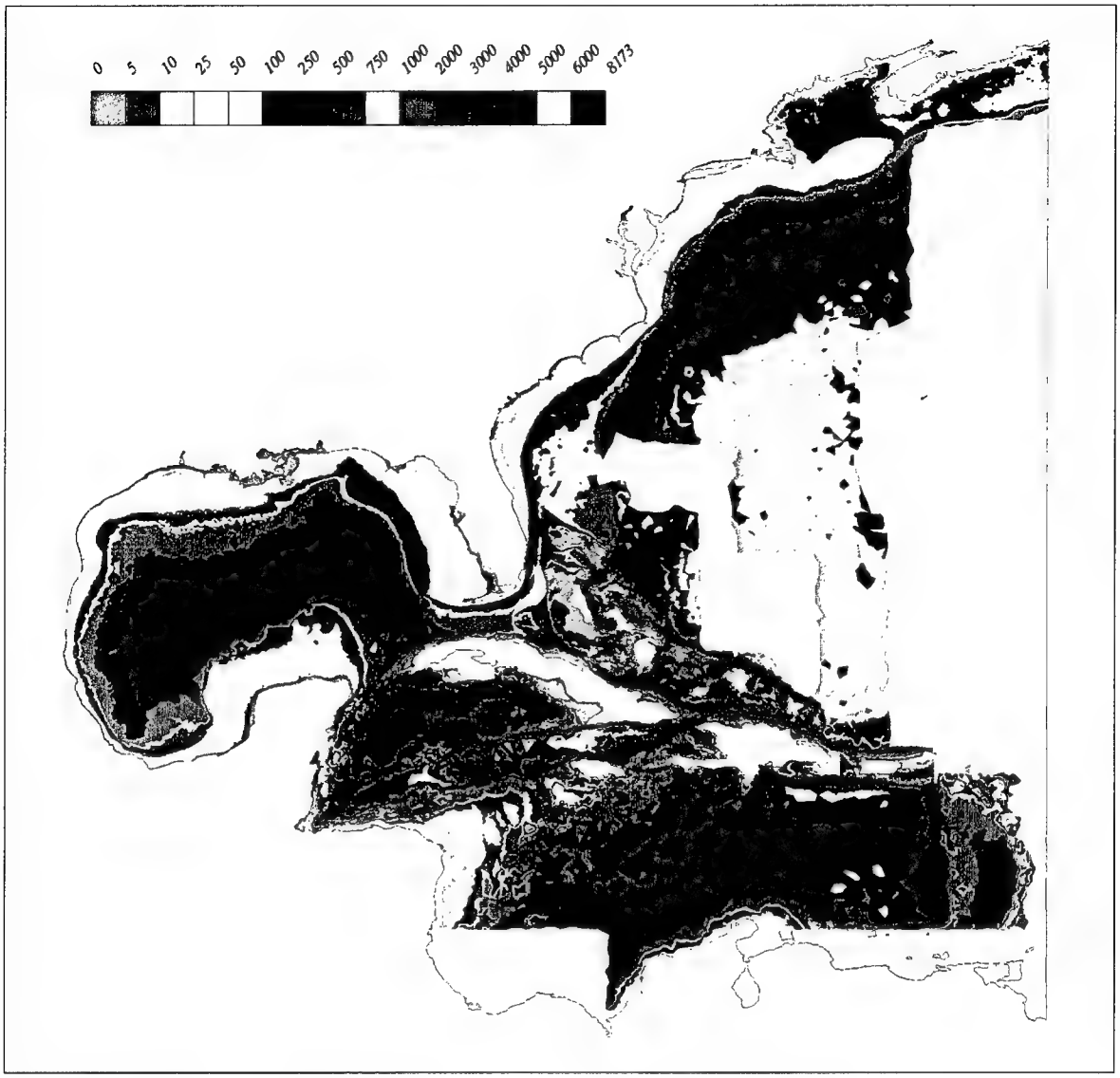

Figure 13. DNC bathymetric database (depths in meters relative to geoid)

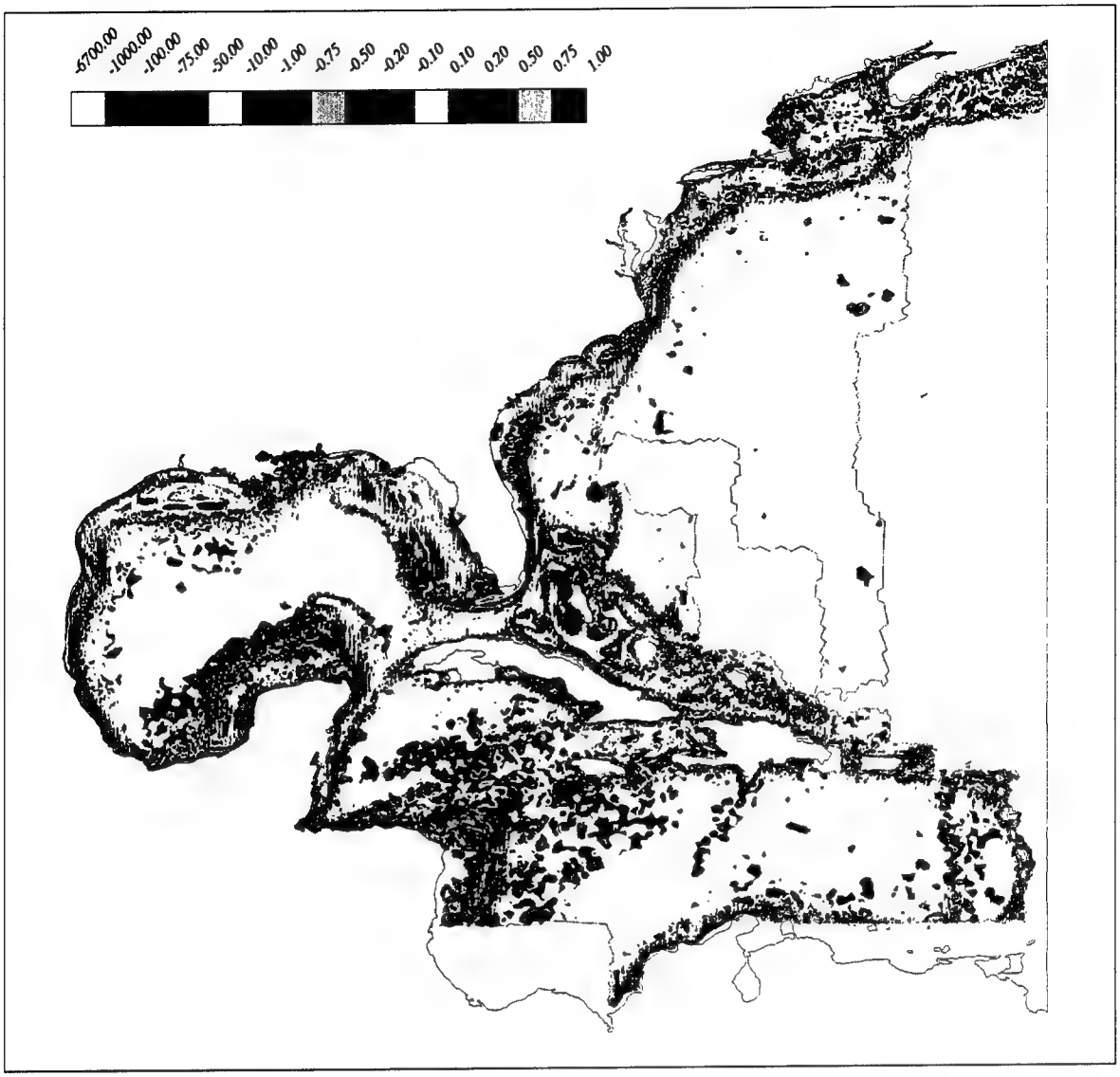

Figure 14. Fractional differences between DNC and ETOPO5 bathymetric databases (multiply legend values by 100 to obtain percentages)

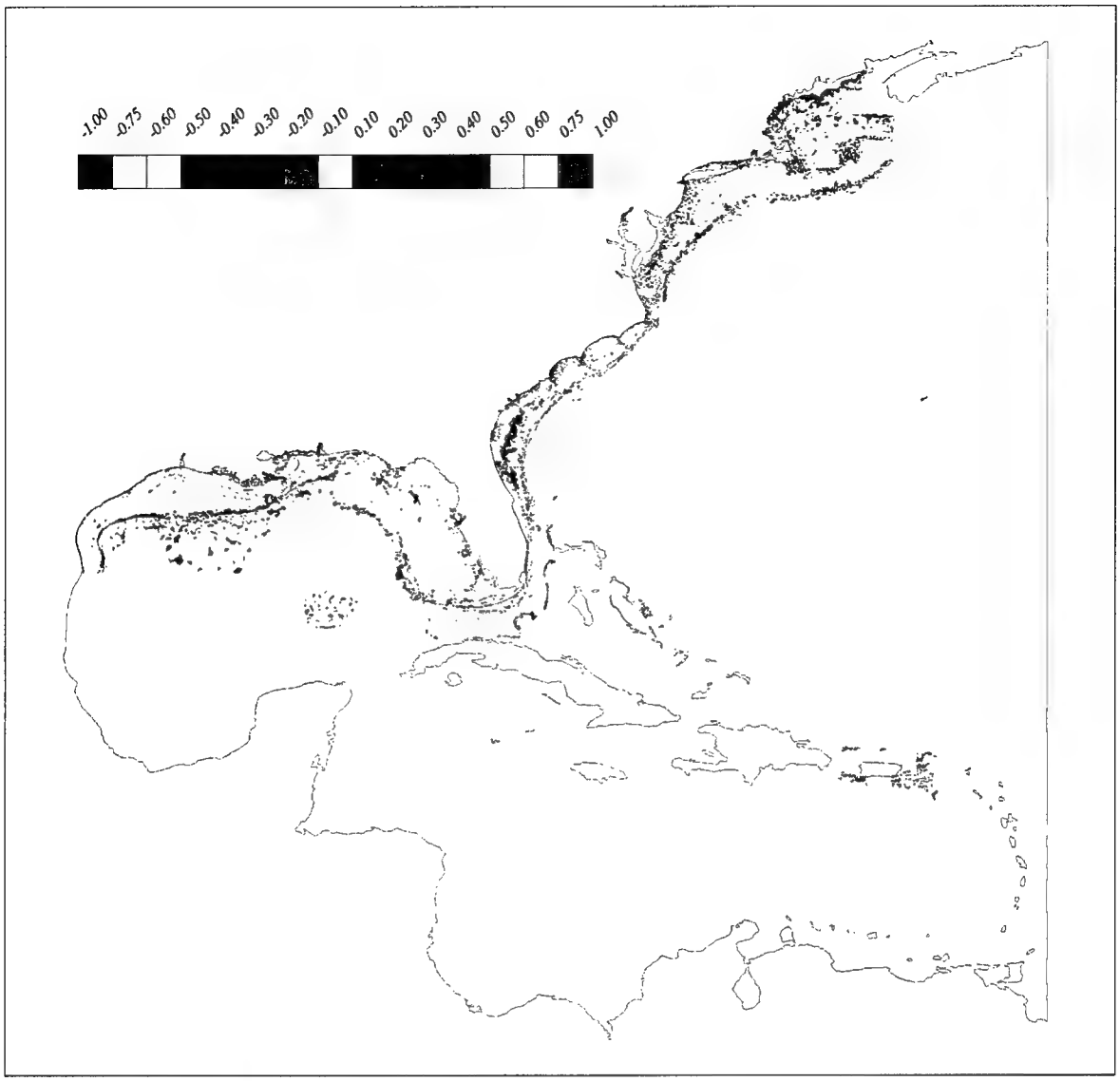

Figure 15. Fractional differences between NOS and DNC bathymetric databases (multiply legend values by 100 to obtain percentages)

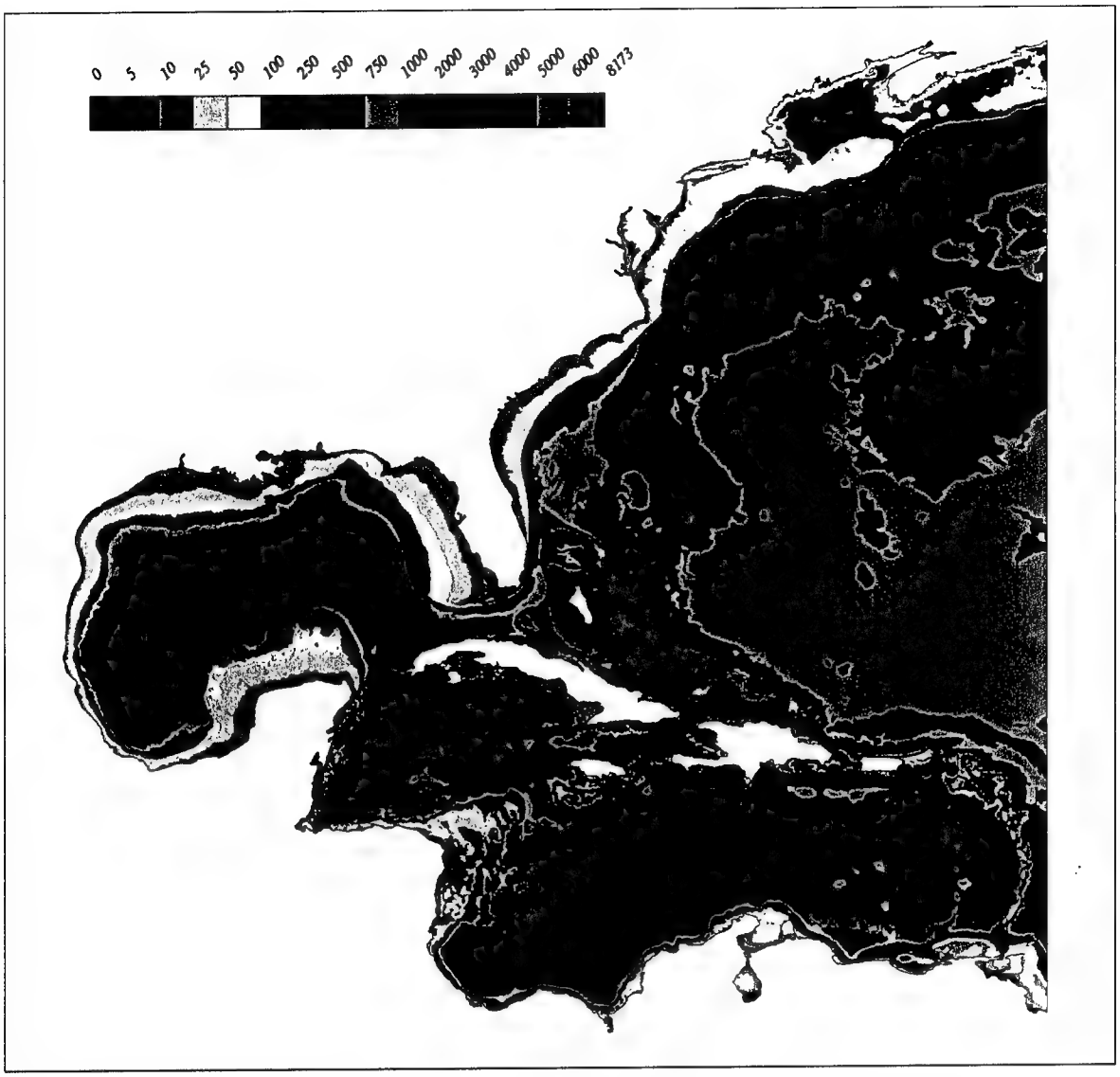

Figure 16. *Eastcoast 2001* composite bathymetry (depths in meters relative to geoid)

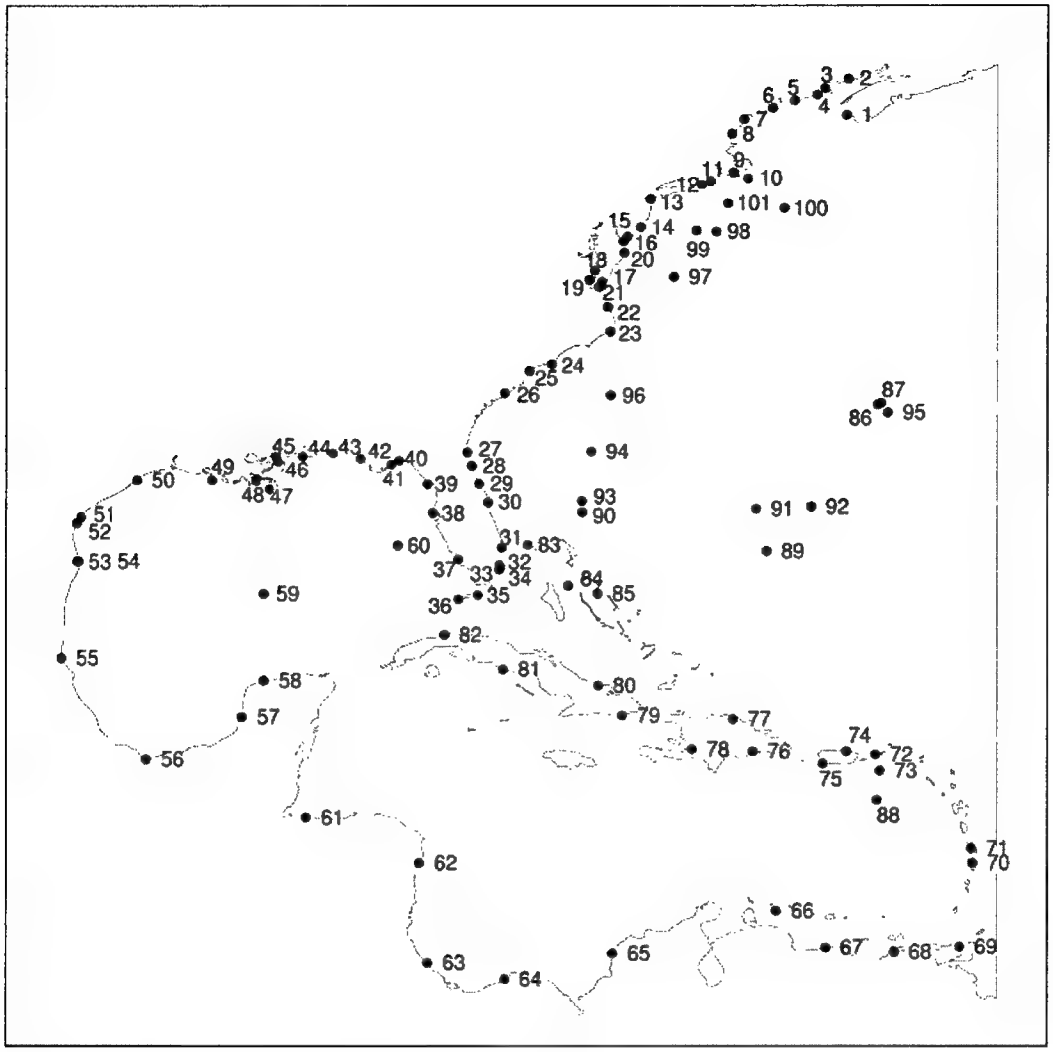

Figure 17. 101 elevation measurement stations

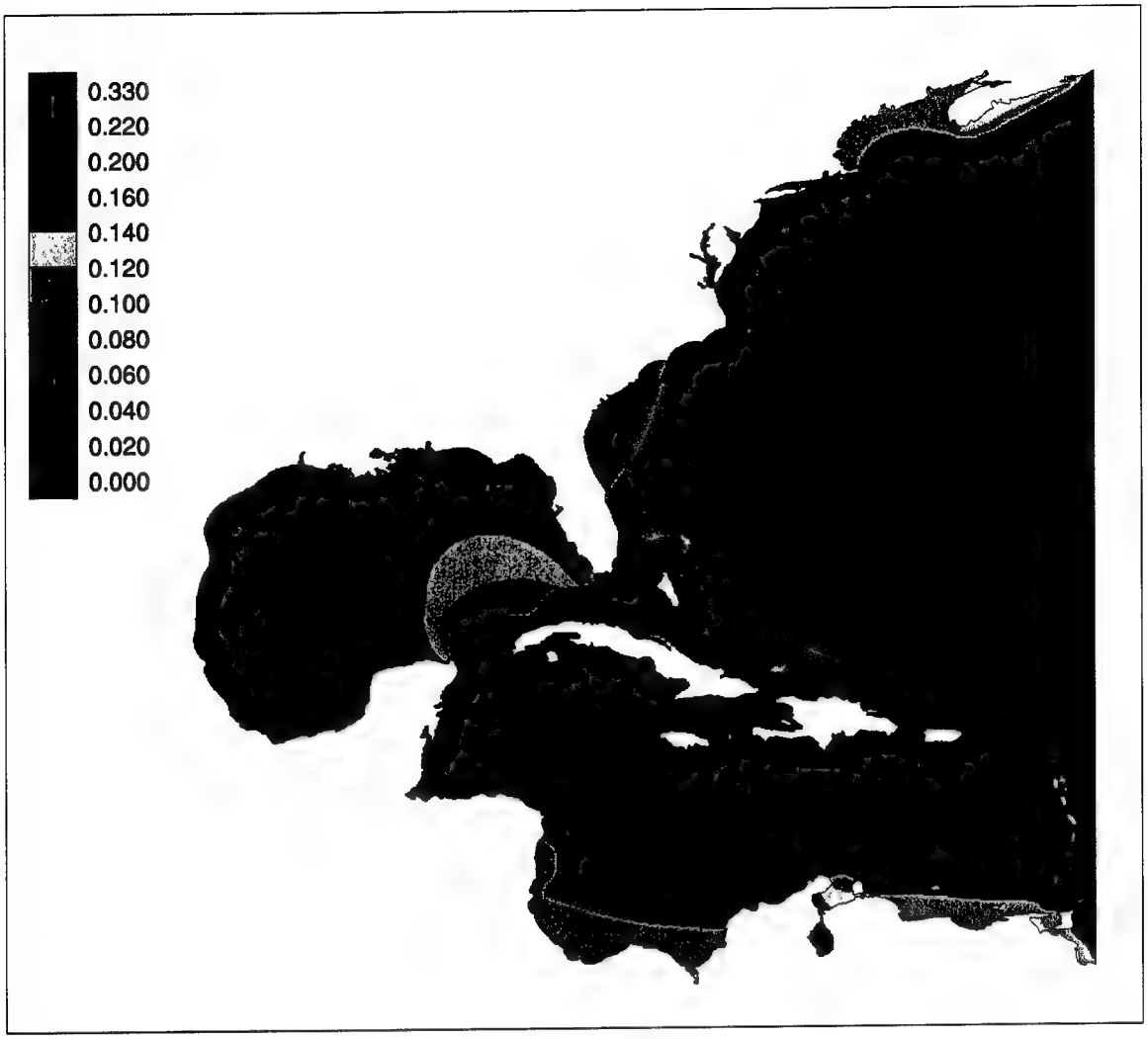

Figure 18. K_1 coamplitude chart (in meters)

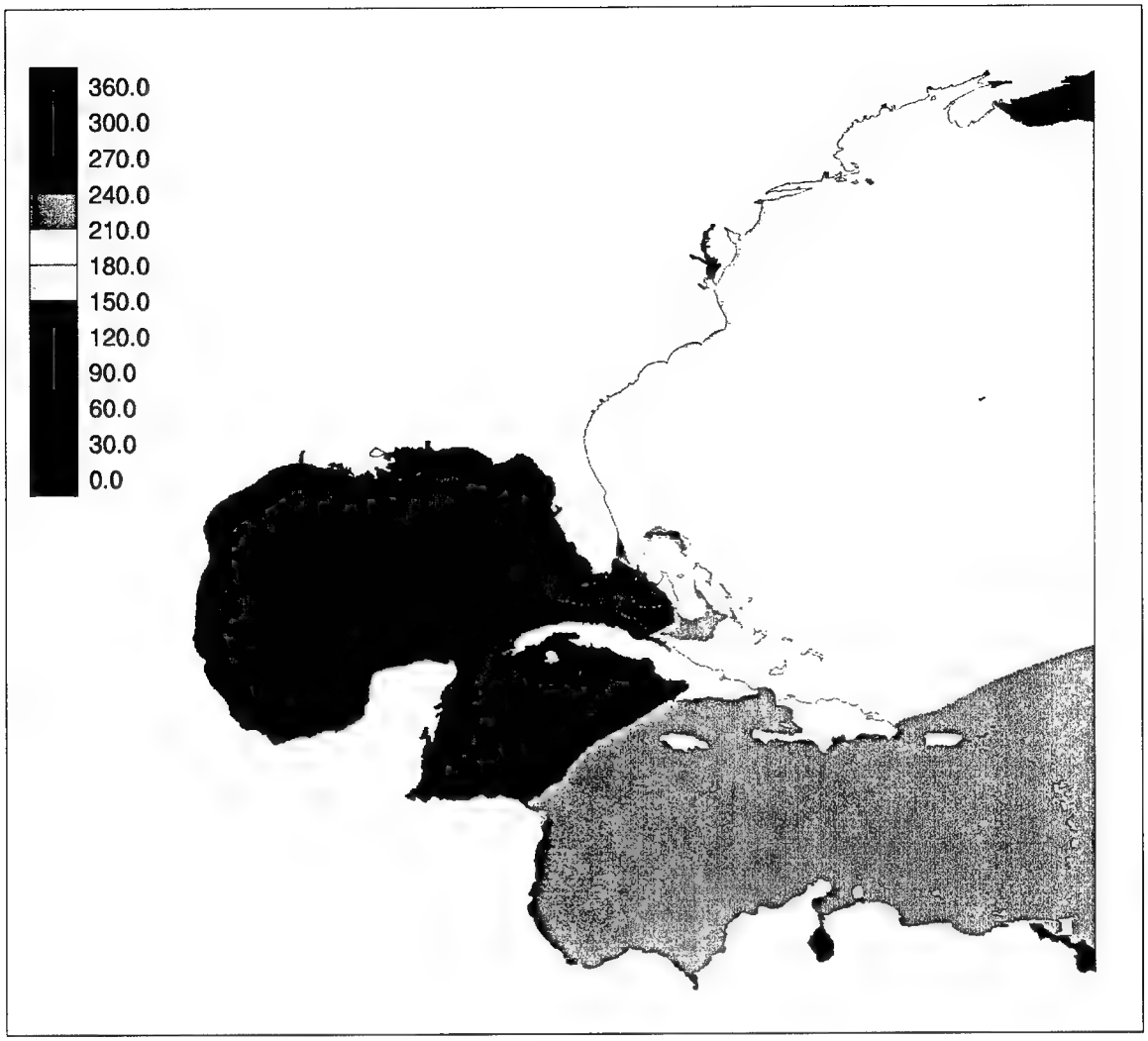

Figure 19. K_1 phase cotidal chart (in degrees relative to GMT)

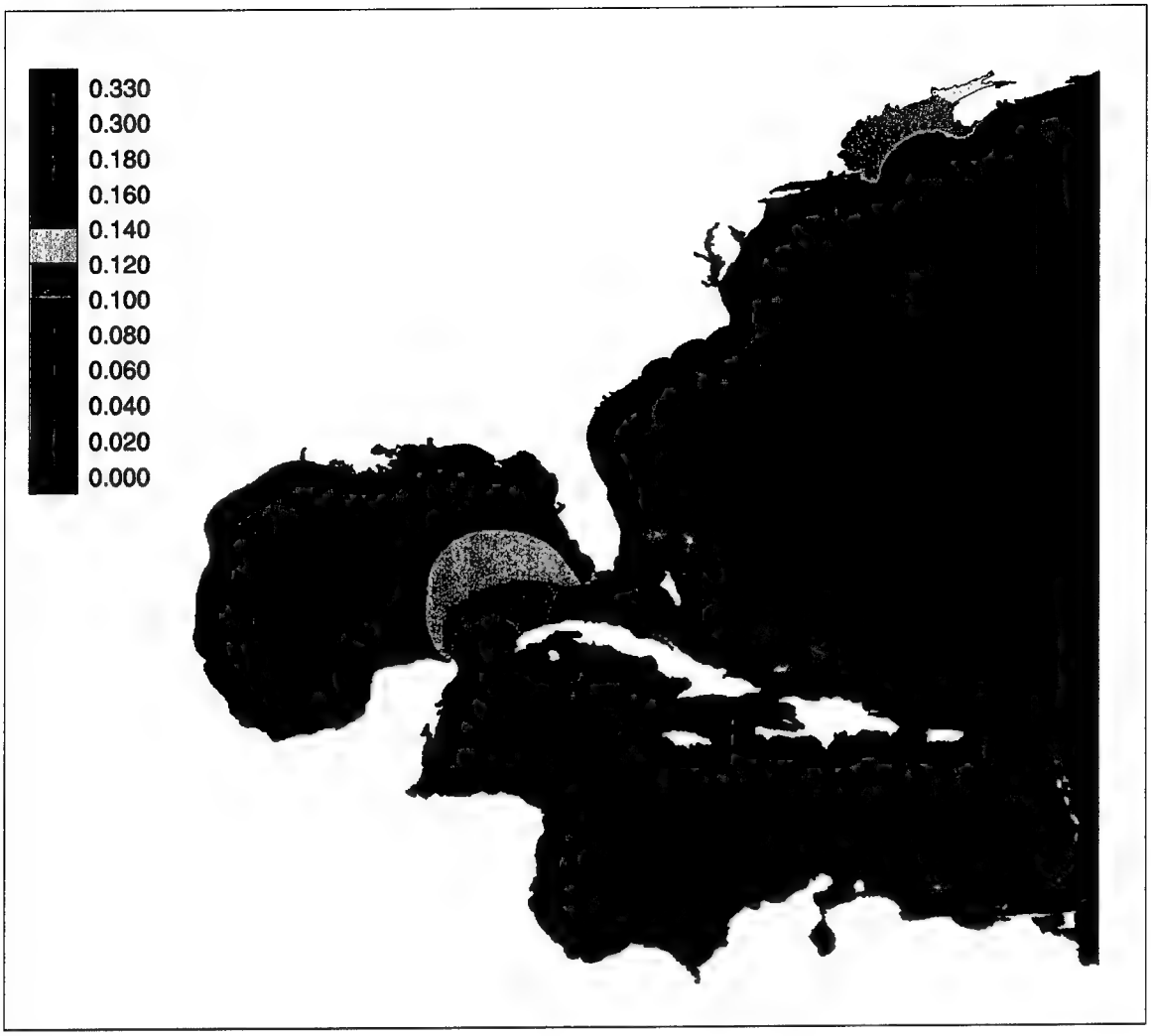

Figure 20. O_1 coamplitude chart (in meters)

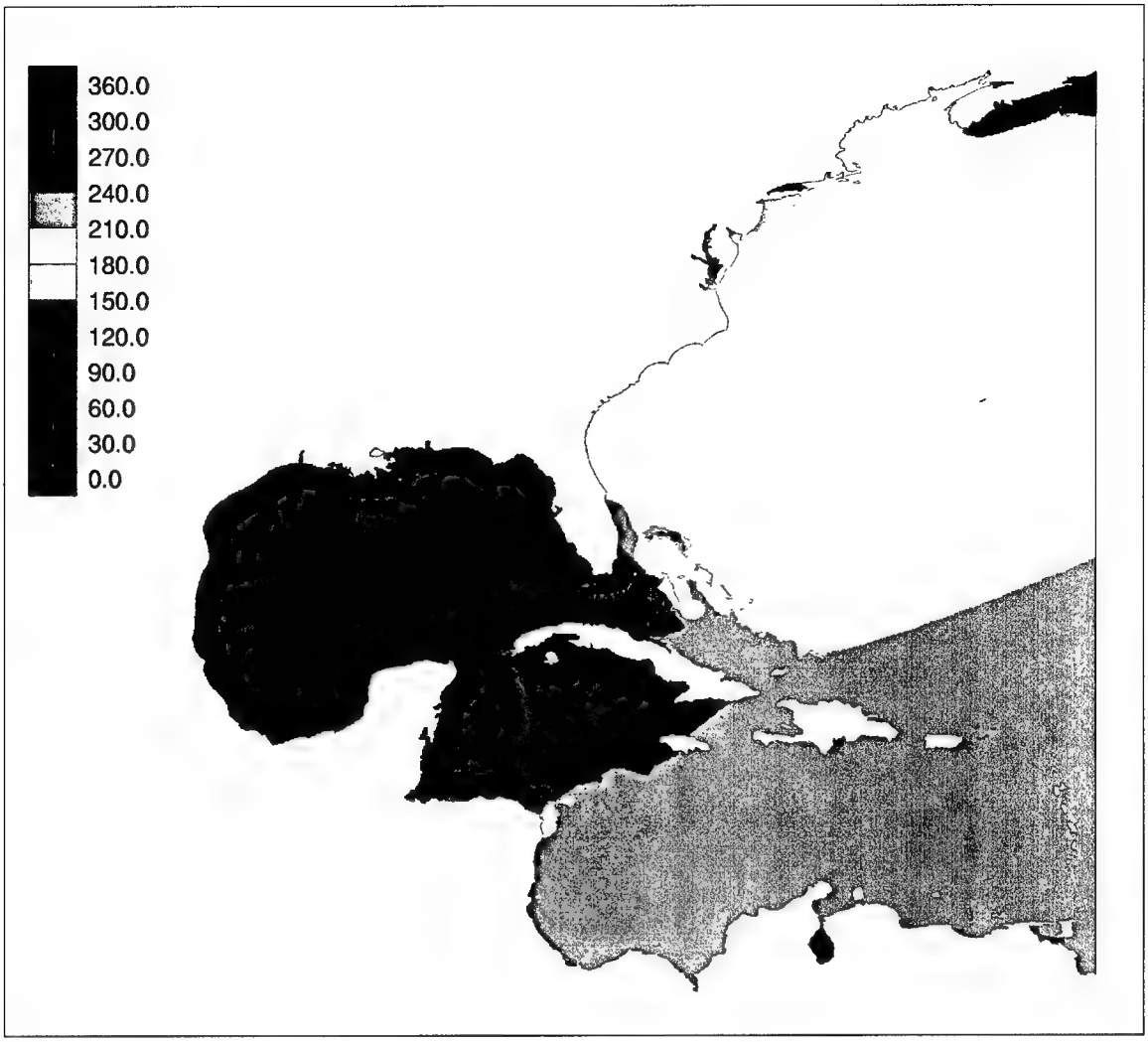

Figure 21. O_1 phase cotidal chart (in degrees relative to GMT)

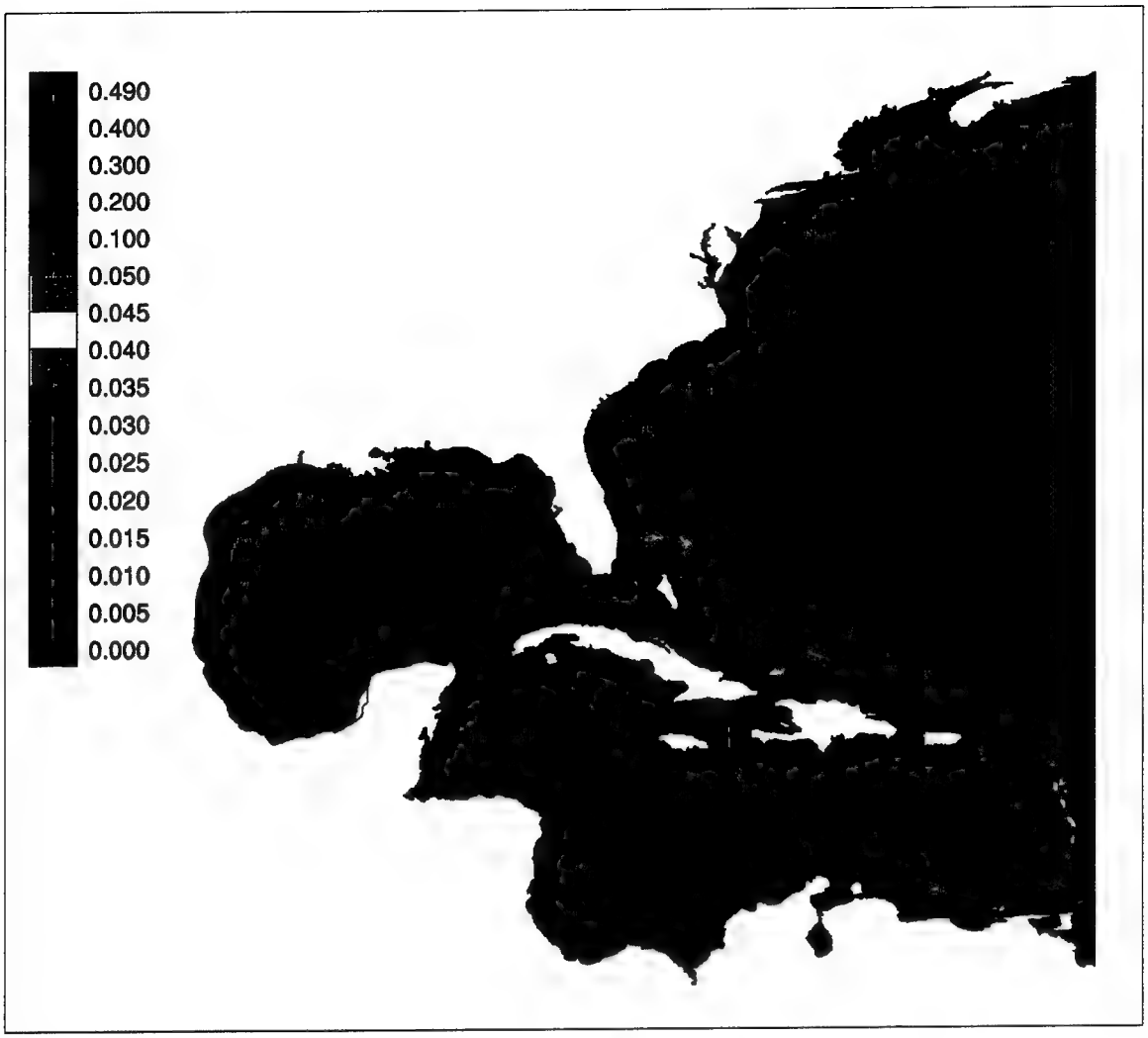

Figure 22. Q_1 coamplitude chart (in meters)

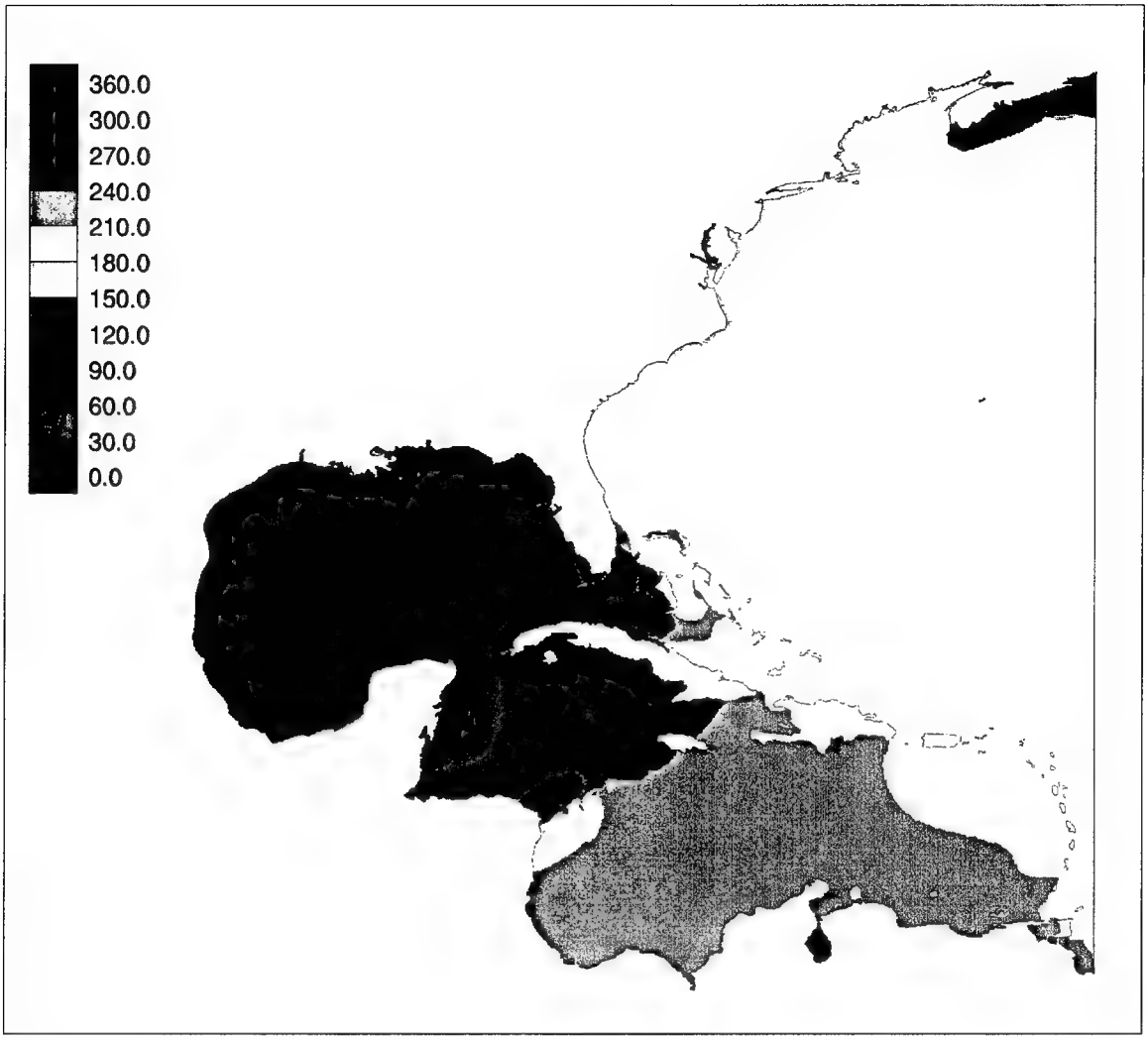

Figure 23. Q_1 phase cotidal chart (in degrees relative to GMT)

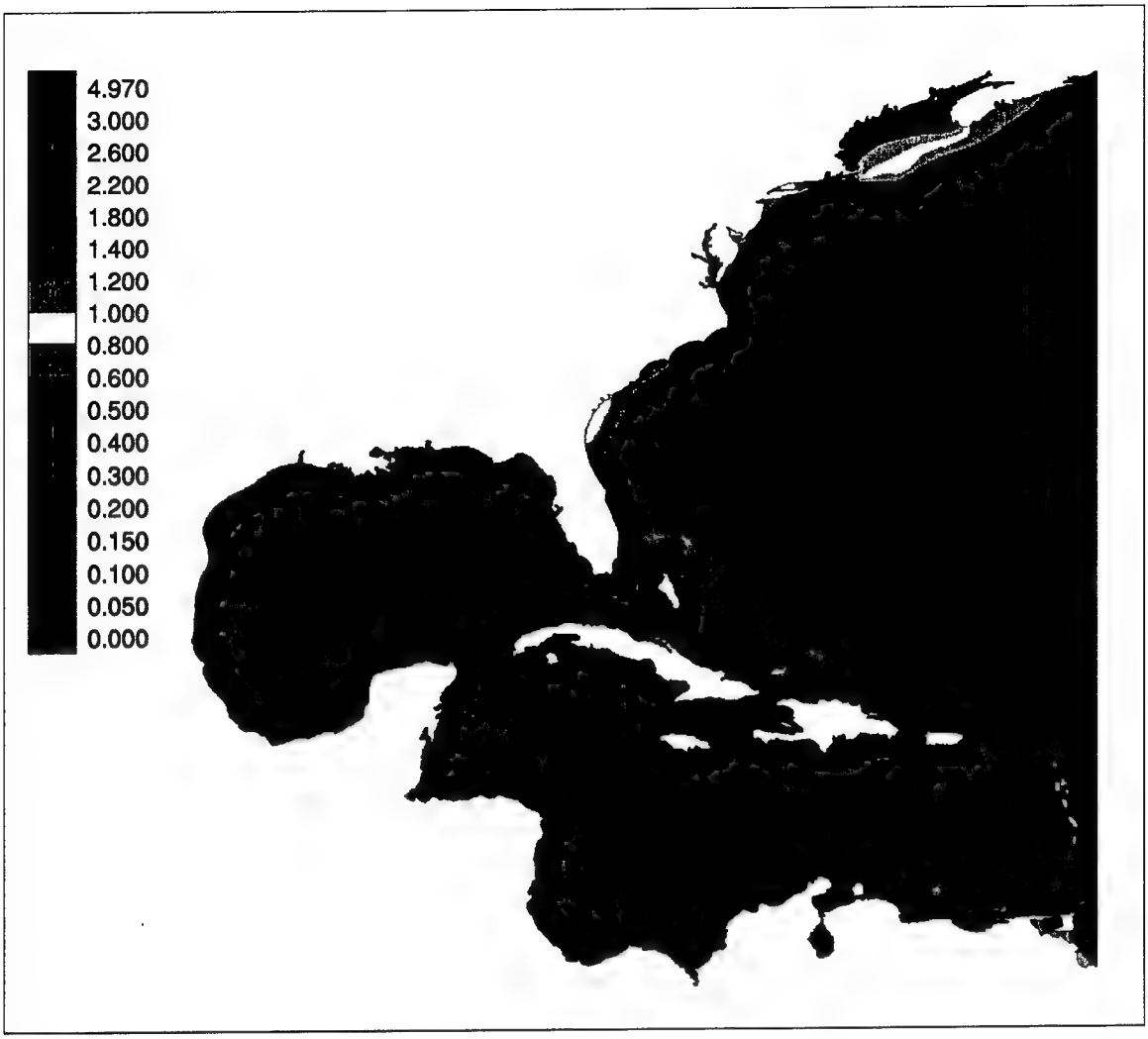

Figure 24. M_2 coamplitude chart (in meters)

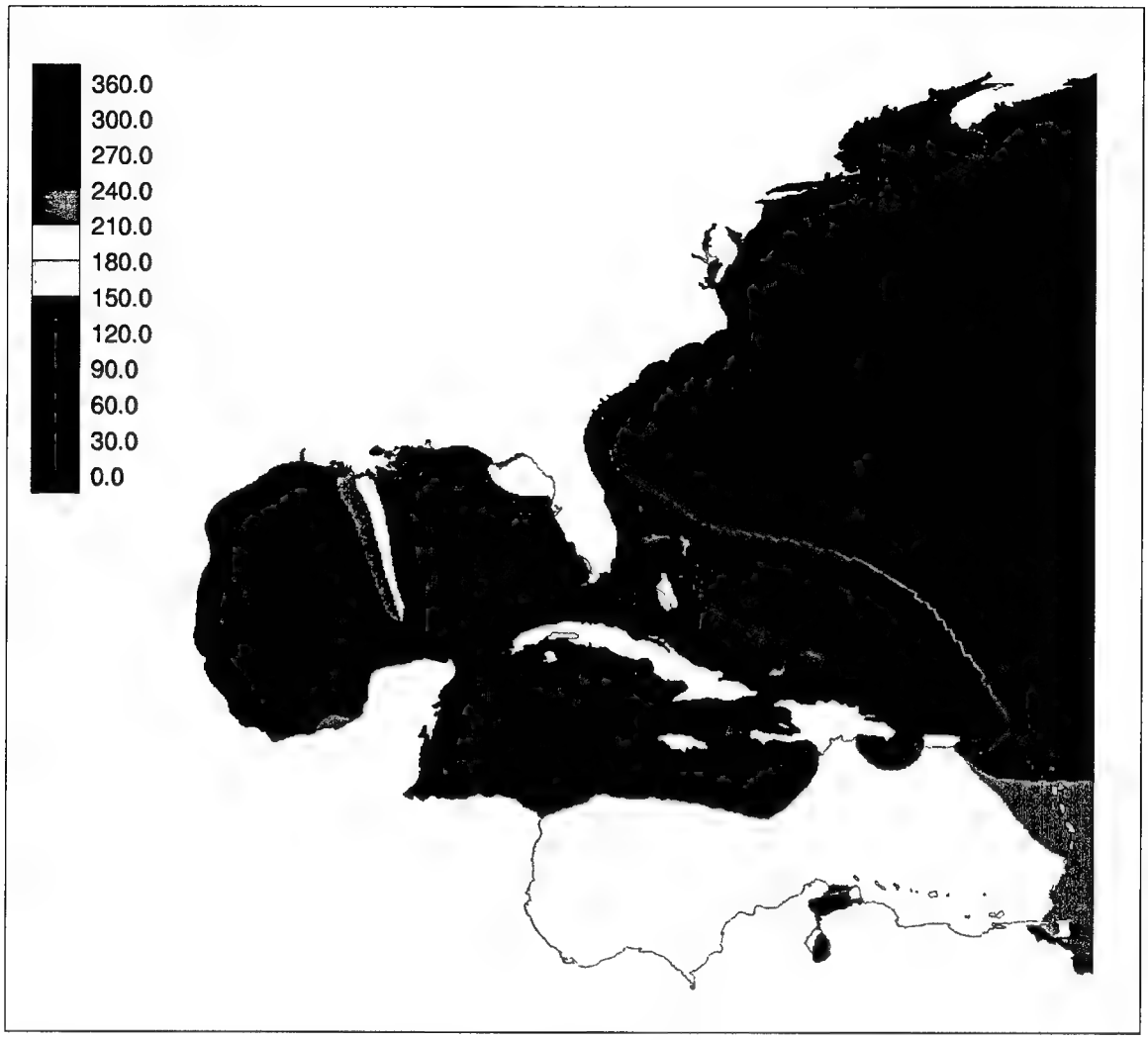

Figure 25. M_2 phase cotidal chart (in degrees relative to GMT)

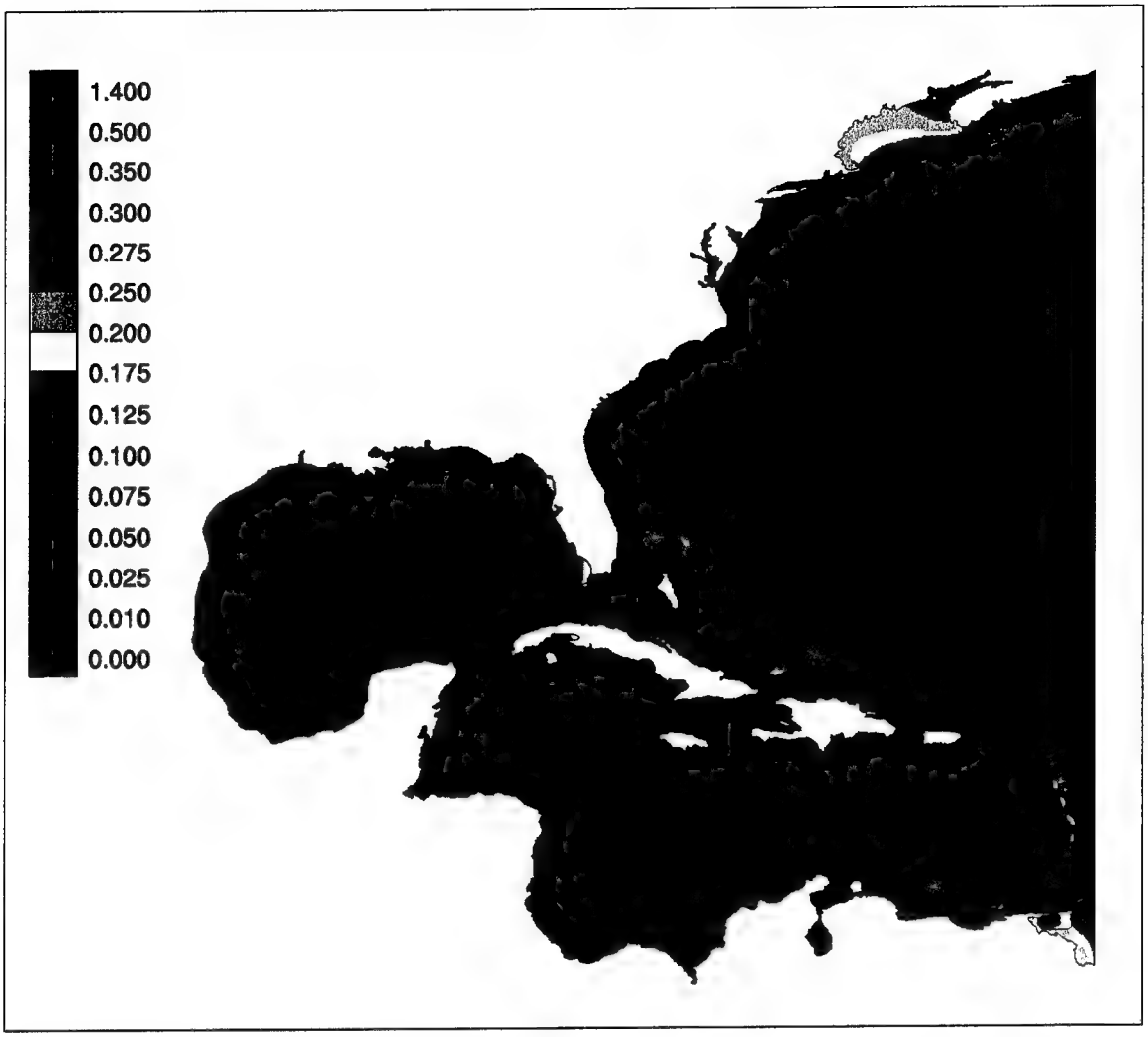

Figure 26. S_2 coamplitude chart (in meters)

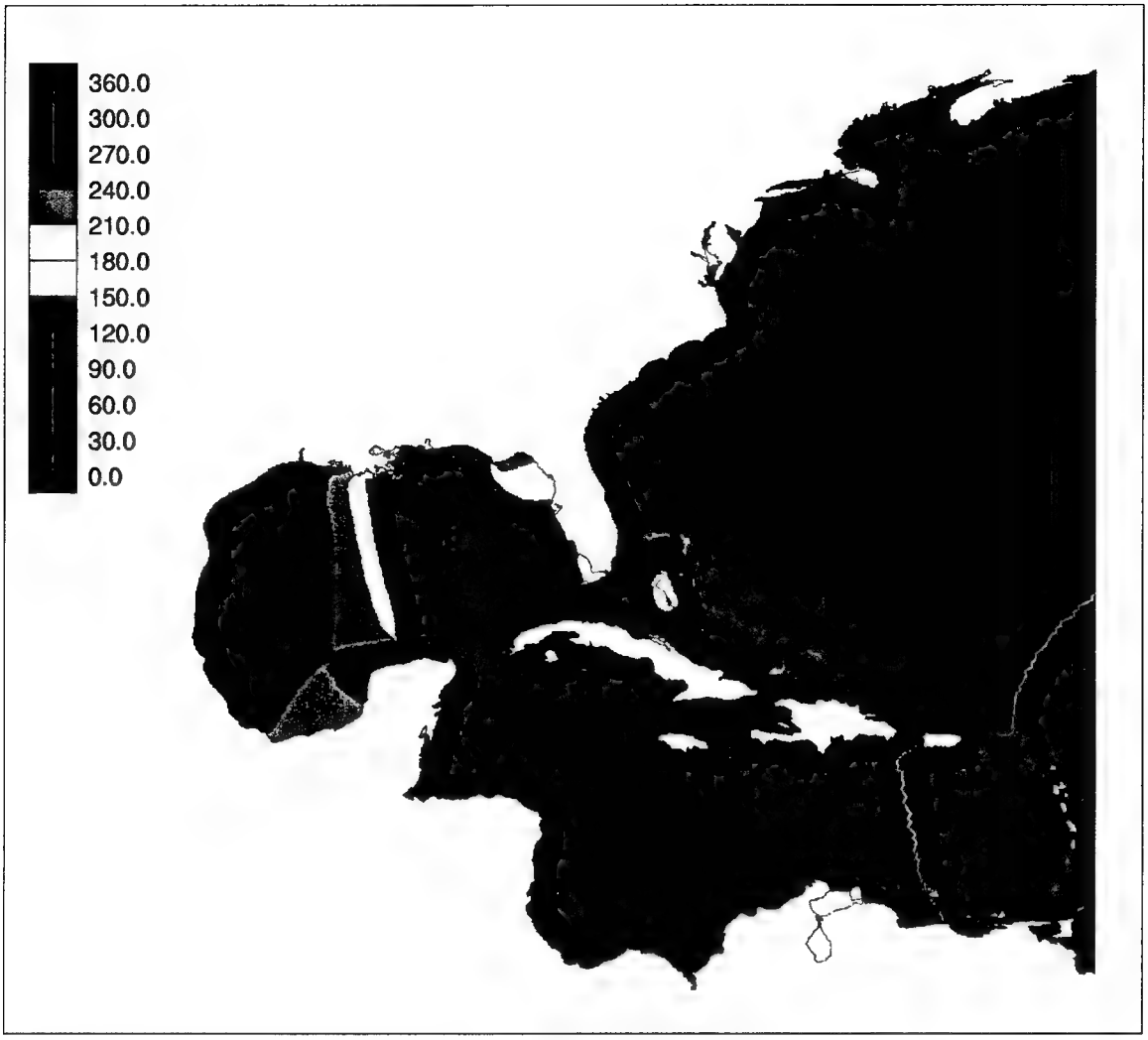

Figure 27. S_2 phase cotidal chart (in degrees relative to GMT)

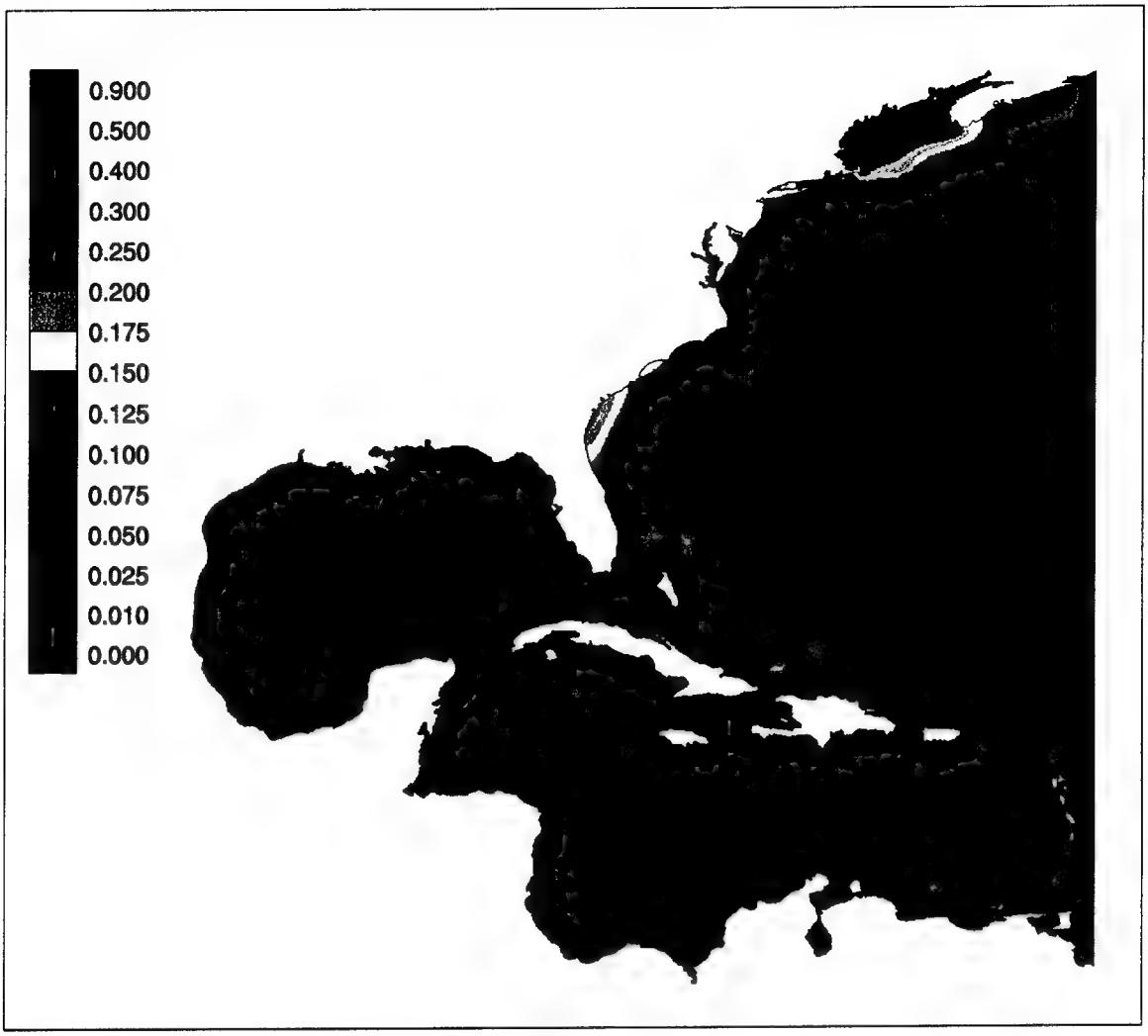

Figure 28. N_2 coamplitude chart (in meters)

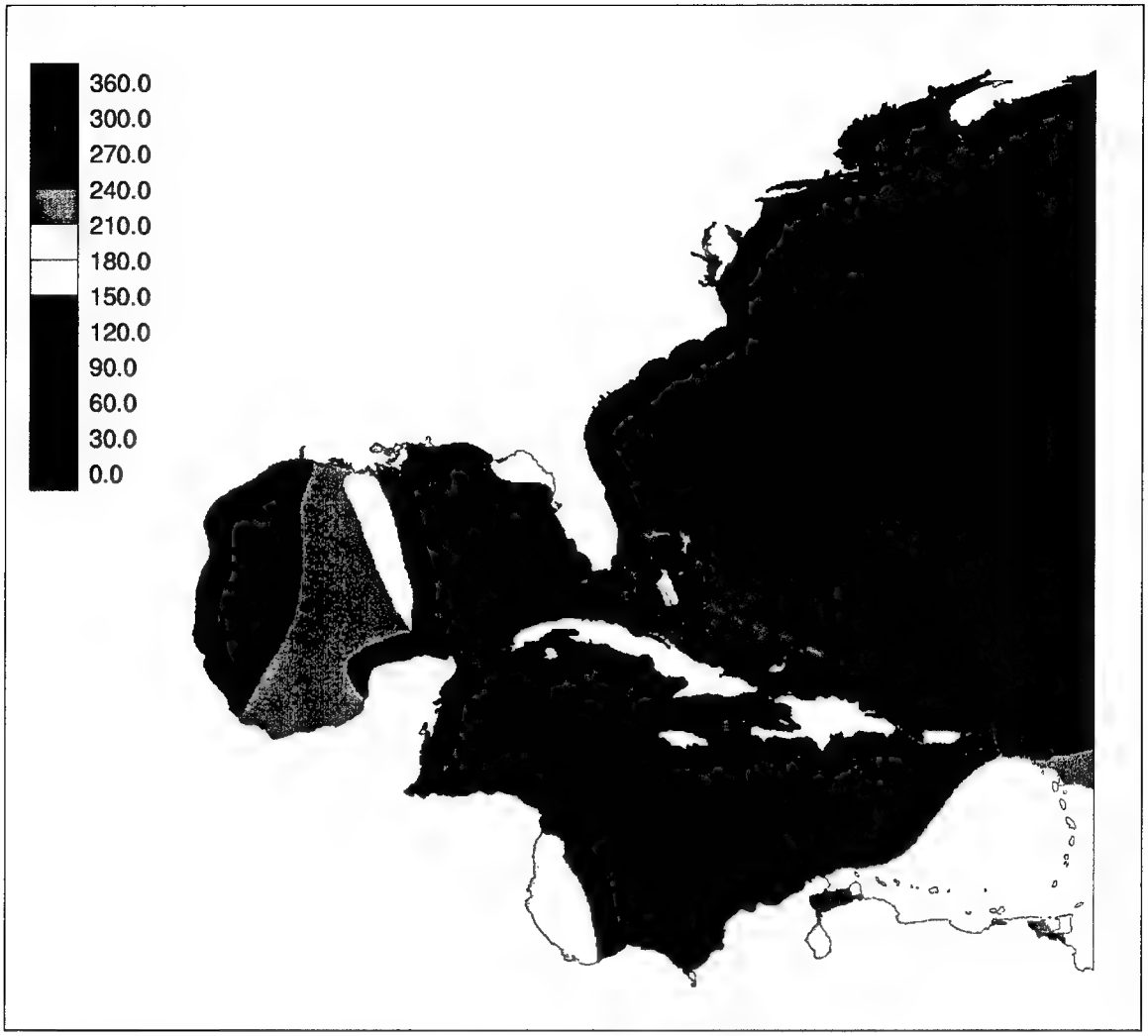

Figure 29. N_2 phase cotidal chart (in degrees relative to GMT)

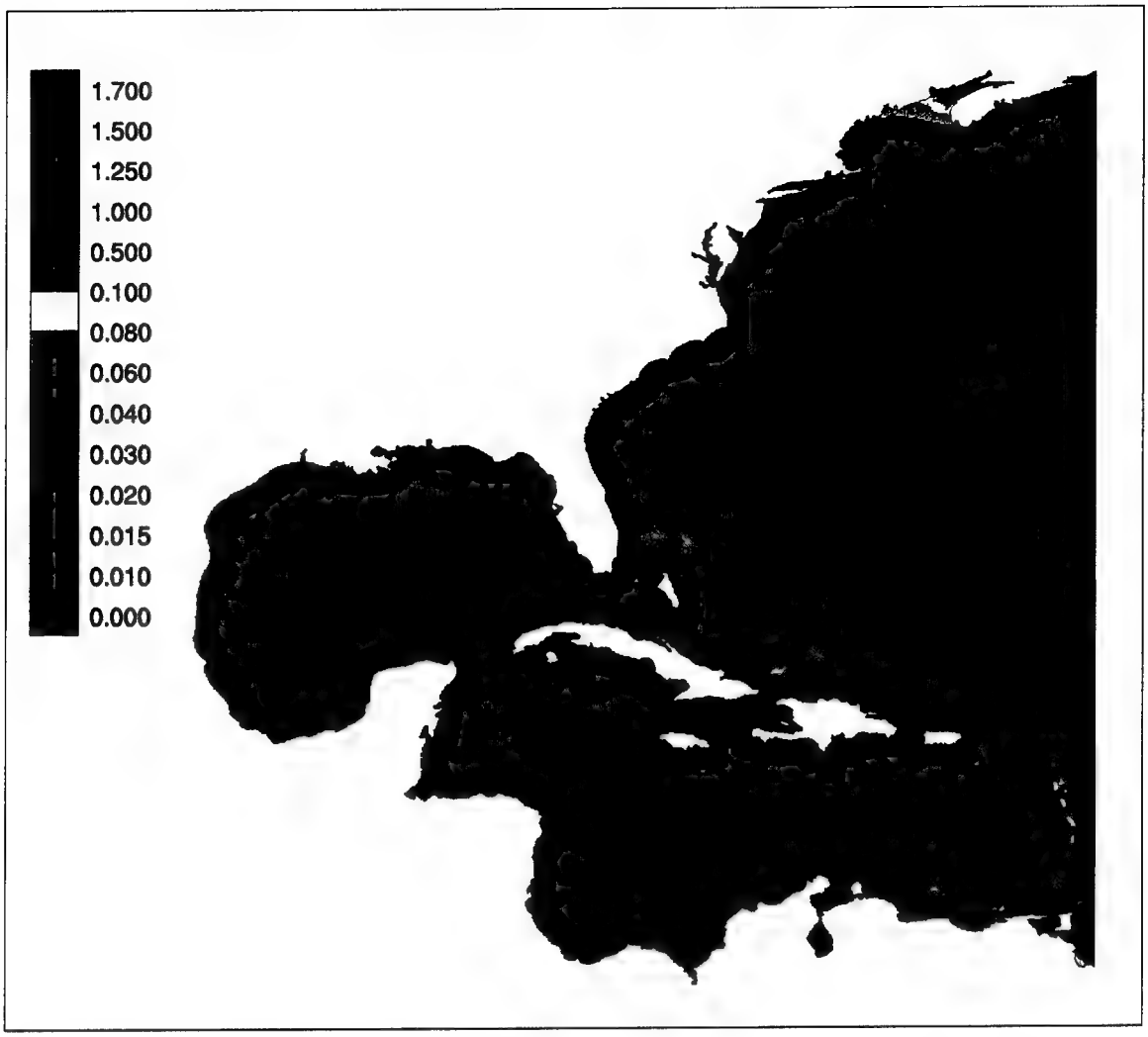

Figure 30. K_2 coamplitude chart (in meters)

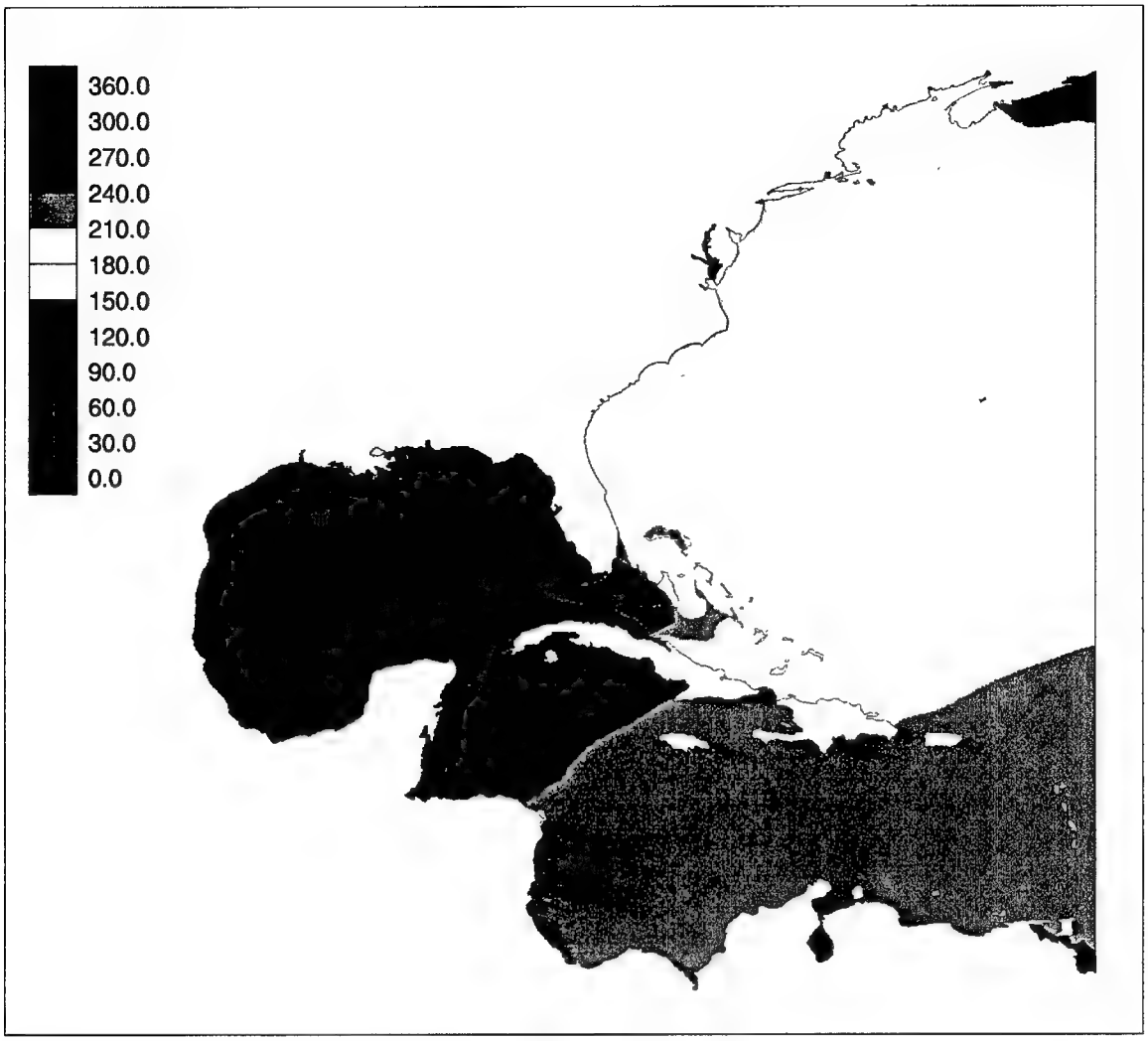

Figure 31. K_2 phase cotidal chart (in degrees relative to GMT)

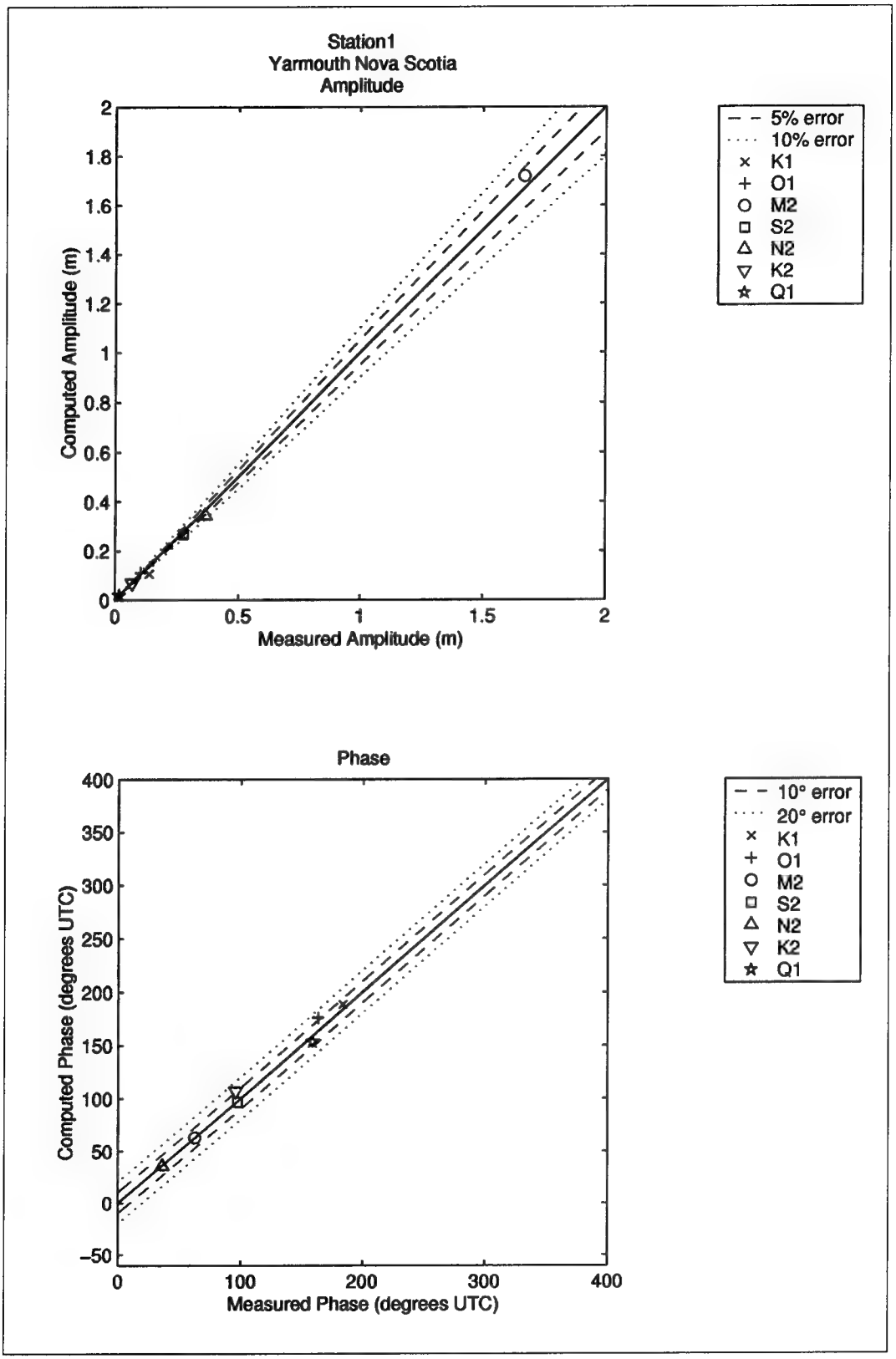

Figure 32. Computed vs. measured harmonic constituents at sta 1

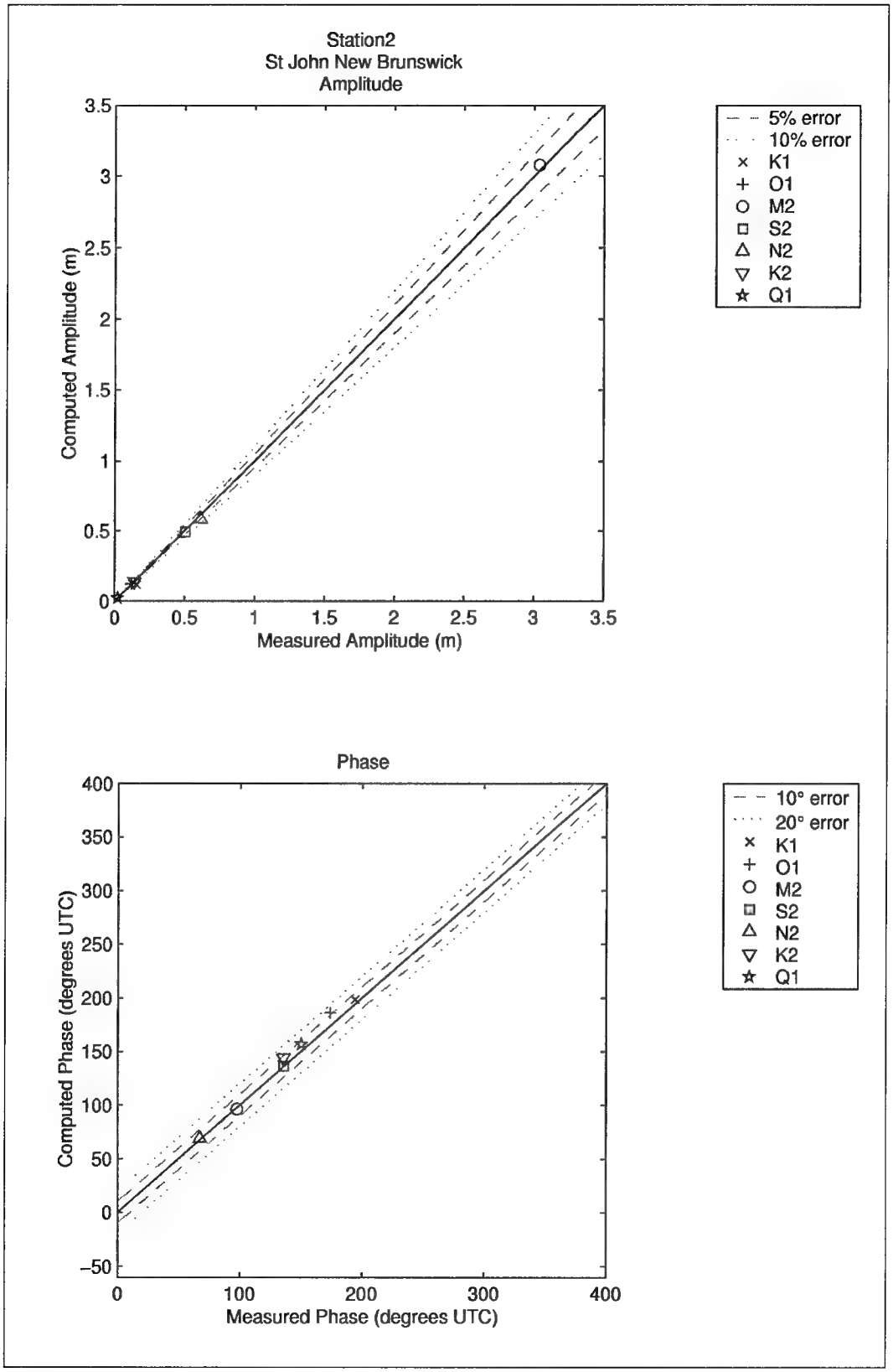

Figure 33. Computed vs. measured harmonic constituents at sta 2

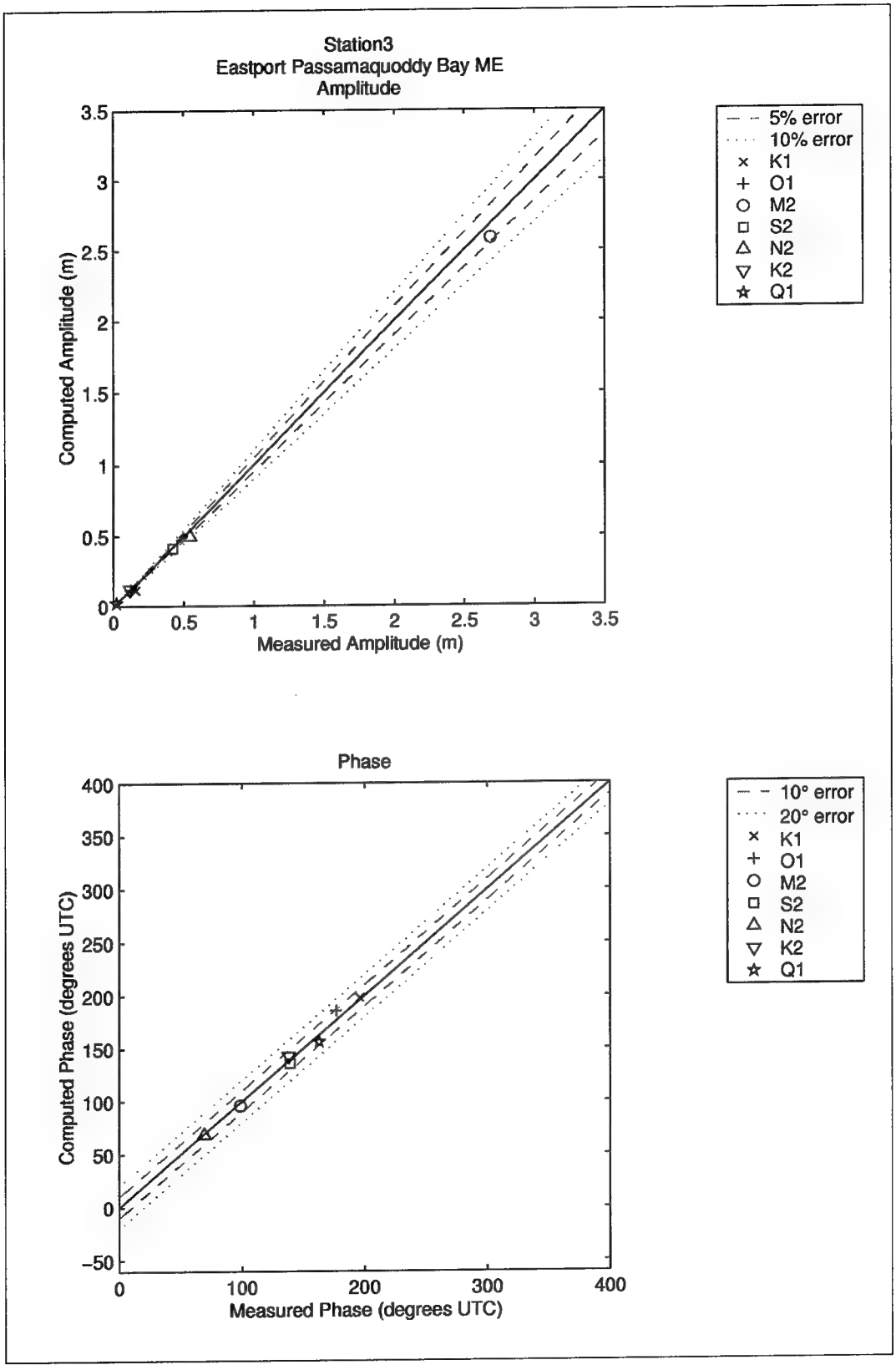

Figure 34. Computed vs. measured harmonic constituents at sta 3

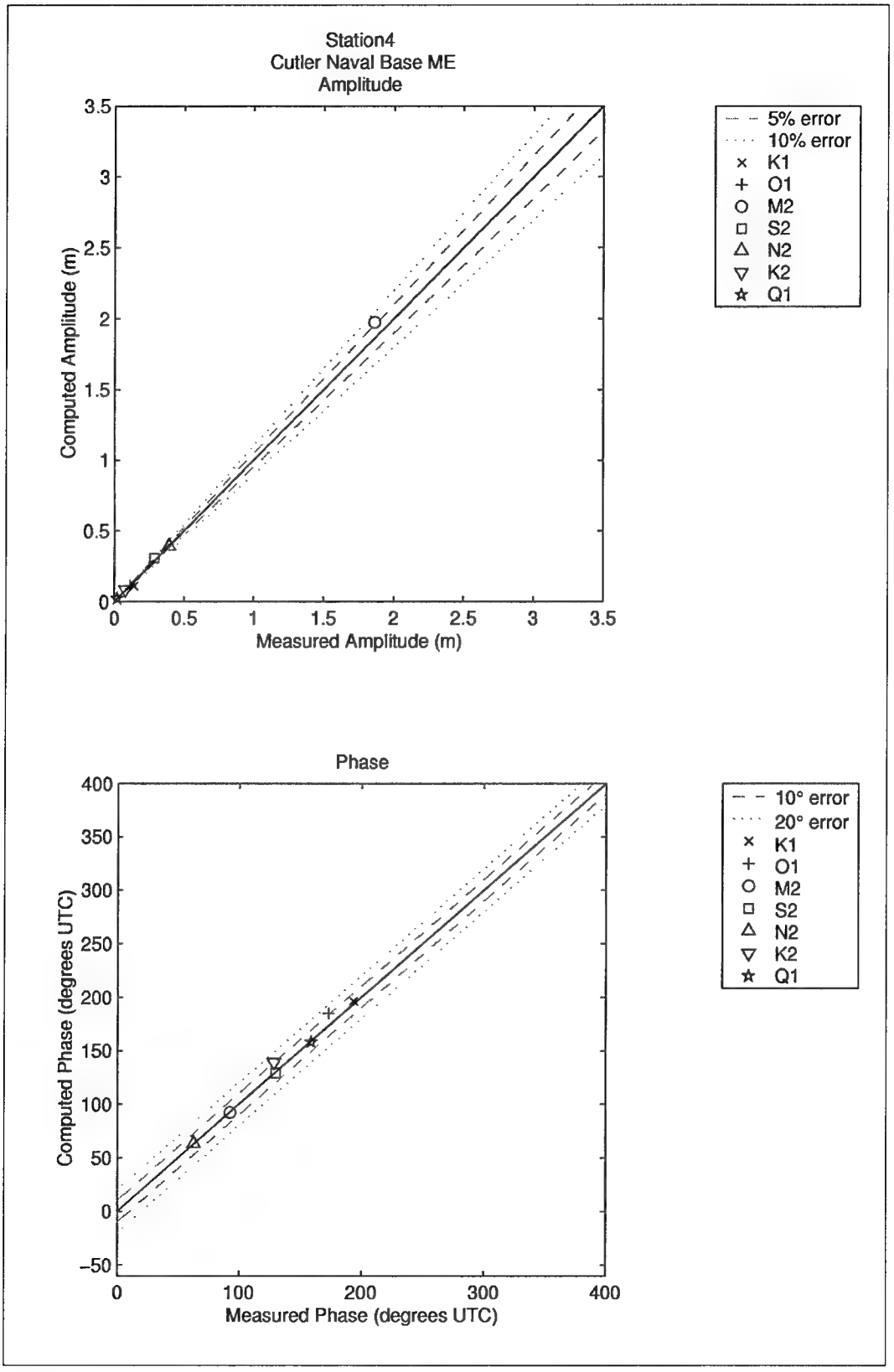

Figure 35. Computed vs. measured harmonic constituents at sta 4

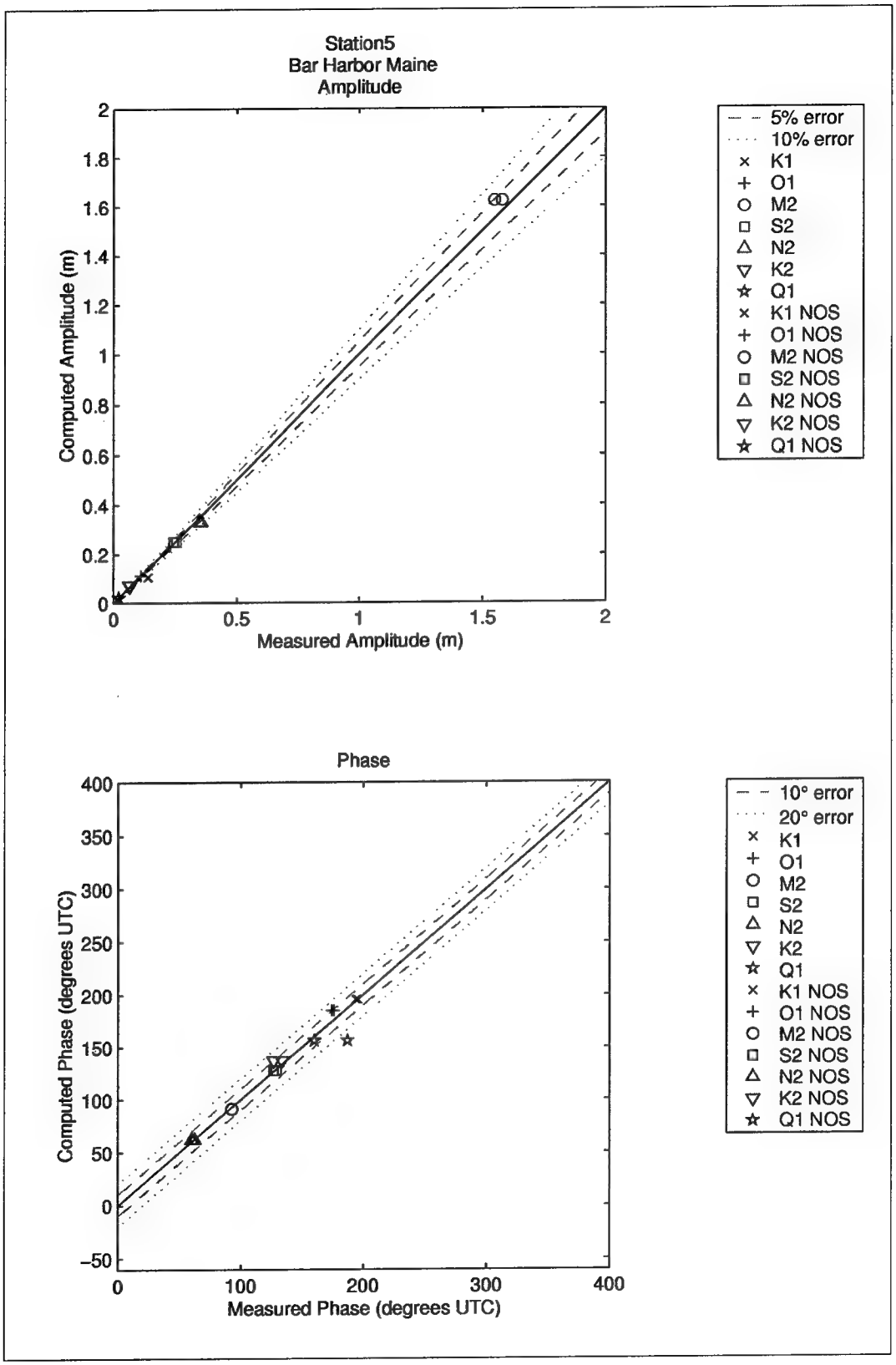

Figure 36. Computed vs. measured harmonic constituents at sta 5

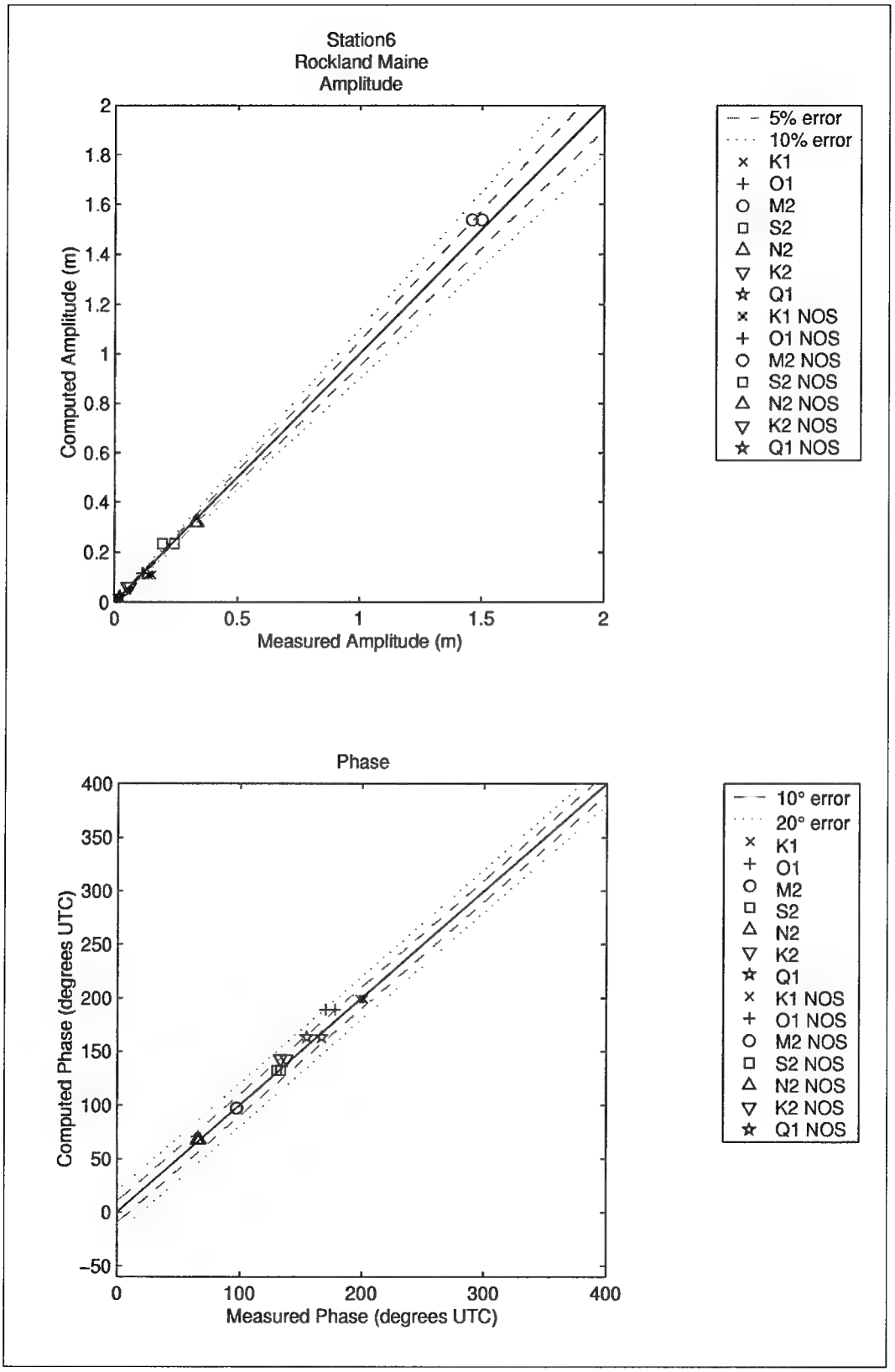

Figure 37. Computed vs. measured harmonic constituents at sta 6

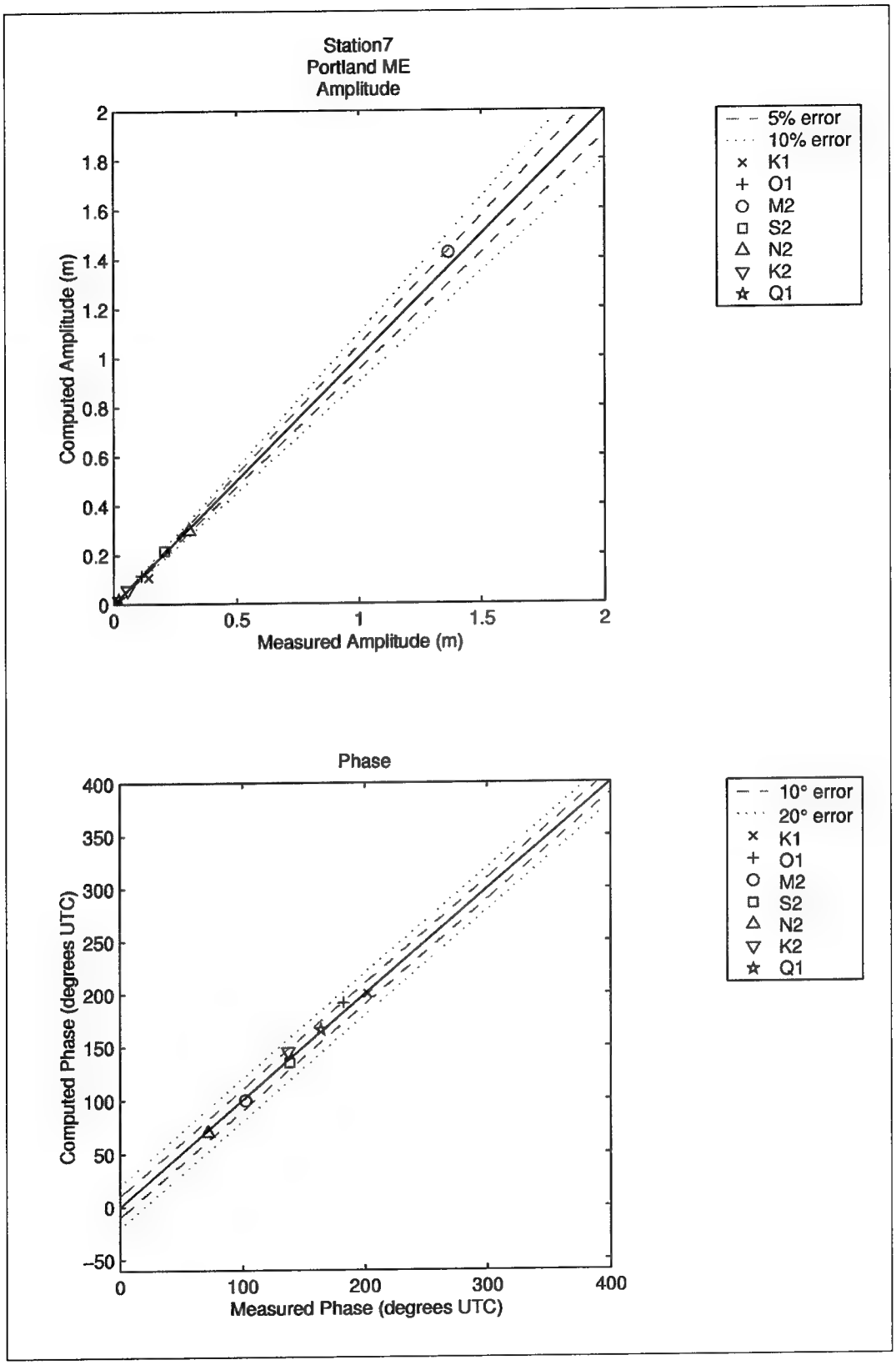

Figure 38. Computed vs. measured harmonic constituents at sta 7

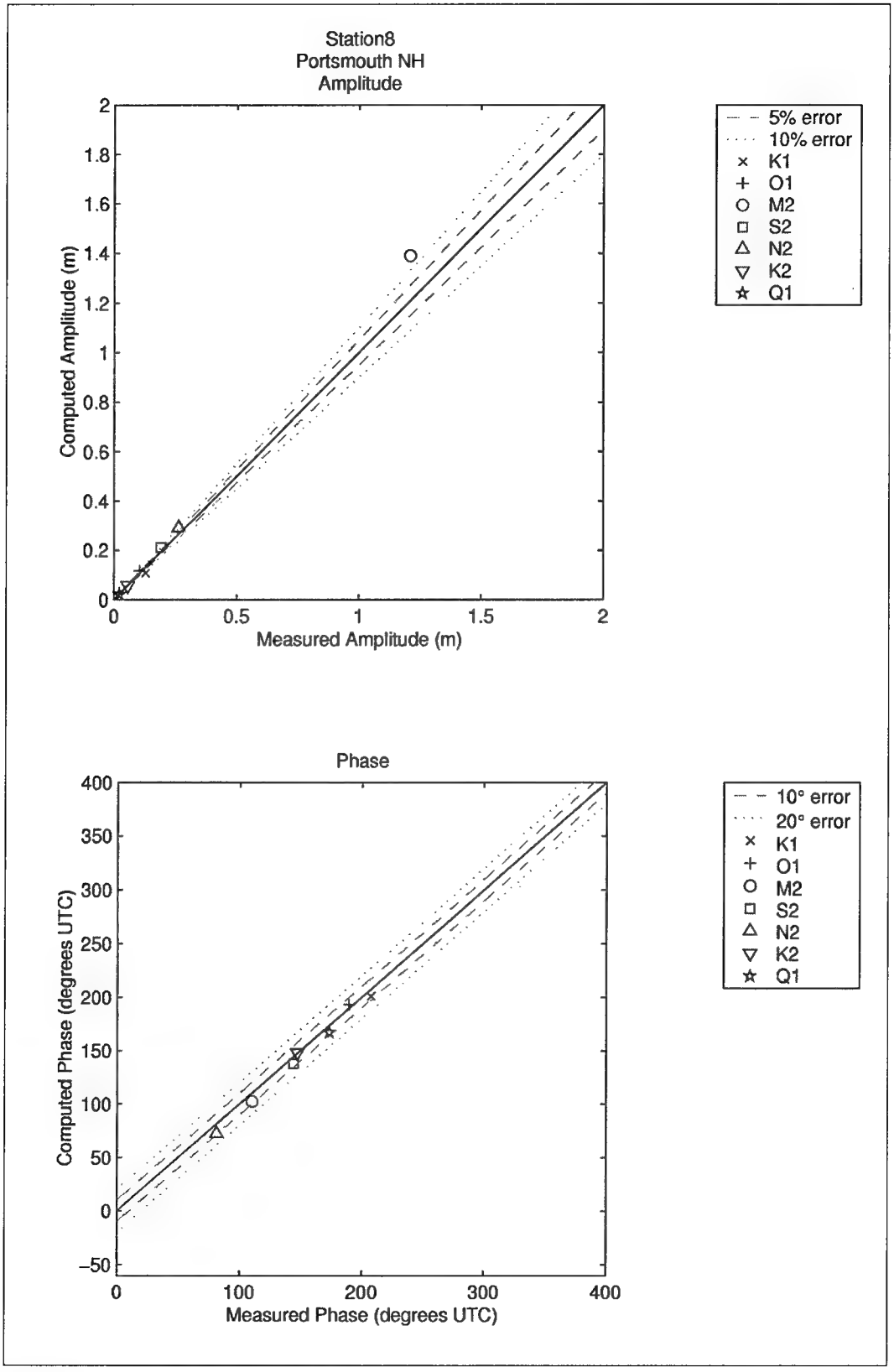

Figure 39. Computed vs. measured harmonic constituents at sta 8

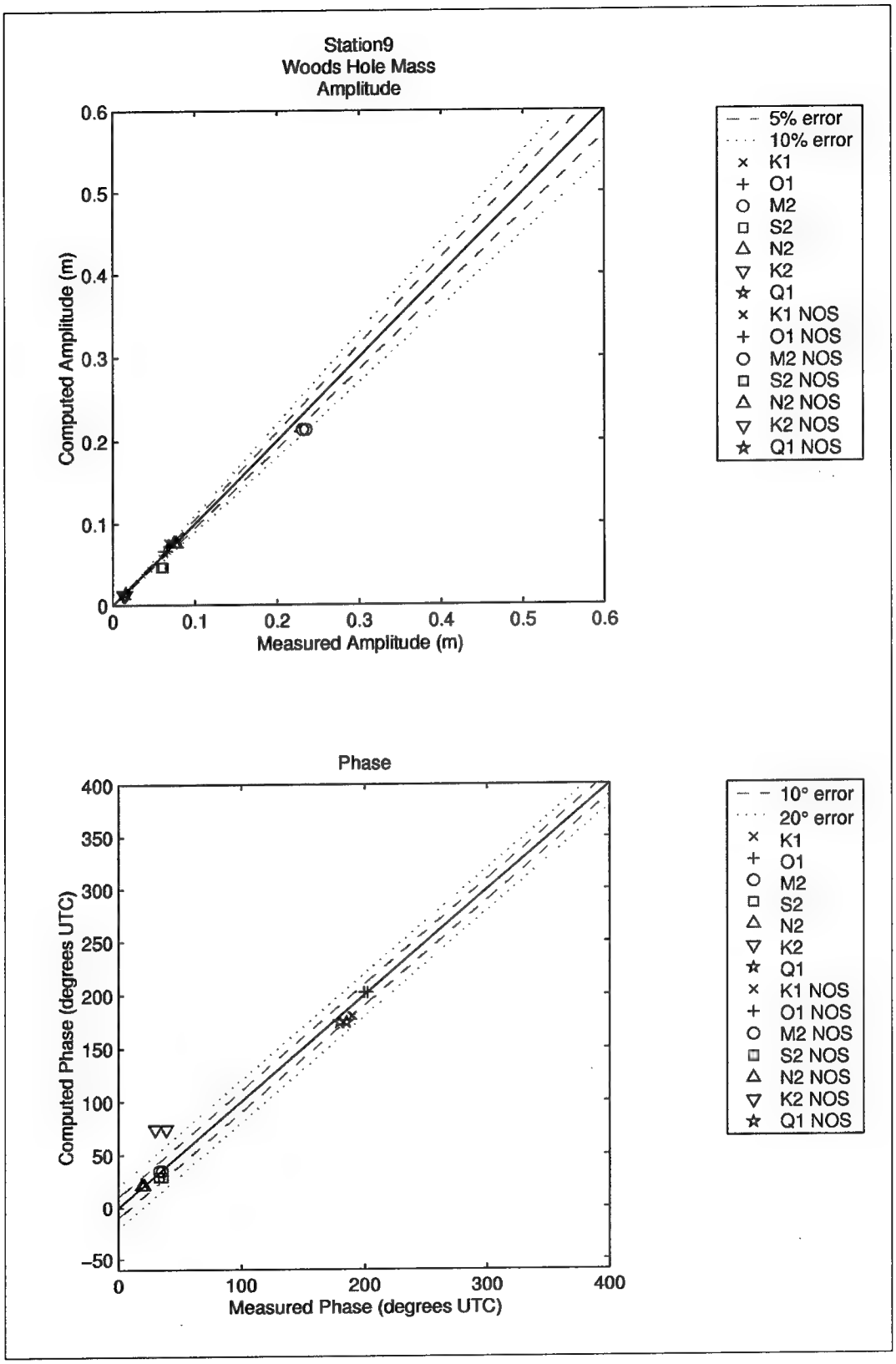

Figure 40. Computed vs. measured harmonic constituents at sta 9

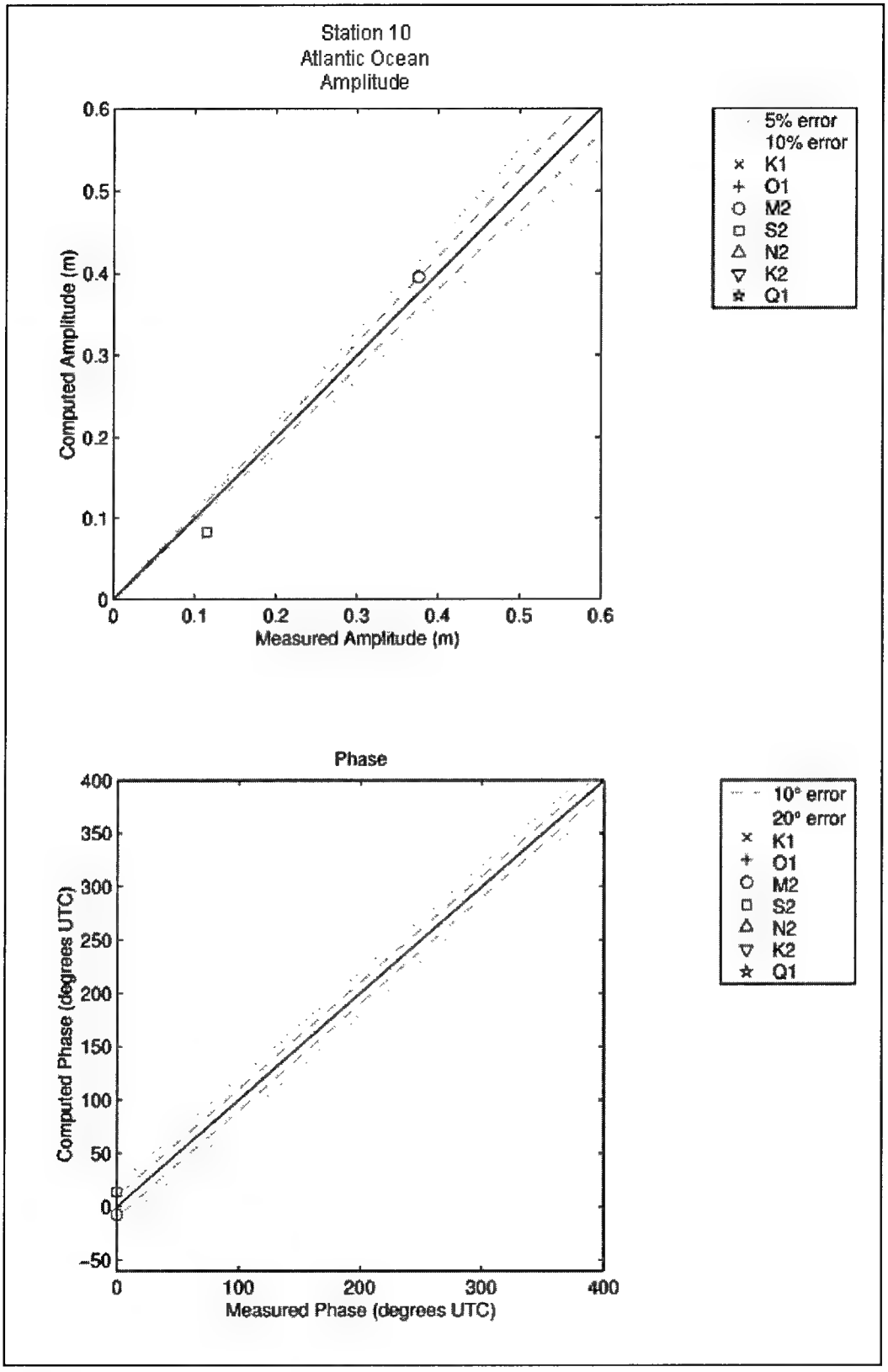

Figure 41. Computed vs. measured harmonic constituents at sta 10

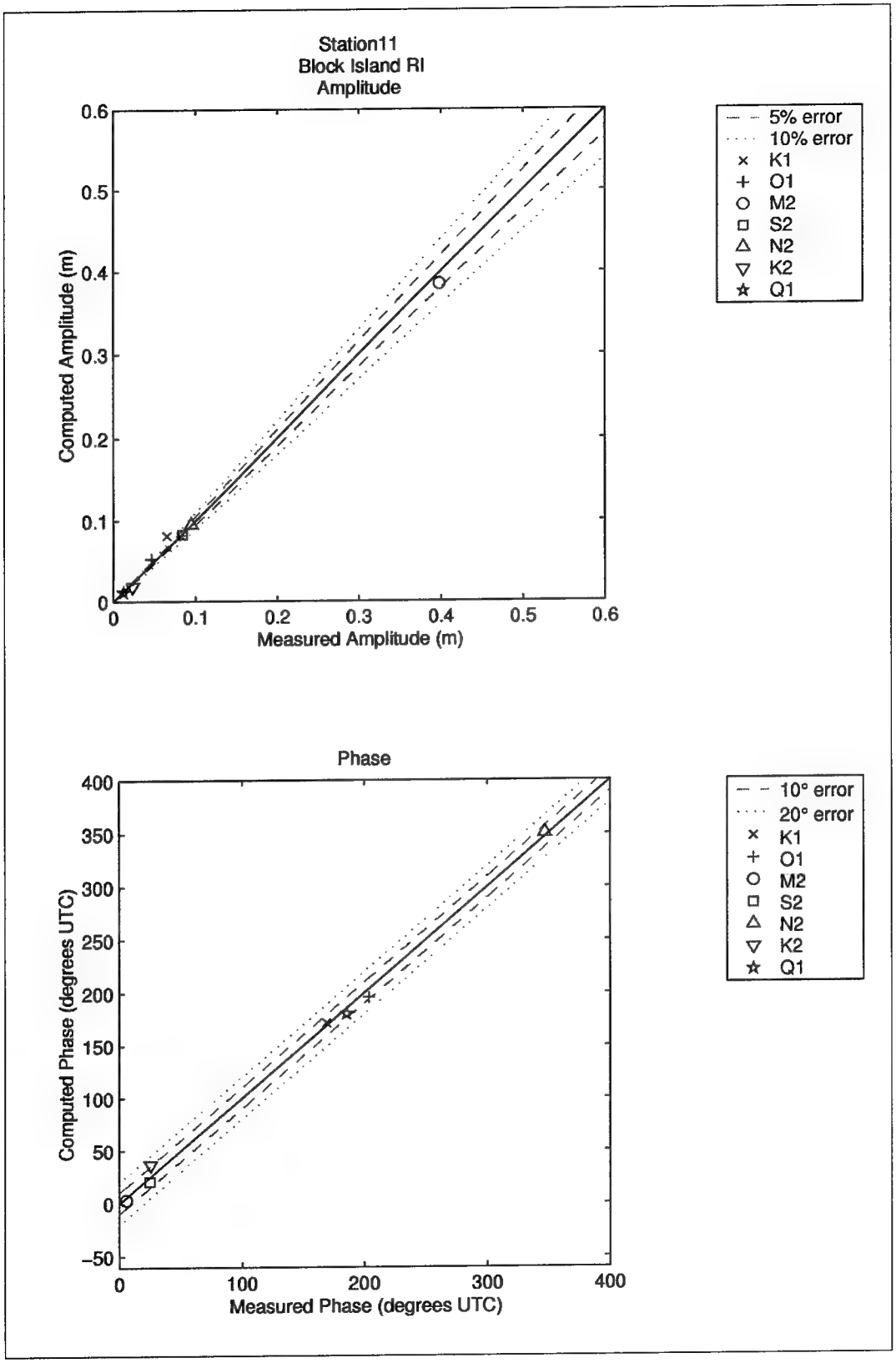

Figure 42. Computed vs. measured harmonic constituents at sta 11

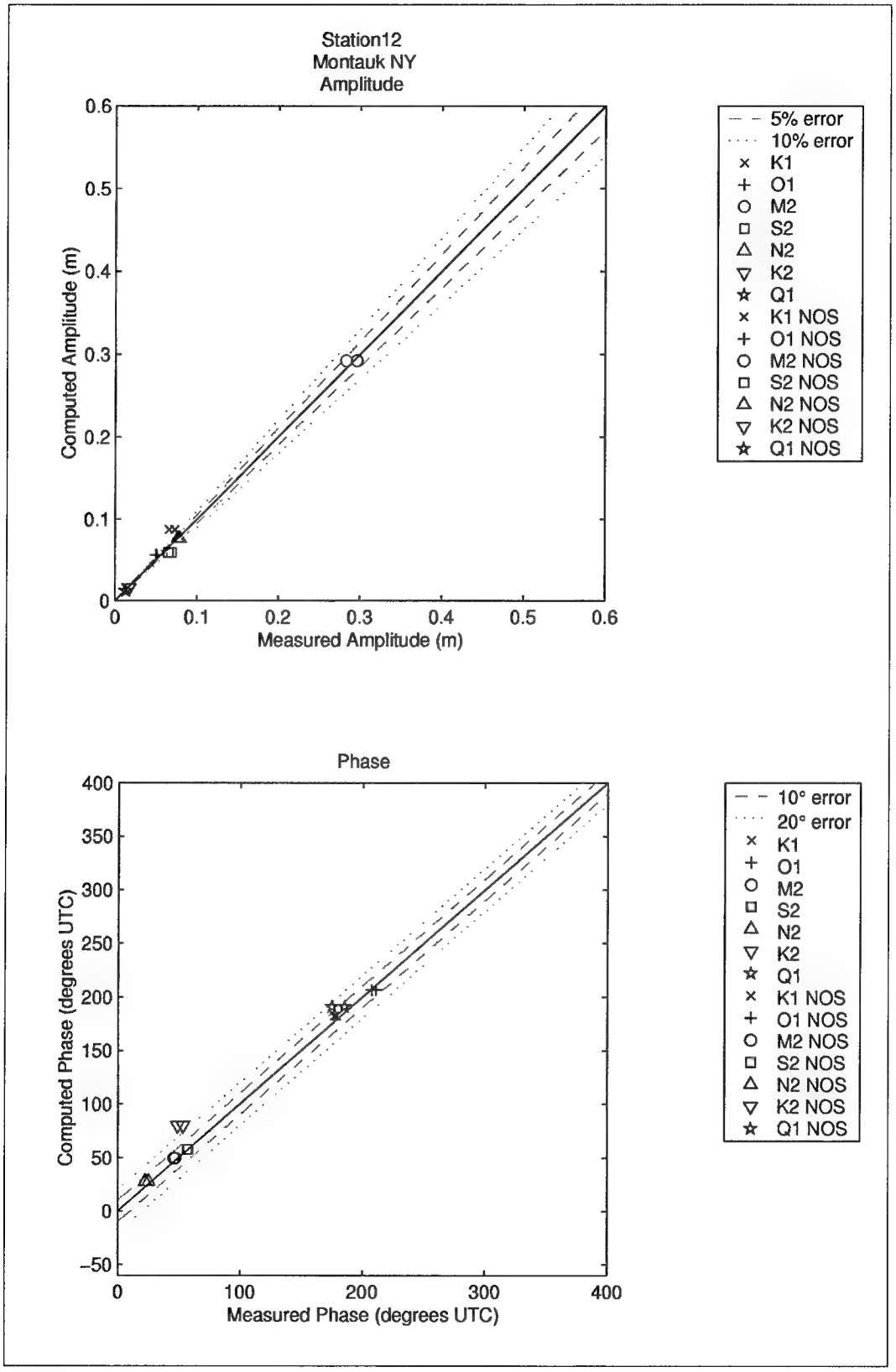

Figure 43. Computed vs. measured harmonic constituents at sta 12

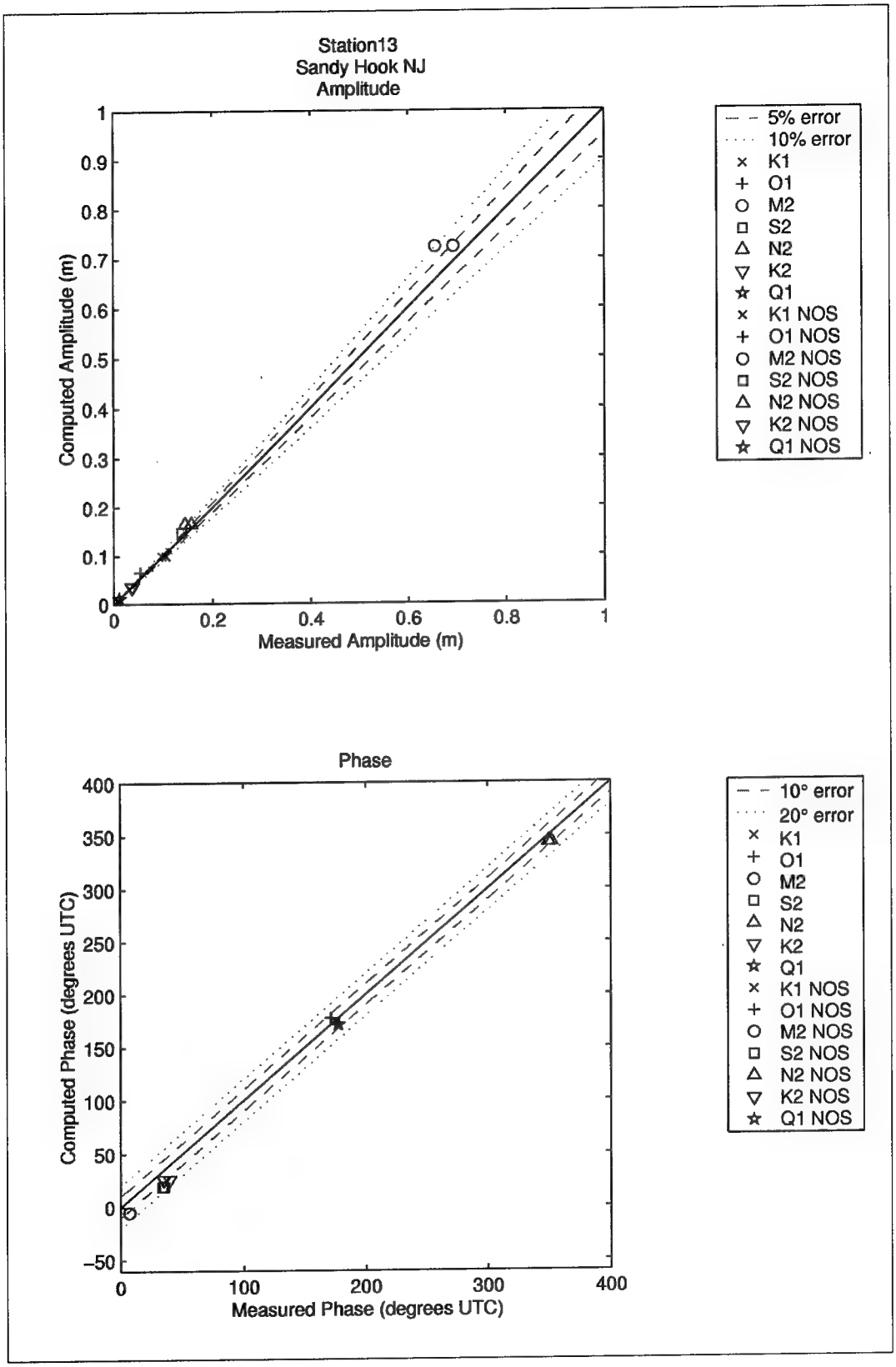

Figure 44. Computed vs. measured harmonic constituents at sta 13

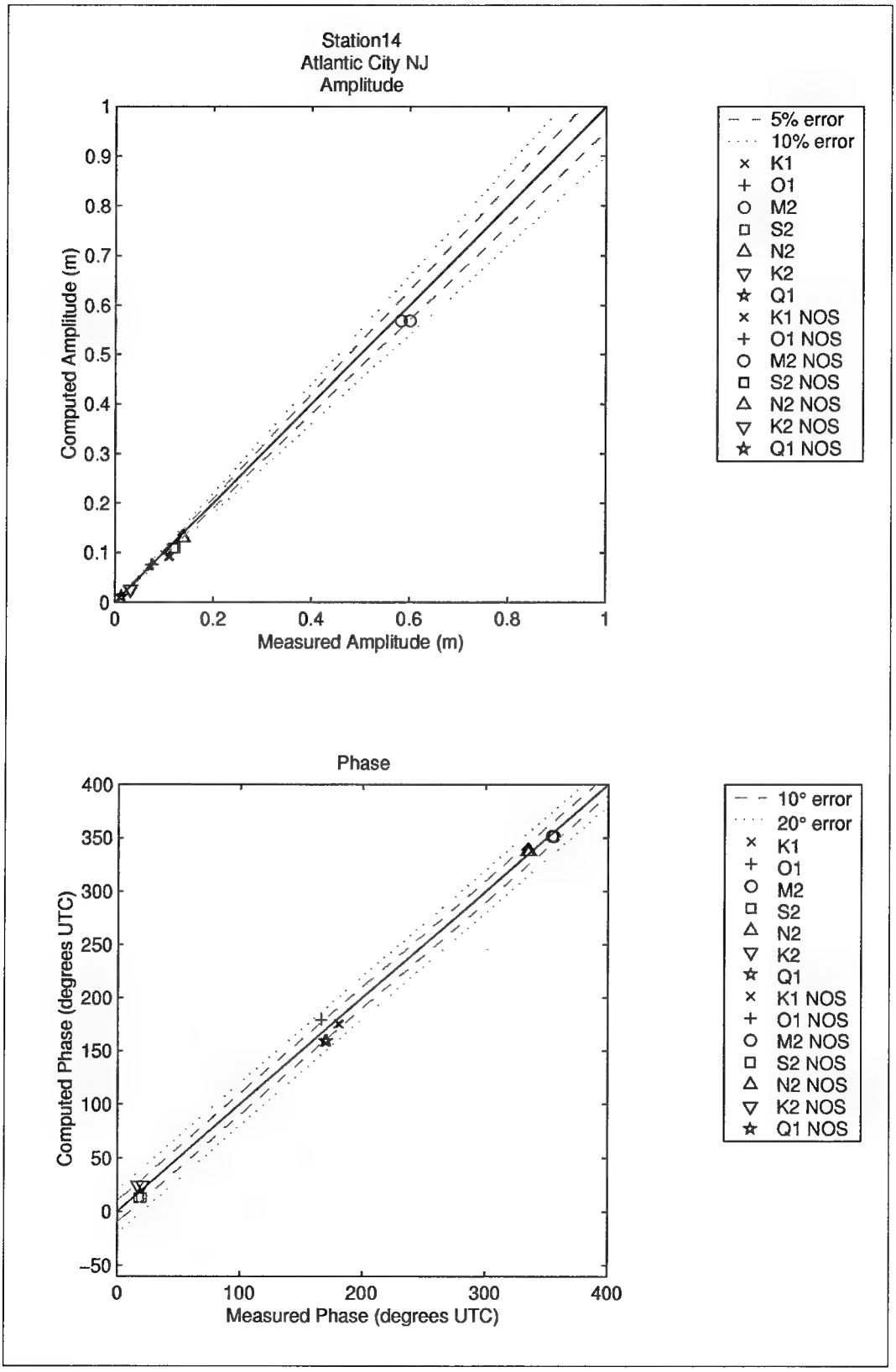

Figure 45. Computed vs. measured harmonic constituents at sta 14

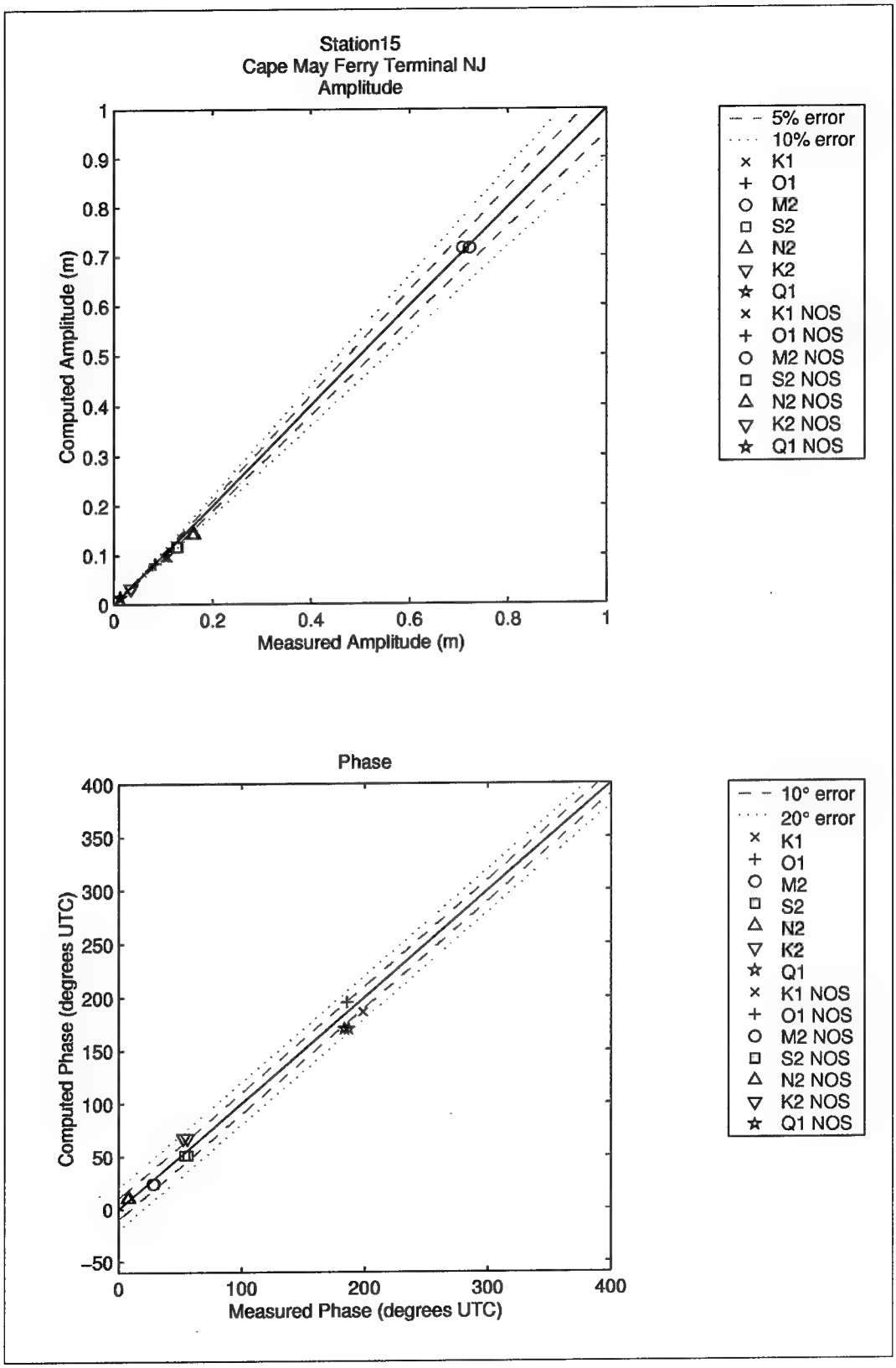

Figure 46. Computed vs. measured harmonic constituents at sta 15

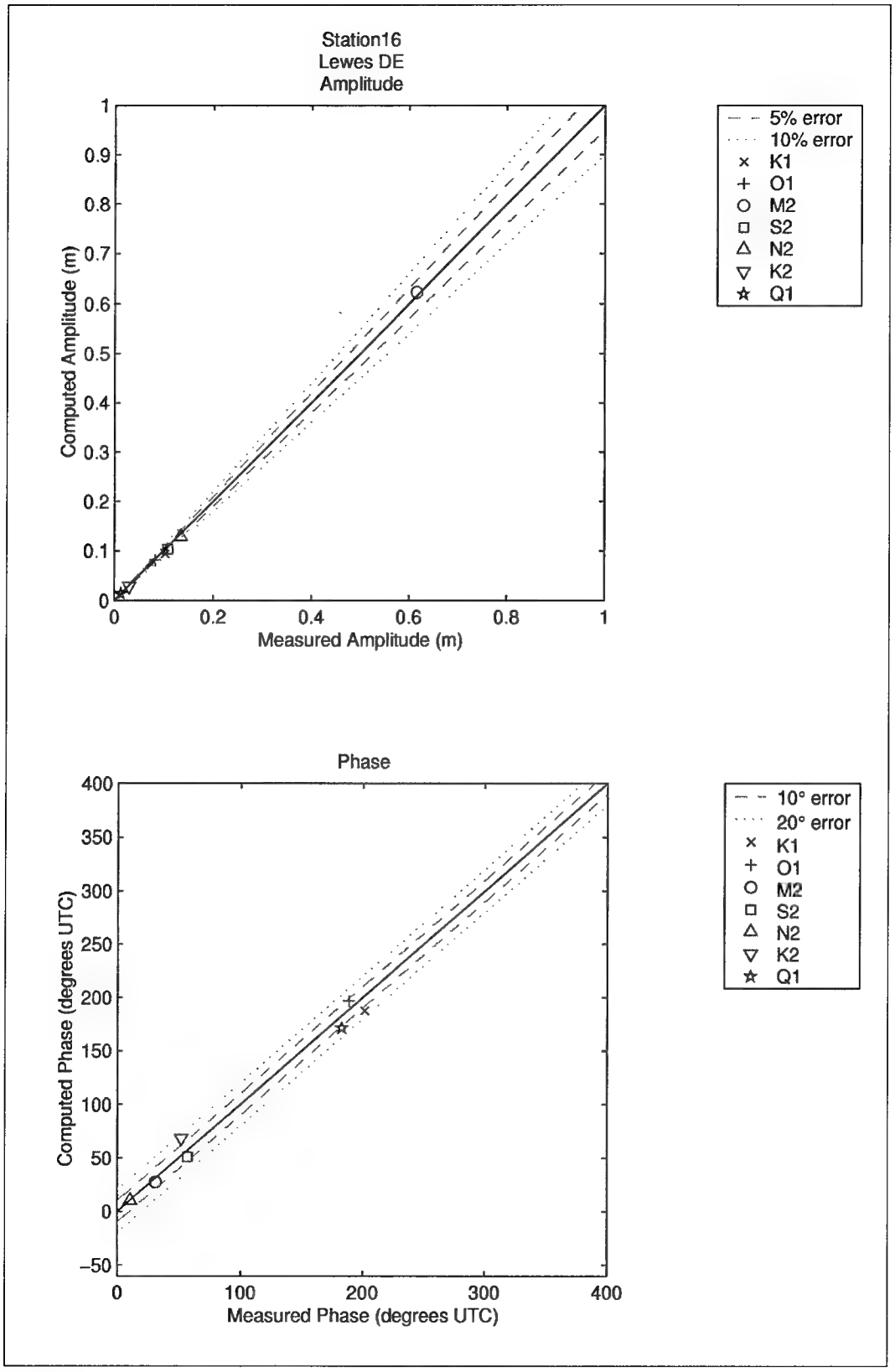

Figure 47. Computed vs. measured harmonic constituents at sta 16

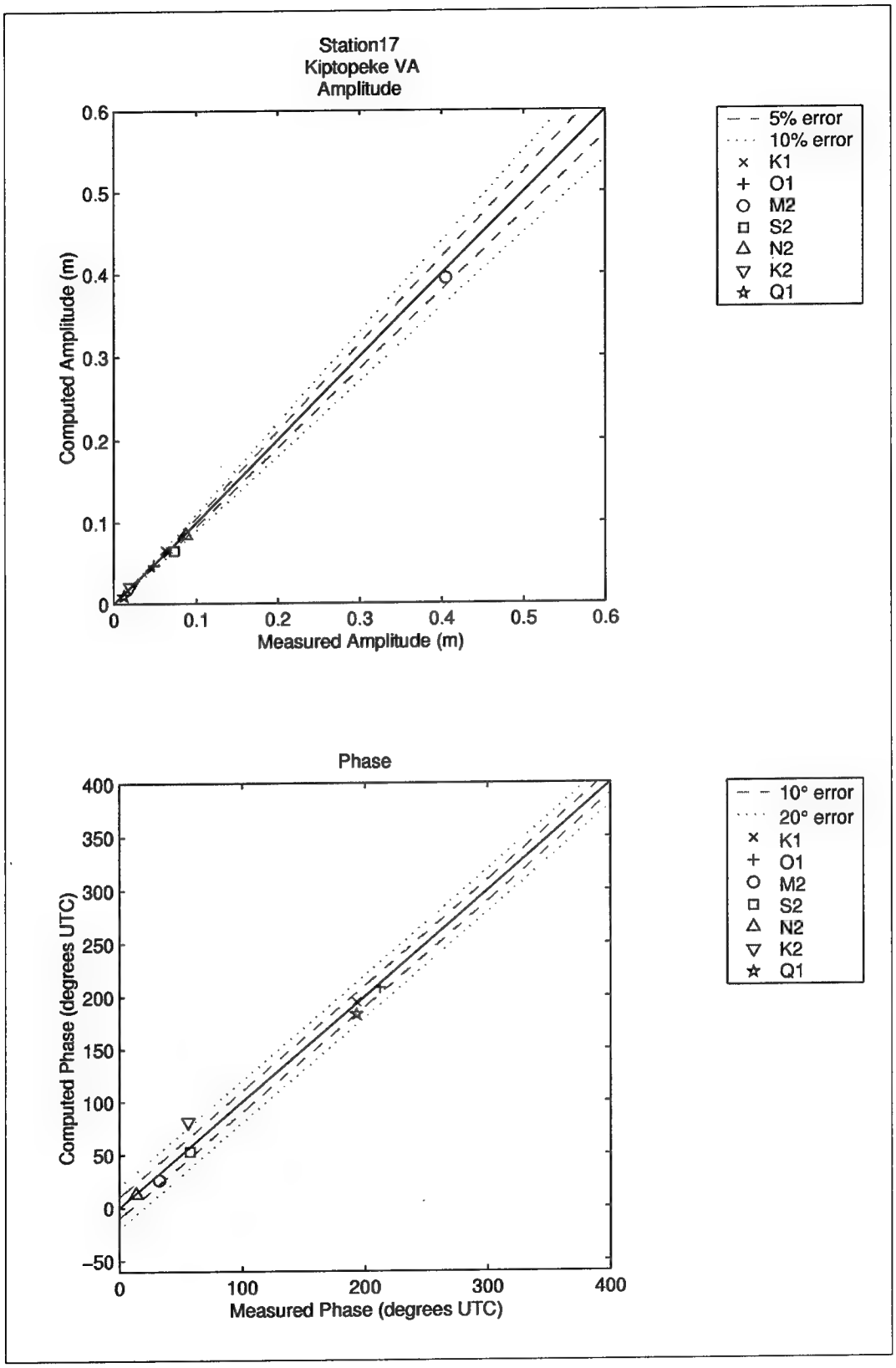

Figure 48. Computed vs. measured harmonic constituents at sta 17

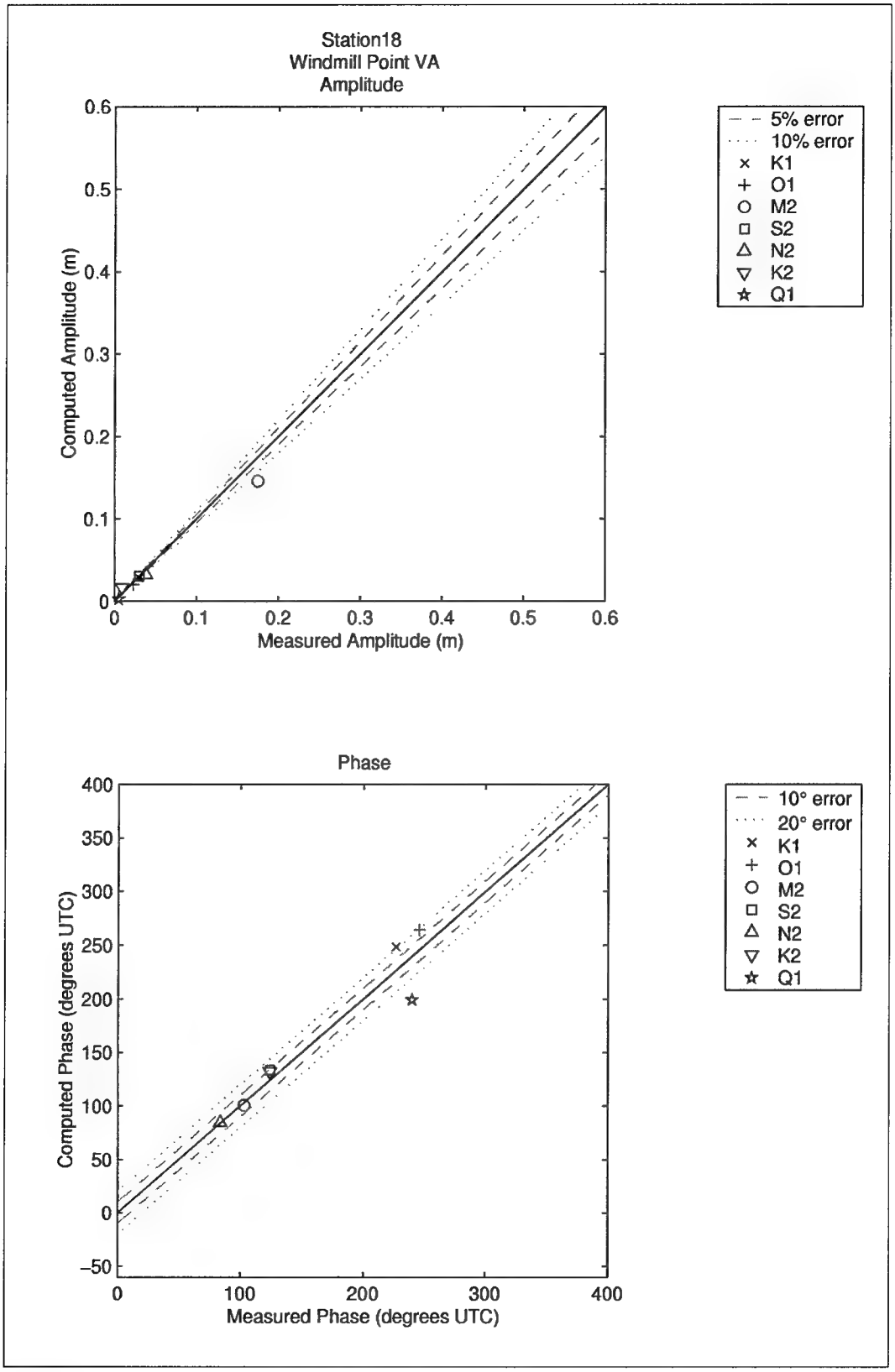

Figure 49. Computed vs. measured harmonic constituents at sta 18

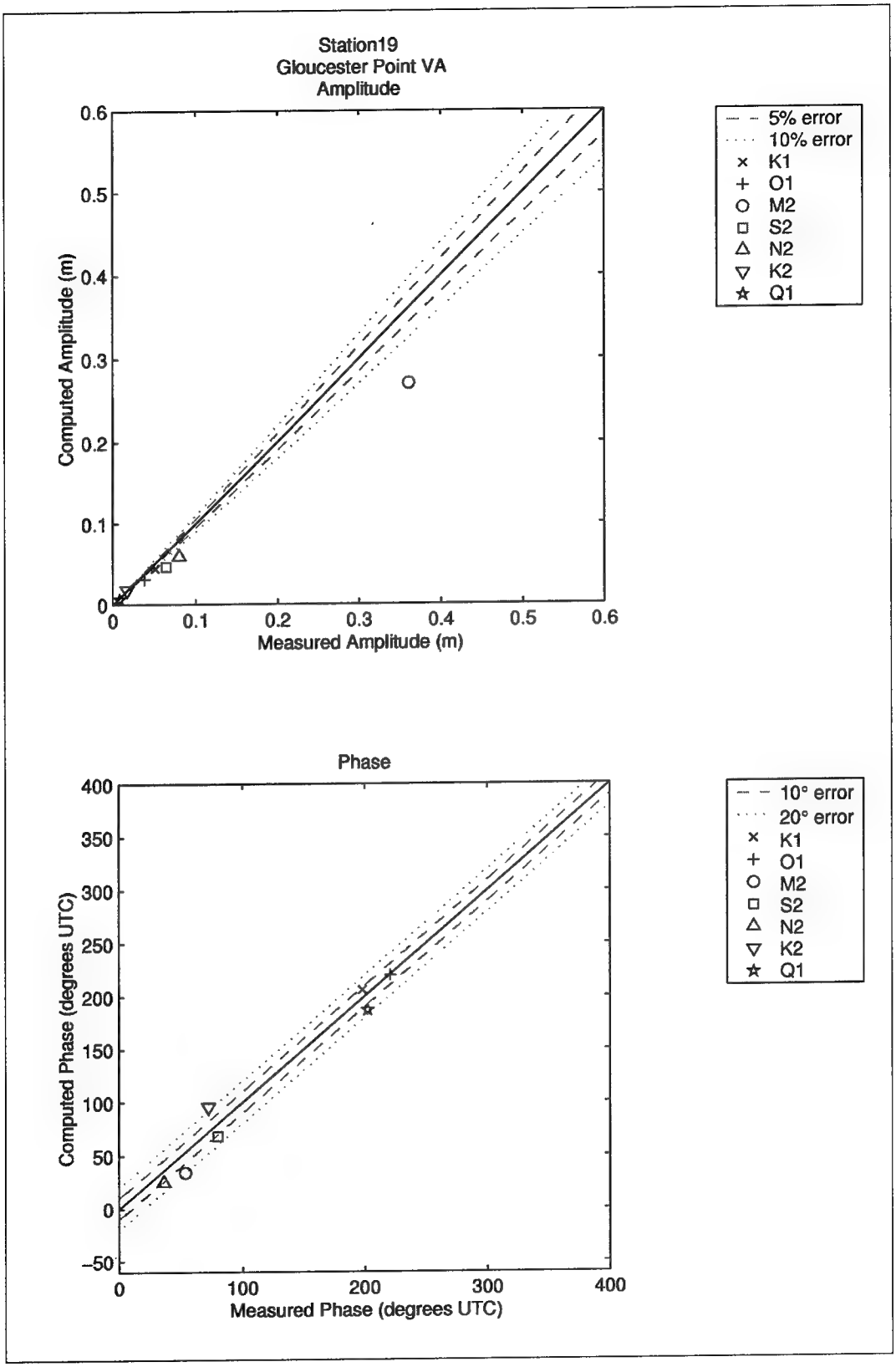

Figure 50. Computed vs. measured harmonic constituents at sta 19

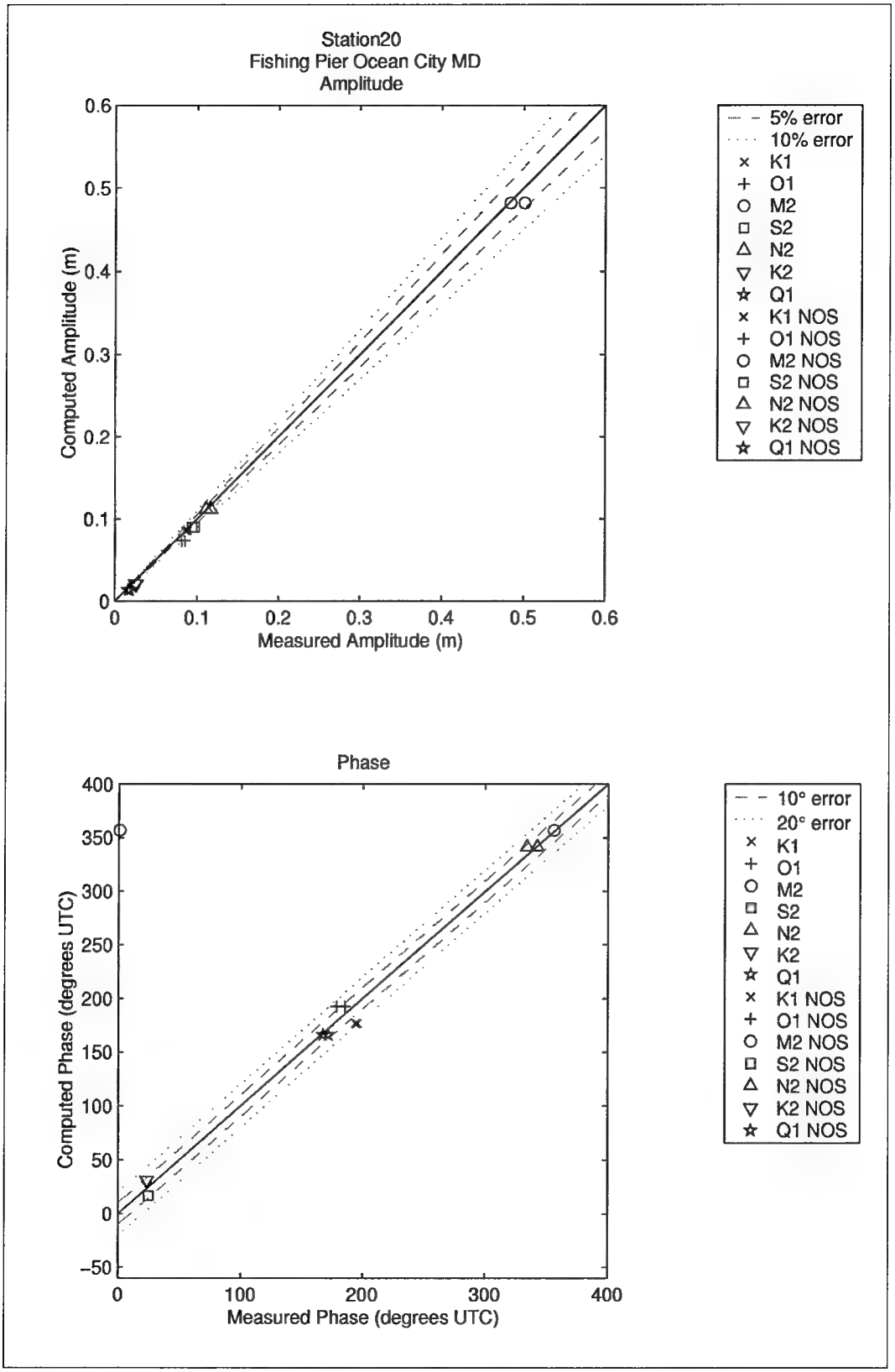

Figure 51. Computed vs. measured harmonic constituents at sta 20

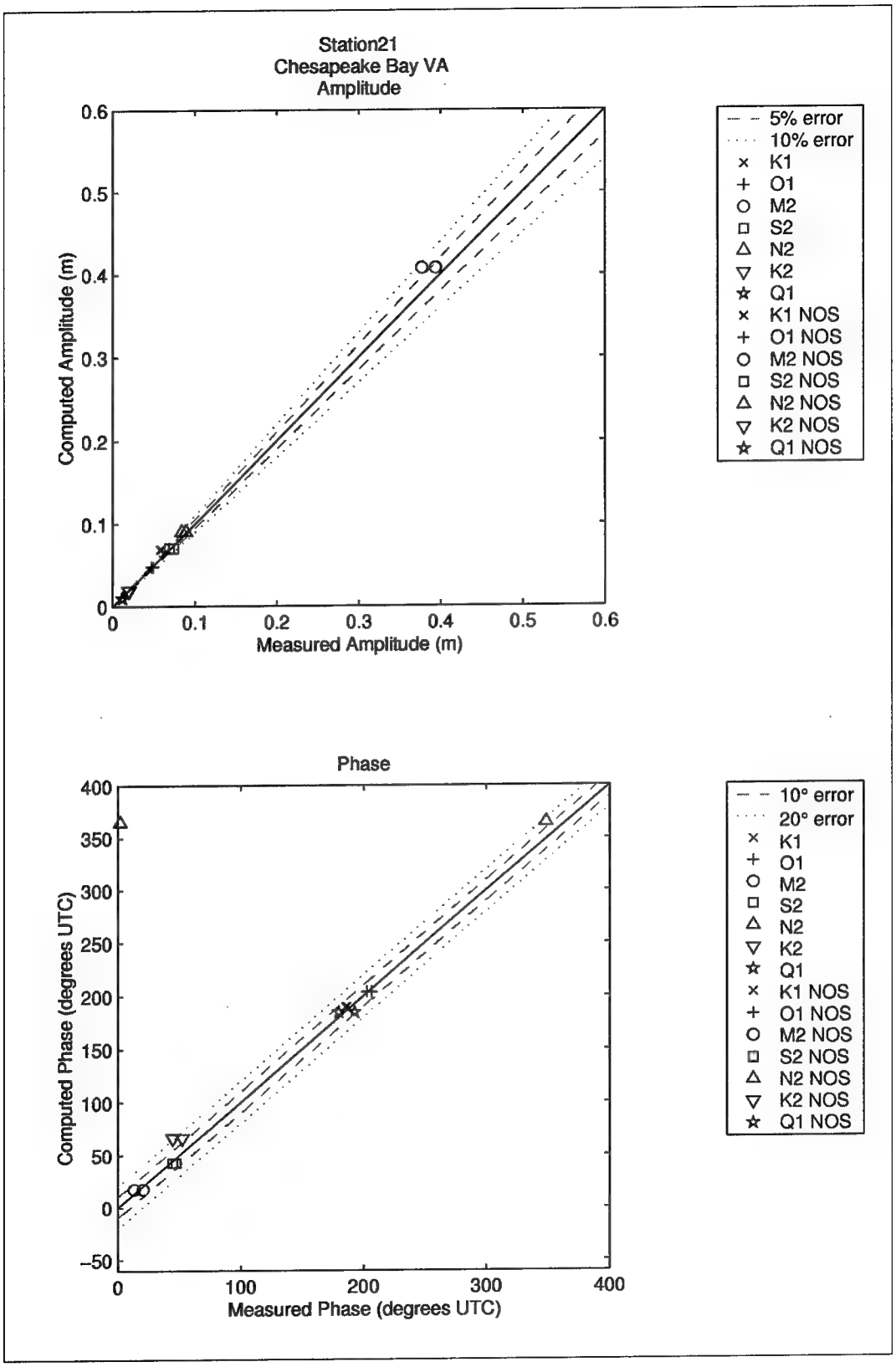

Figure 52. Computed vs. measured harmonic constituents at sta 21

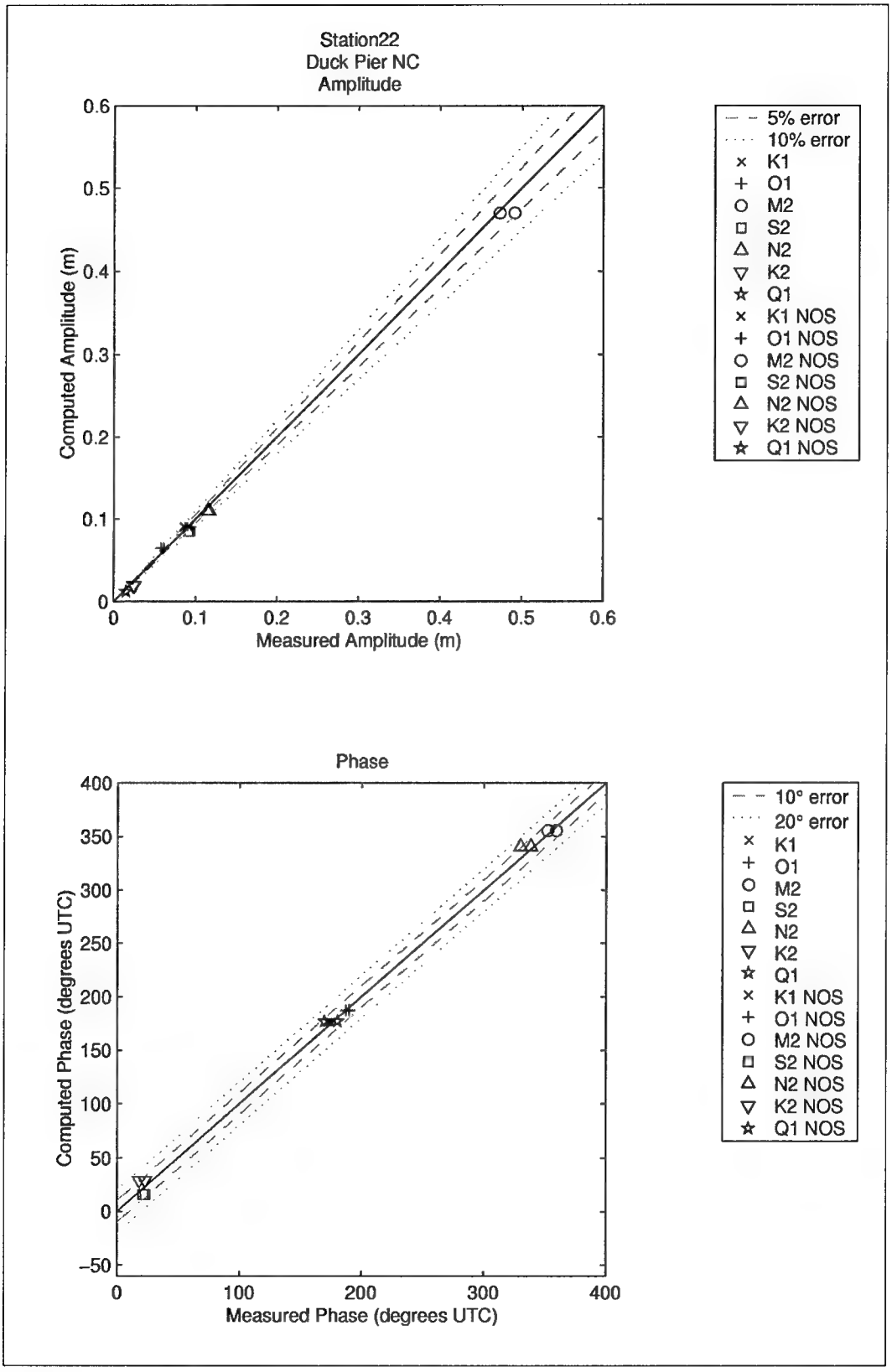

Figure 53. Computed vs. measured harmonic constituents at sta 22

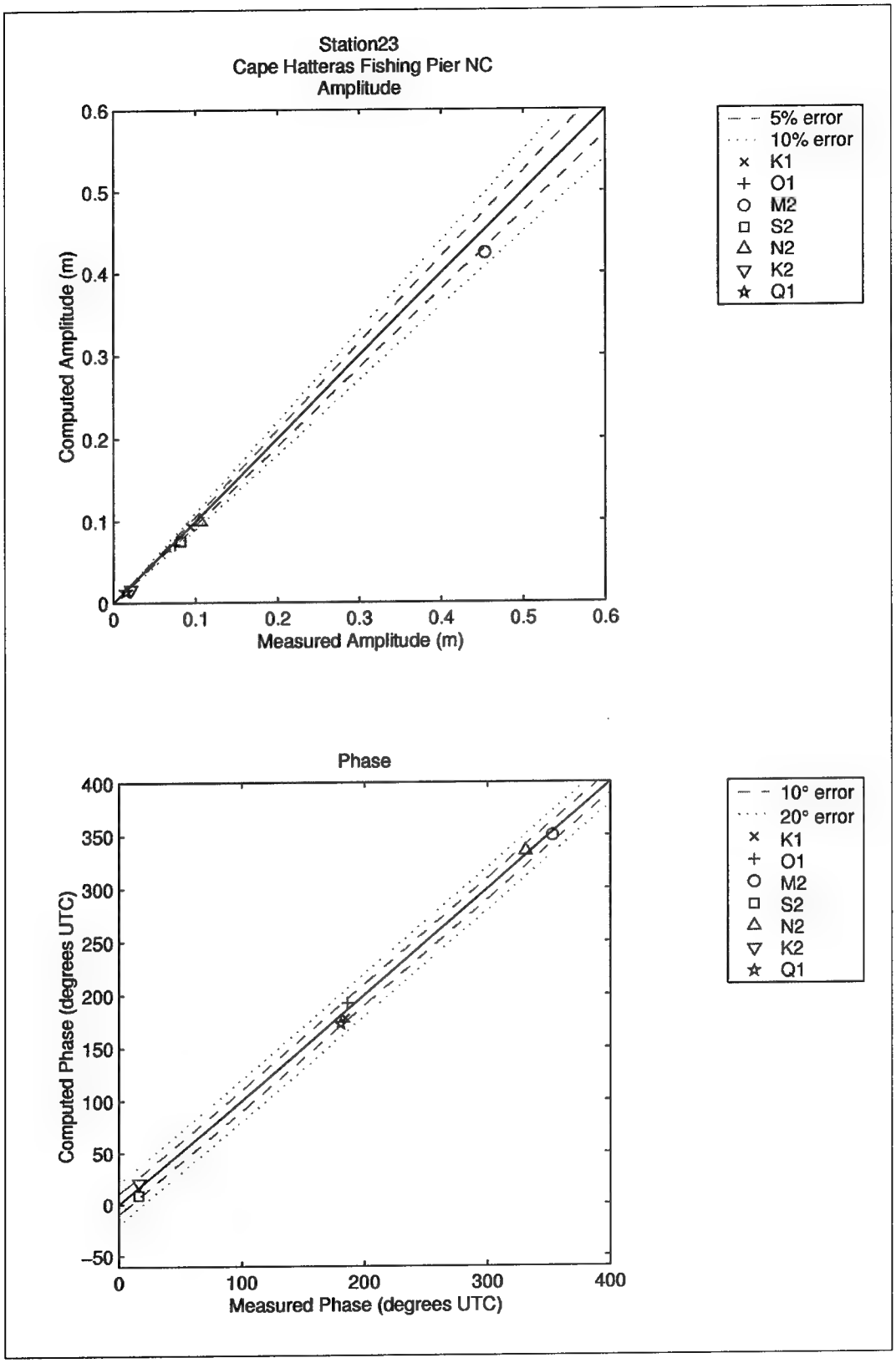

Figure 54. Computed vs. measured harmonic constituents at sta 23

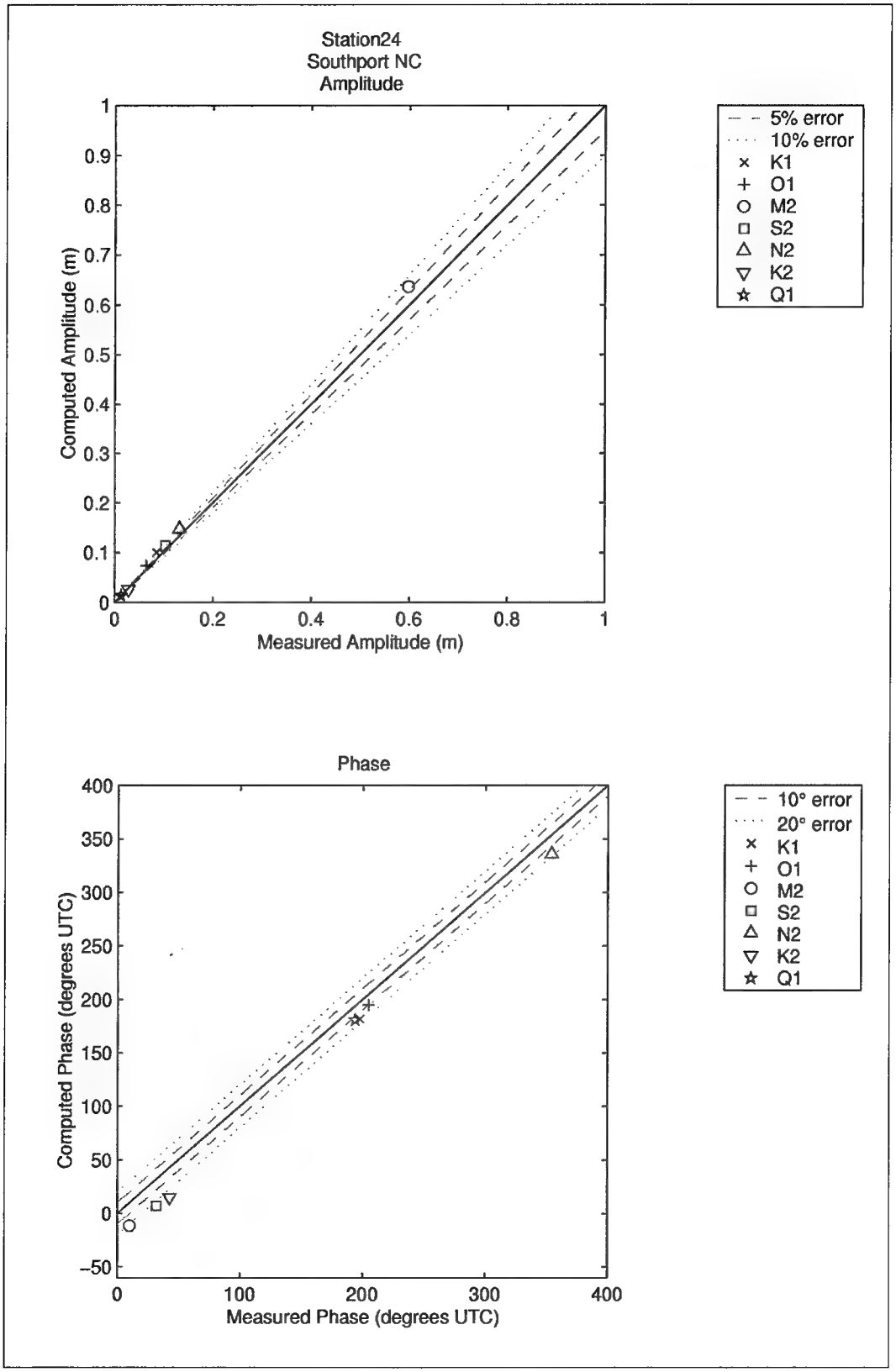

Figure 55. Computed vs. measured harmonic constituents at sta 24

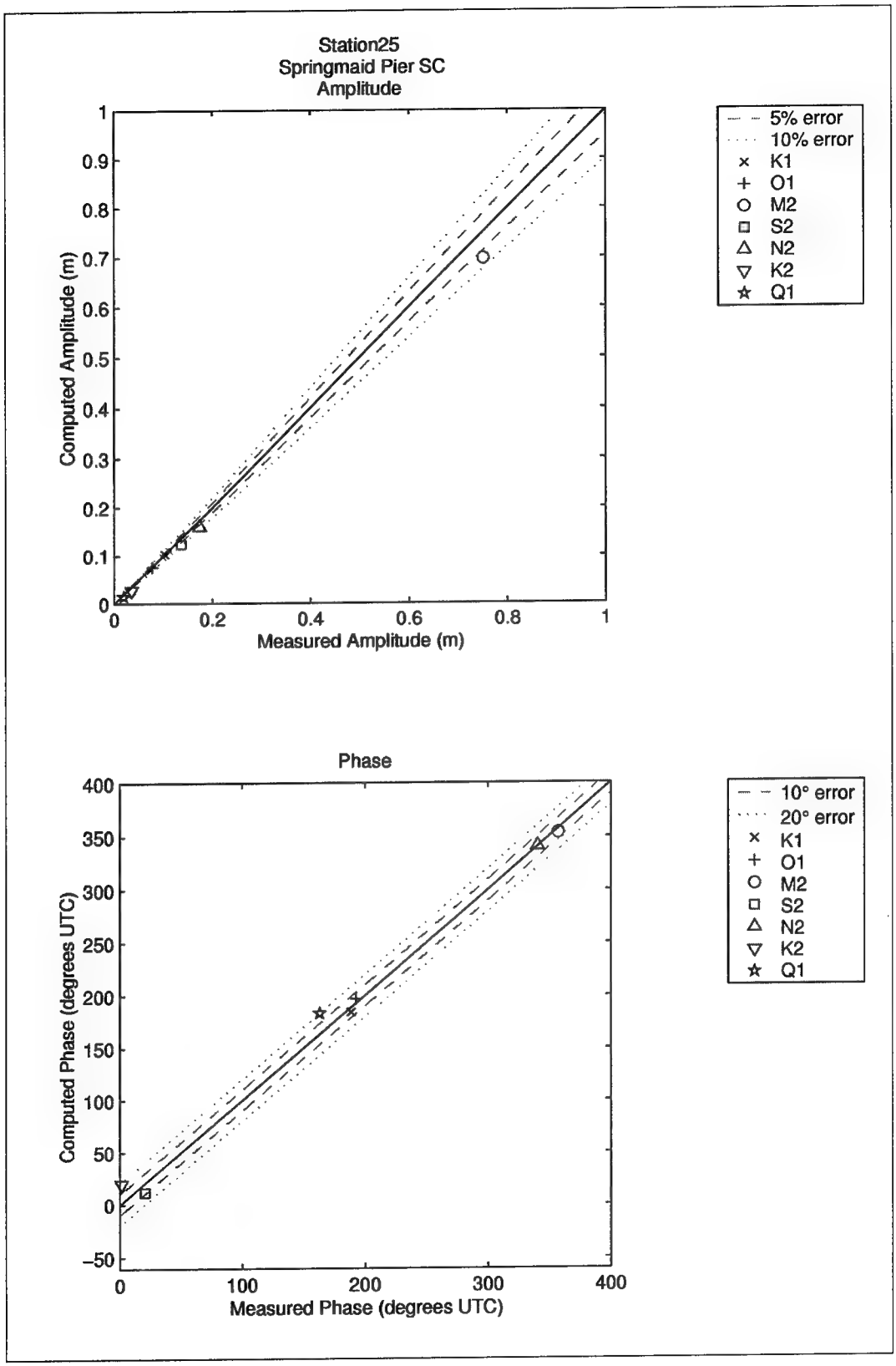

Figure 56. Computed vs. measured harmonic constituents at sta 25

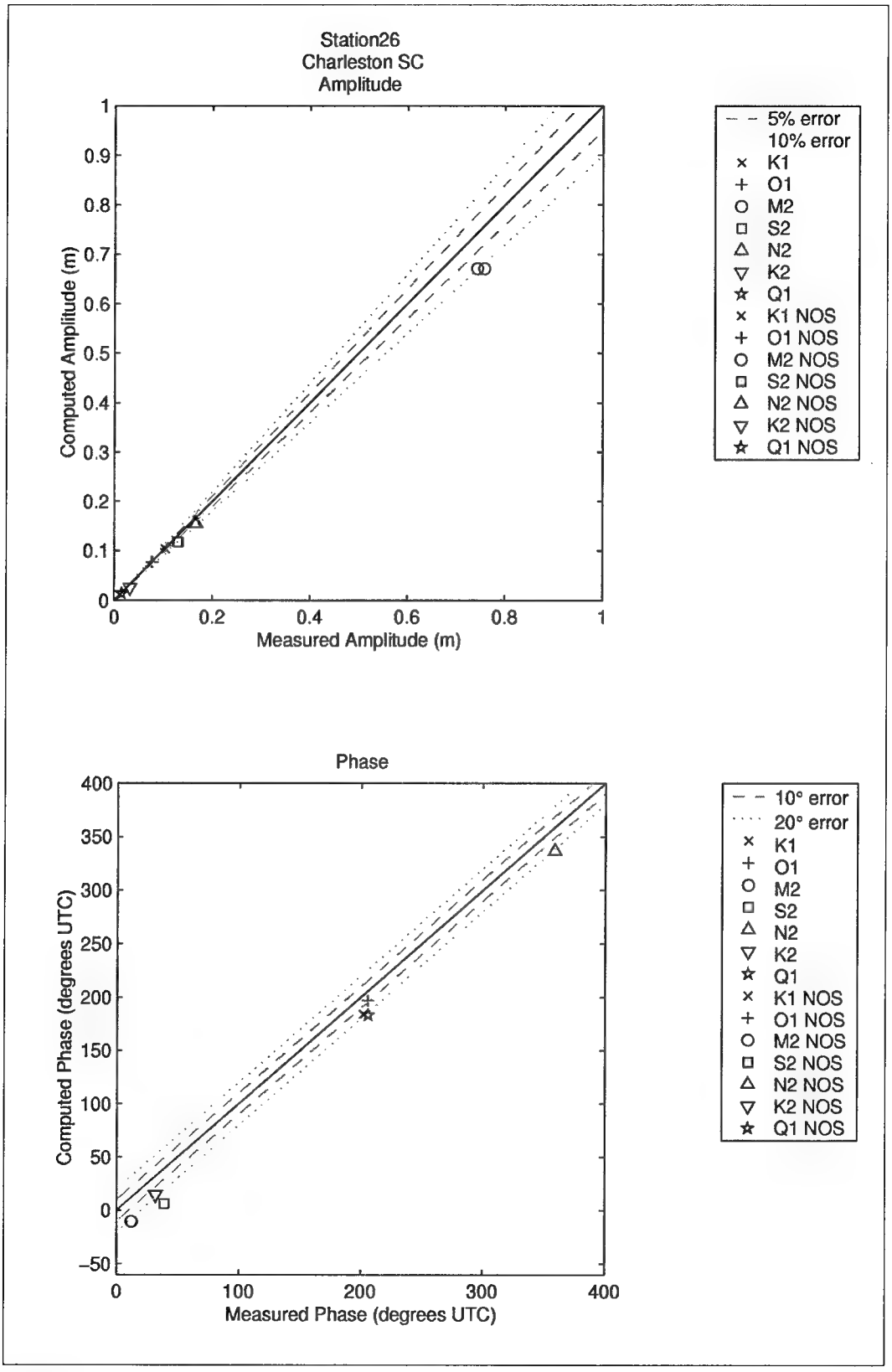

Figure 57. Computed vs. measured harmonic constituents at sta 26

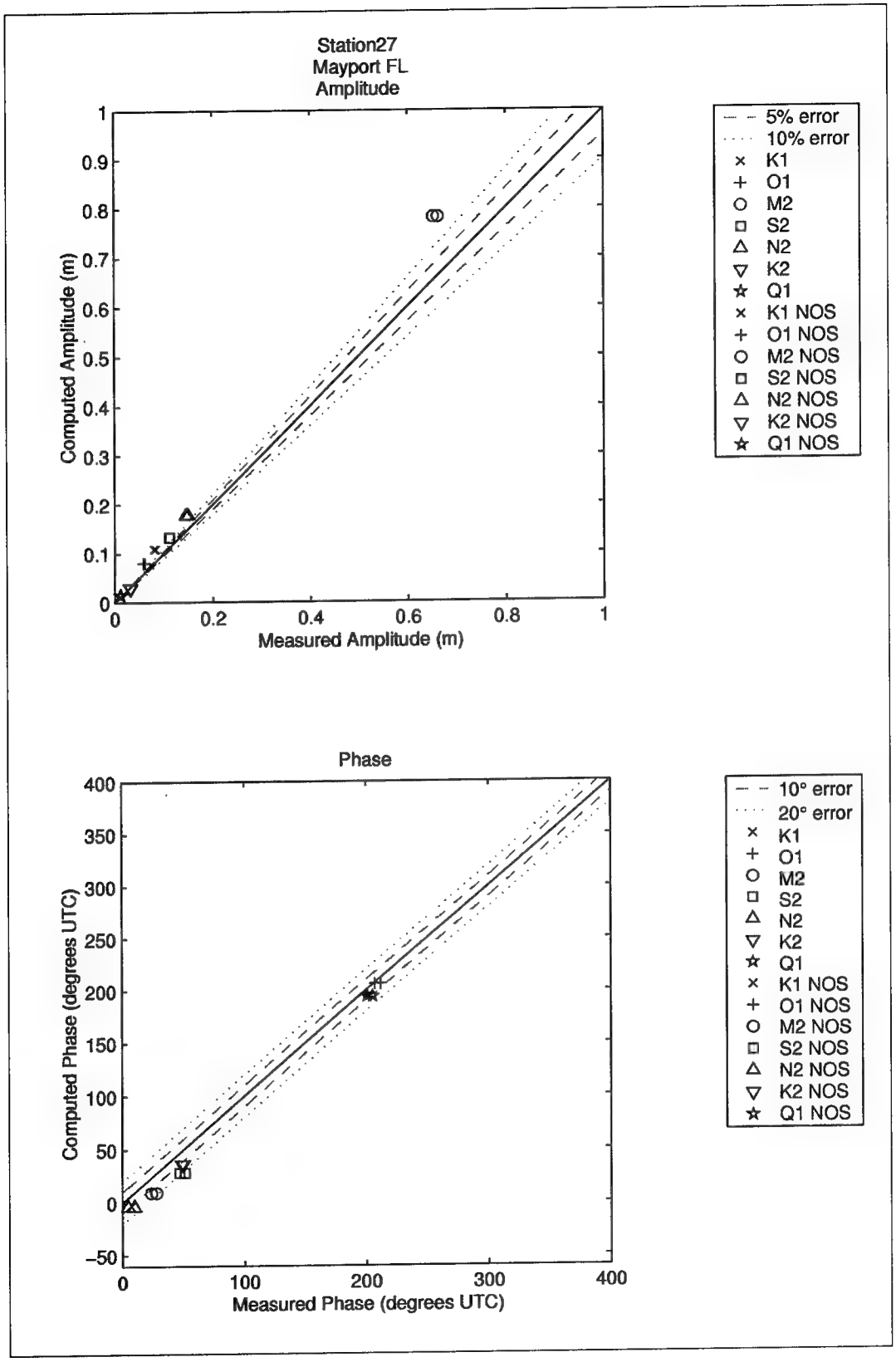

Figure 58. Computed vs. measured harmonic constituents at sta 27

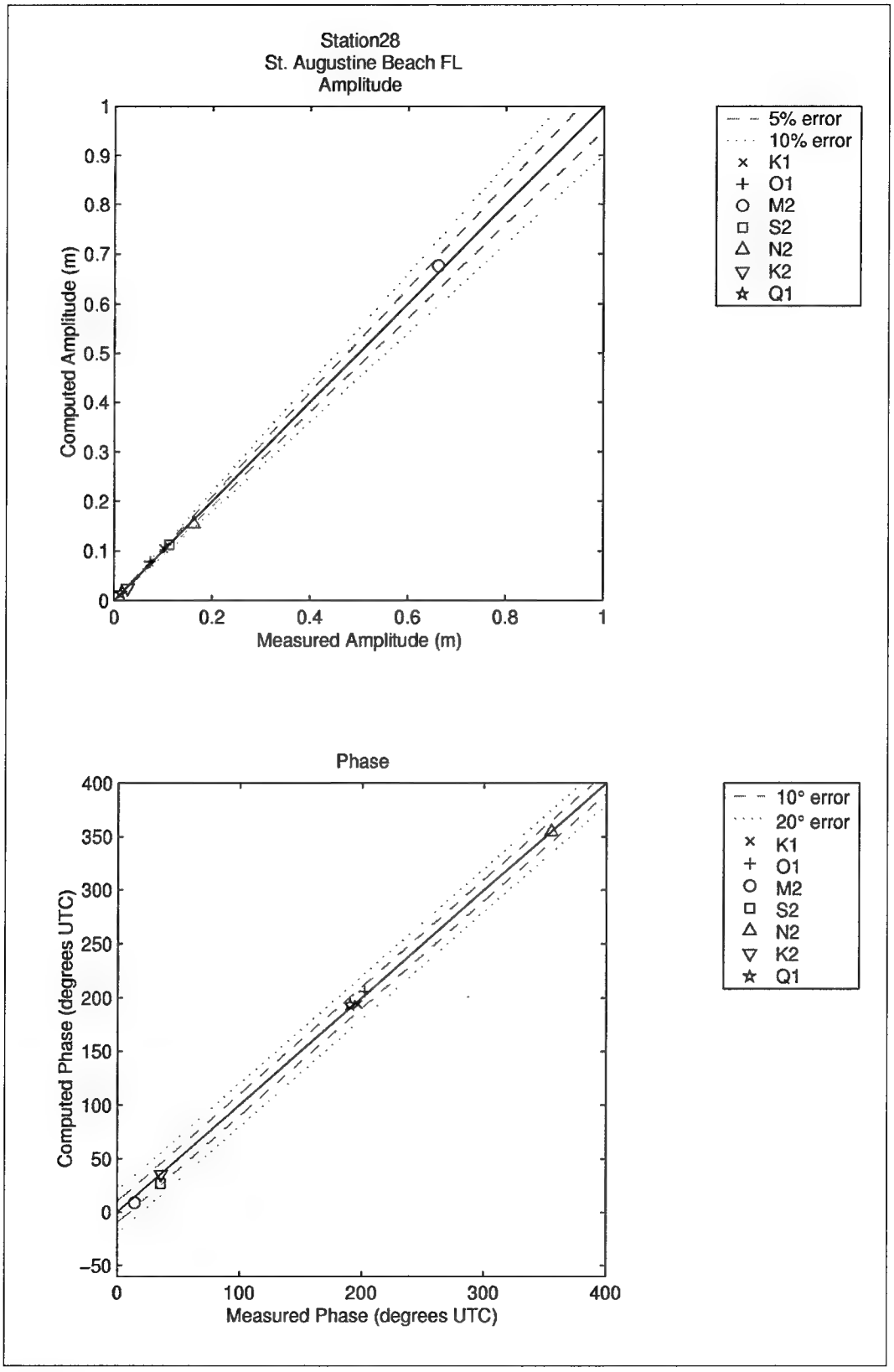

Figure 59. Computed vs. measured harmonic constituents at sta 28

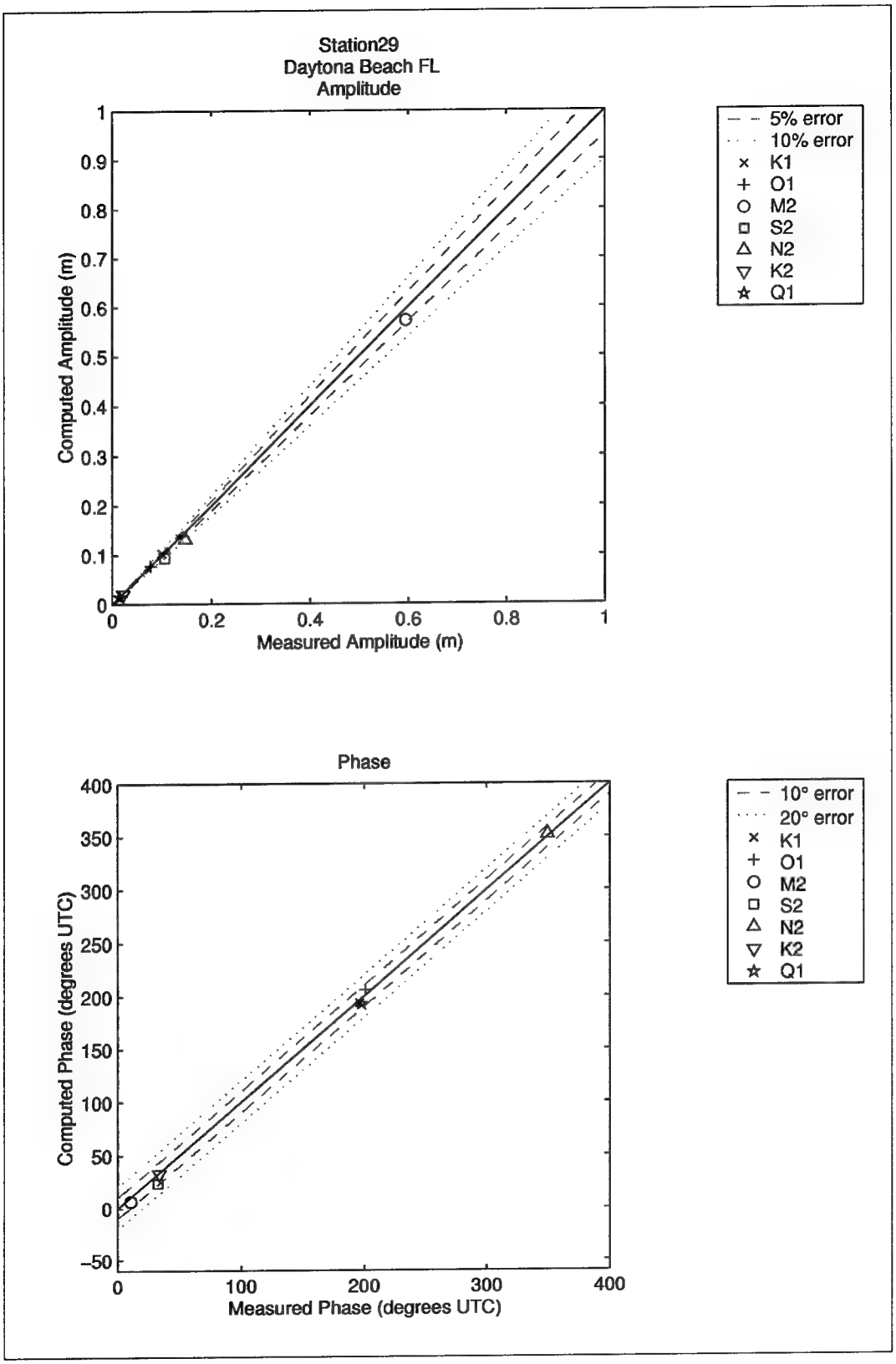

Figure 60. Computed vs. measured harmonic constituents at sta 29

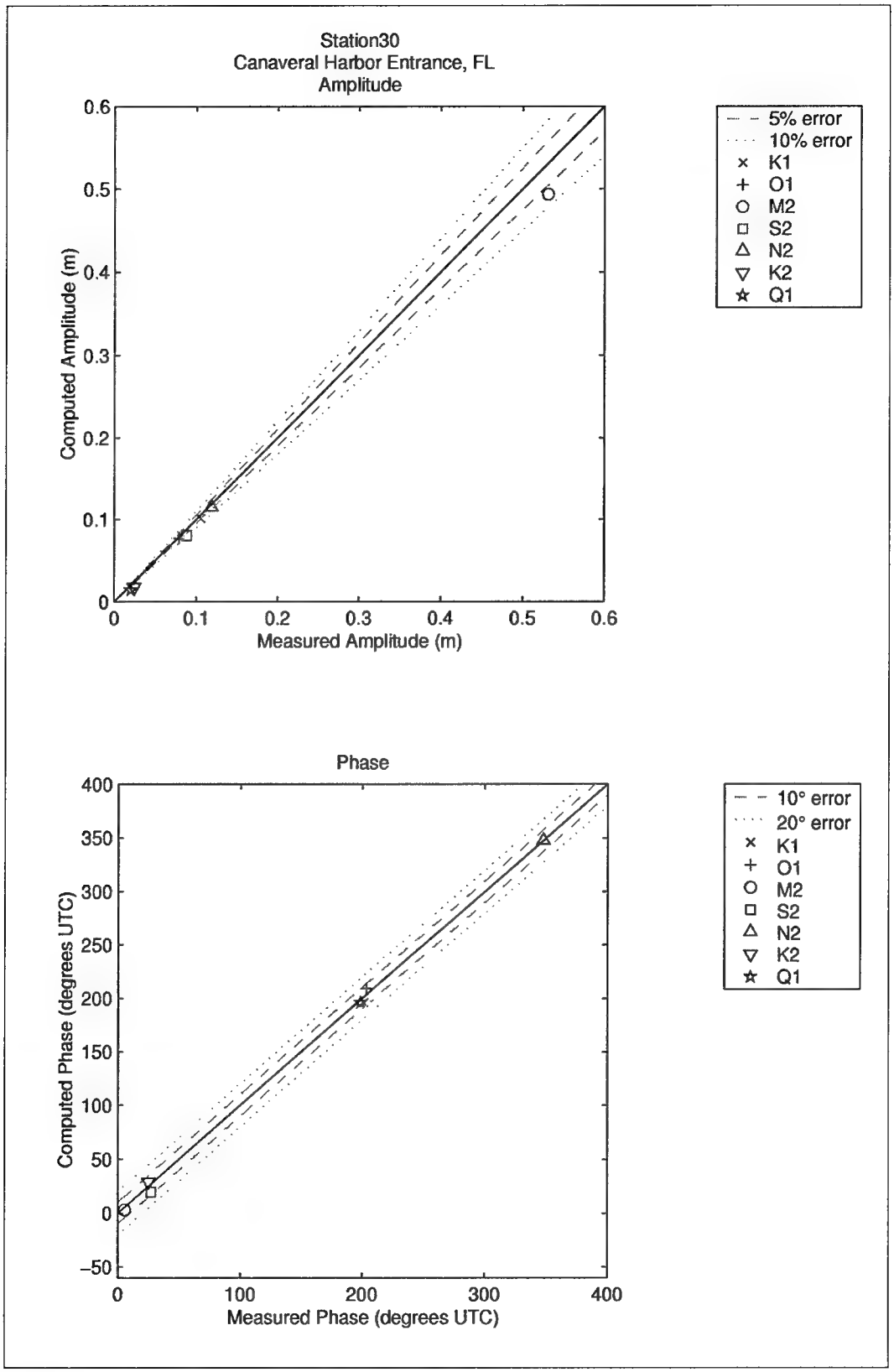

Figure 61. Computed vs. measured harmonic constituents at sta 30

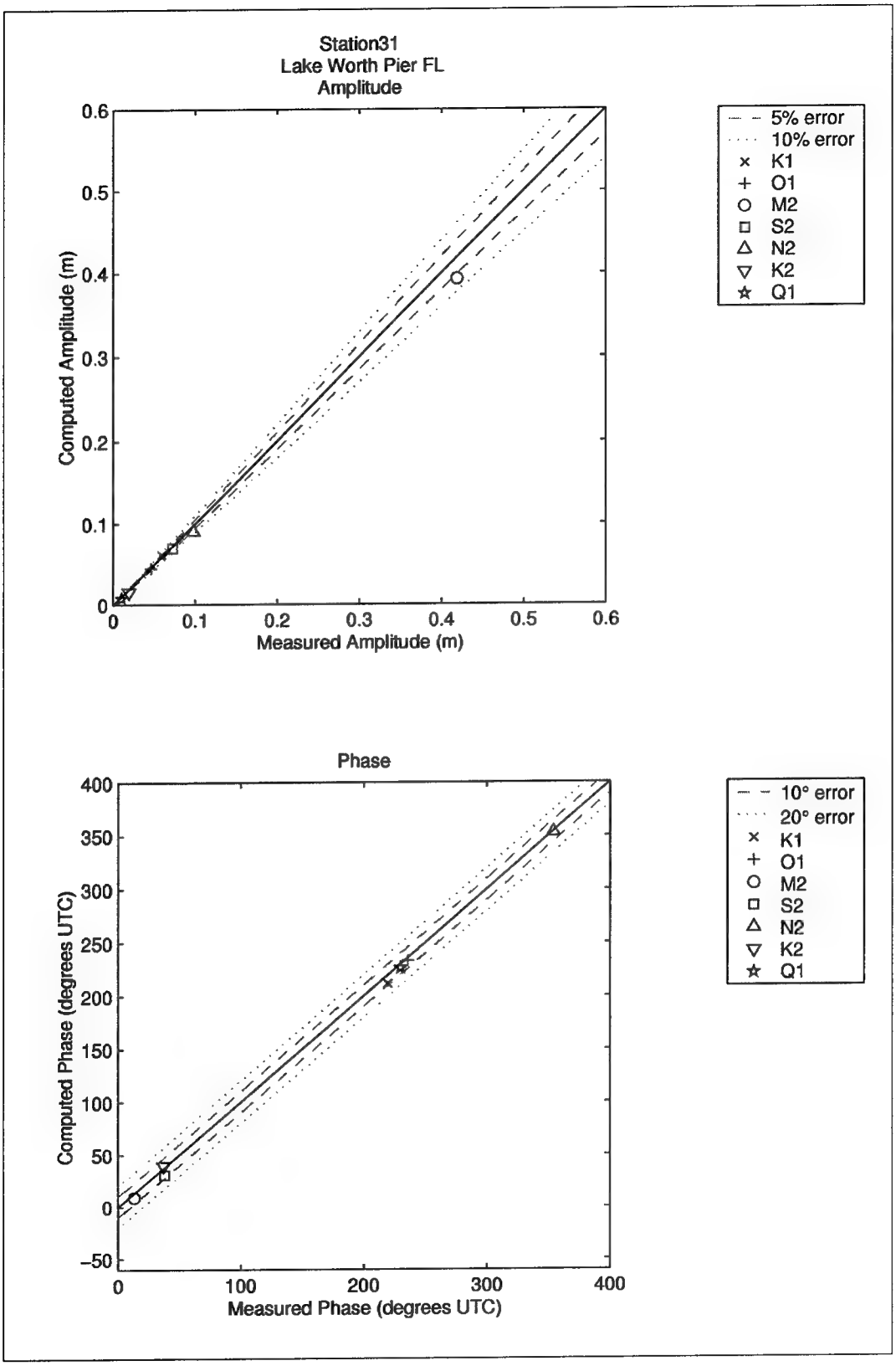

Figure 62. Computed vs. measured harmonic constituents at sta 31

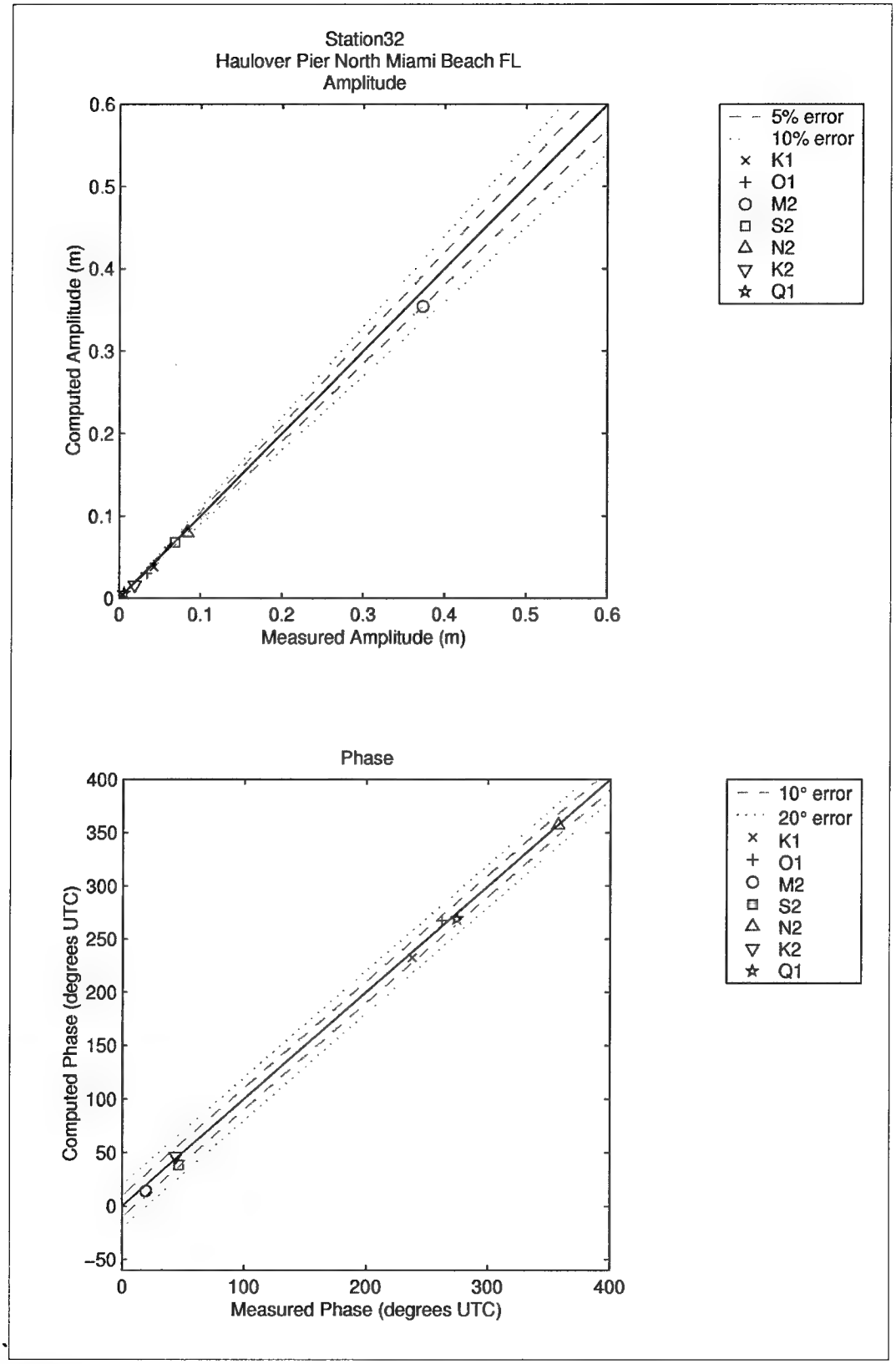

Figure 63. Computed vs. measured harmonic constituents at sta 32

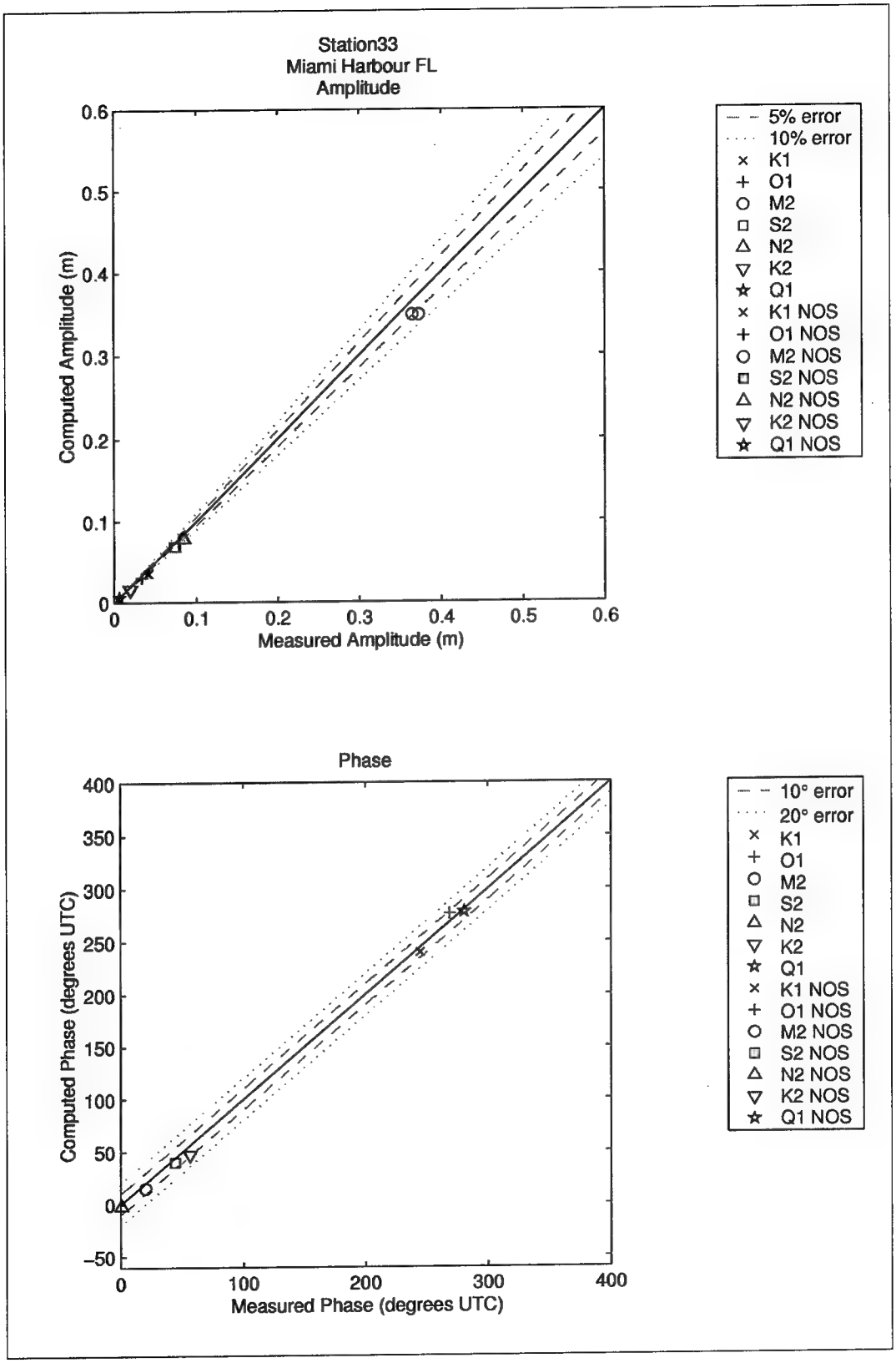

Figure 64. Computed vs. measured harmonic constituents at sta 33

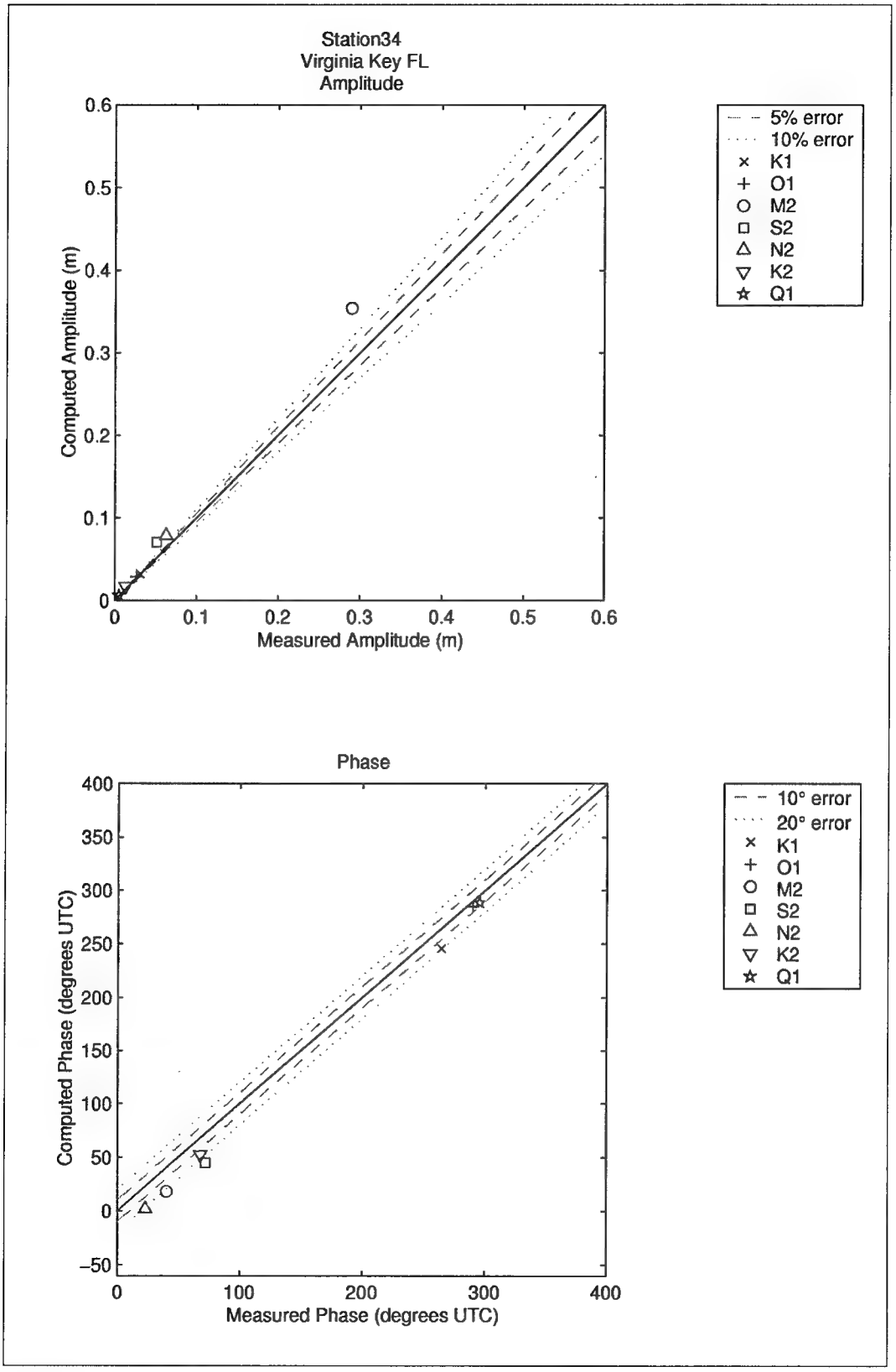

Figure 65. Computed vs. measured harmonic constituents at sta 34

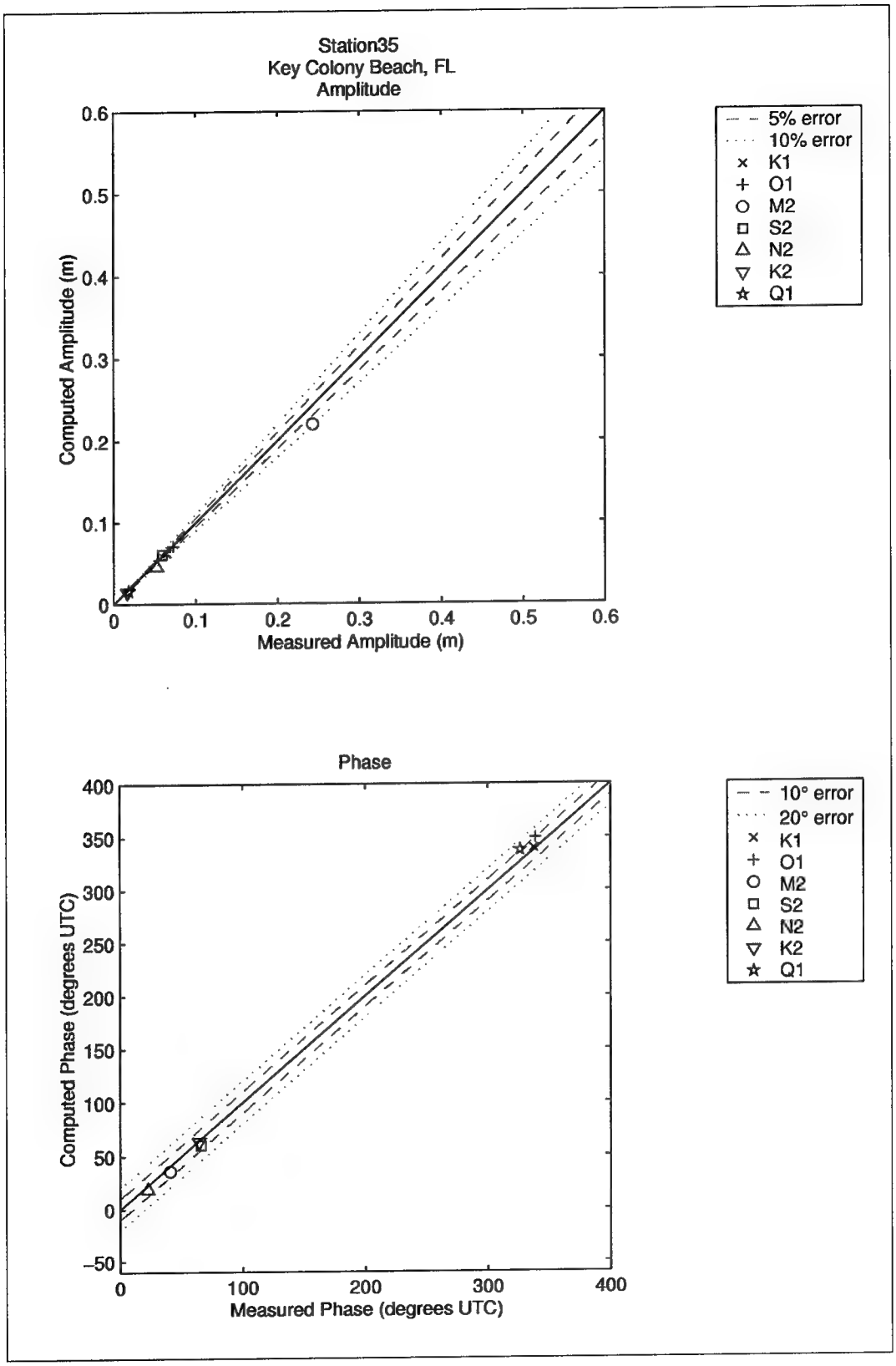

Figure 66. Computed vs. measured harmonic constituents at sta 35

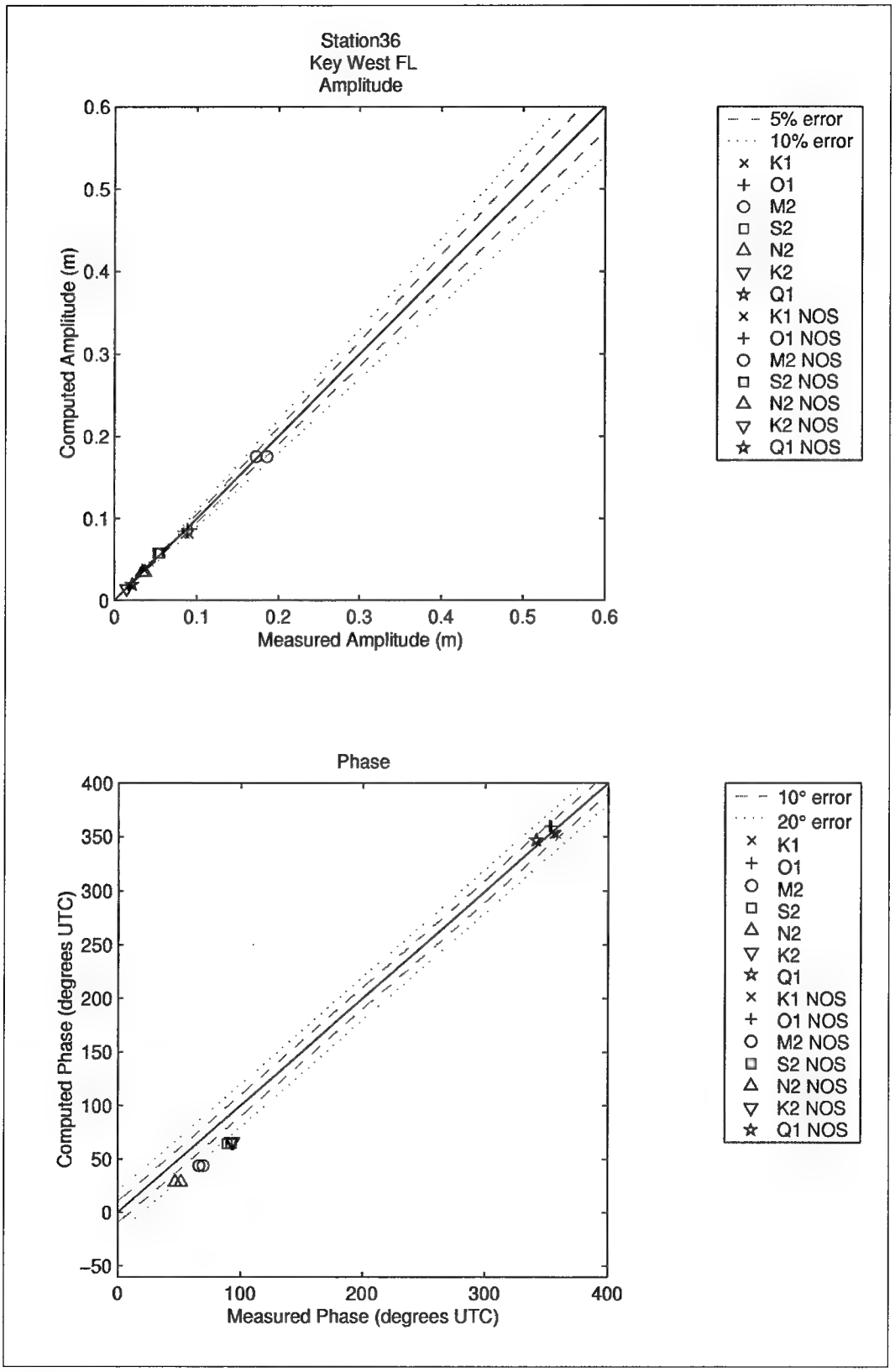

Figure 67. Computed vs. measured harmonic constituents at sta 36

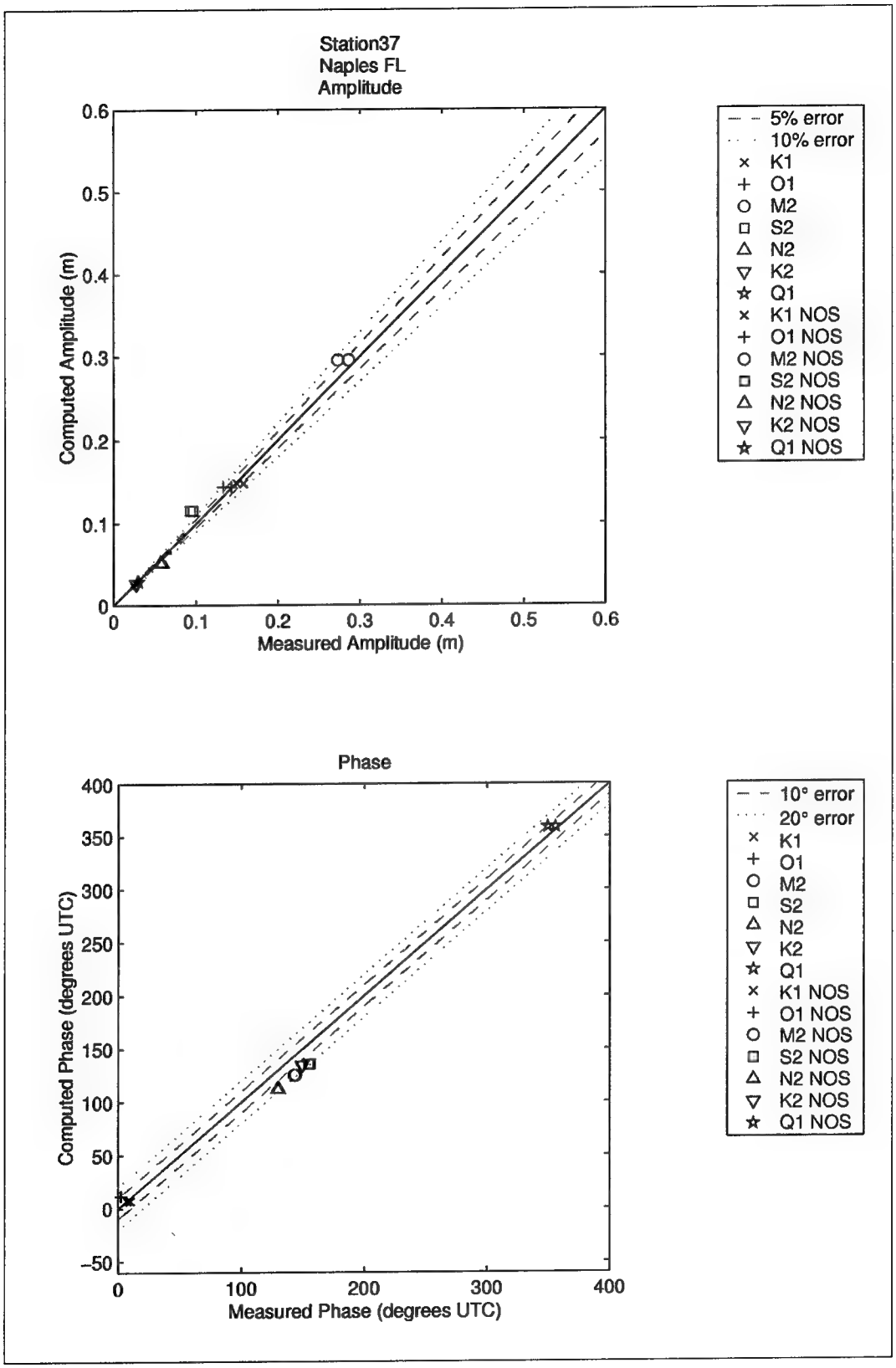

Figure 68. Computed vs. measured harmonic constituents at sta 37

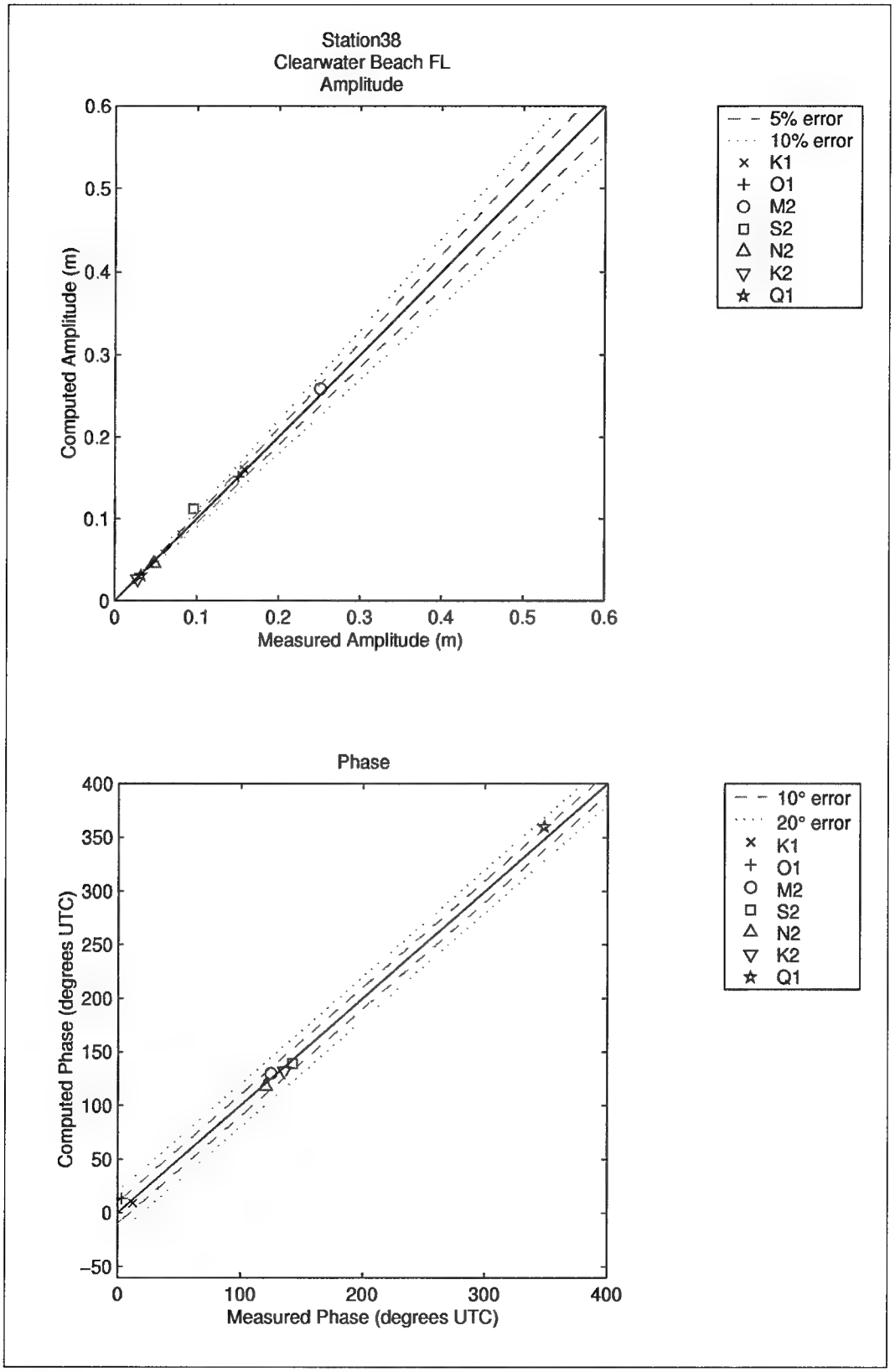

Figure 69. Computed vs. measured harmonic constituents at sta 38

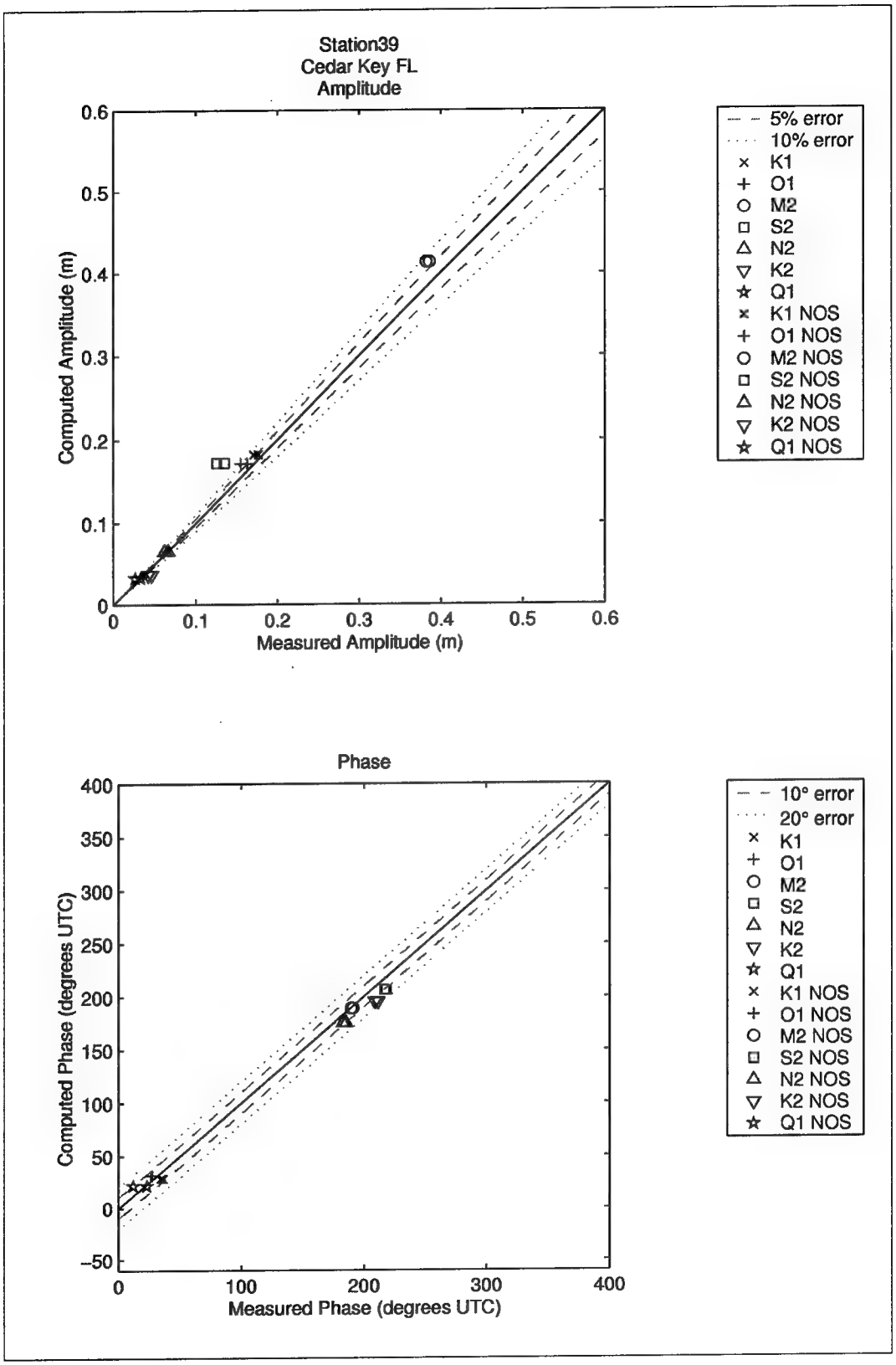

Figure 70. Computed vs. measured harmonic constituents at sta 39

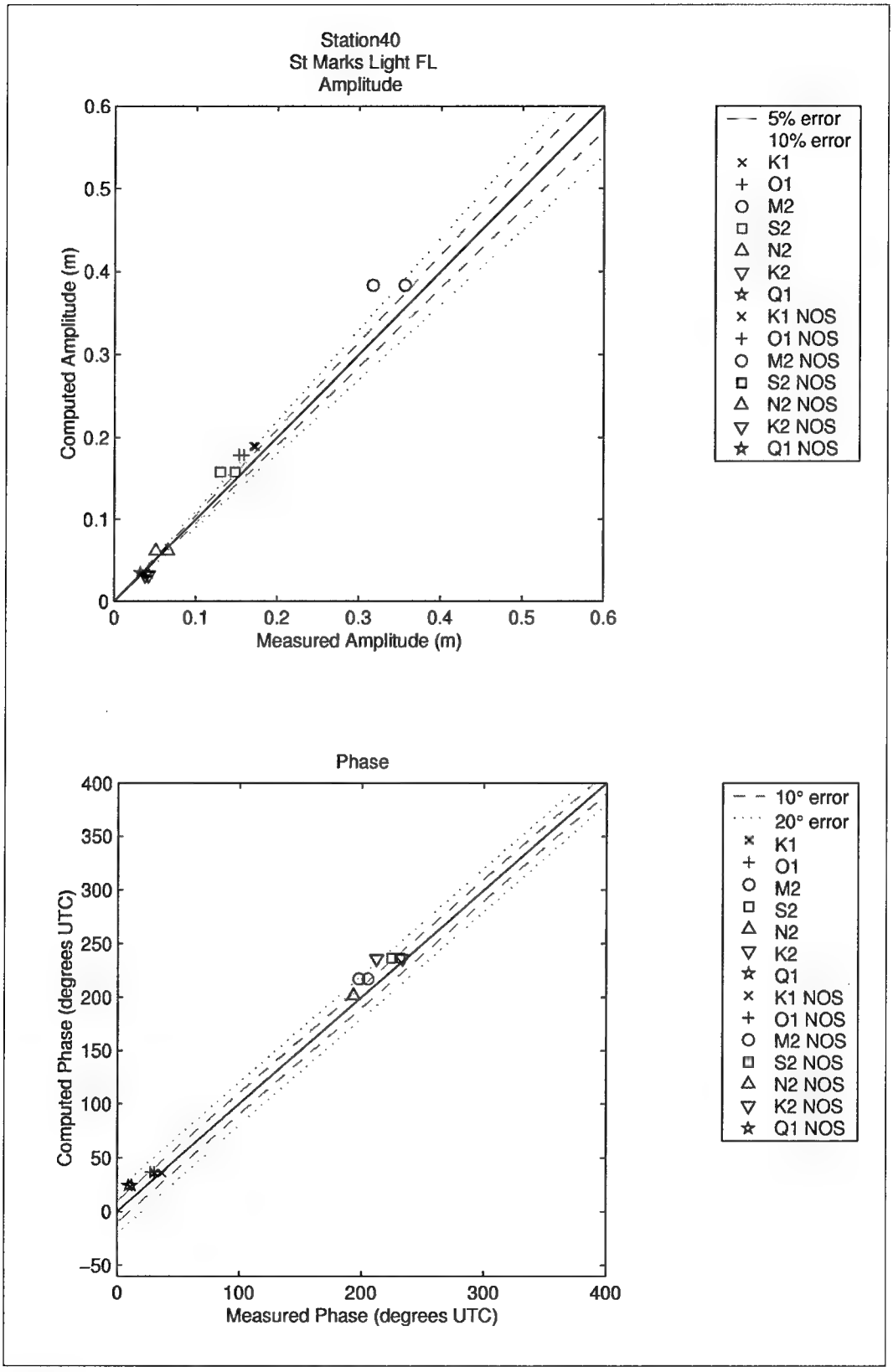

Figure 71. Computed vs. measured harmonic constituents at sta 40

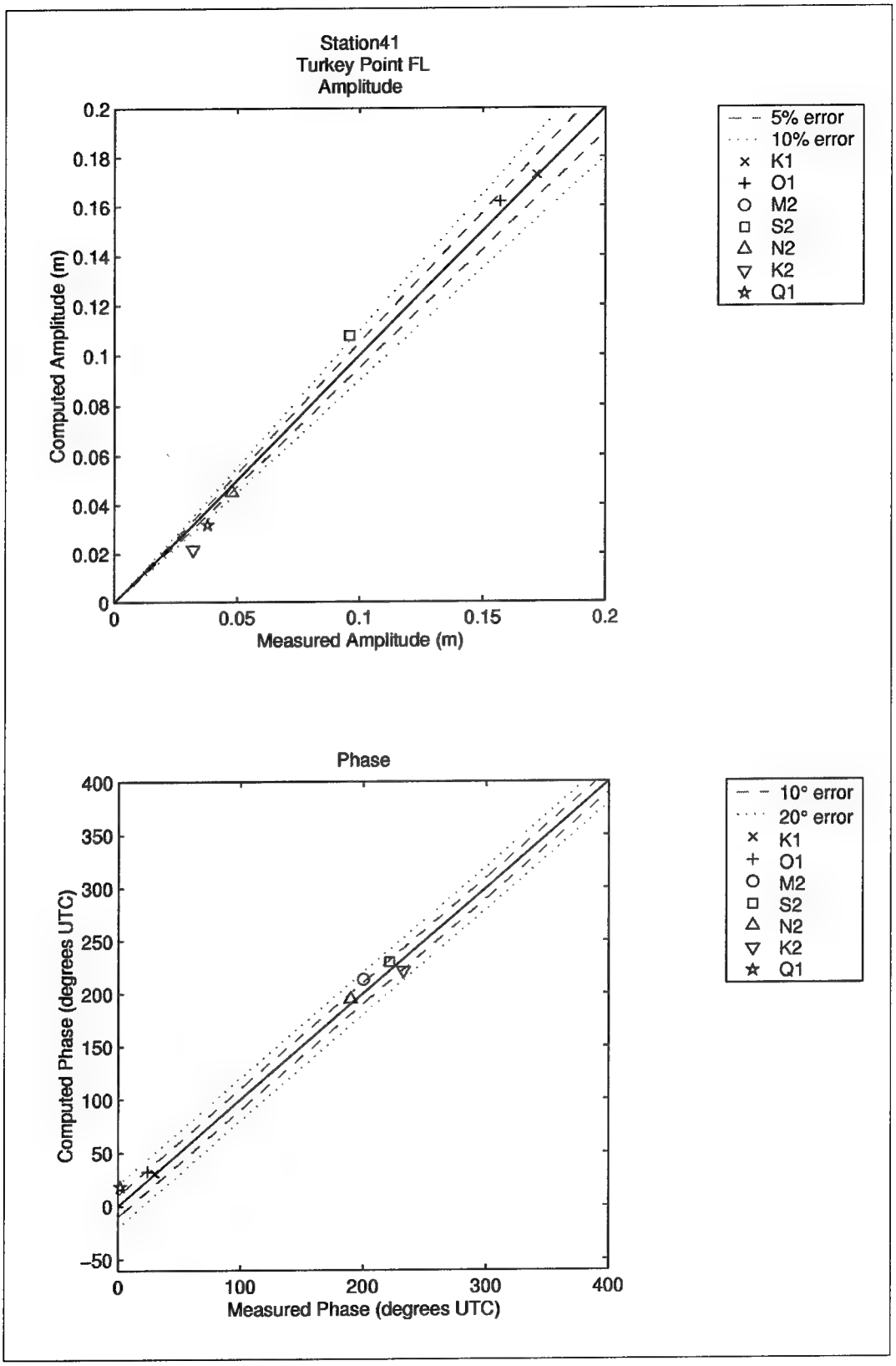

Figure 72. Computed vs. measured harmonic constituents at sta 41

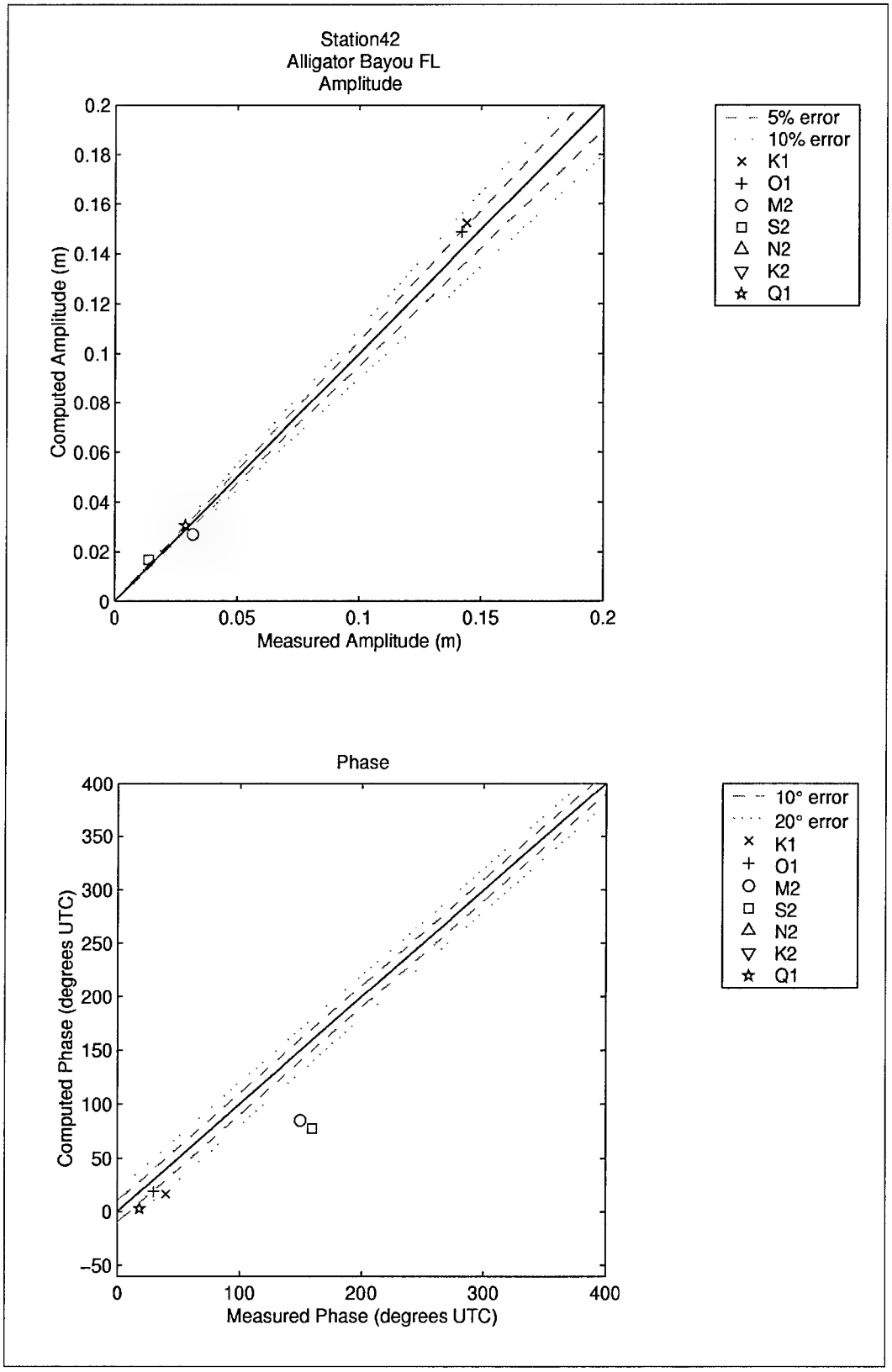

Figure 73. Computed vs. measured harmonic constituents at sta 42

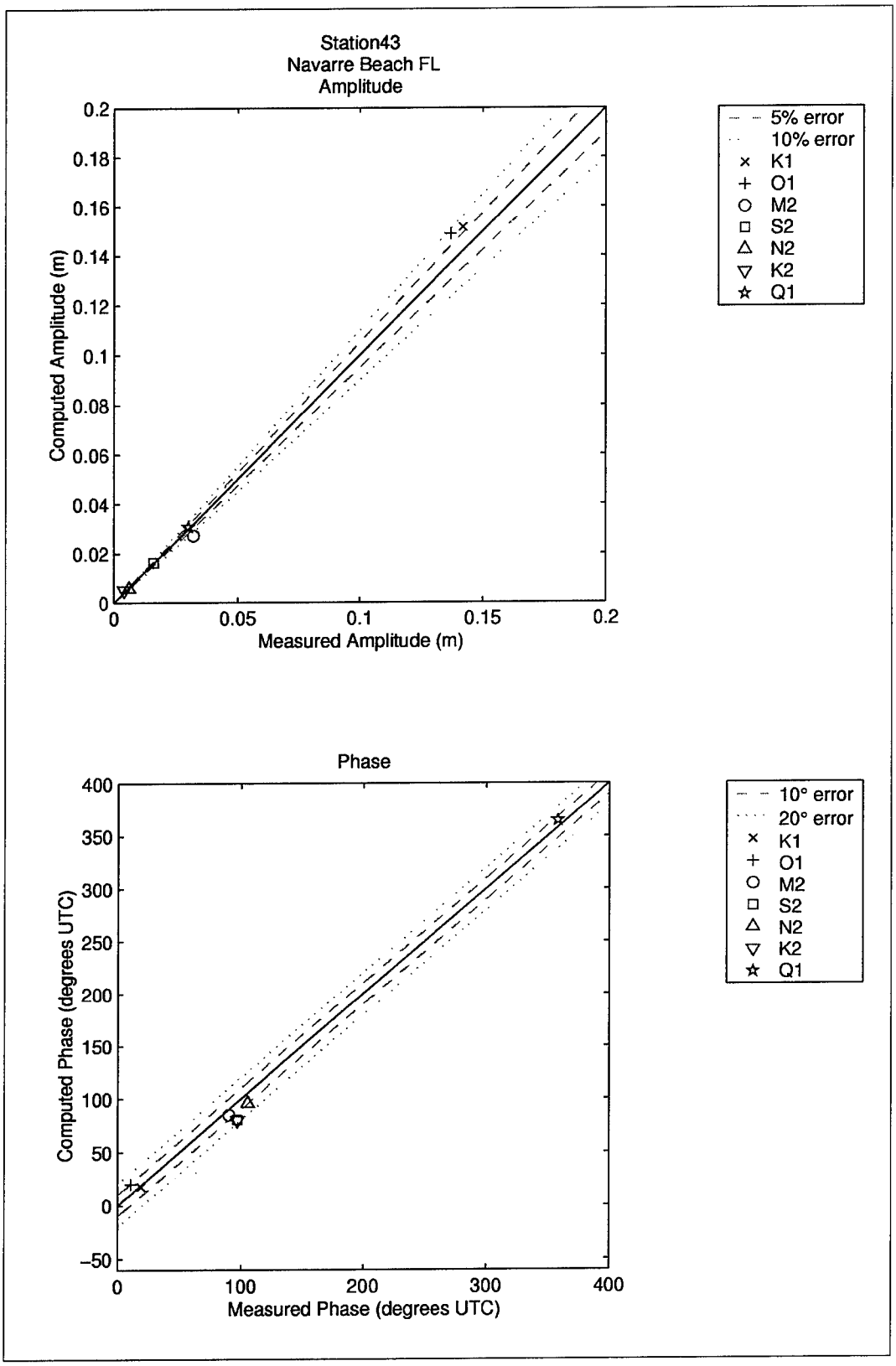

Figure 74. Computed vs. measured harmonic constituents at sta 43

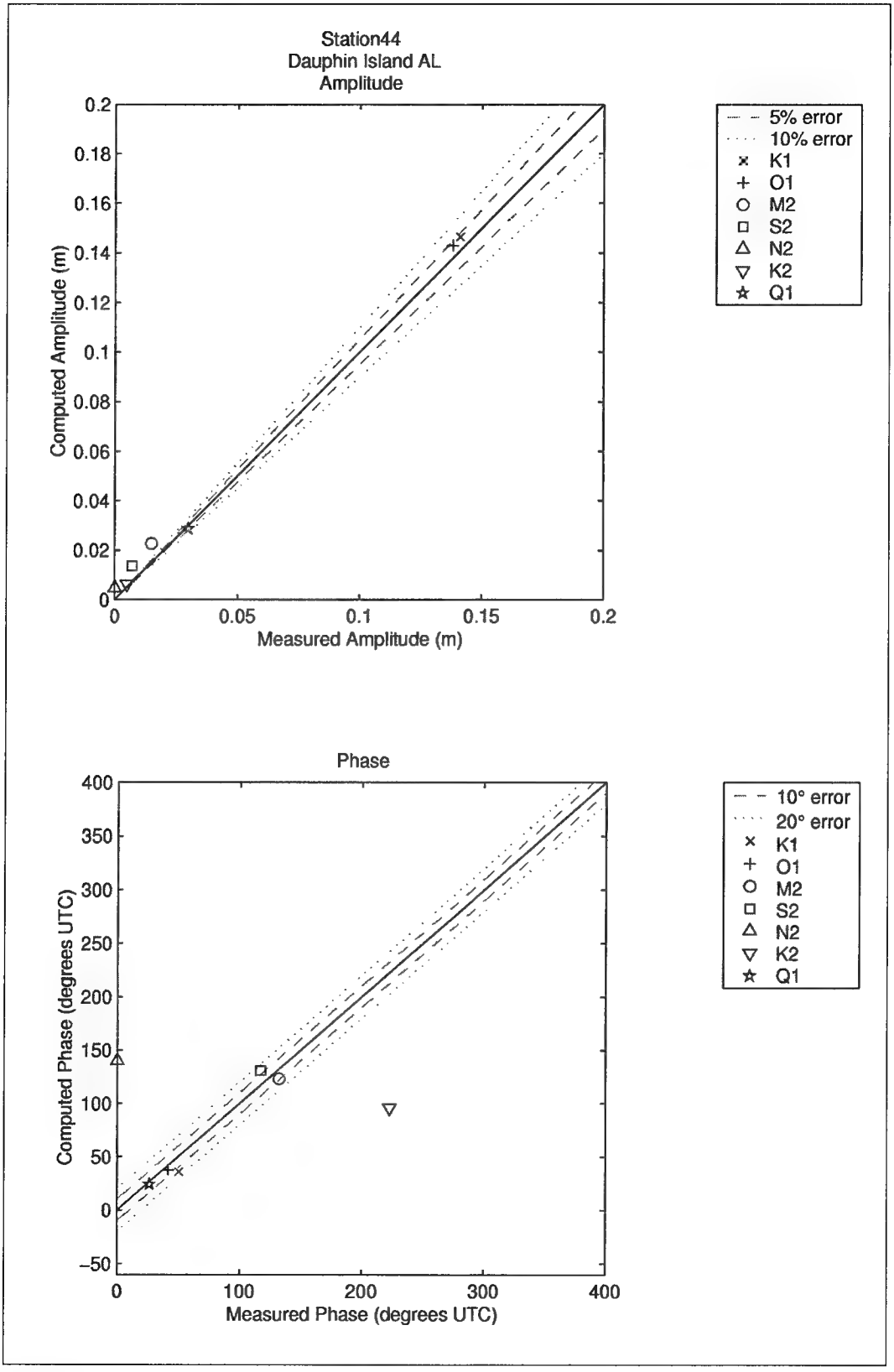

Figure 75. Computed vs. measured harmonic constituents at sta 44

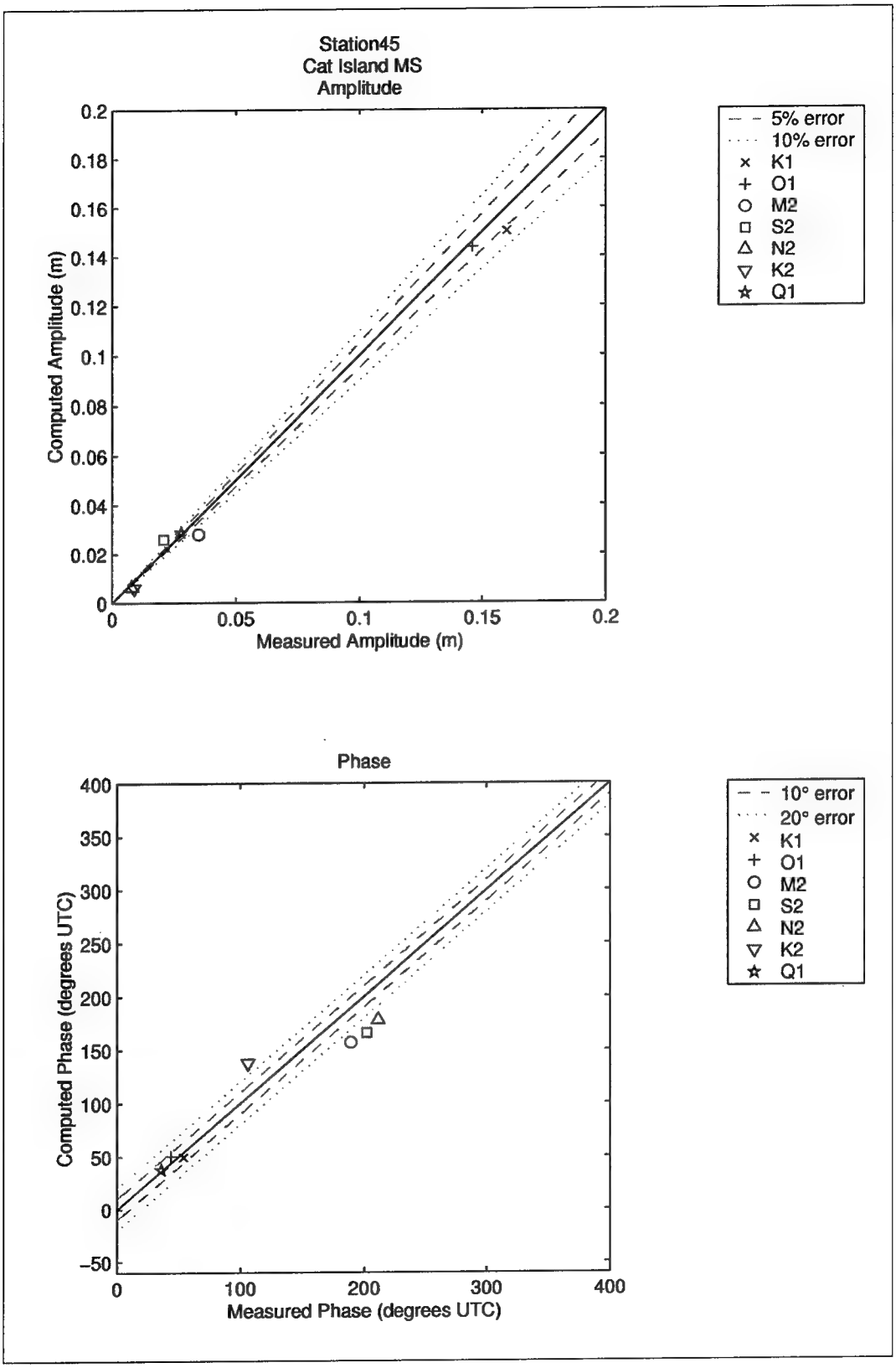

Figure 76. Computed vs. measured harmonic constituents at sta 45

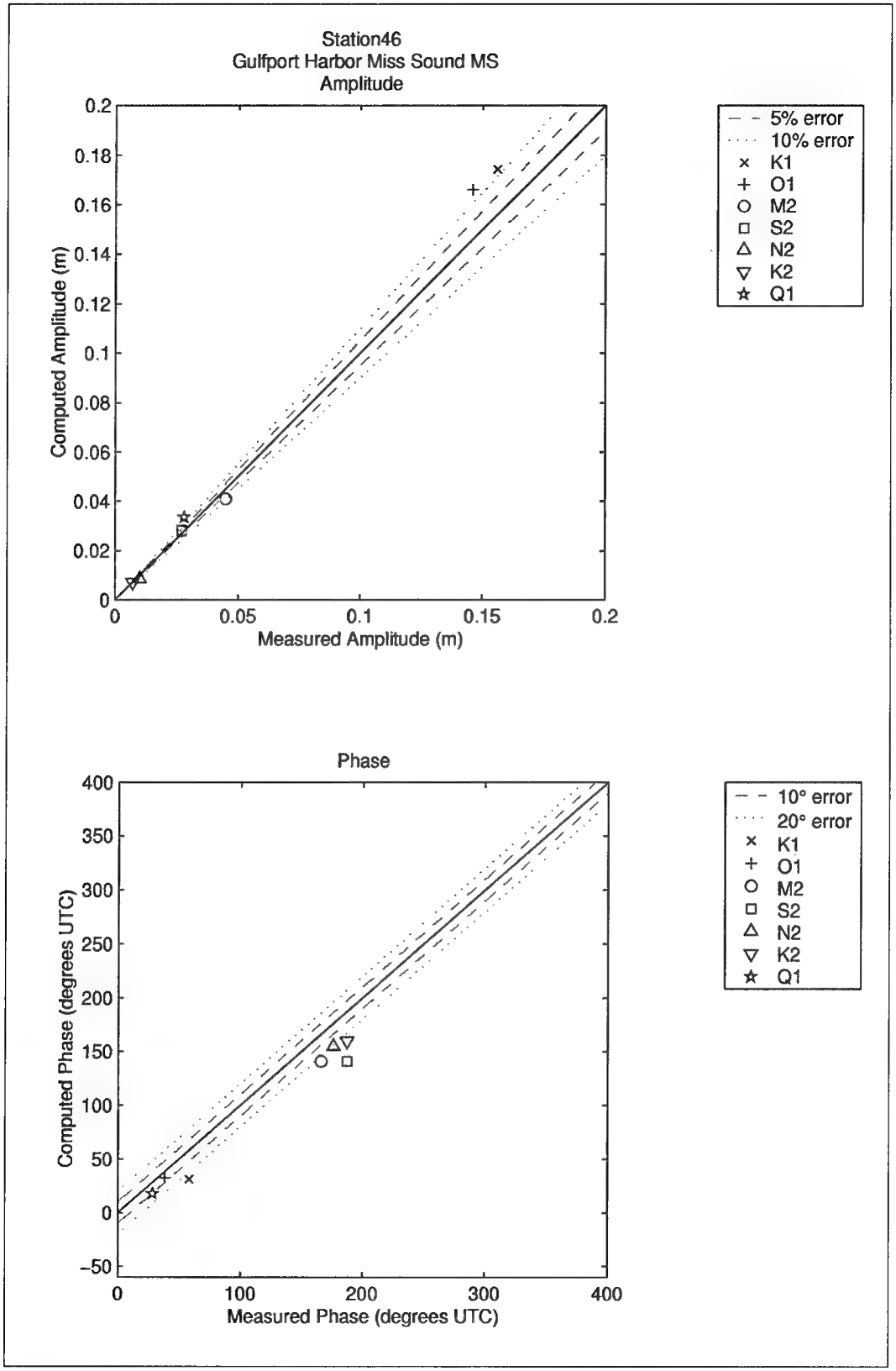

Figure 77. Computed vs. measured harmonic constituents at sta 46

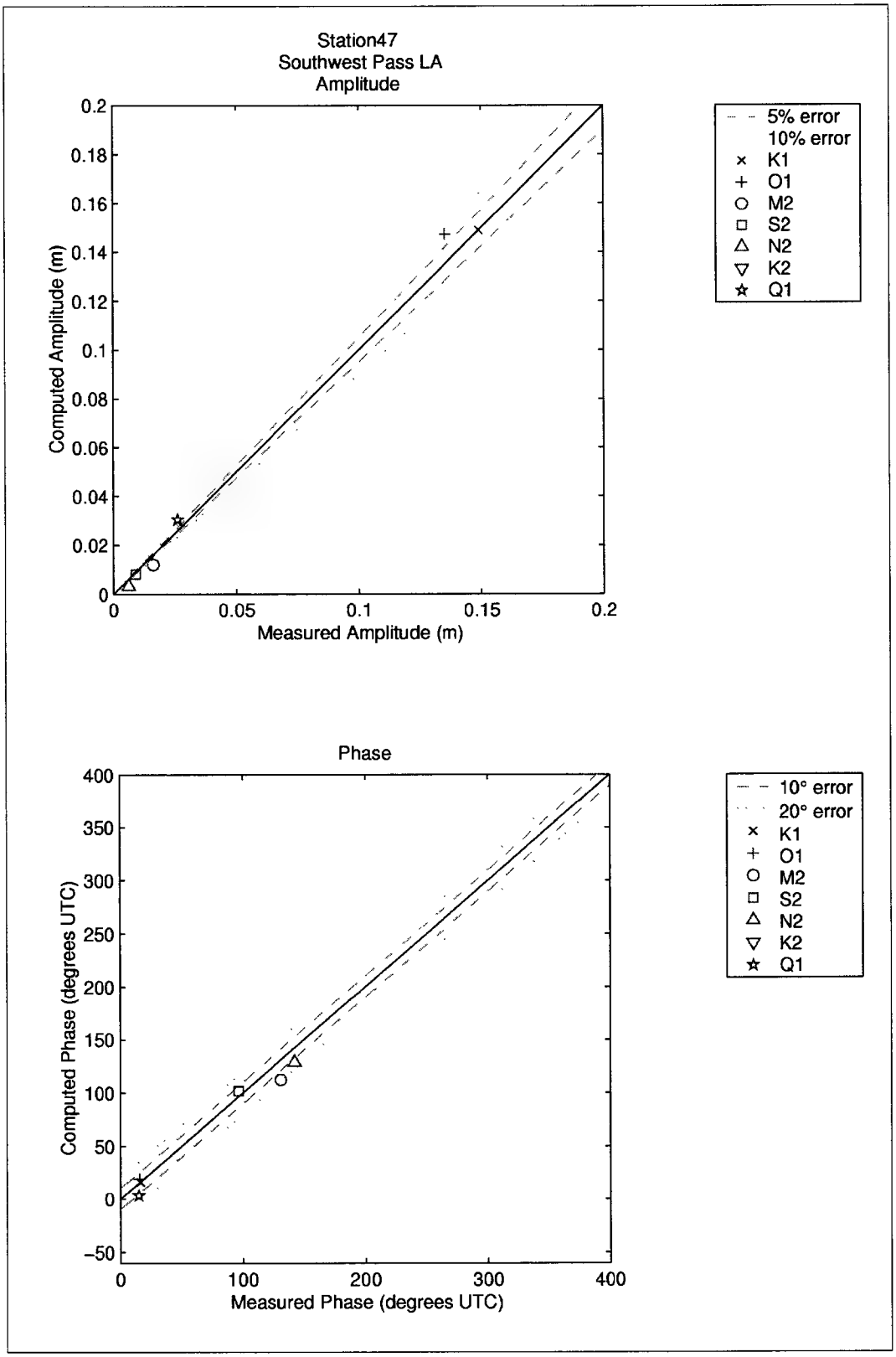

Figure 78. Computed vs. measured harmonic constituents at sta 47

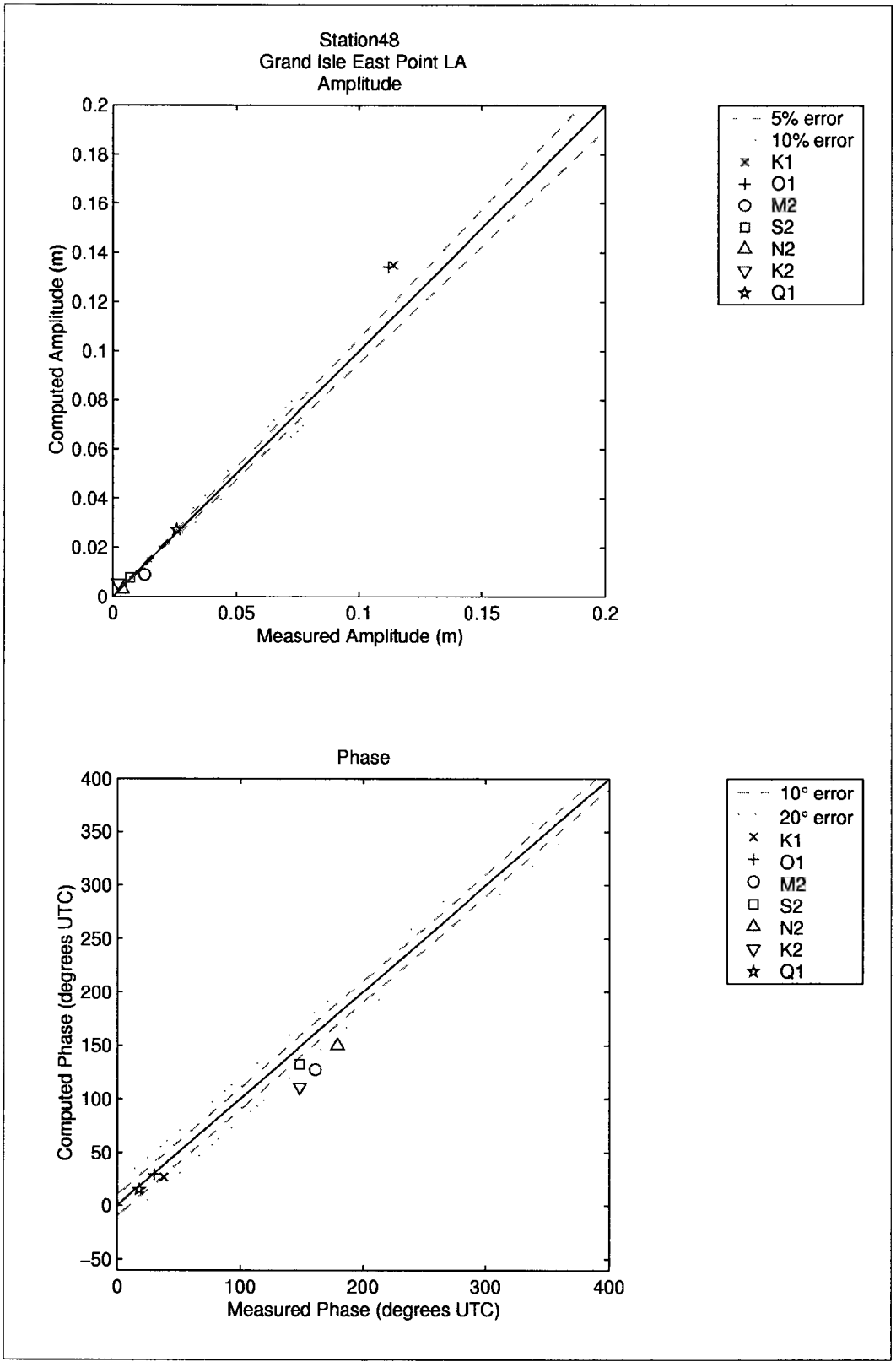

Figure 79. Computed vs. measured harmonic constituents at sta 48

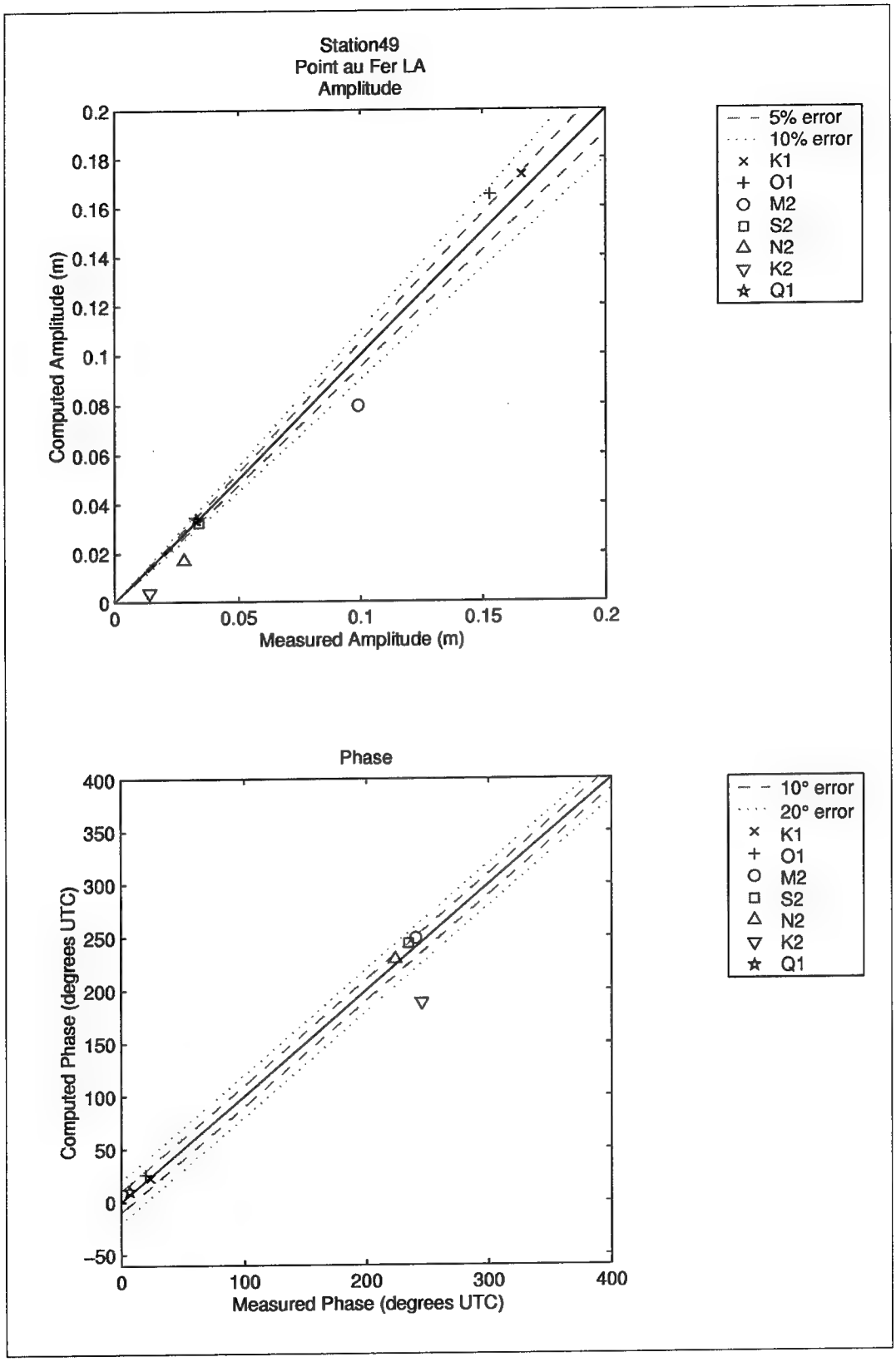

Figure 80. Computed vs. measured harmonic constituents at sta 49

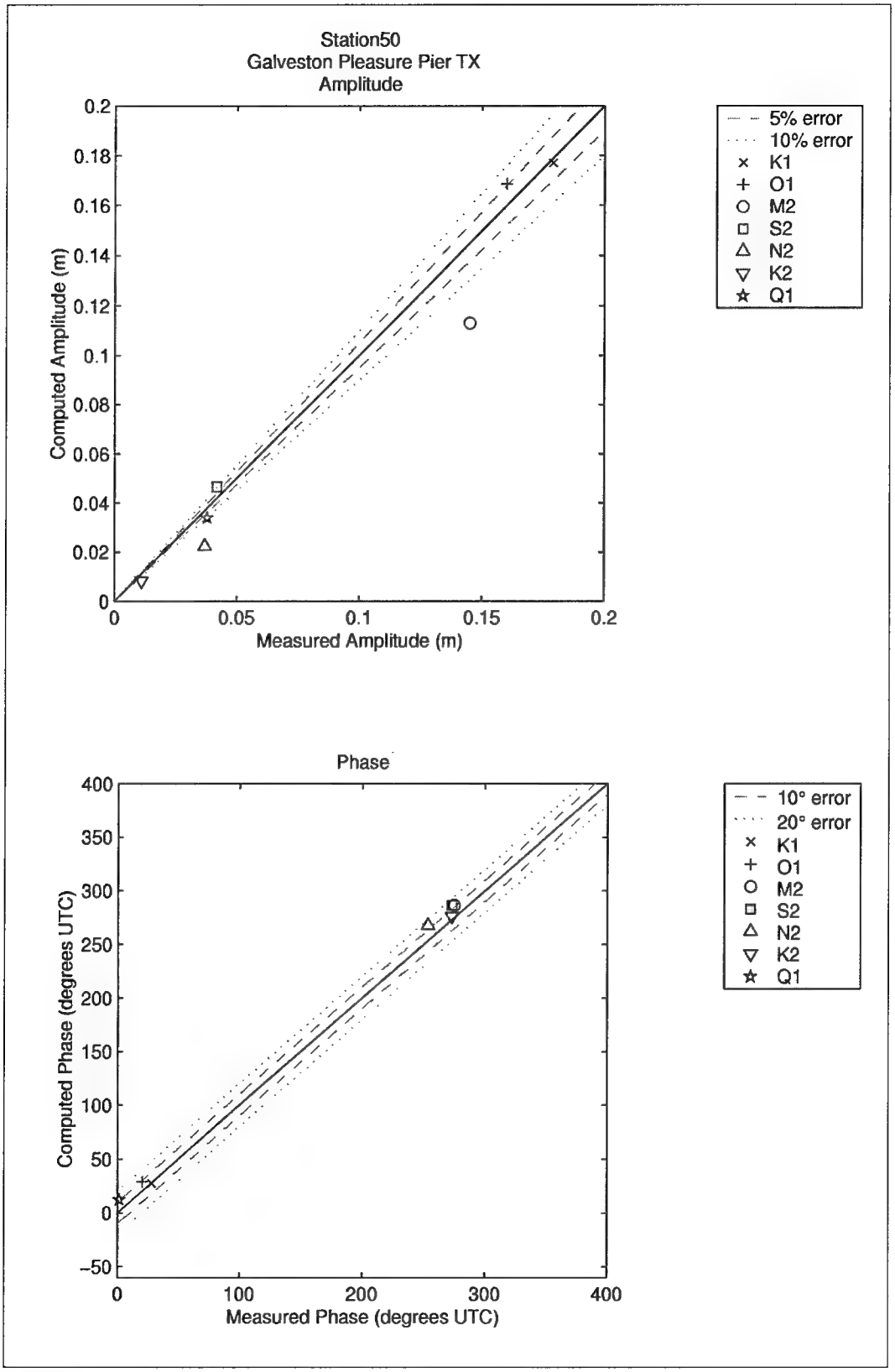

Figure 81. Computed vs. measured harmonic constituents at sta 50

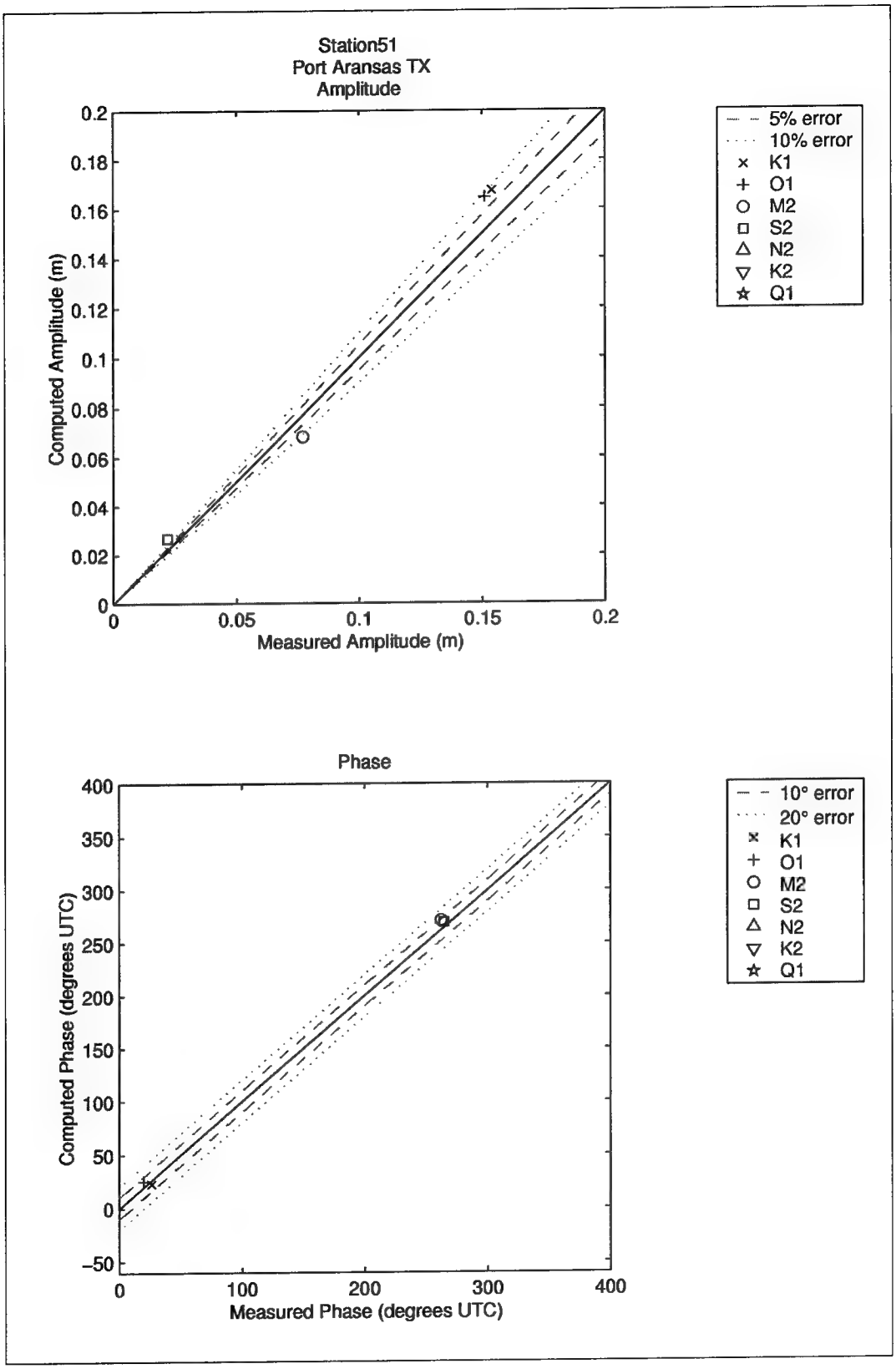

Figure 82. Computed vs. measured harmonic constituents at sta 51

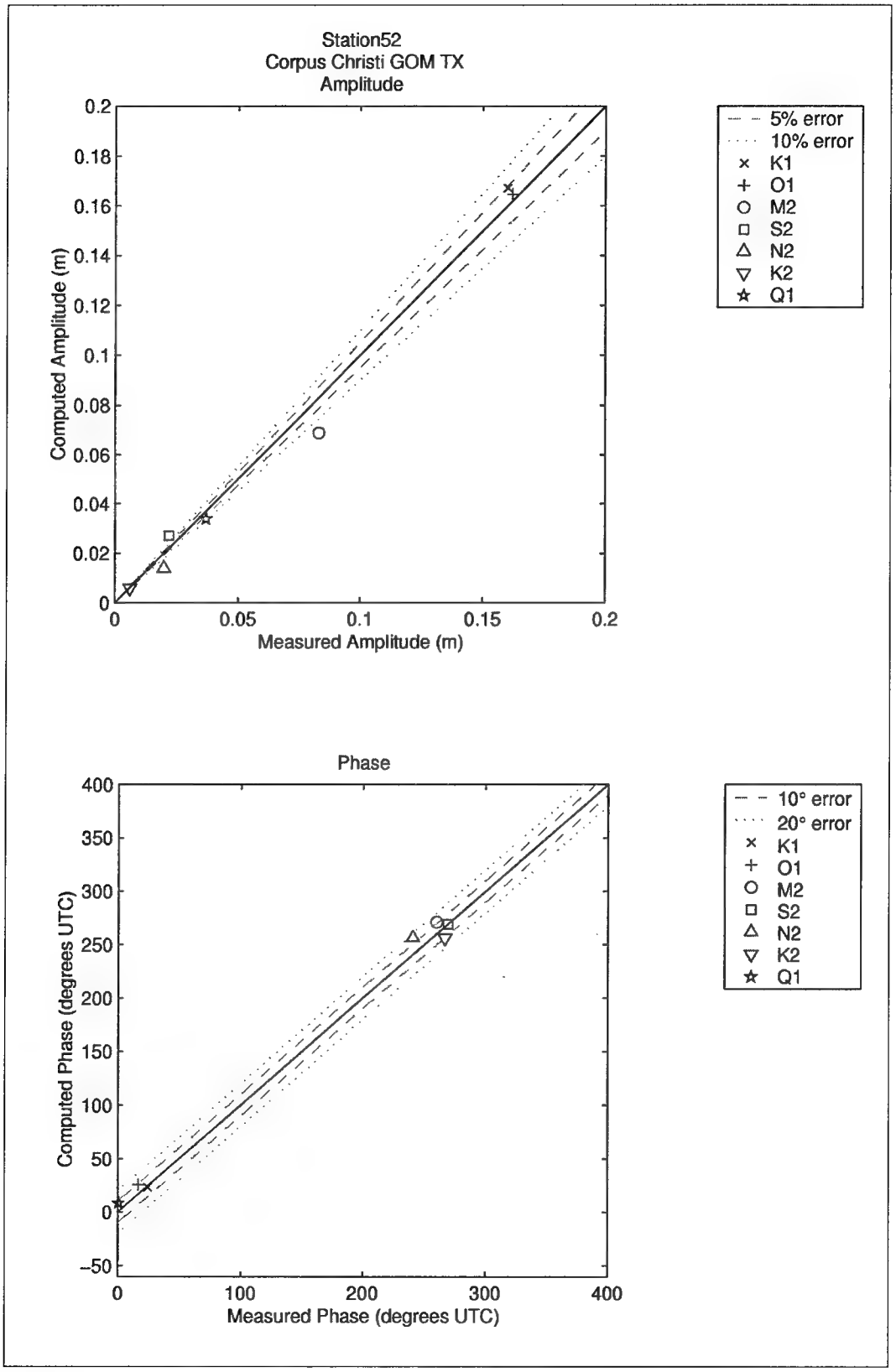

Figure 83. Computed vs. measured harmonic constituents at sta 52

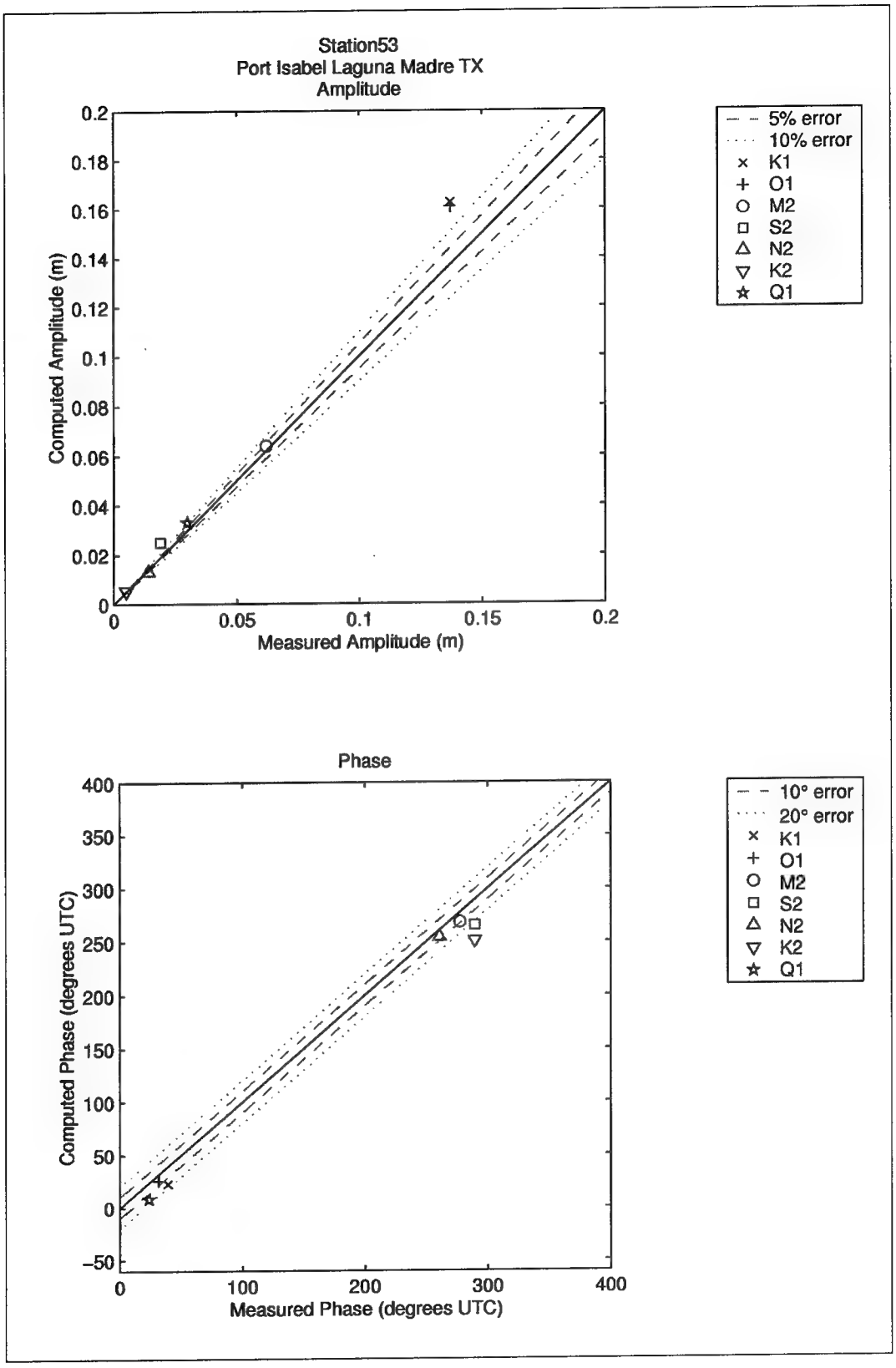

Figure 84. Computed vs. measured harmonic constituents at sta 53

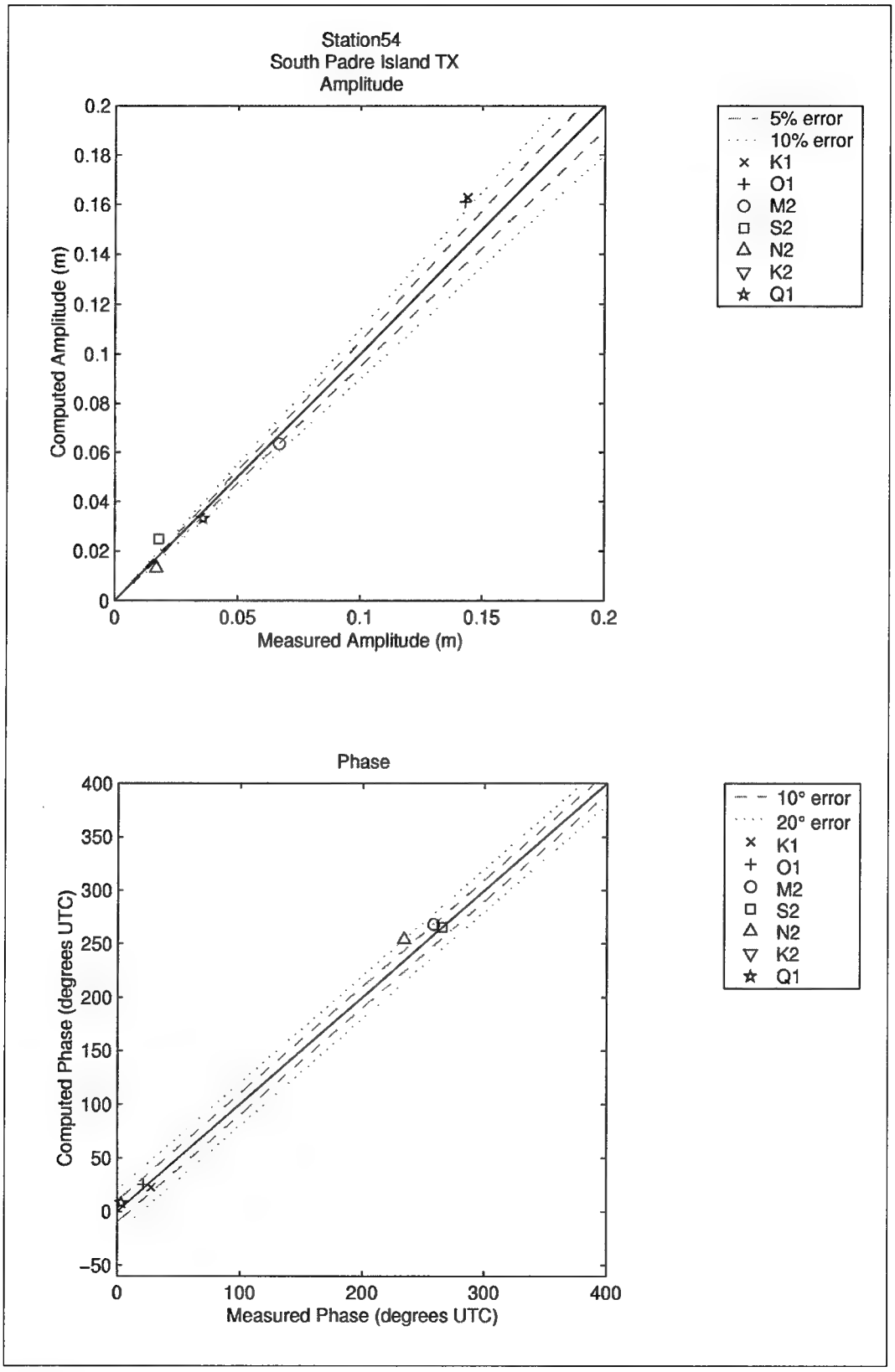

Figure 85. Computed vs. measured harmonic constituents at sta 54

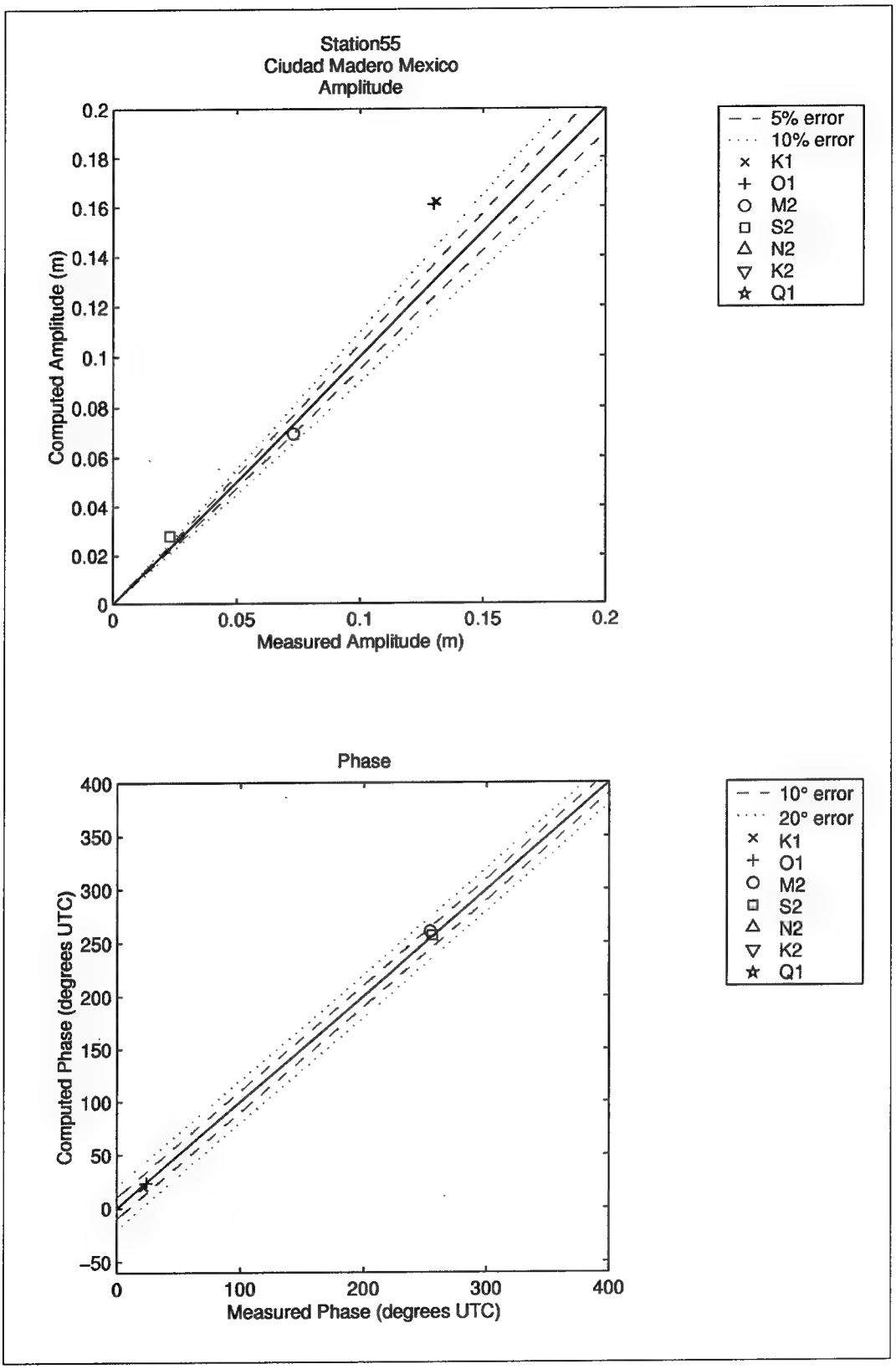

Figure 86. Computed vs. measured harmonic constituents at sta 55

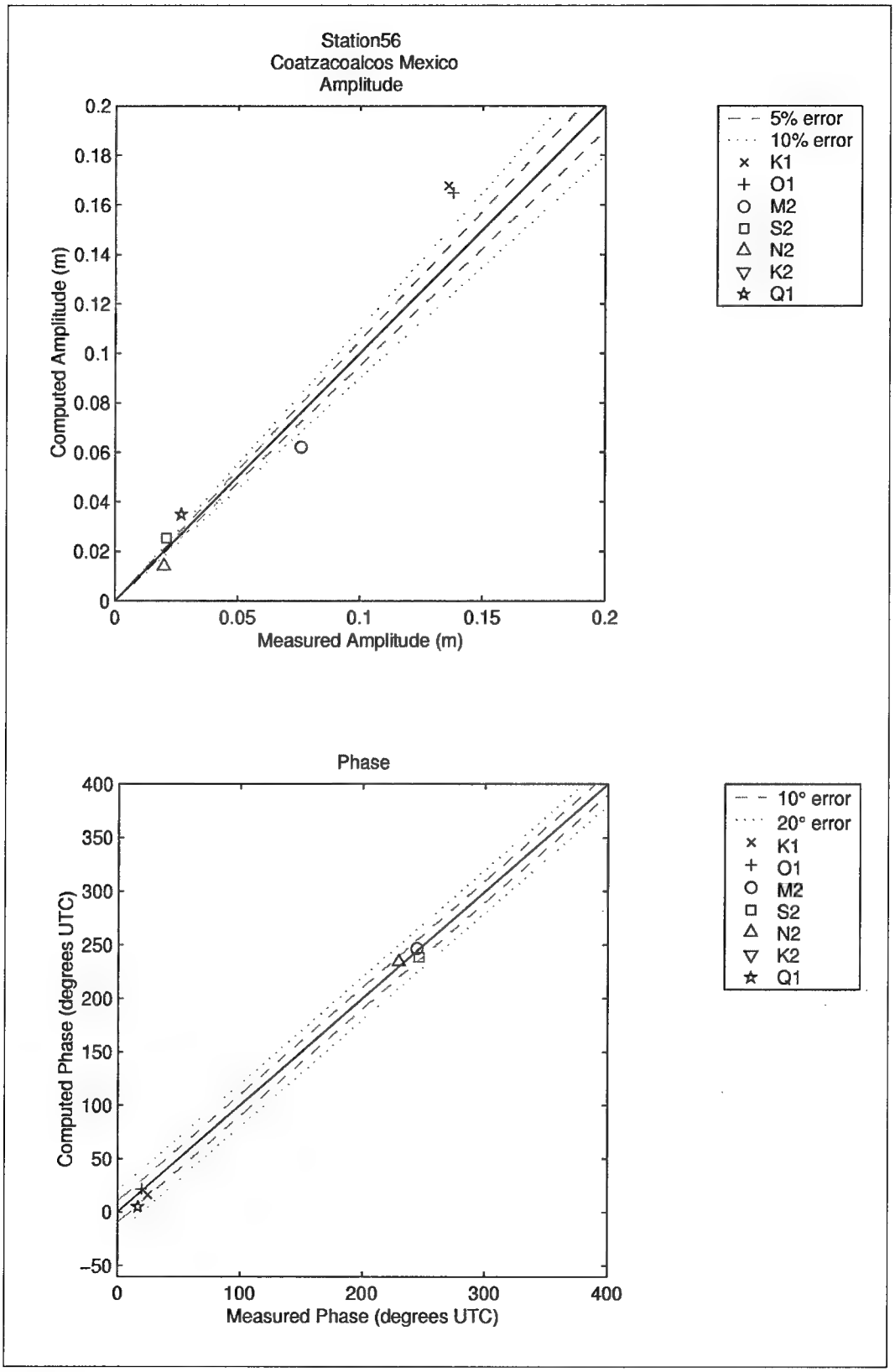

Figure 87. Computed vs. measured harmonic constituents at sta 56

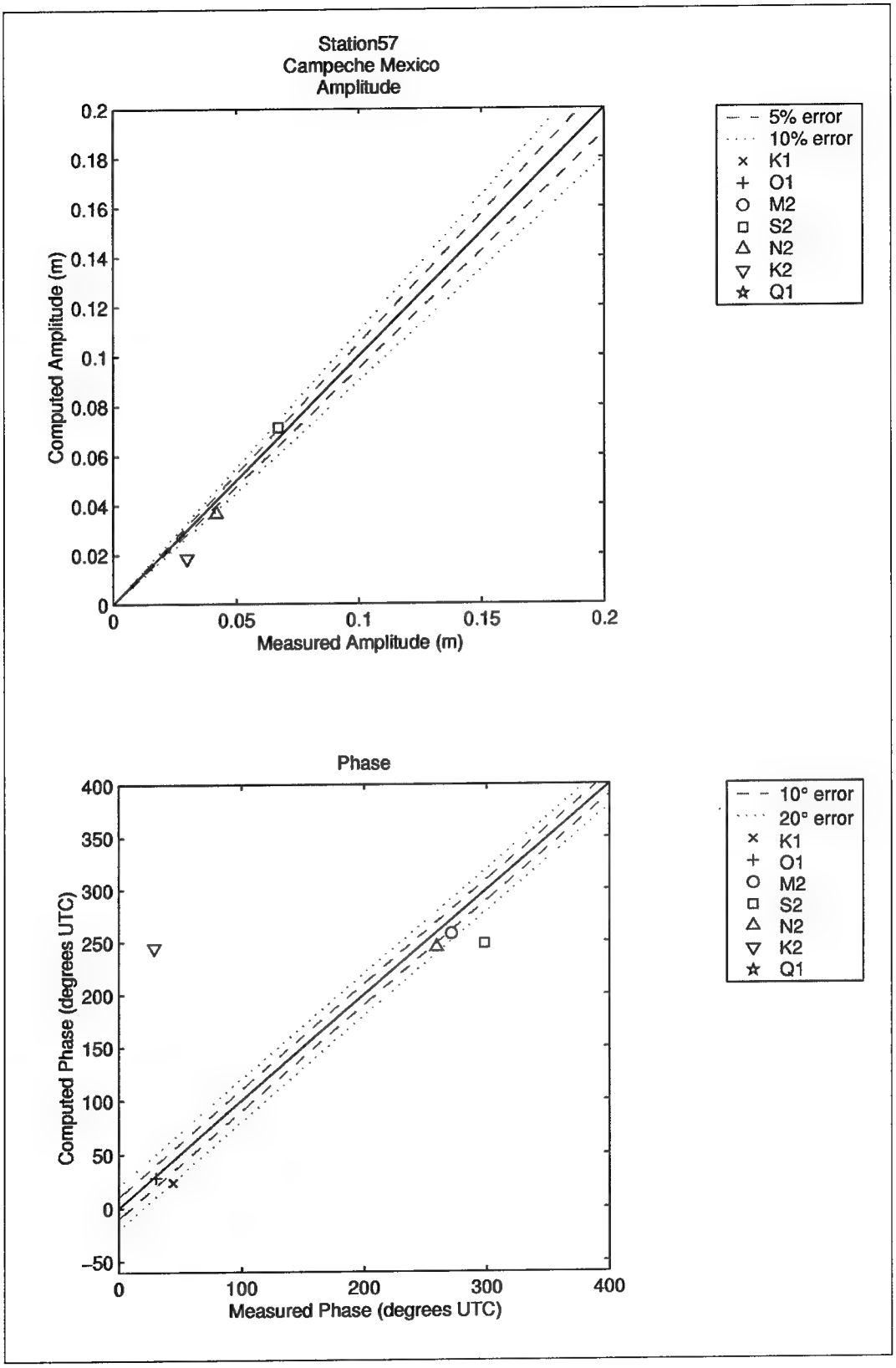

Figure 88. Computed vs. measured harmonic constituents at sta 57

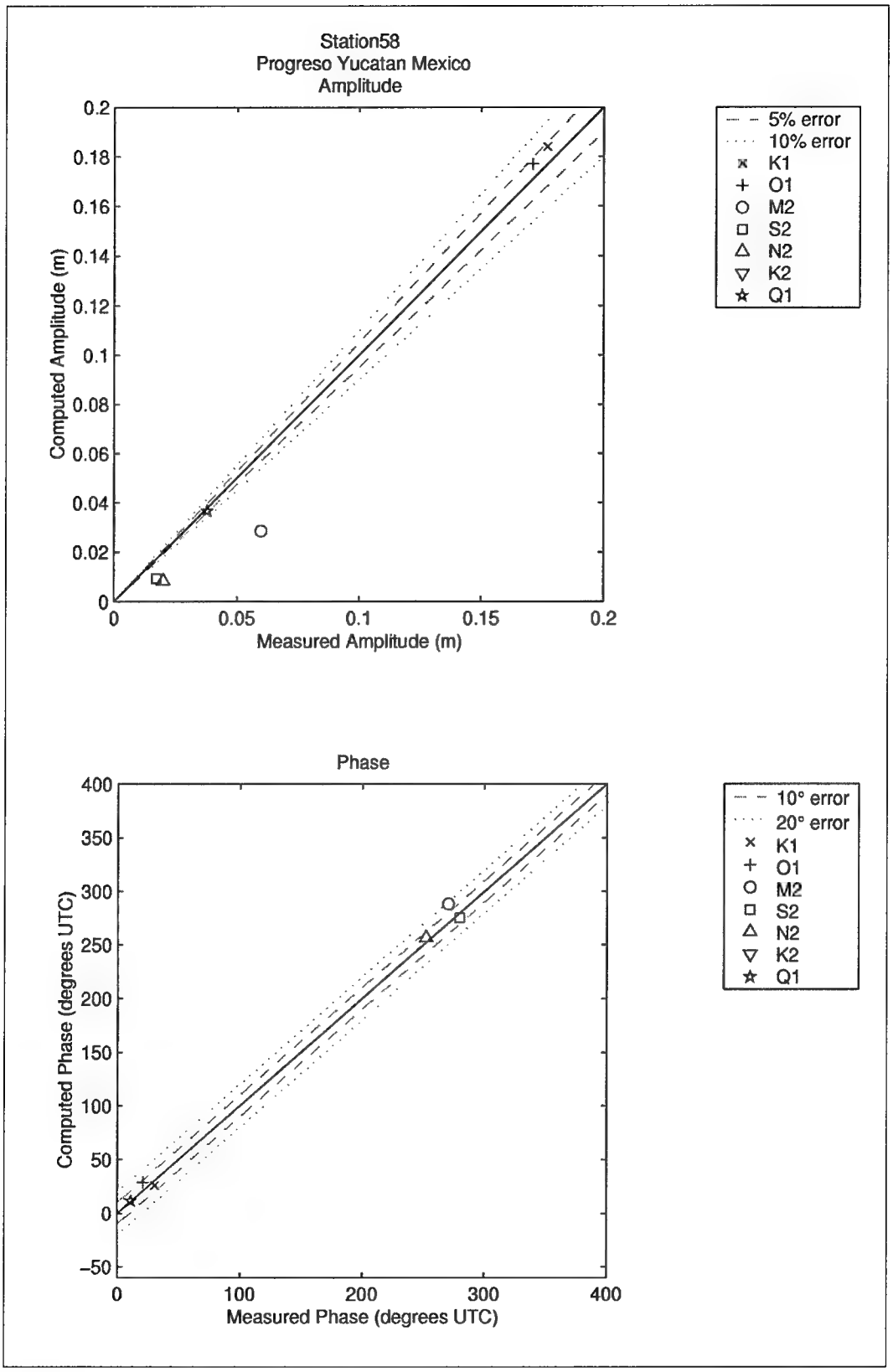

Figure 89. Computed vs. measured harmonic constituents at sta 58

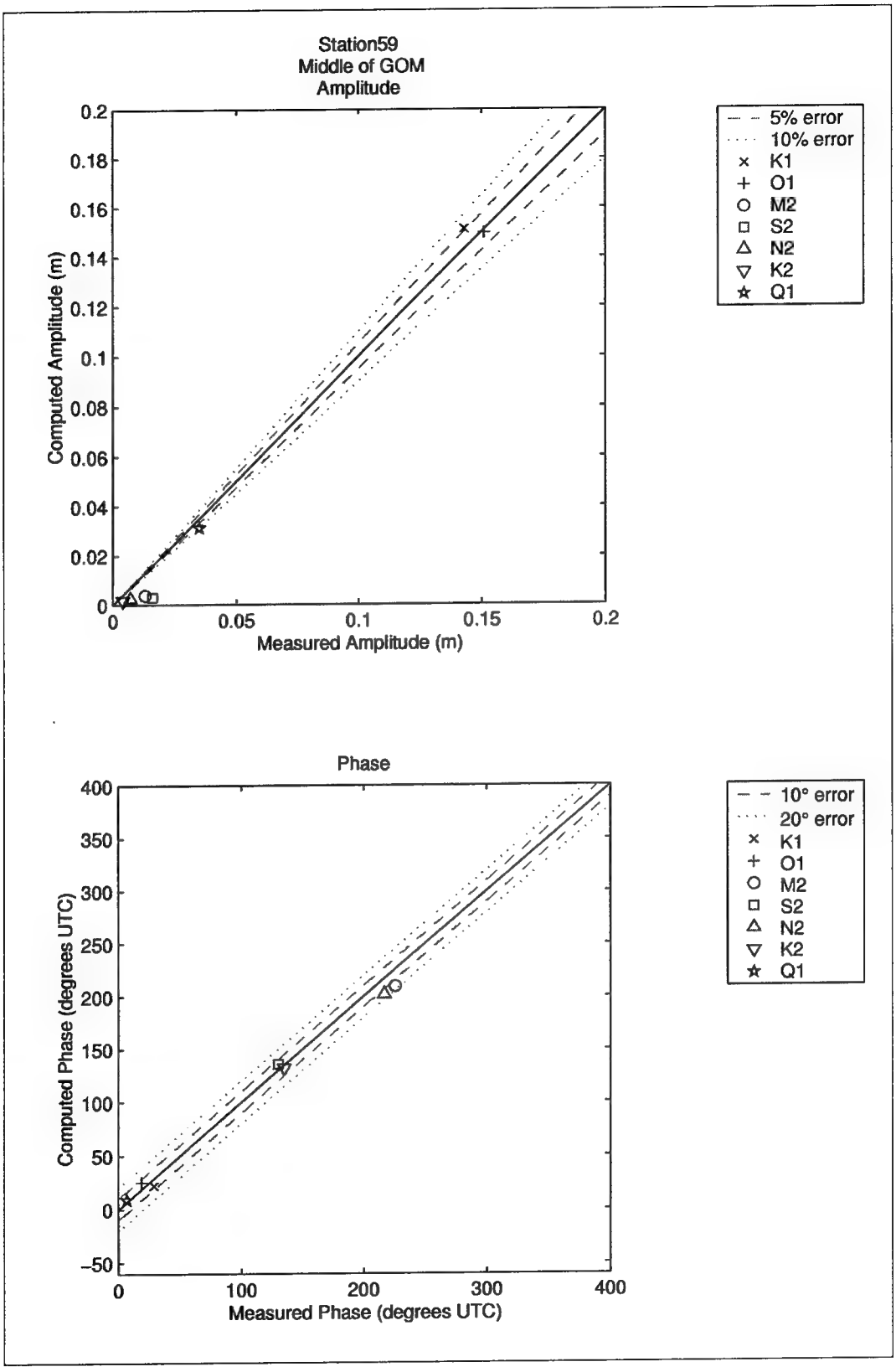

Figure 90. Computed vs. measured harmonic constituents at sta 59

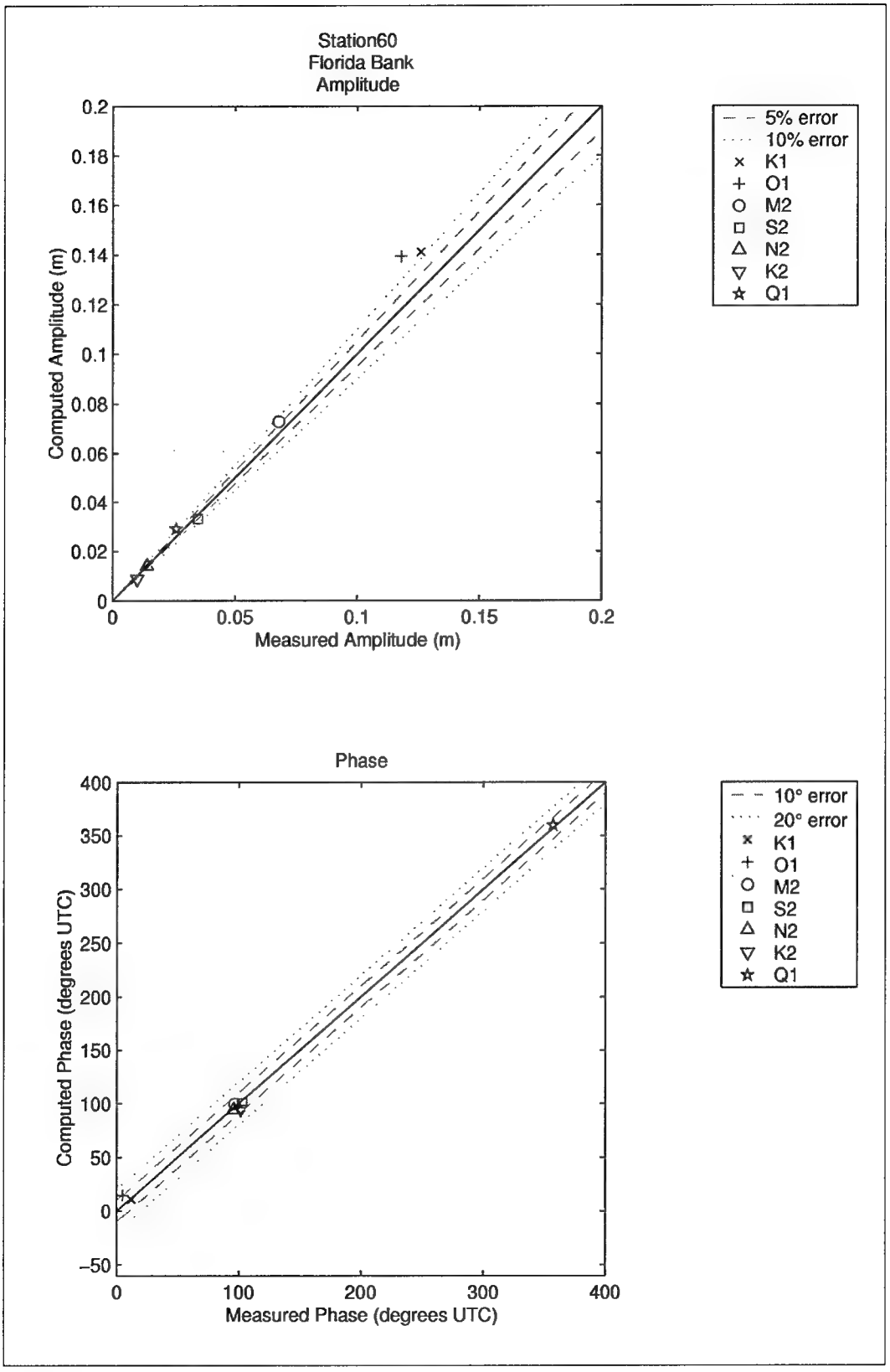

Figure 91. Computed vs. measured harmonic constituents at sta 60

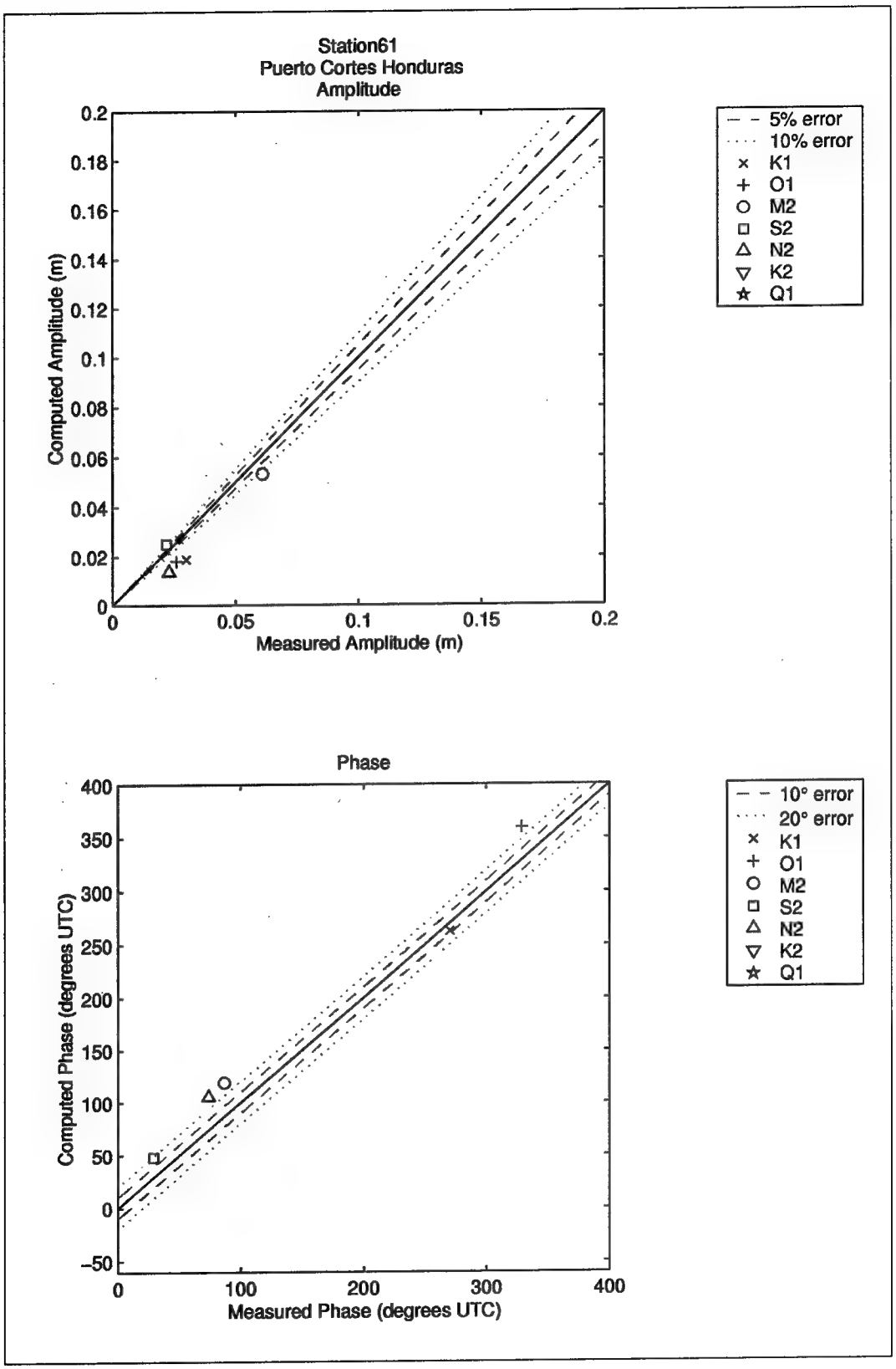

Figure 92. Computed vs. measured harmonic constituents at sta 61

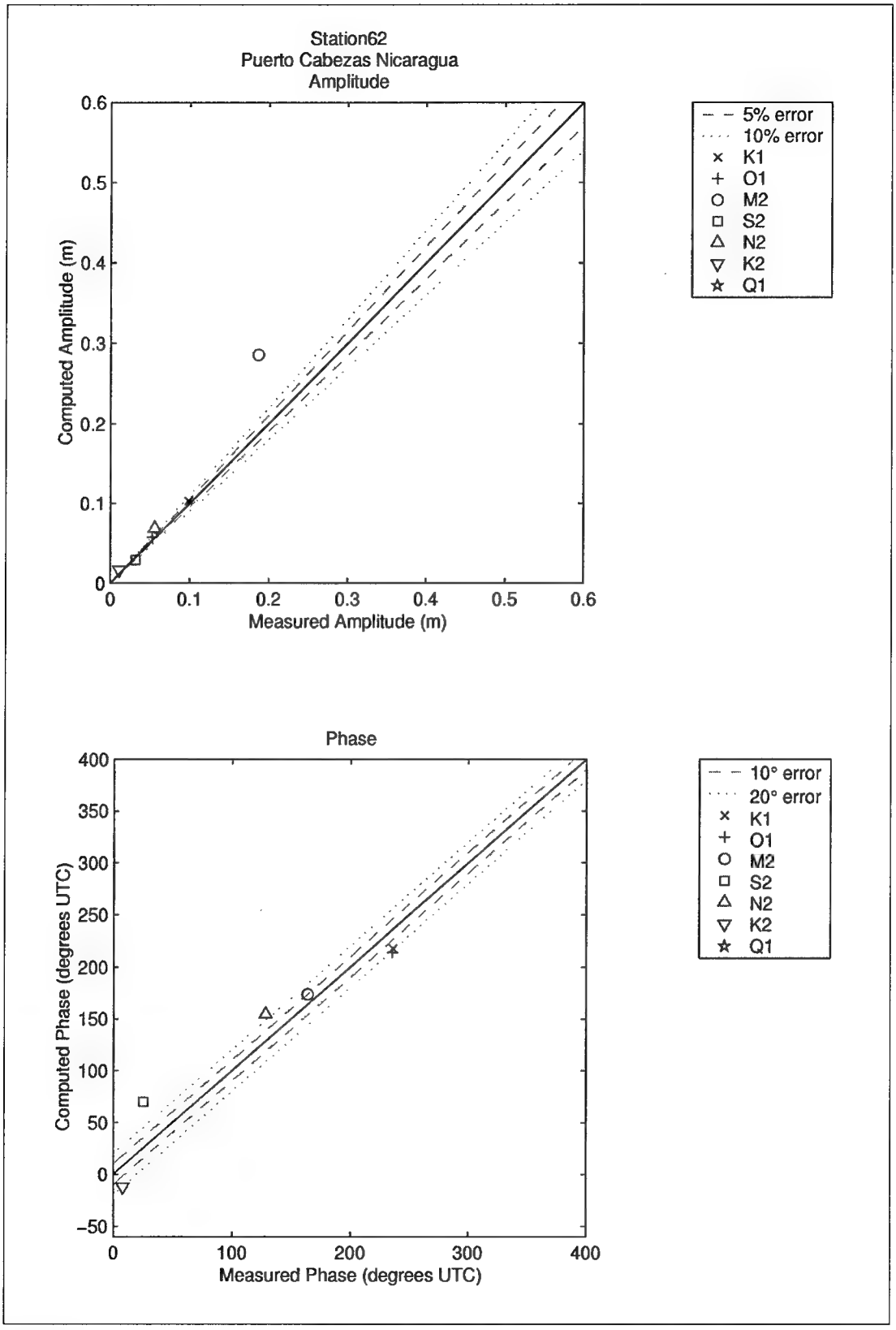

Figure 93. Computed vs. measured harmonic constituents at sta 62

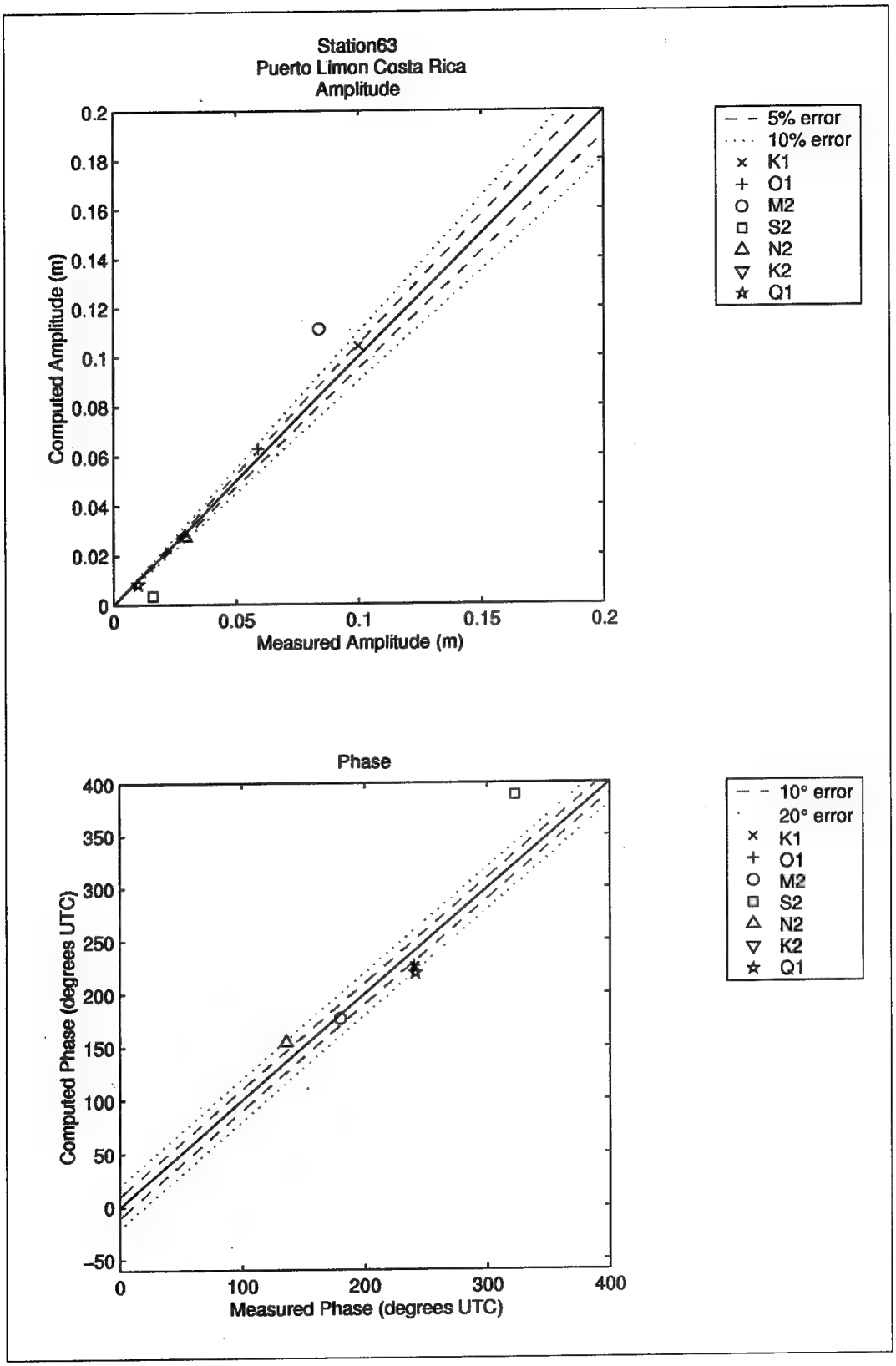

Figure 94. Computed vs. measured harmonic constituents at sta 63

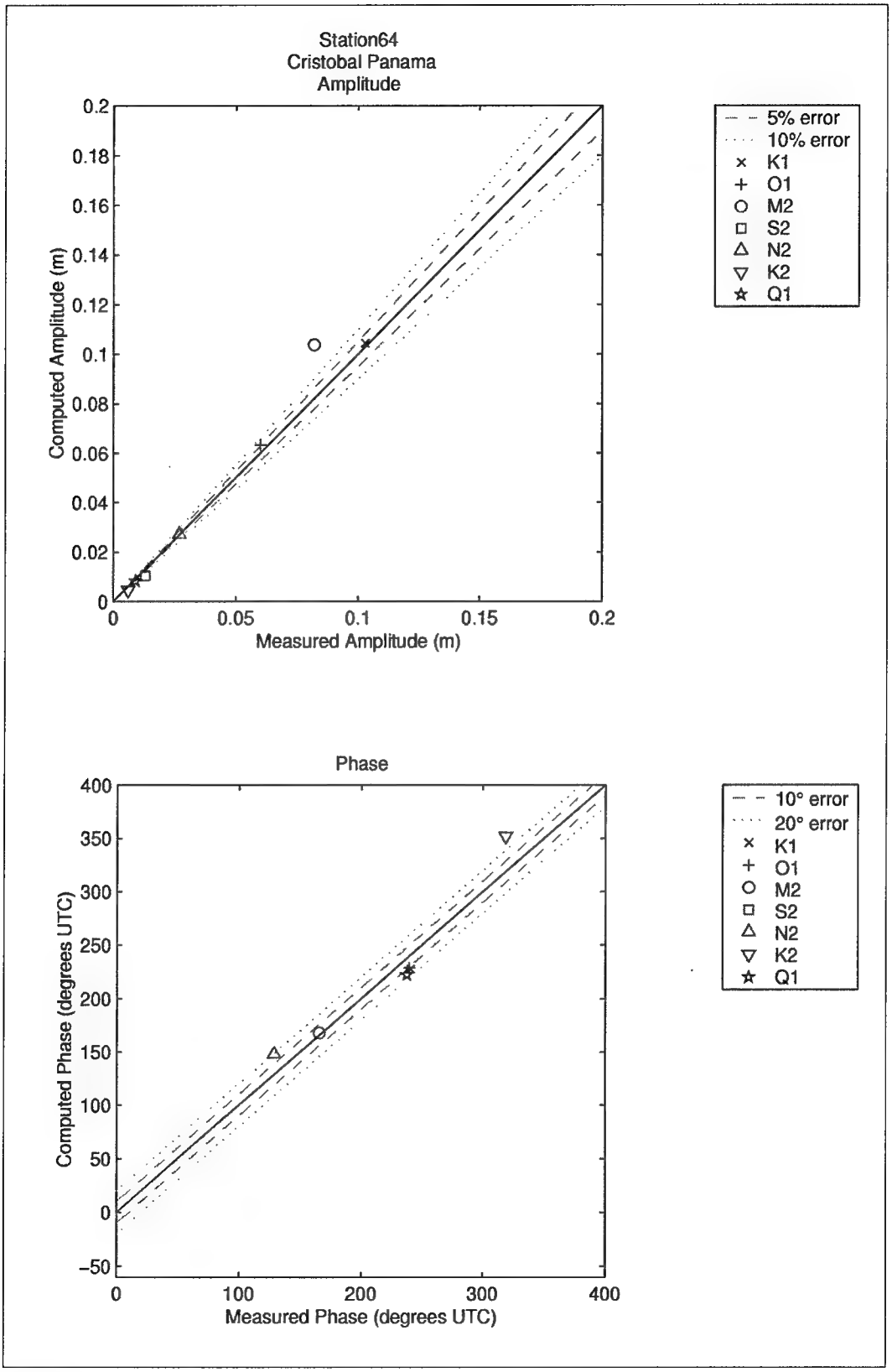

Figure 95. Computed vs. measured harmonic constituents at sta 64

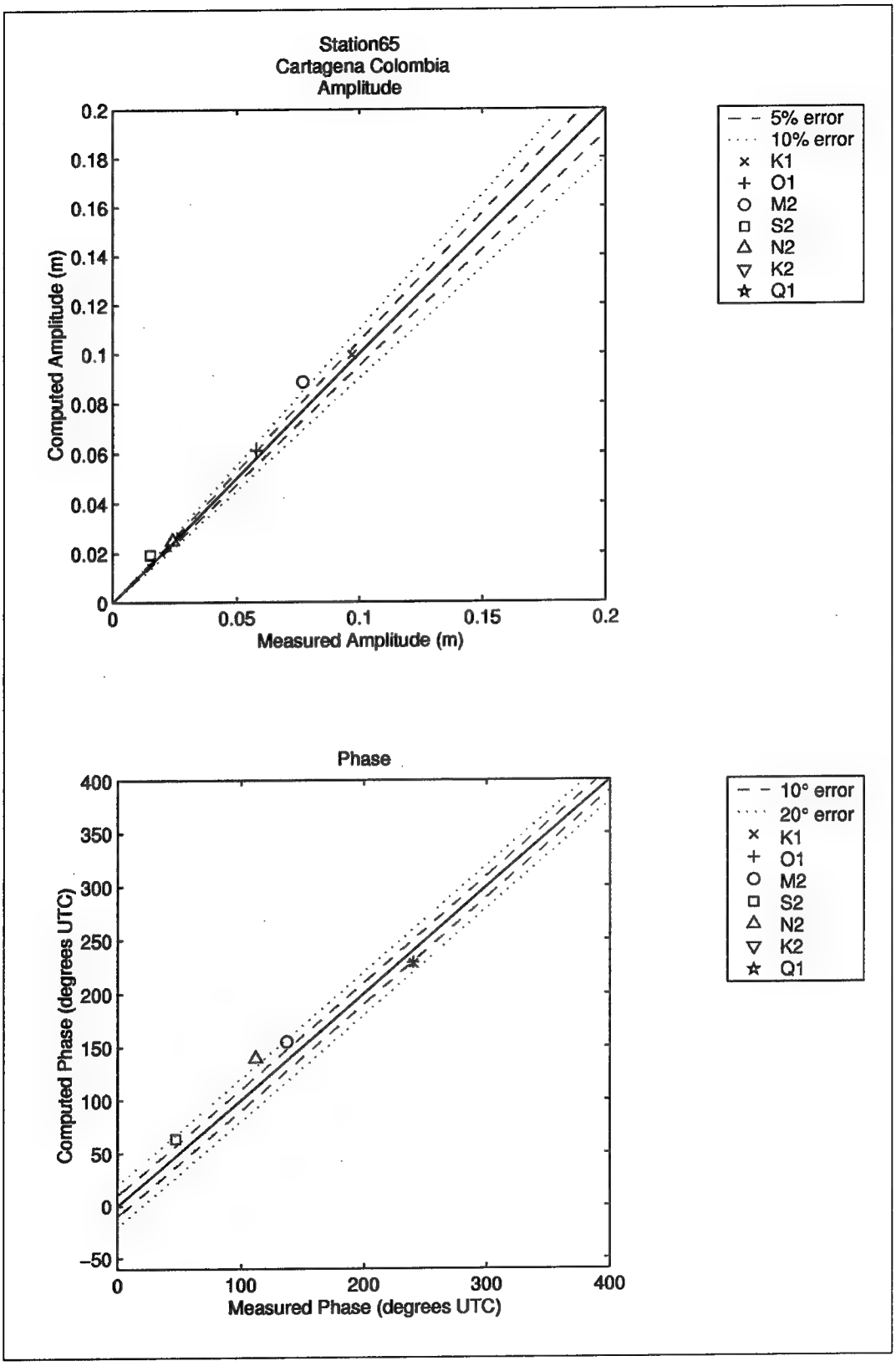

Figure 96. Computed vs. measured harmonic constituents at sta 65

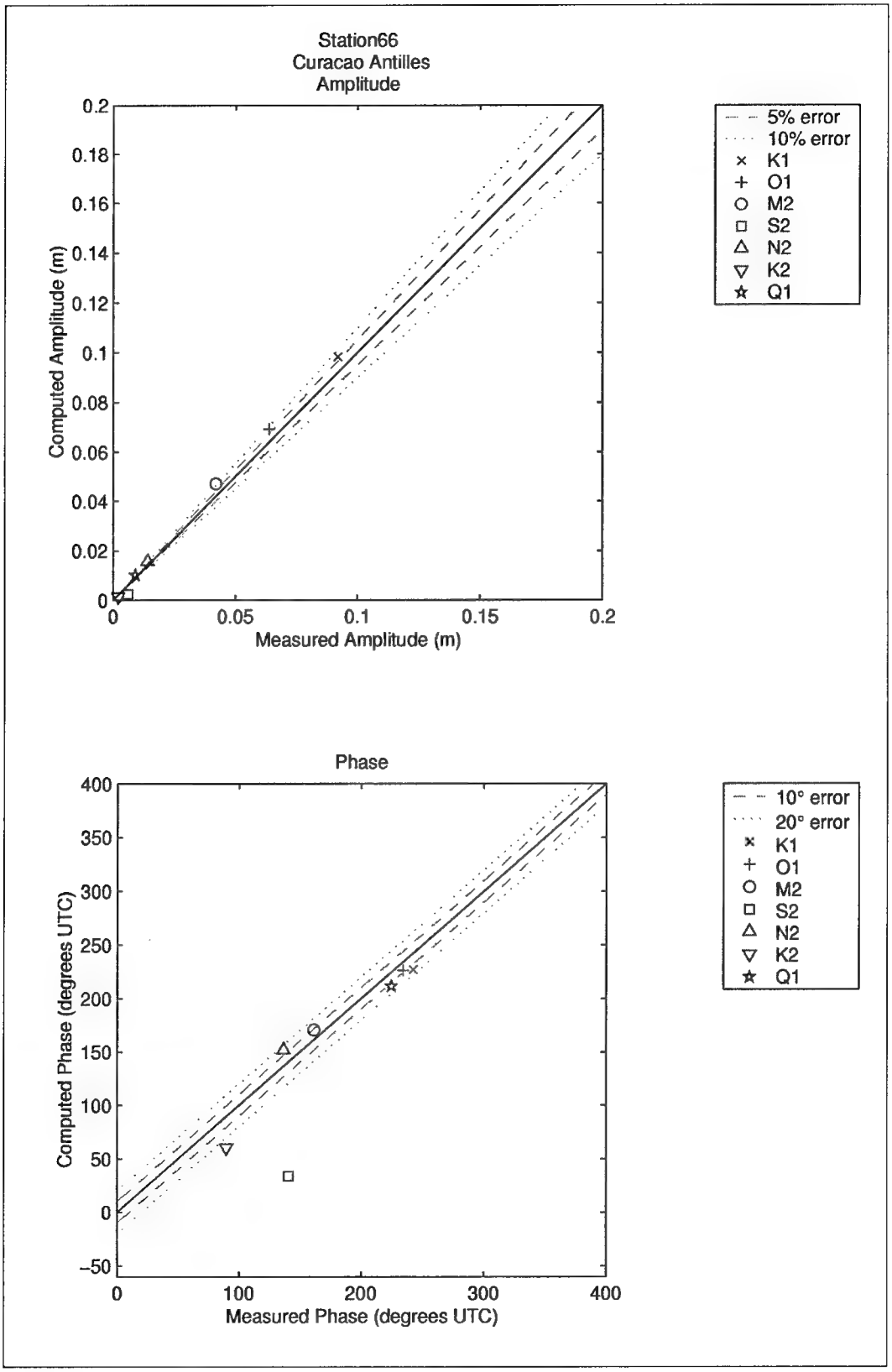

Figure 97. Computed vs. measured harmonic constituents at sta 66

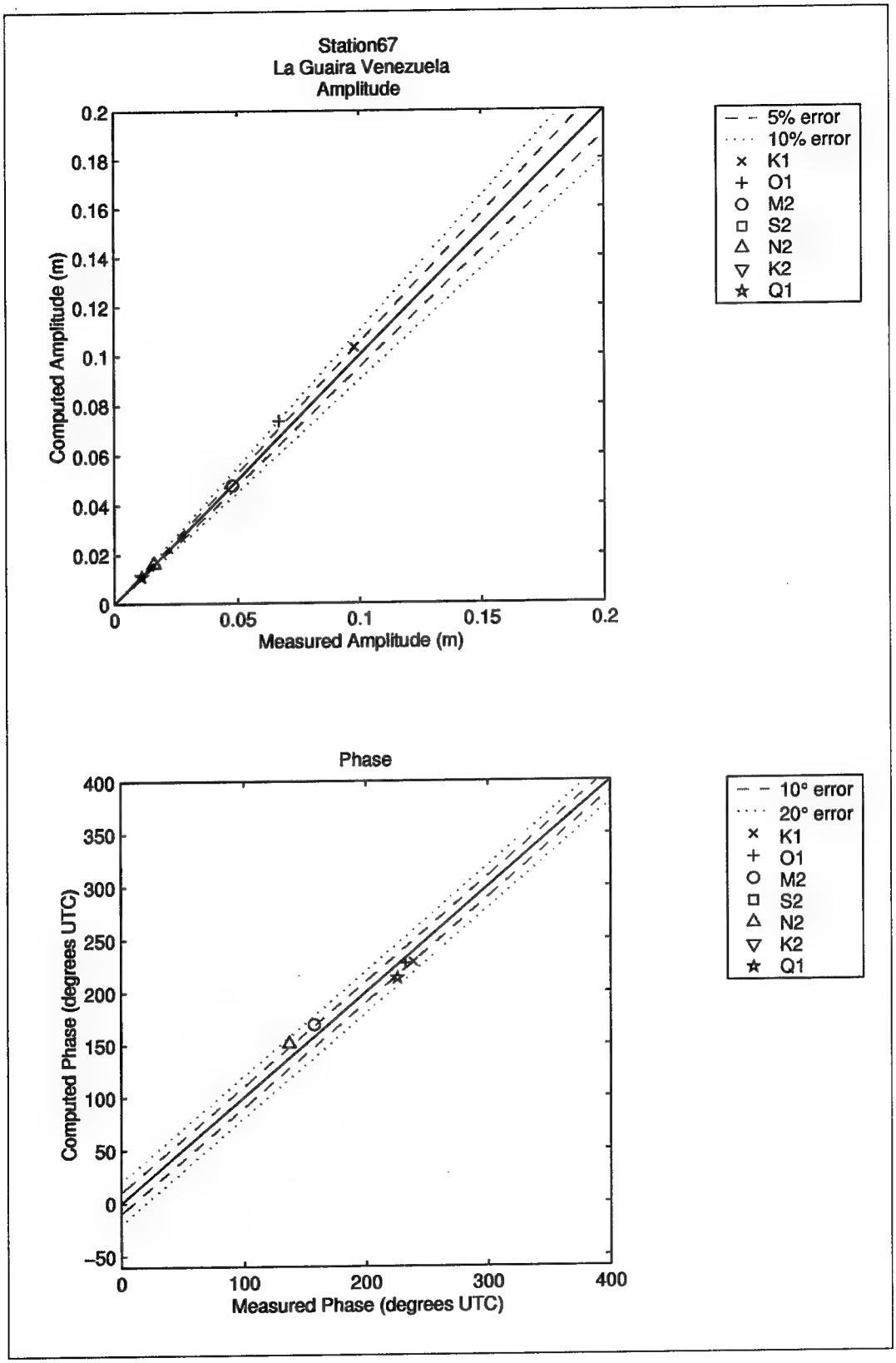

Figure 98. Computed vs. measured harmonic constituents at sta 67

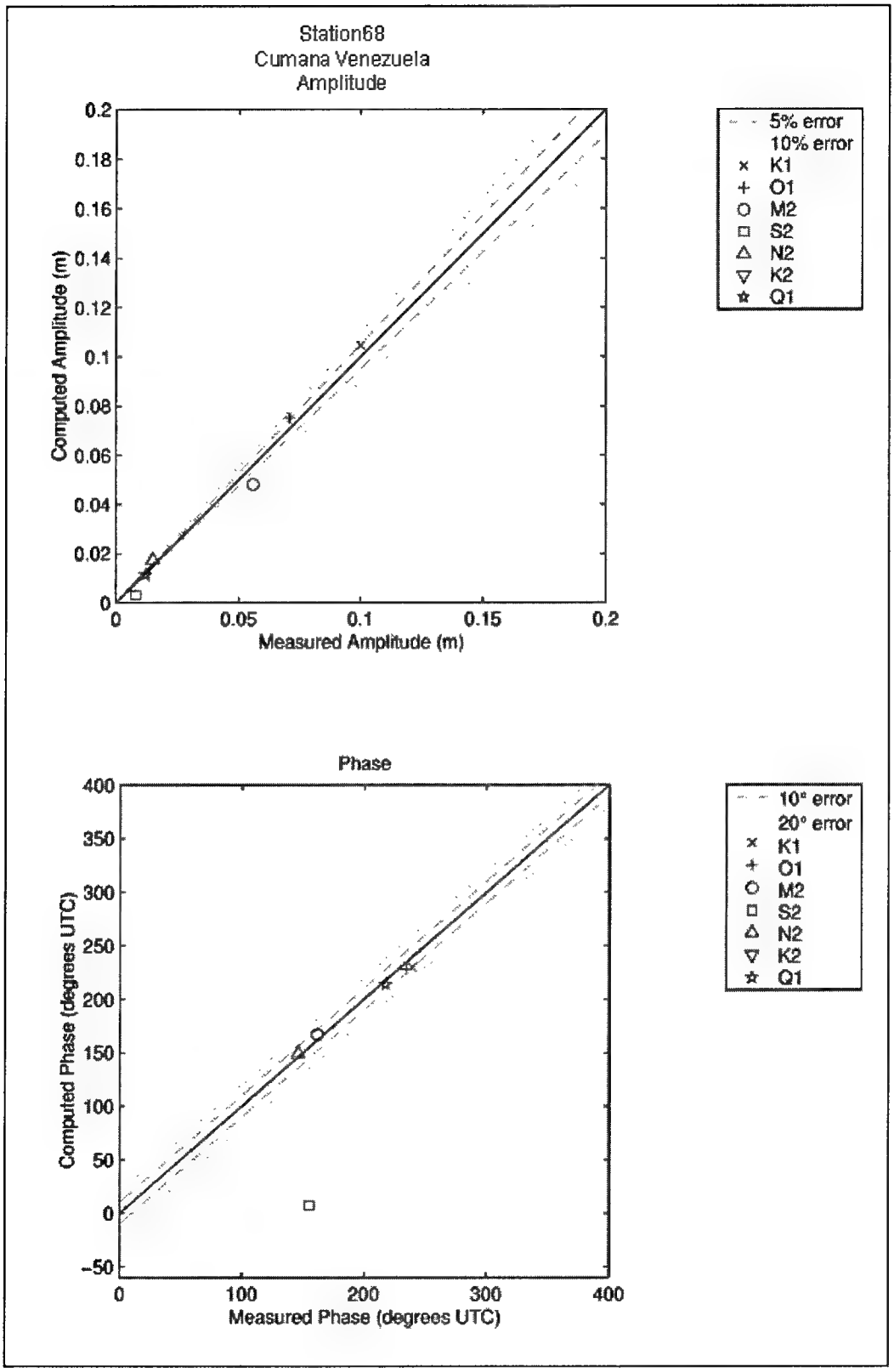

Figure 99. Computed vs. measured harmonic constituents at sta 68

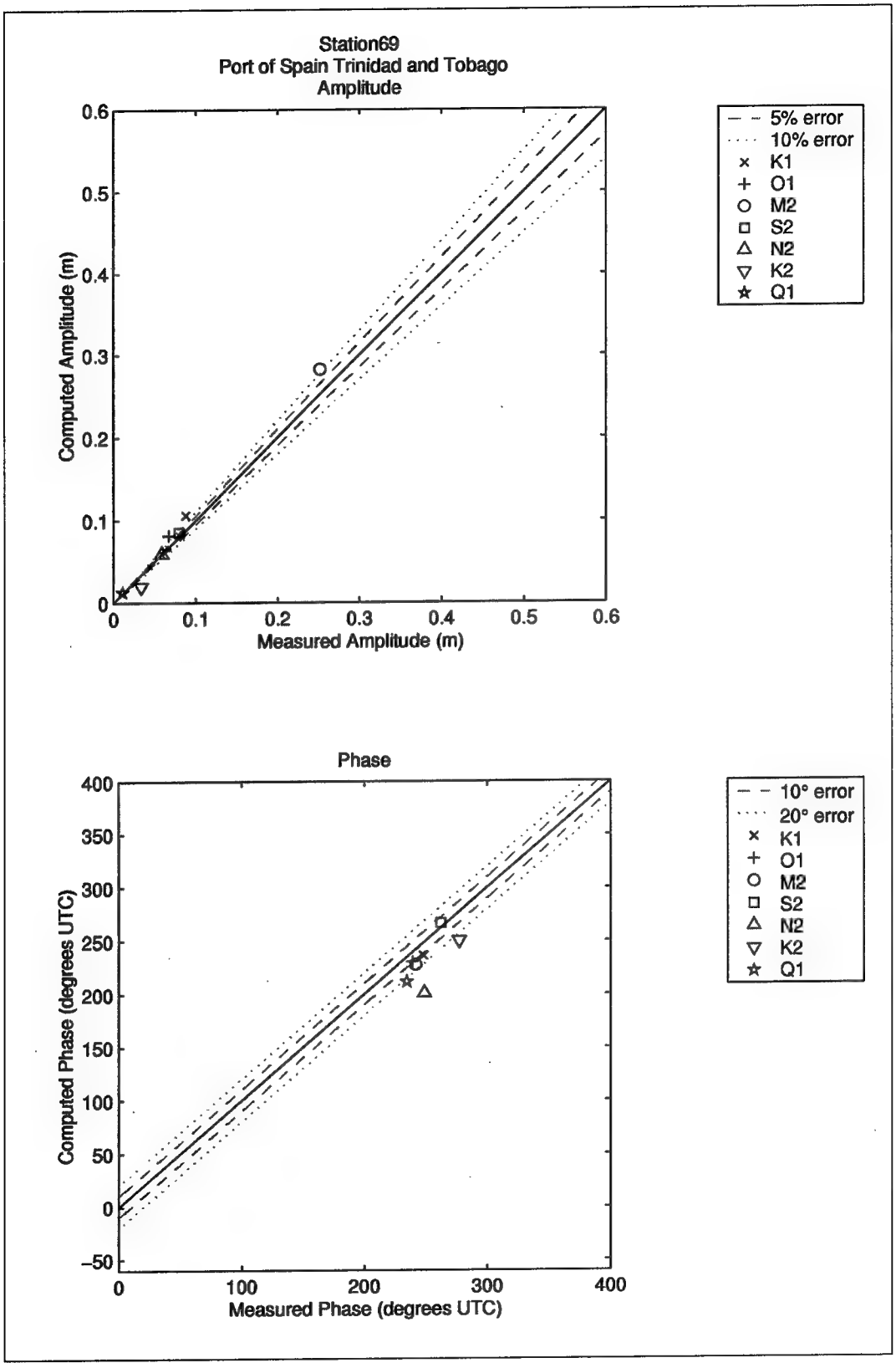

Figure 100. Computed vs. measured harmonic constituents at sta 69

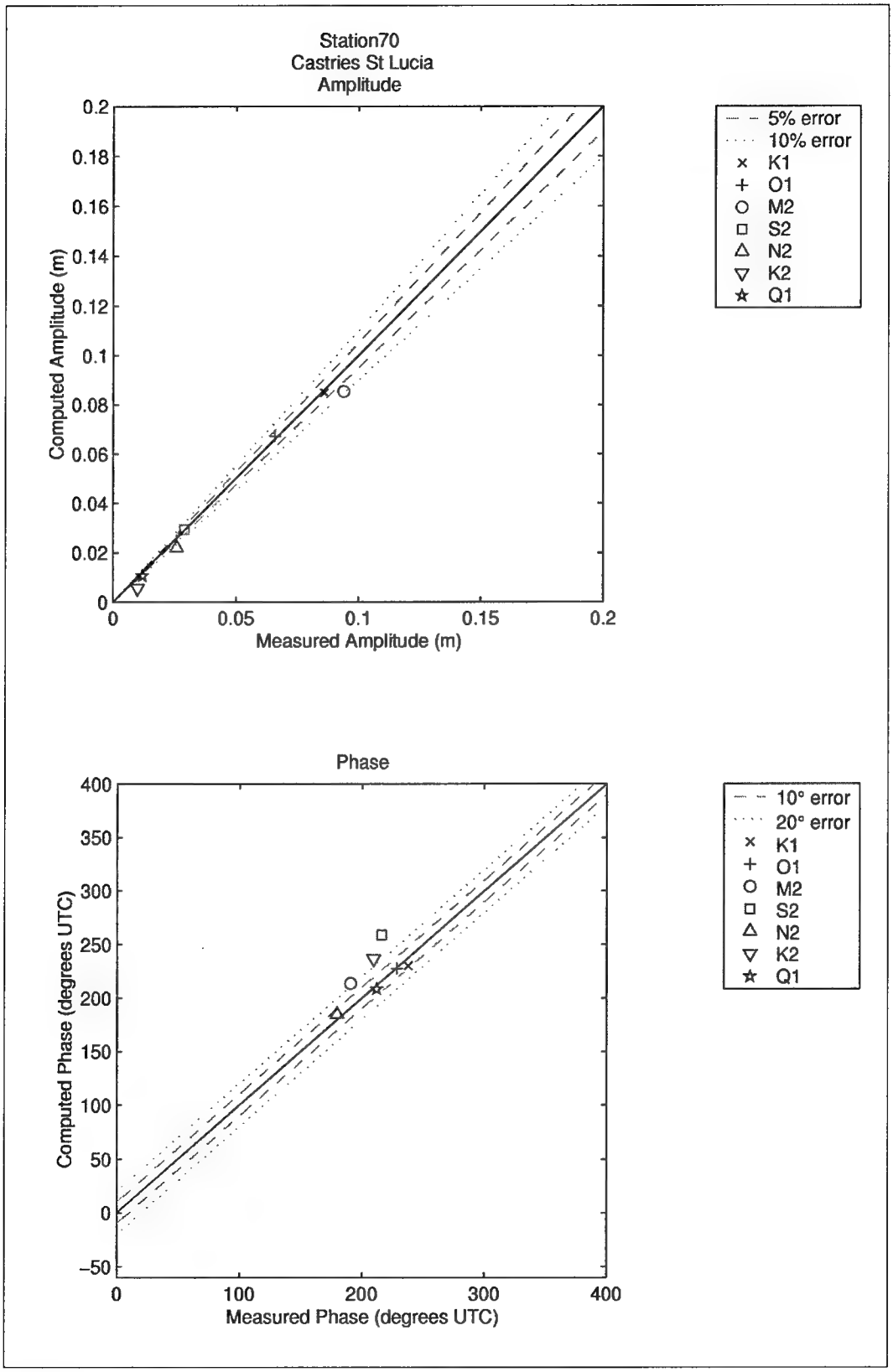

Figure 101. Computed vs. measured harmonic constituents at sta 70

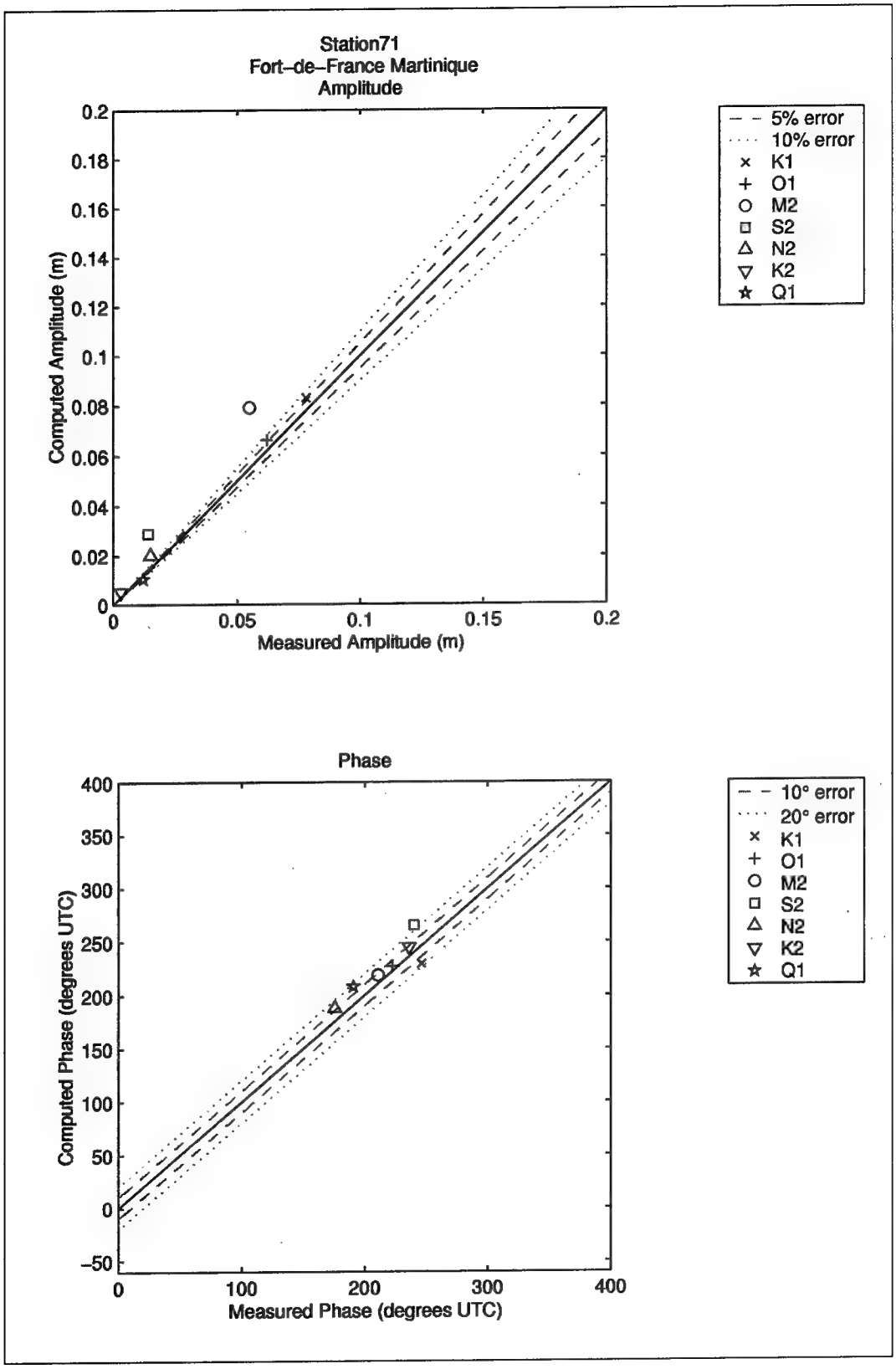

Figure 102. Computed vs. measured harmonic constituents at sta 71

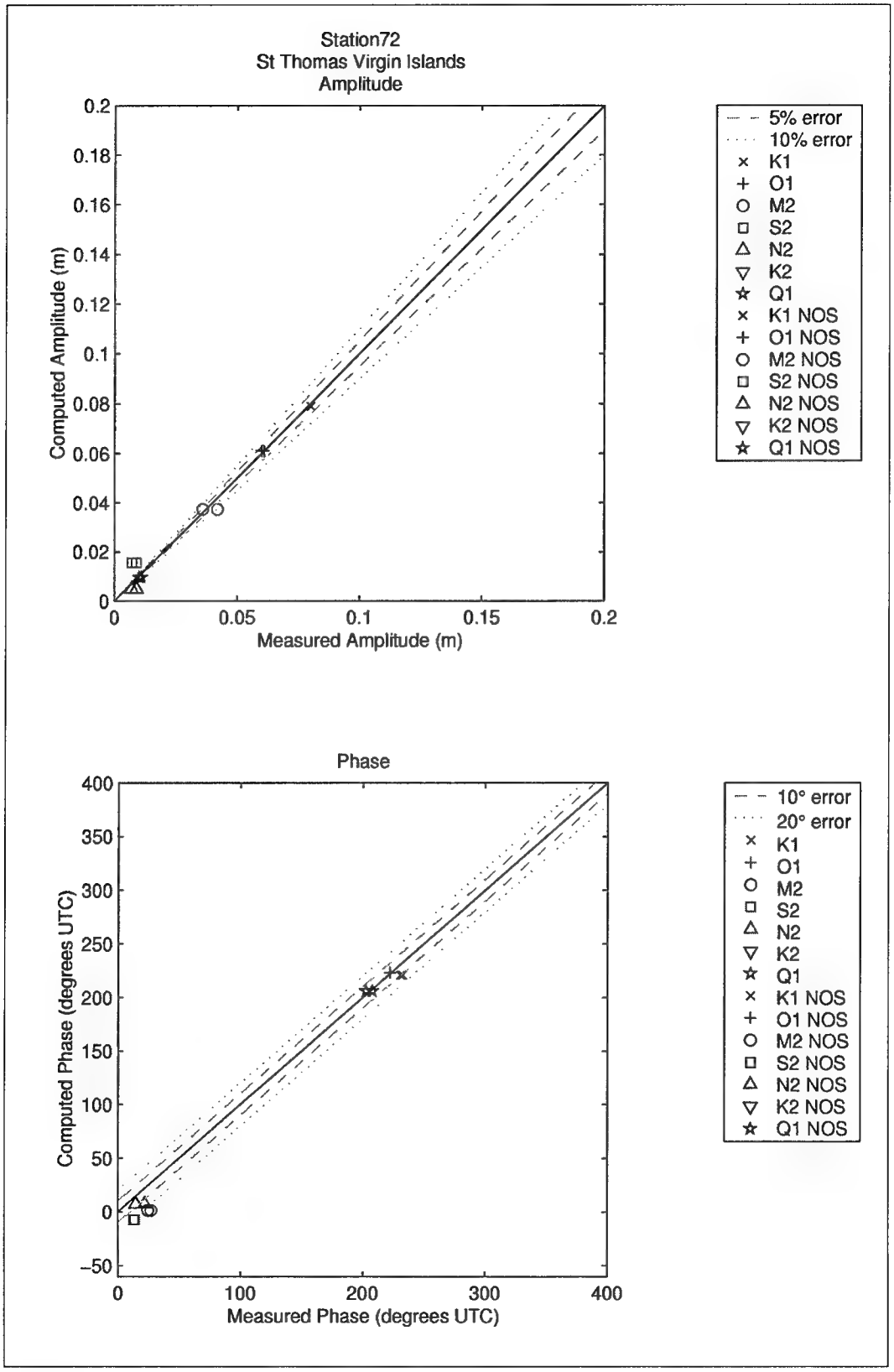

Figure 103. Computed vs. measured harmonic constituents at sta 72

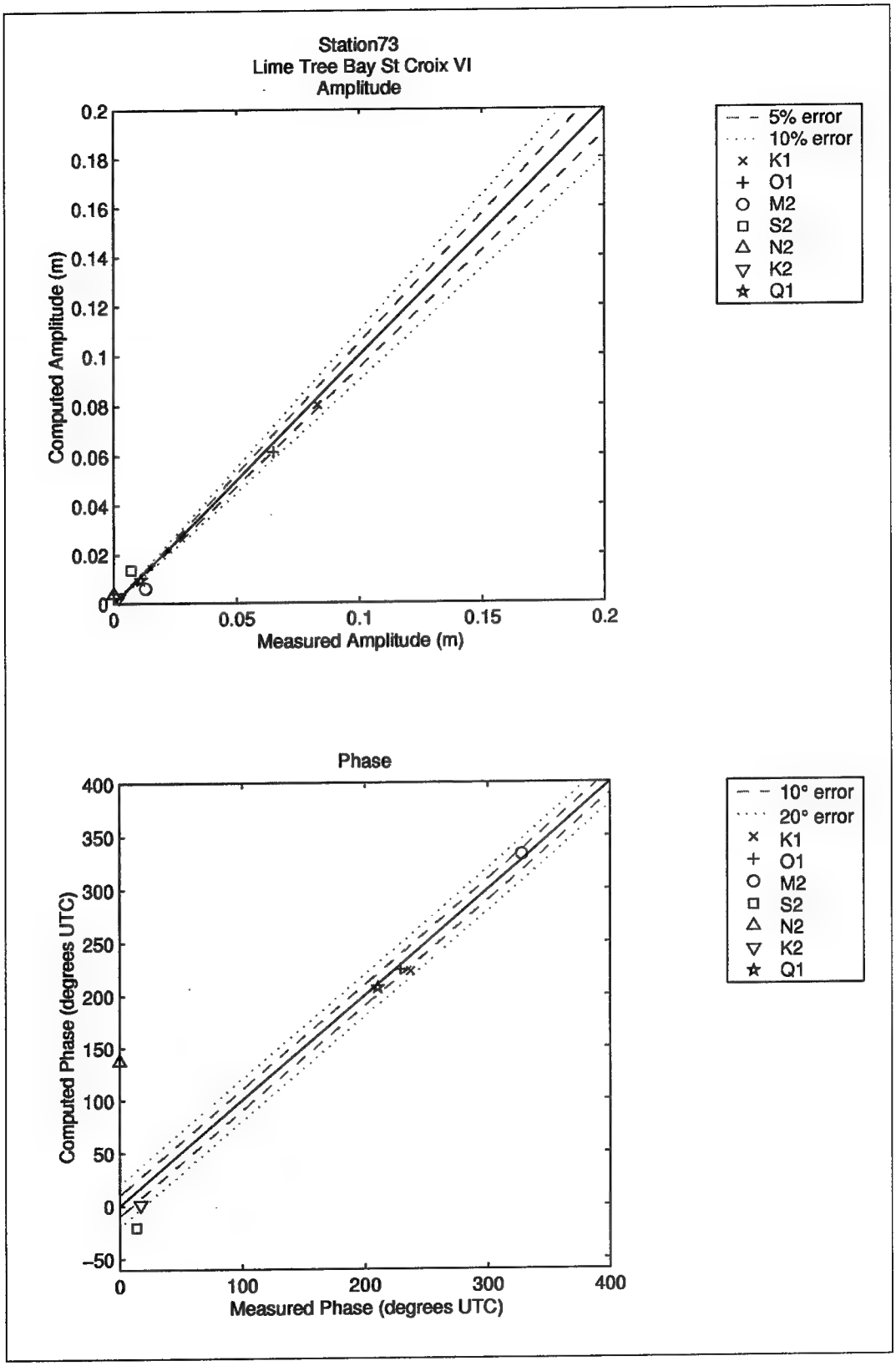

Figure 104. Computed vs. measured harmonic constituents at sta 73

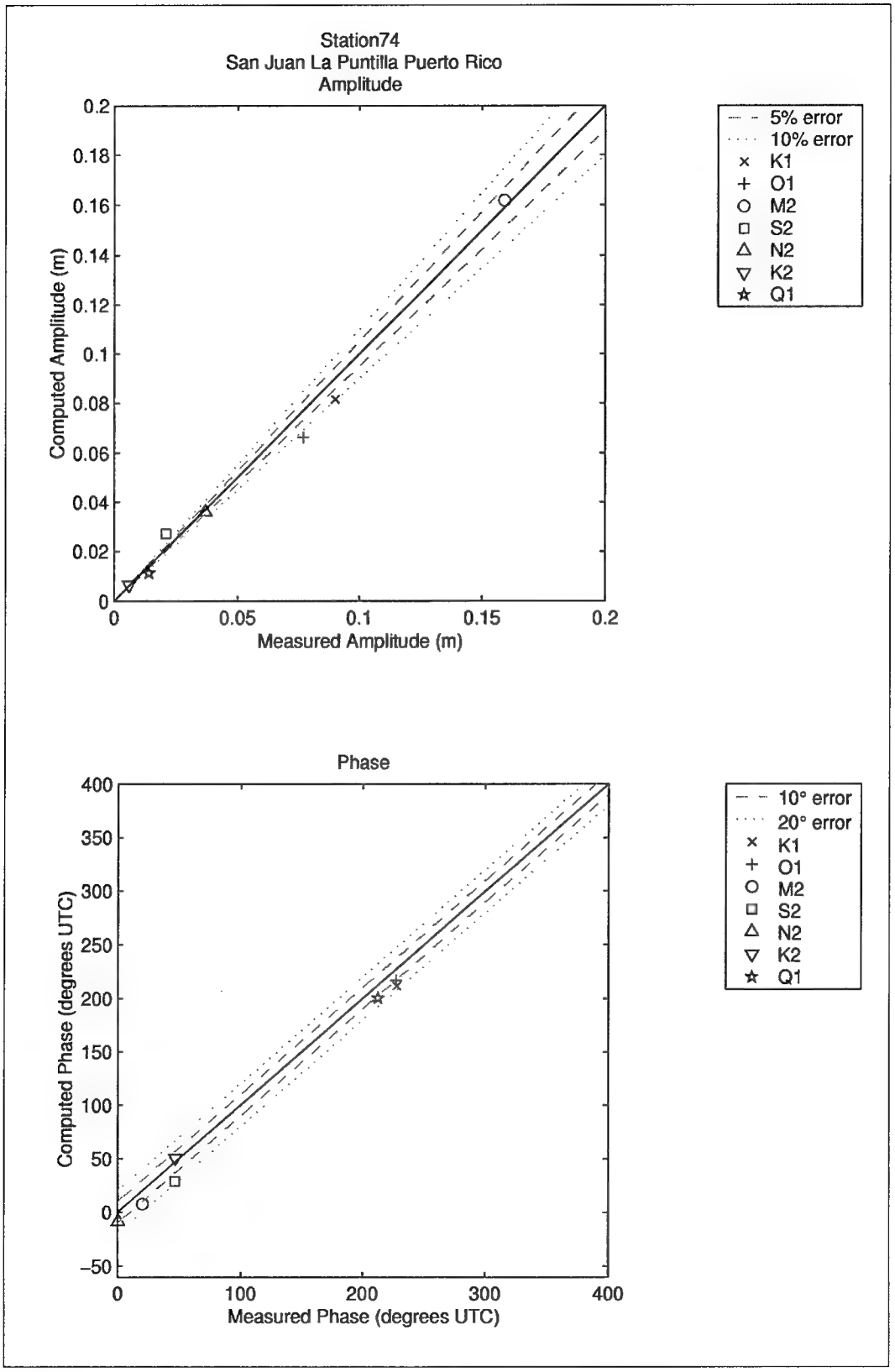

Figure 105. Computed vs. measured harmonic constituents at sta 74

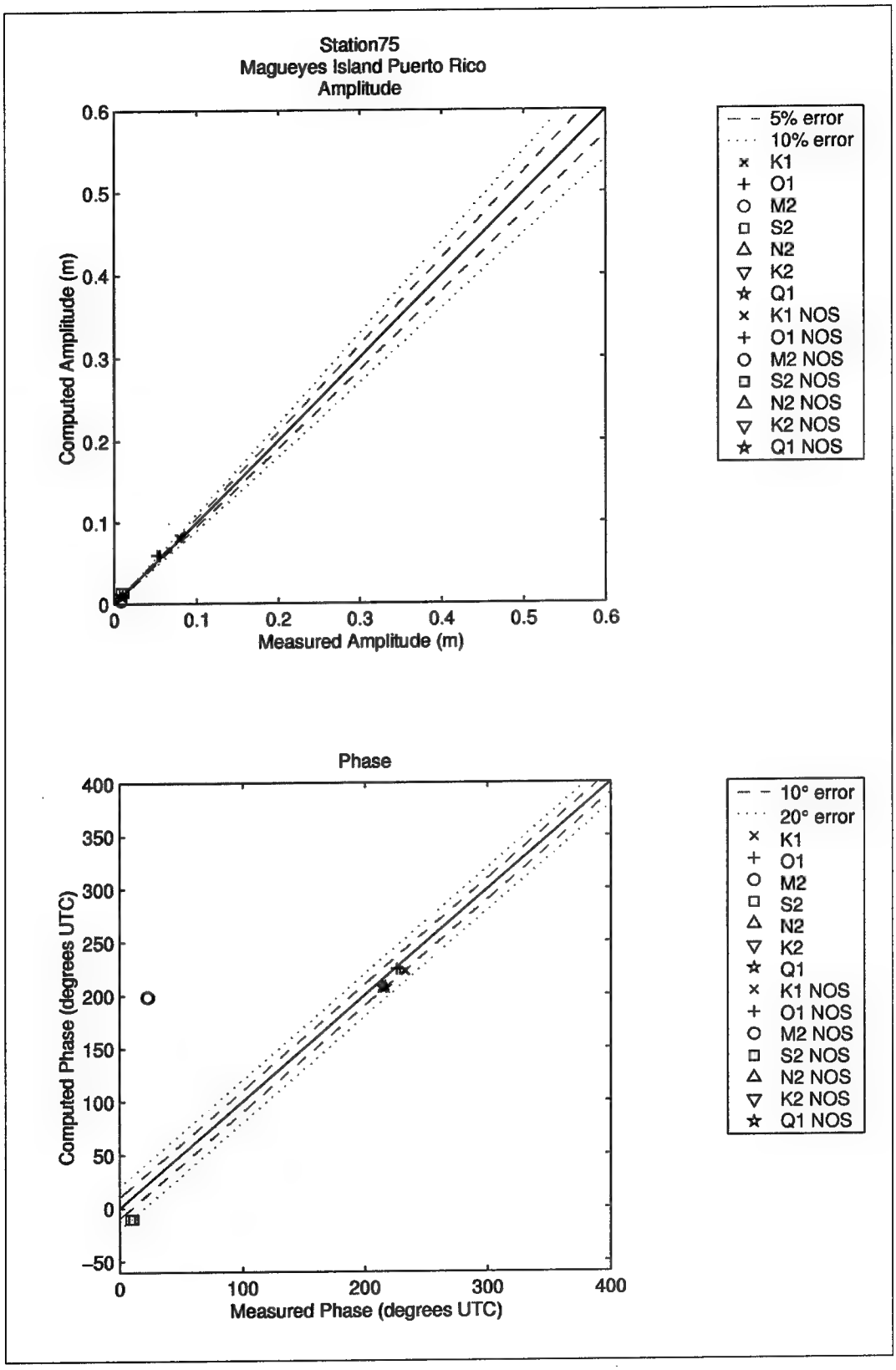

Figure 106. Computed vs. measured harmonic constituents at sta 75

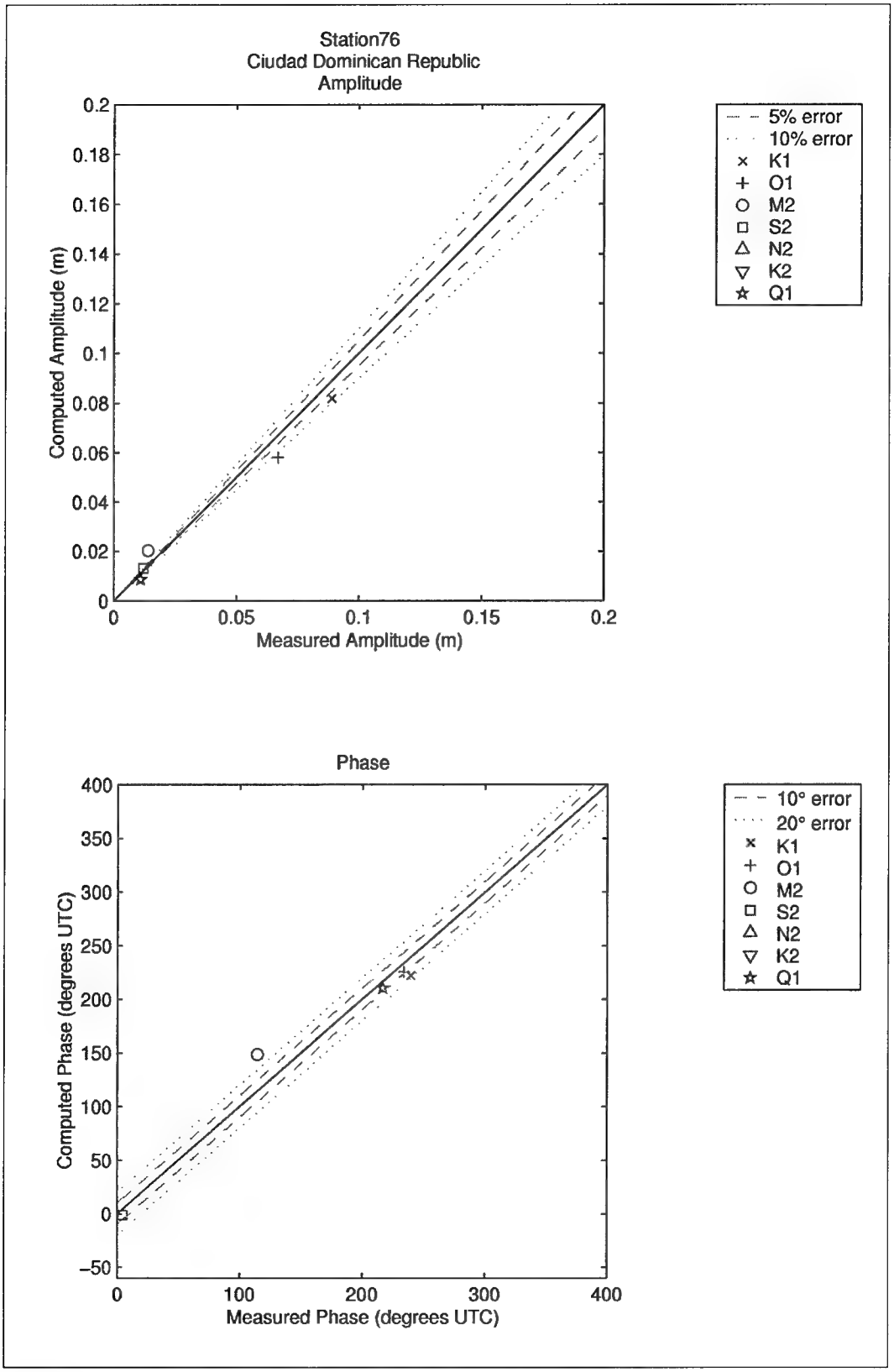

Figure 107. Computed vs. measured harmonic constituents at sta 76

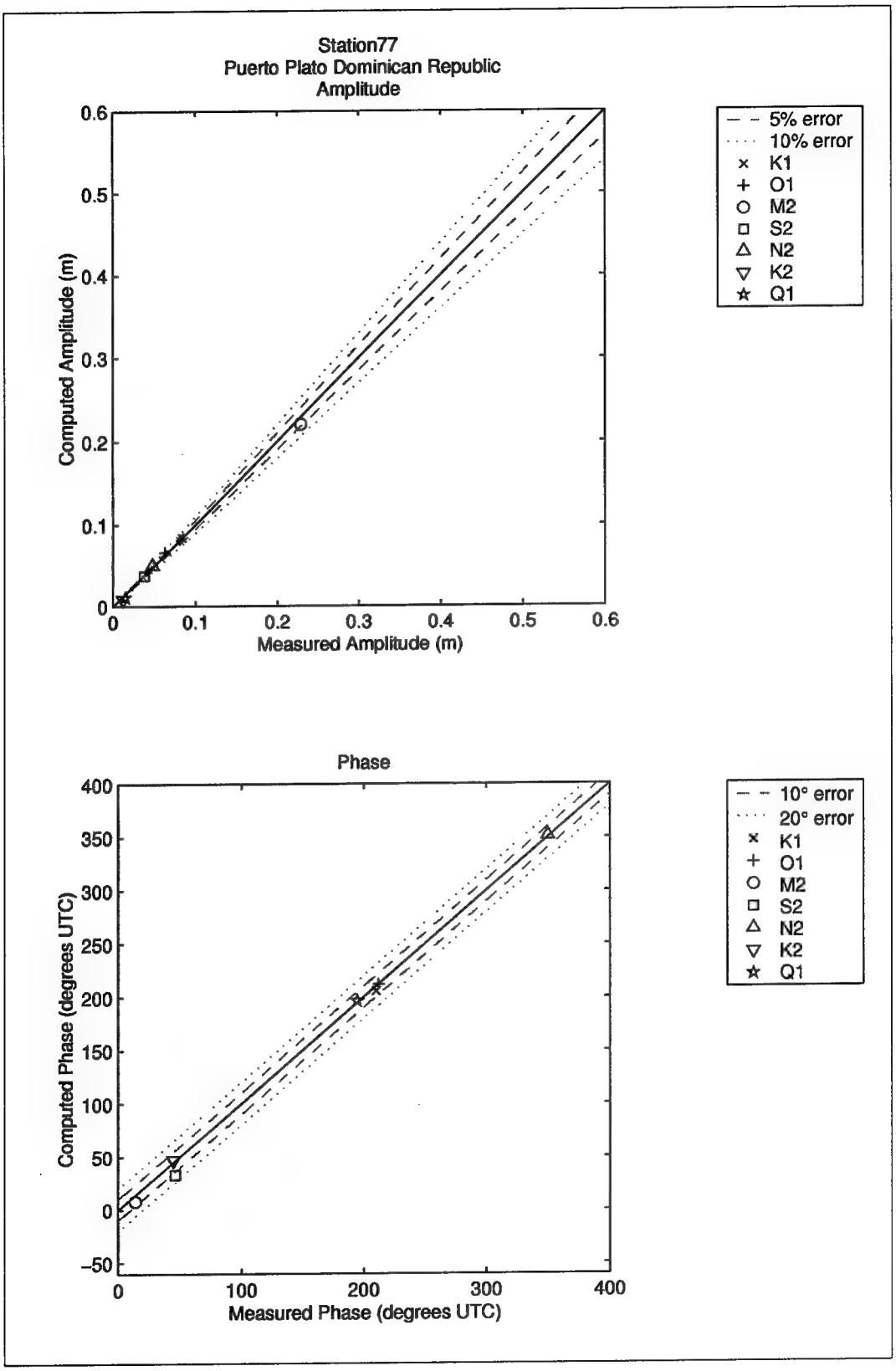

Figure 108. Computed vs. measured harmonic constituents at sta 77

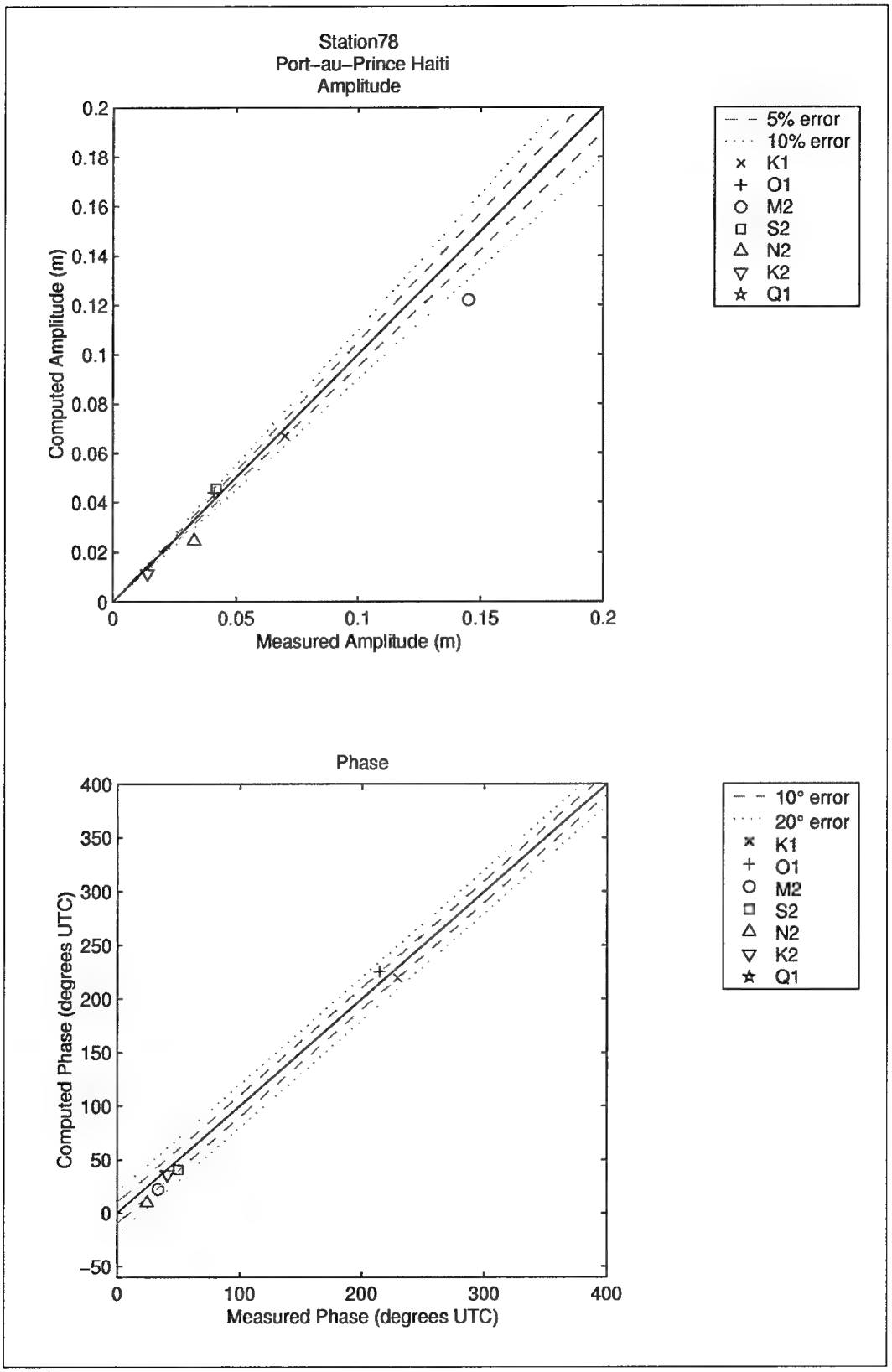

Figure 109. Computed vs. measured harmonic constituents at sta 78

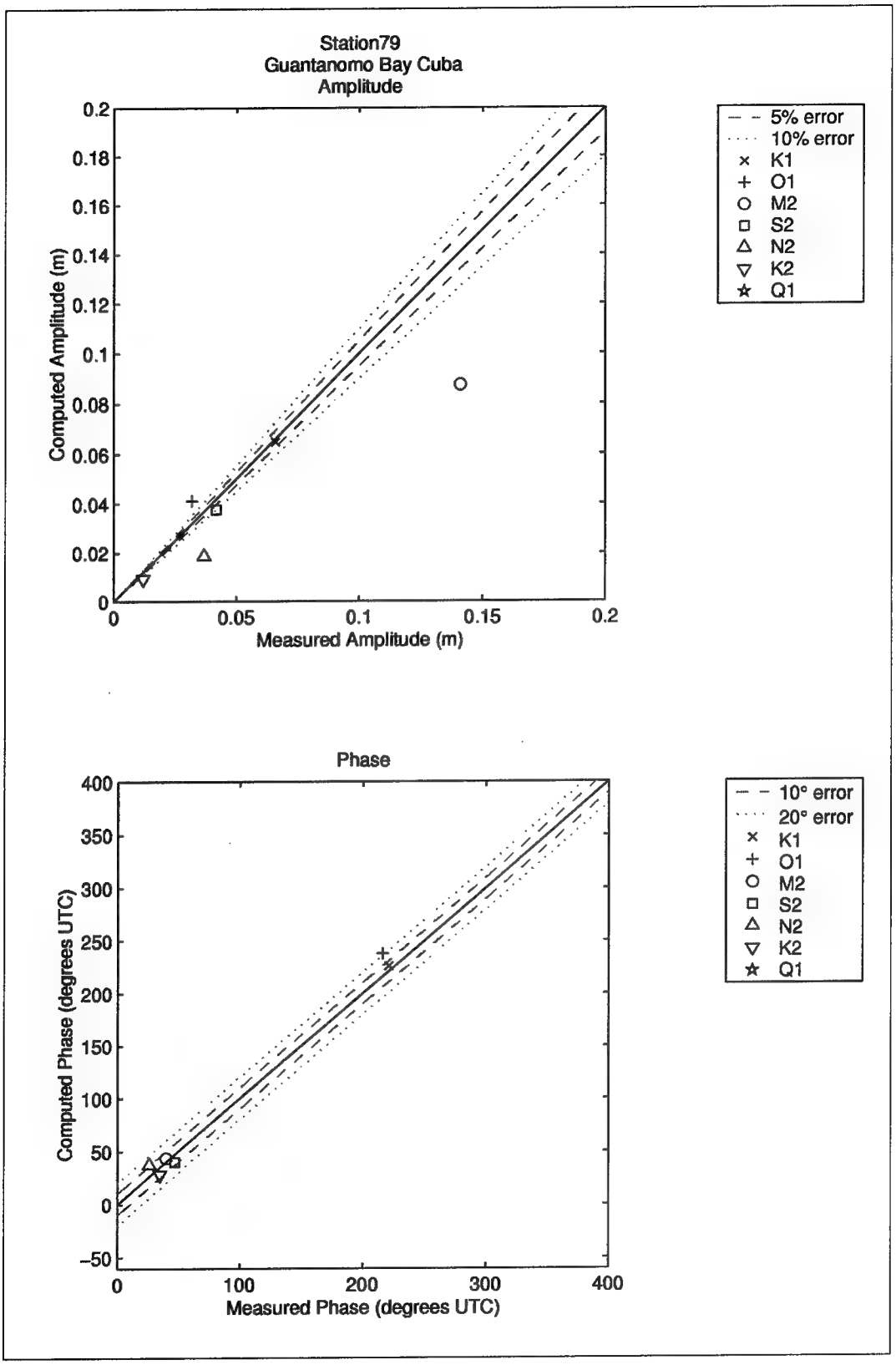

Figure 110. Computed vs. measured harmonic constituents at sta 79

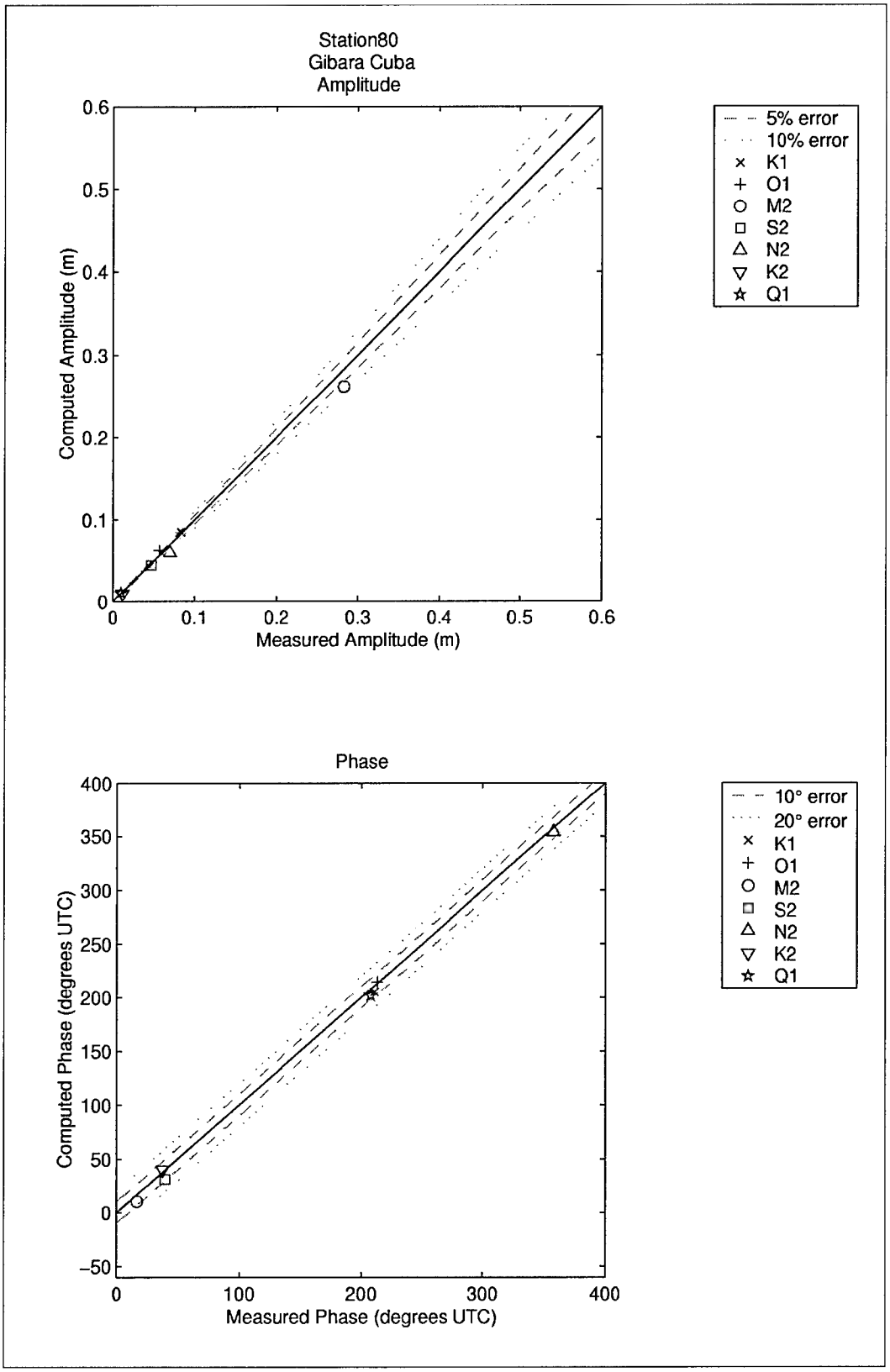

Figure 111. Computed vs. measured harmonic constituents at sta 80

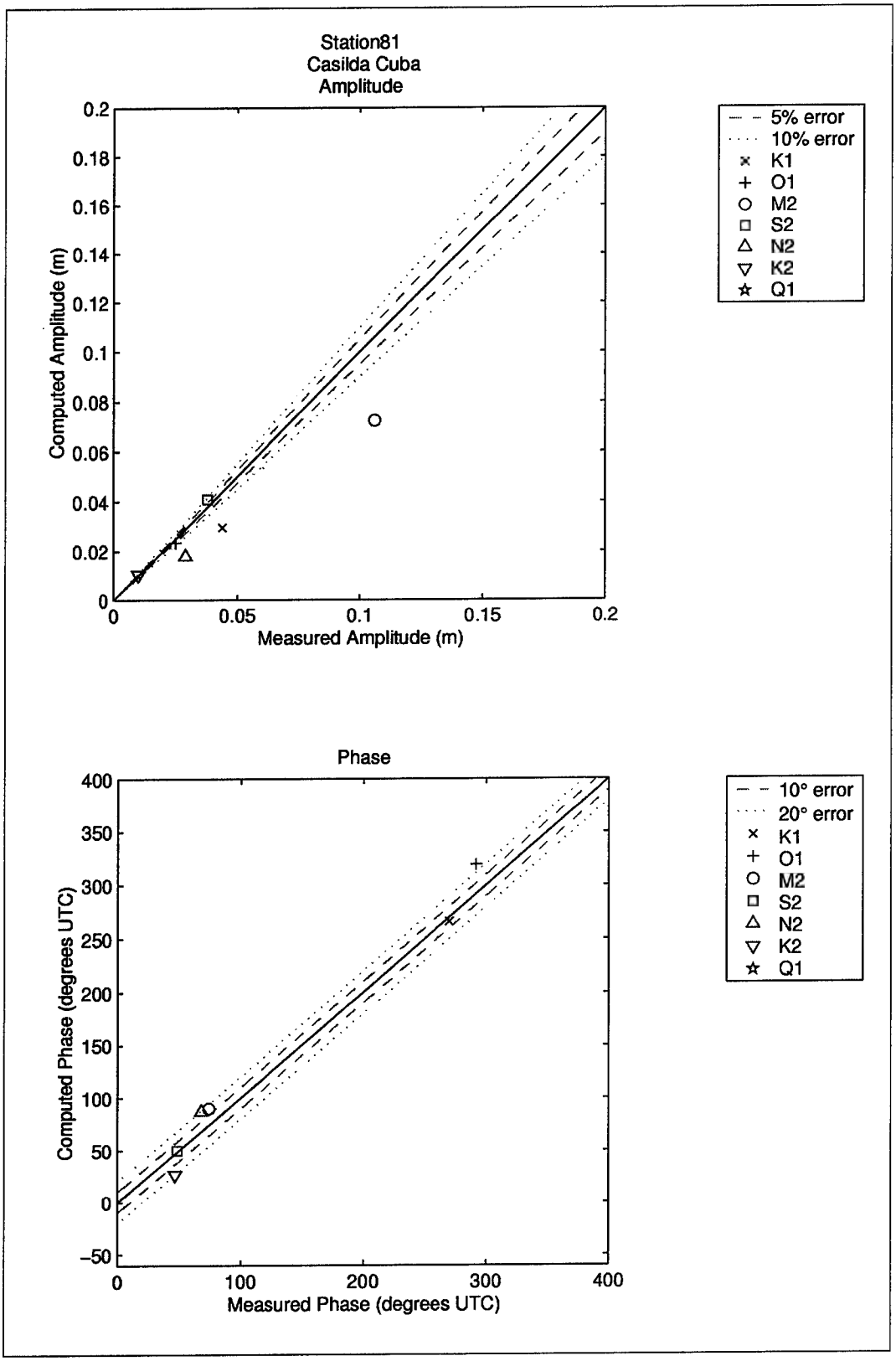

Figure 112. Computed vs. measured harmonic constituents at sta 81

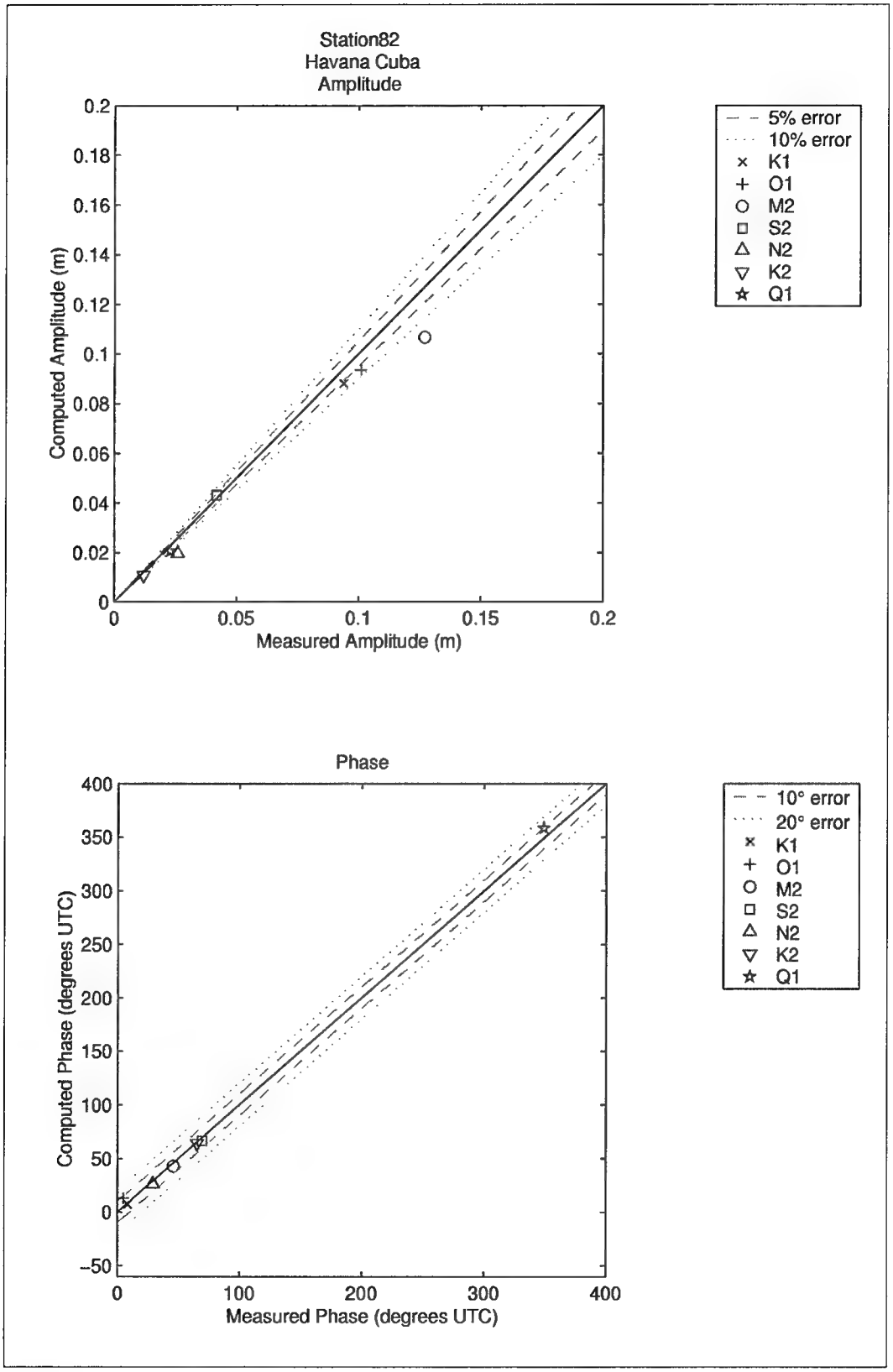

Figure 113. Computed vs. measured harmonic constituents at sta 82

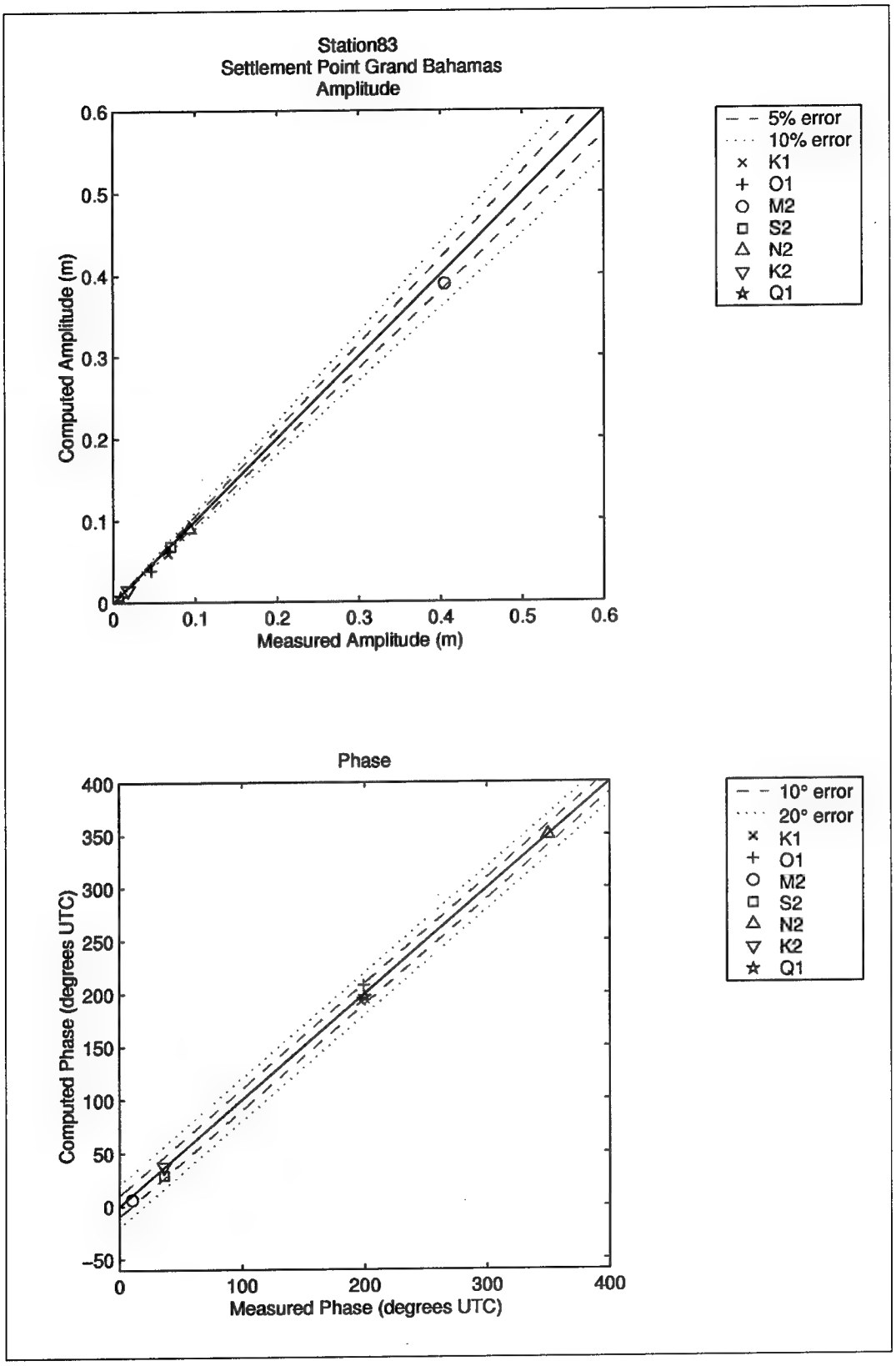

Figure 114. Computed vs. measured harmonic constituents at sta 83

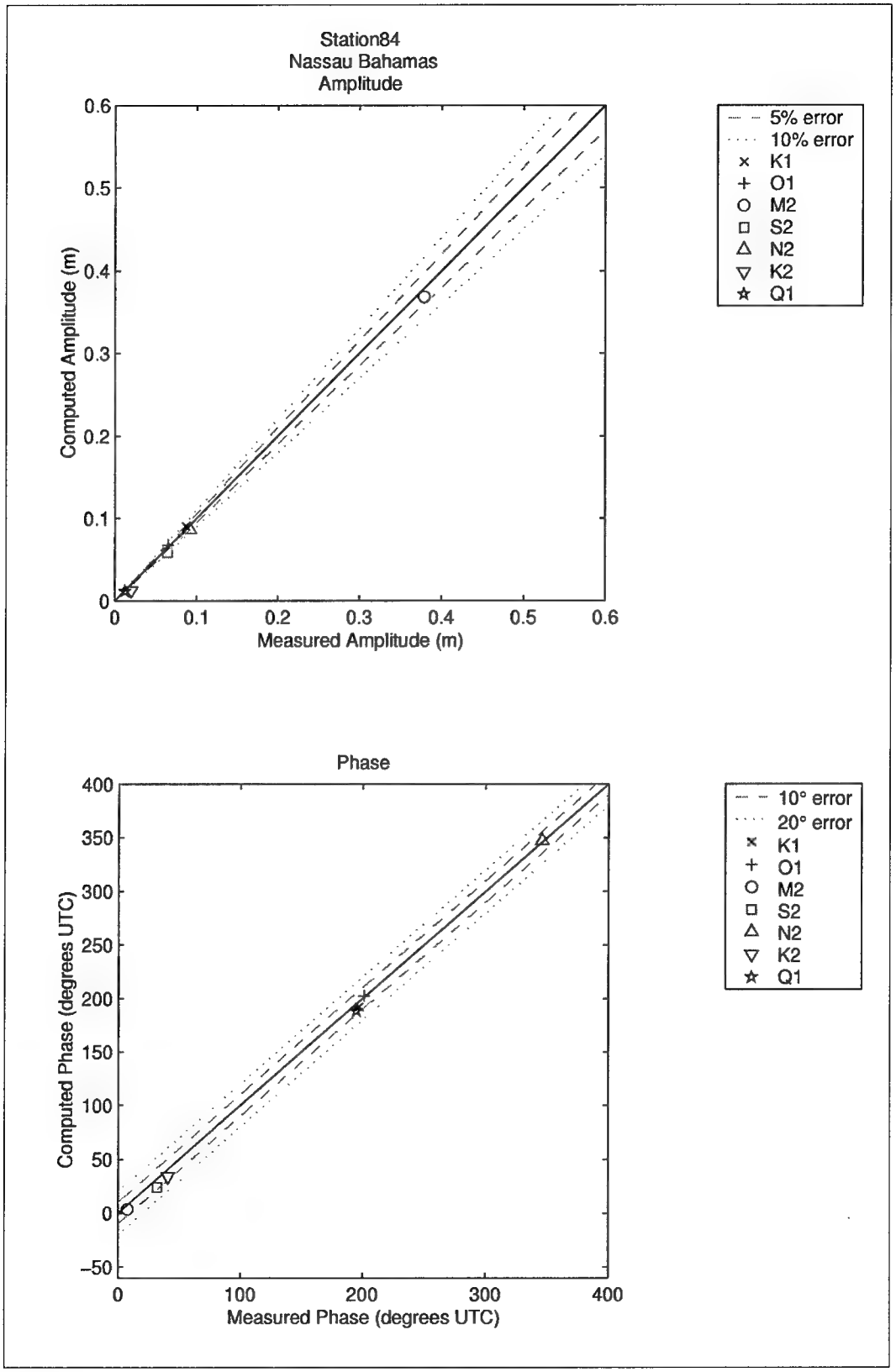

Figure 115. Computed vs. measured harmonic constituents at sta 84

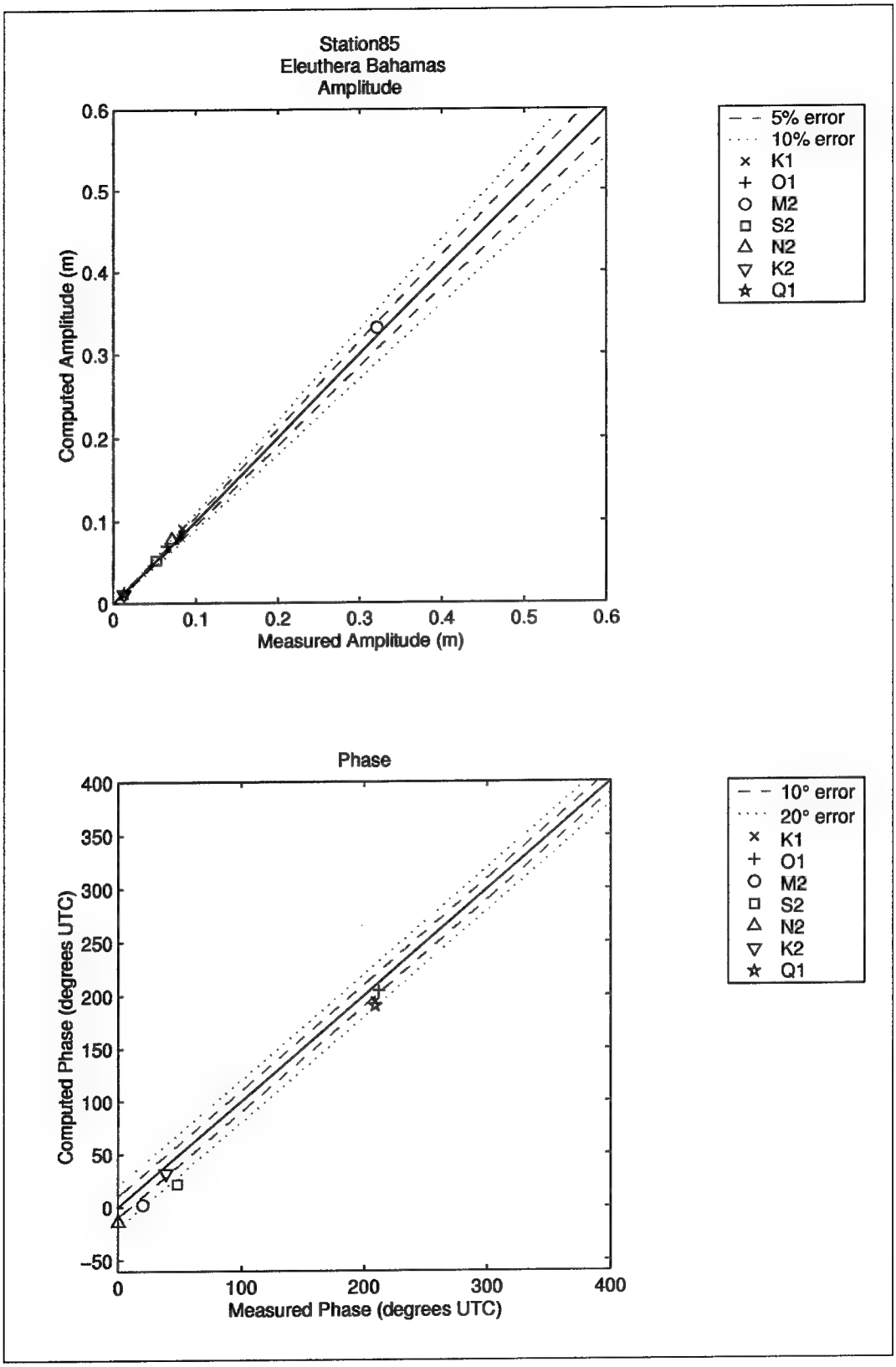

Figure 116. Computed vs. measured harmonic constituents at sta 85

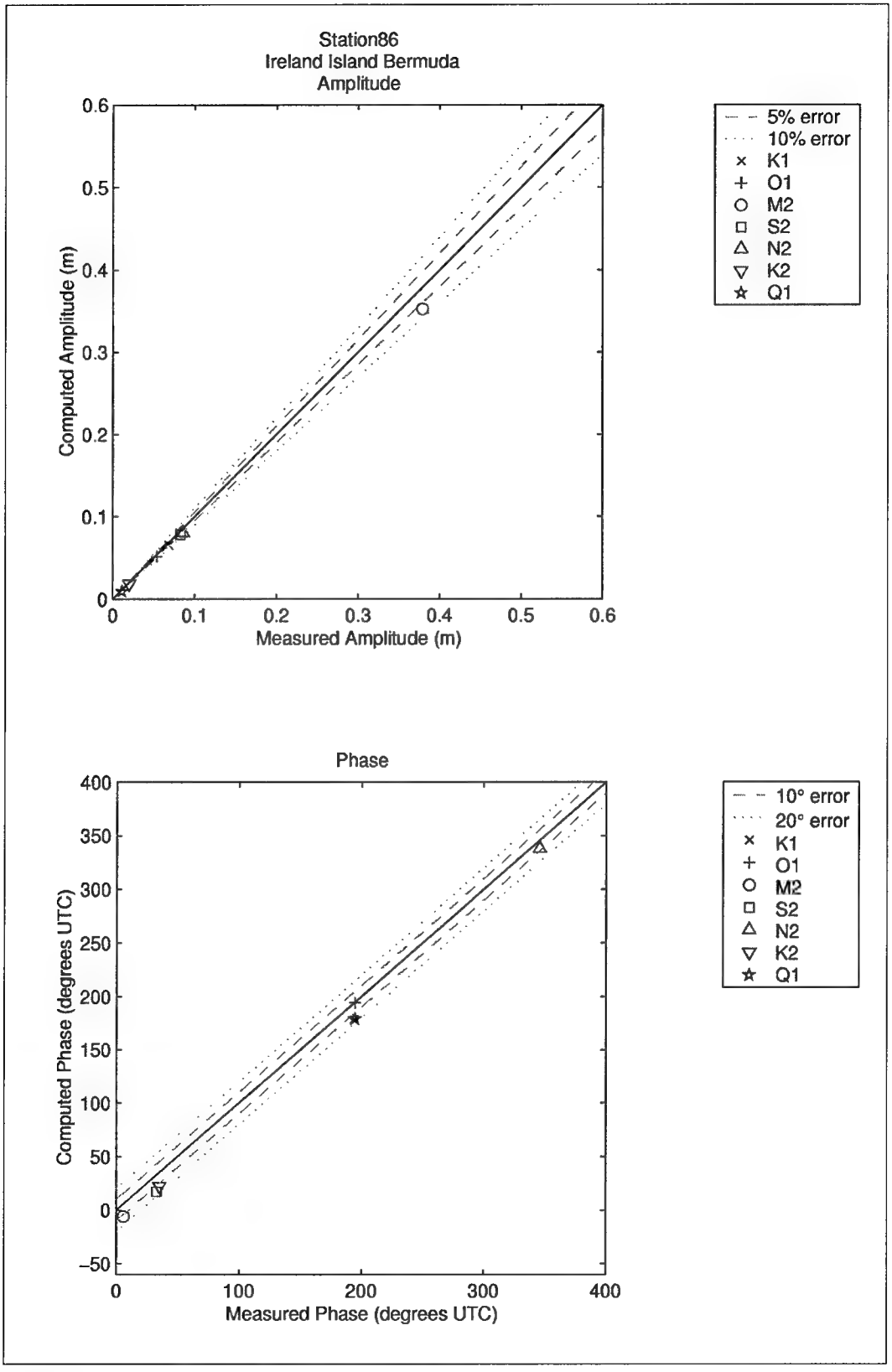

Figure 117. Computed vs. measured harmonic constituents at sta 86

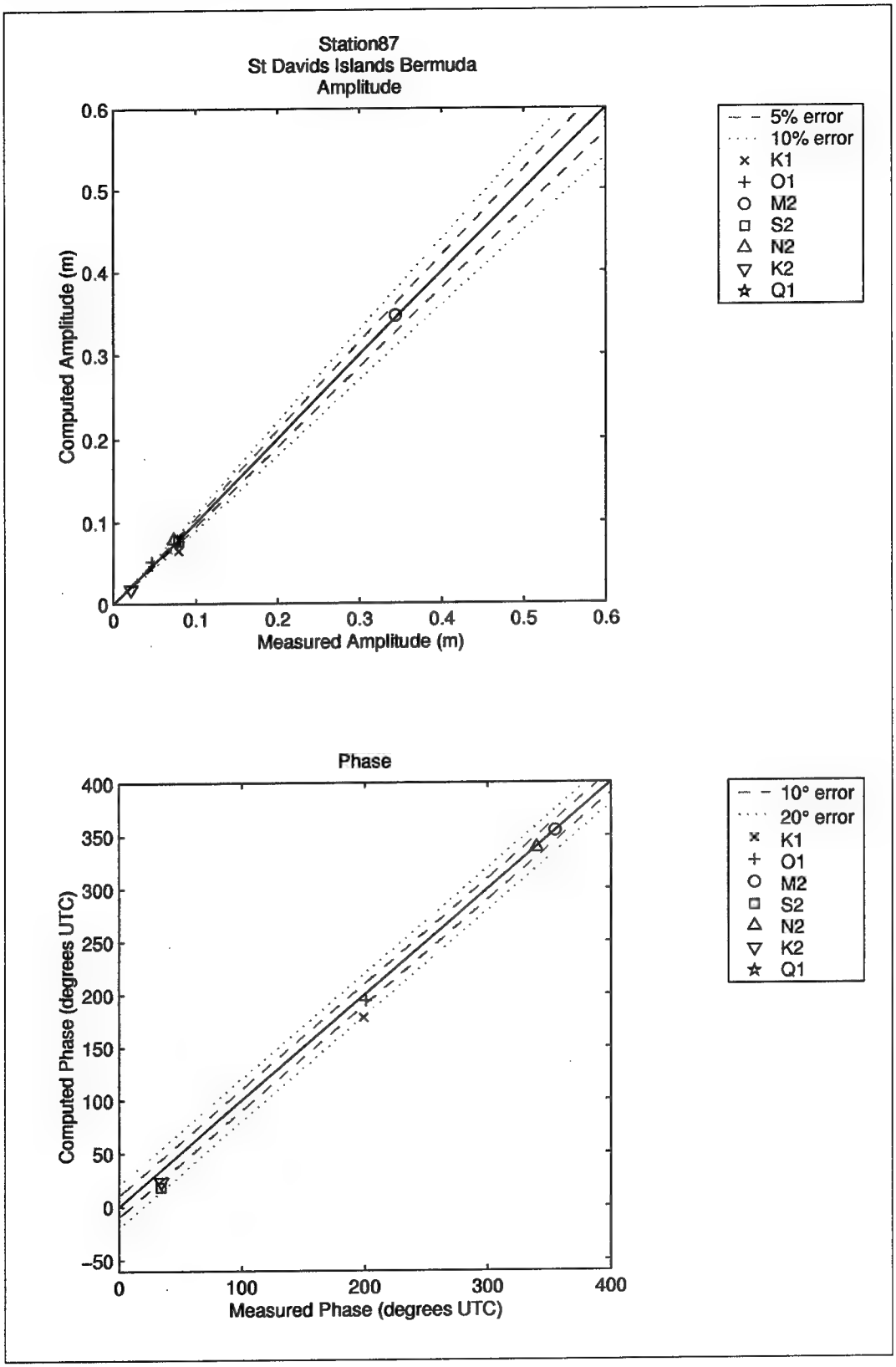

Figure 118. Computed vs. measured harmonic constituents at sta 87

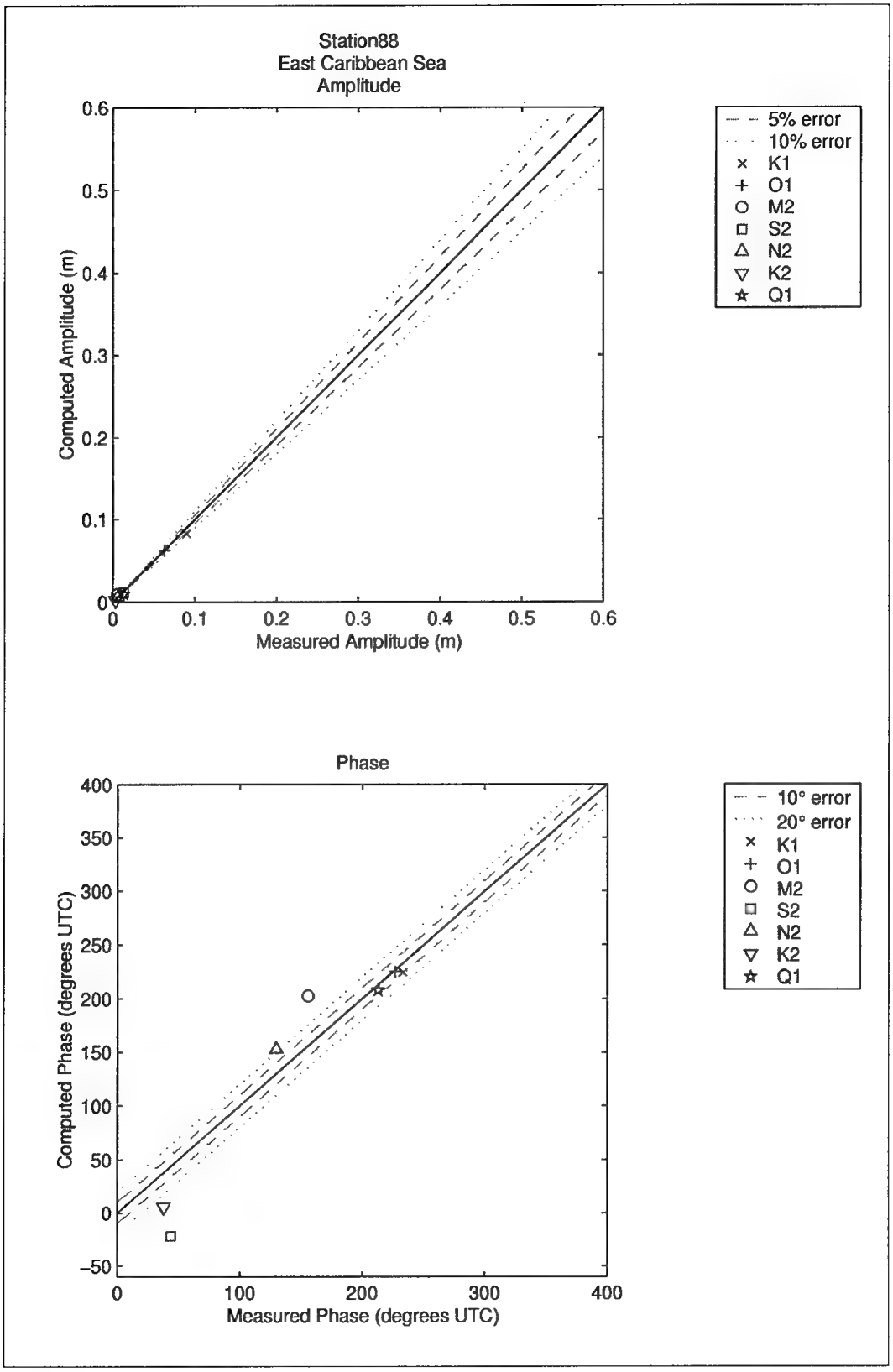

Figure 119. Computed vs. measured harmonic constituents at sta 88

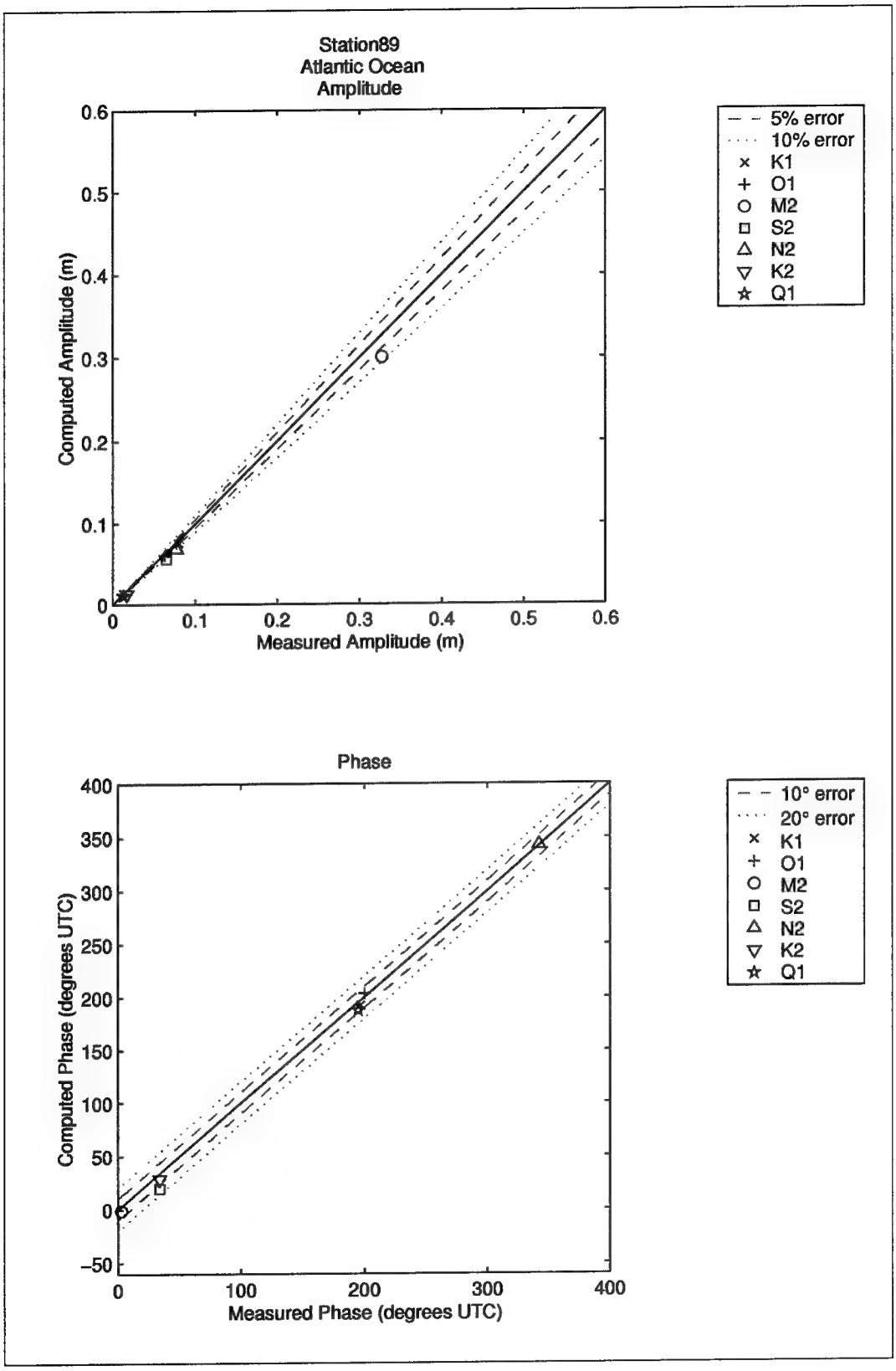

Figure 120. Computed vs. measured harmonic constituents at sta 89

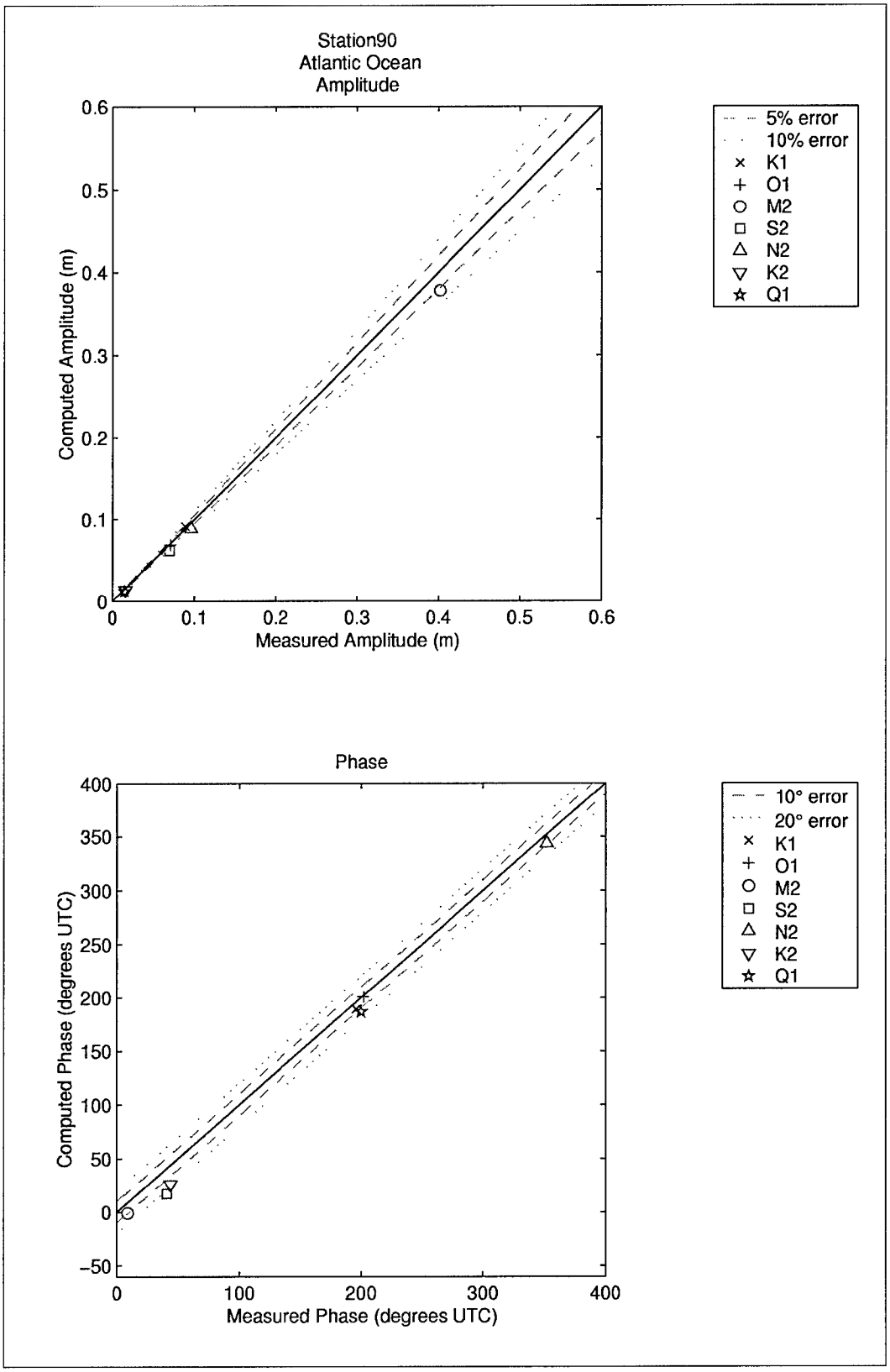

Figure 121. Computed vs. measured harmonic constituents at sta 90

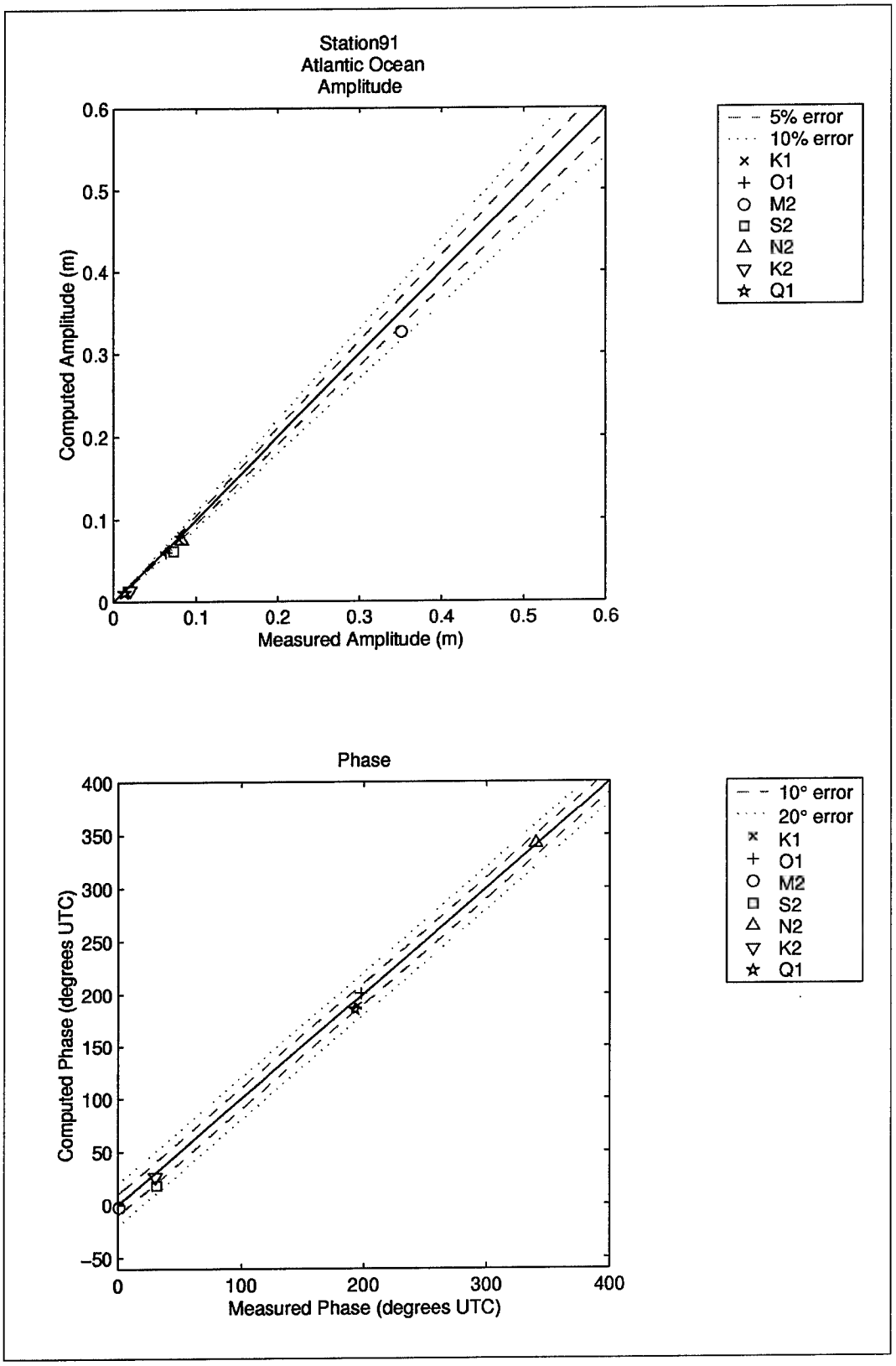

Figure 122. Computed vs. measured harmonic constituents at sta 91

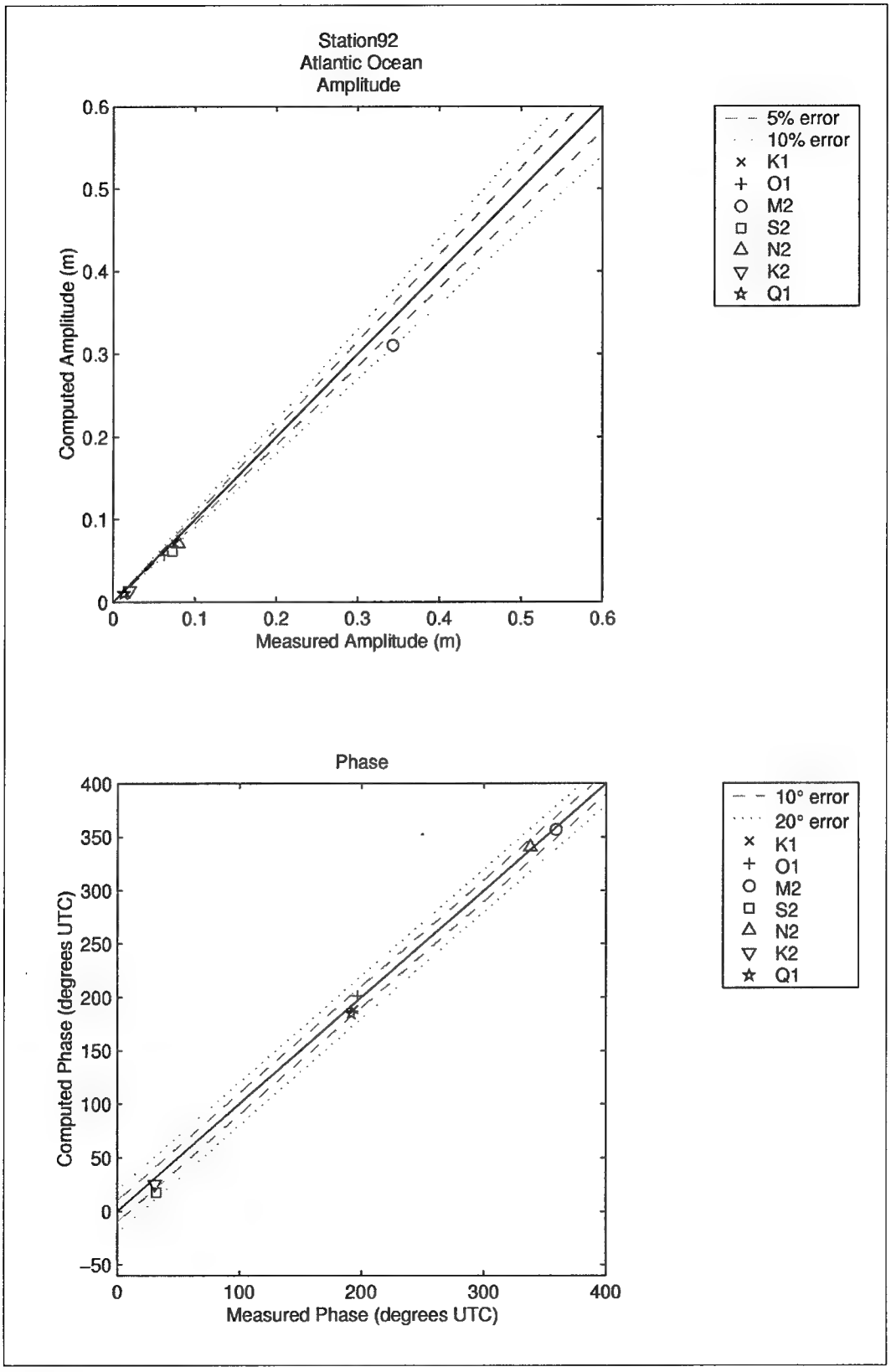

Figure 123. Computed vs. measured harmonic constituents at sta 92

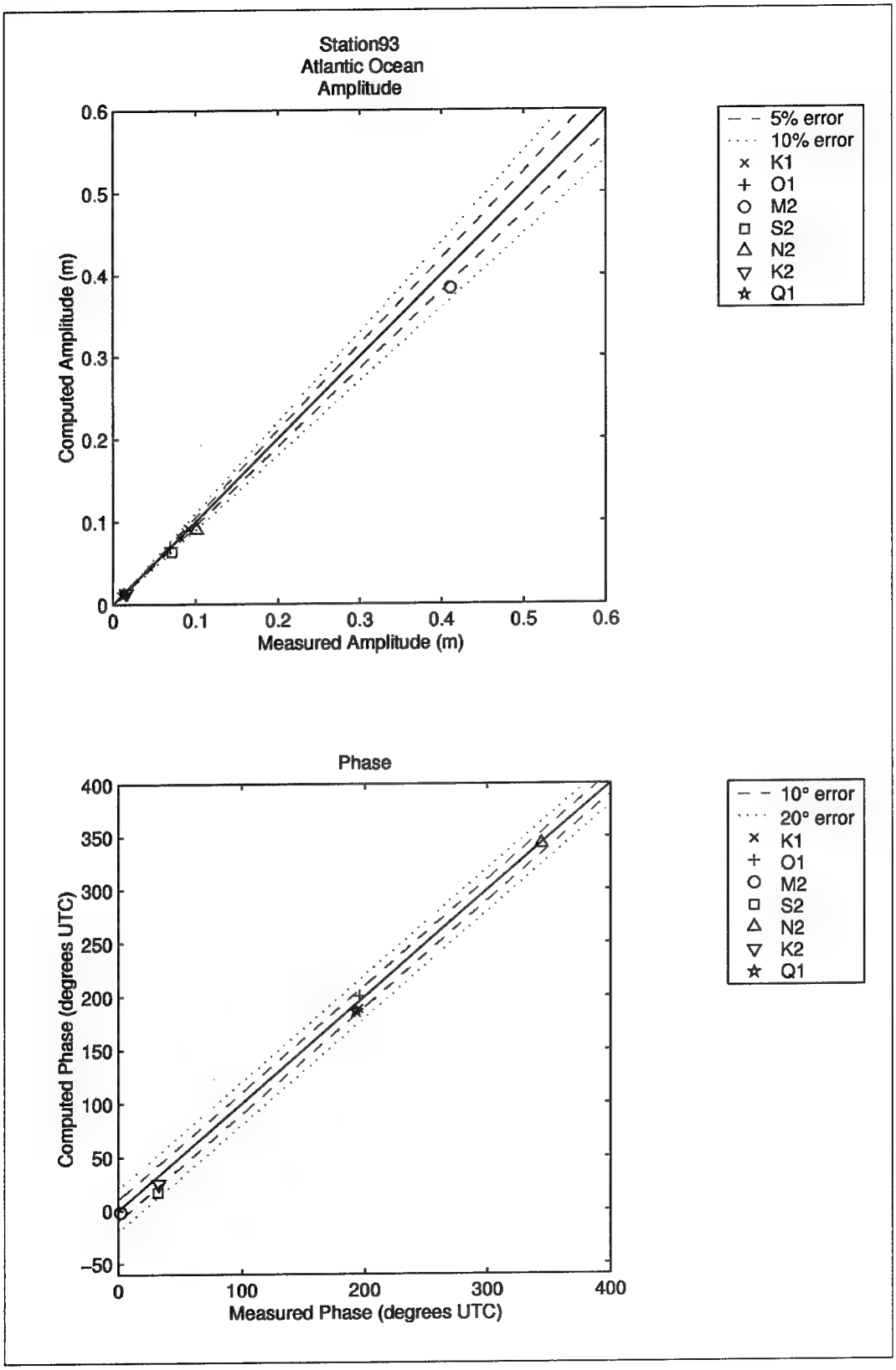

Figure 124. Computed vs. measured harmonic constituents at sta 93

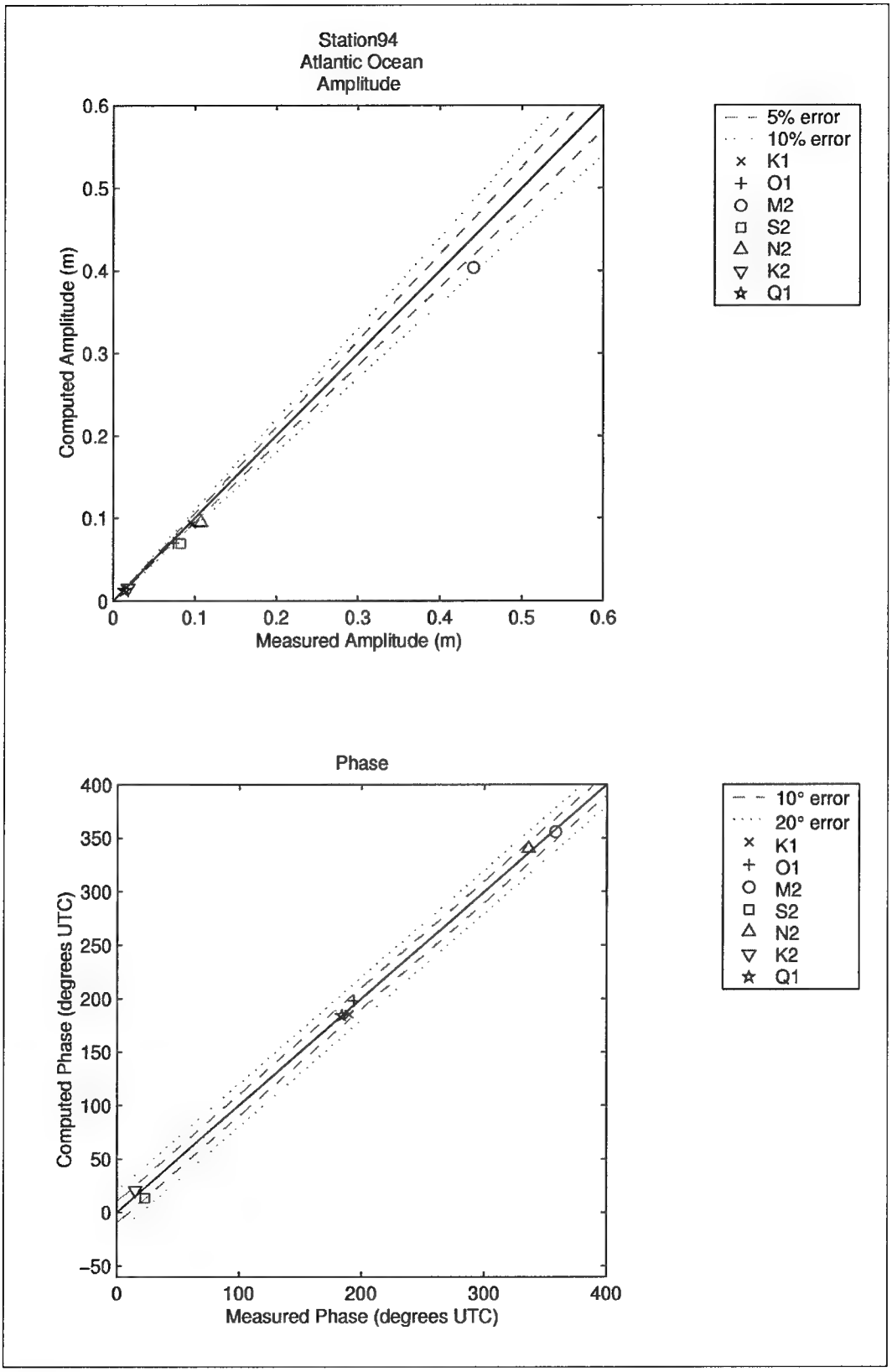

Figure 125. Computed vs. measured harmonic constituents at sta 94

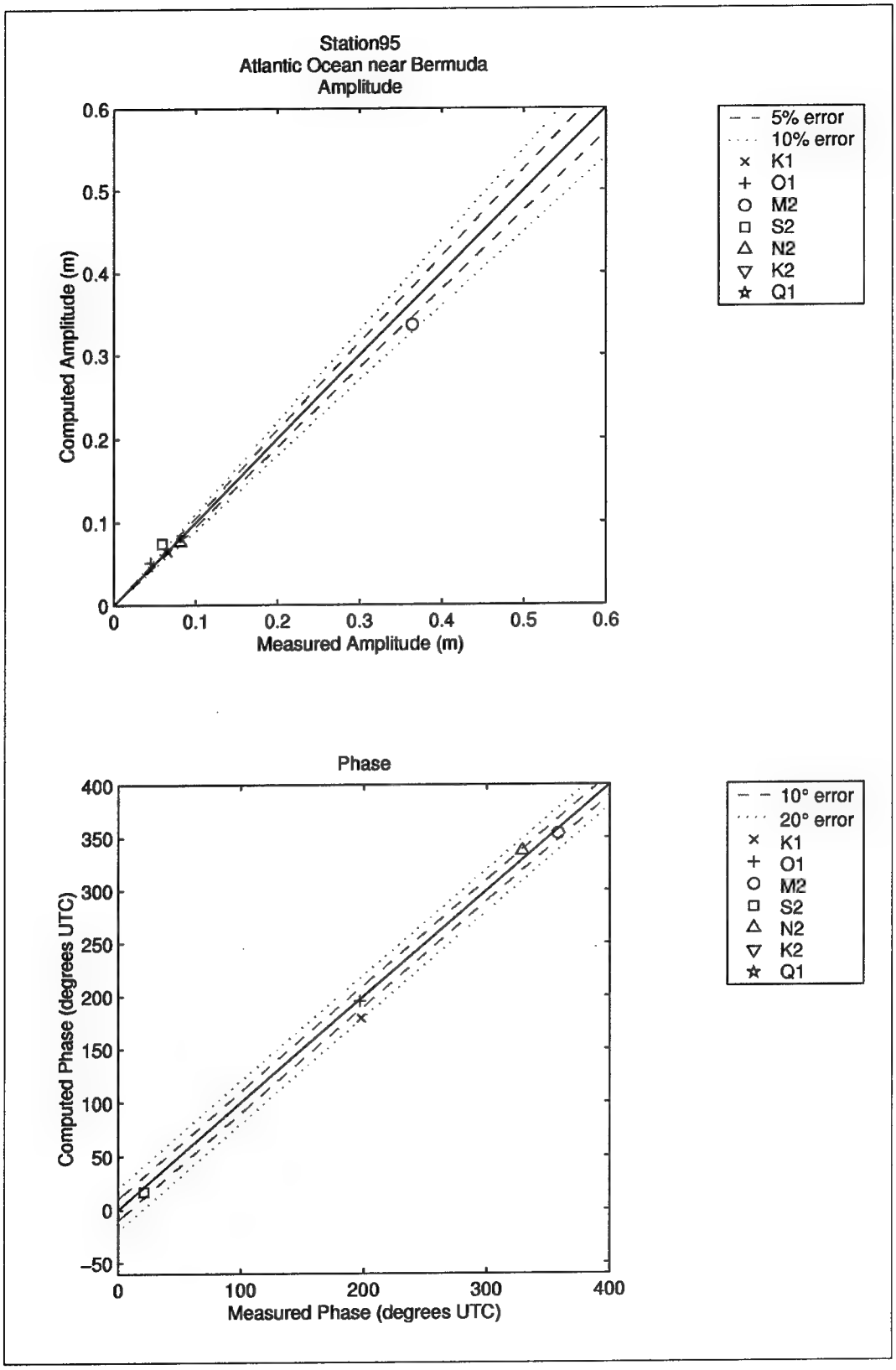

Figure 126. Computed vs. measured harmonic constituents at sta 95

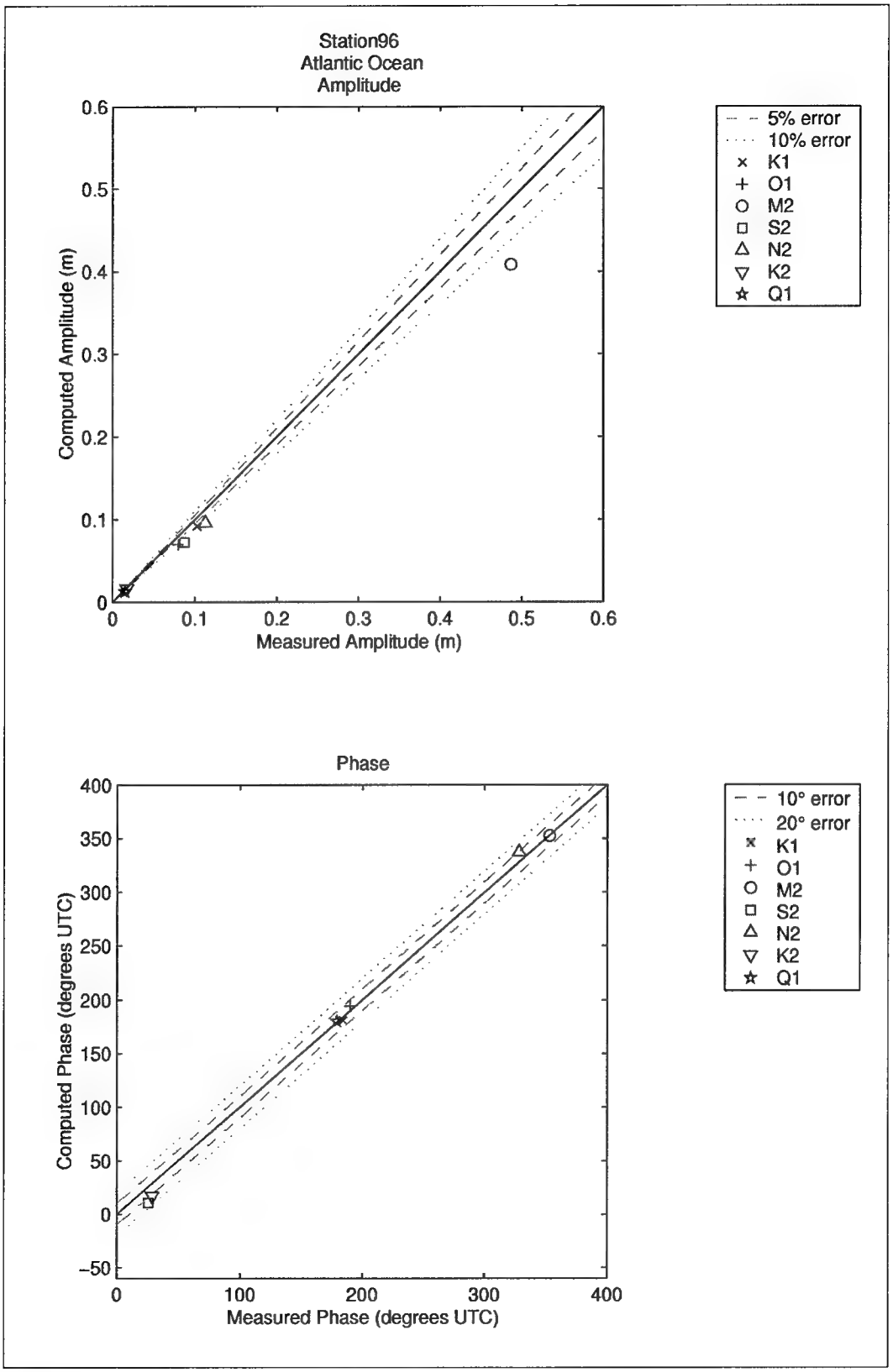

Figure 127. Computed vs. measured harmonic constituents at sta 96

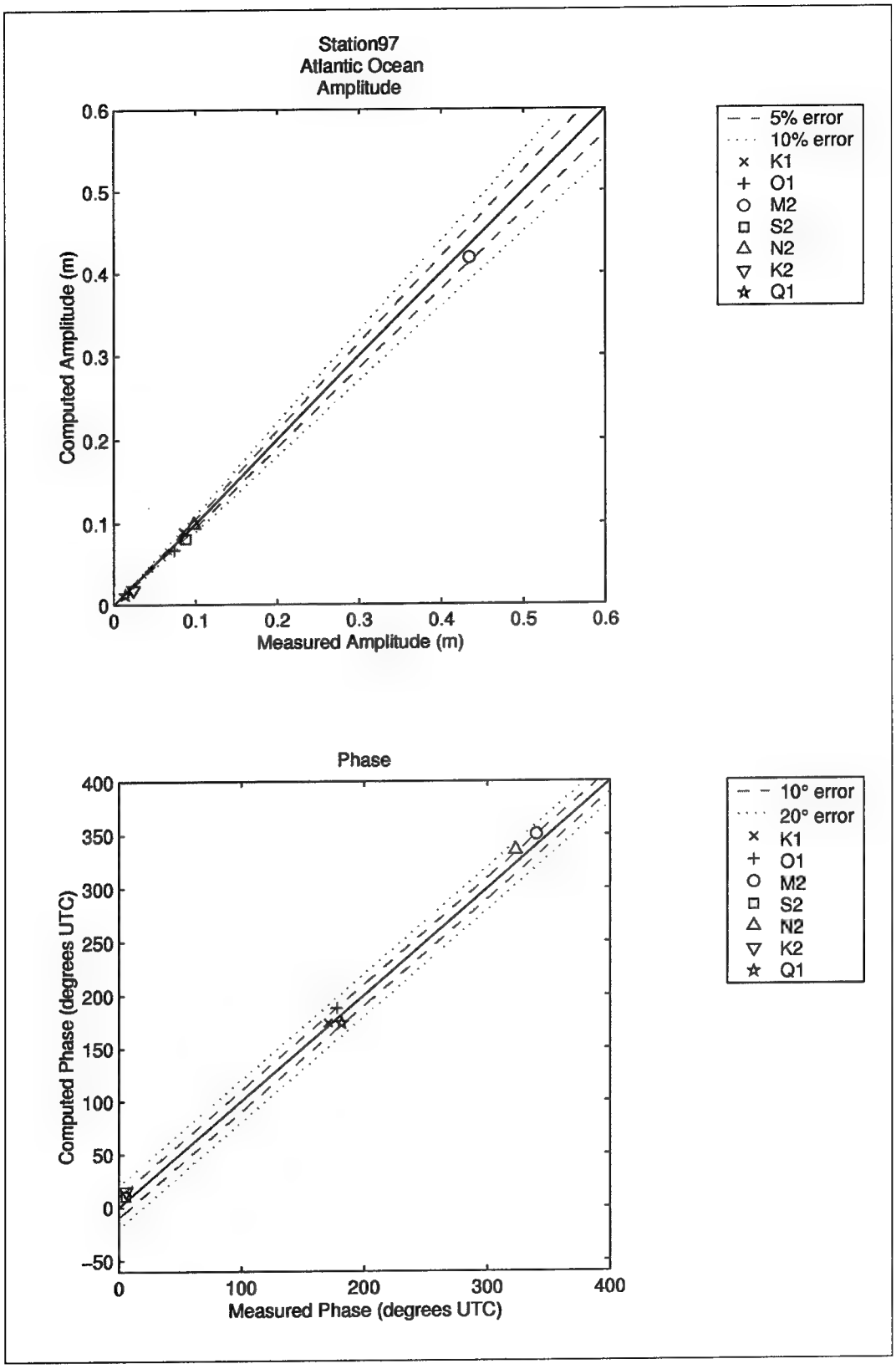

Figure 128. Computed vs. measured harmonic constituents at sta 97

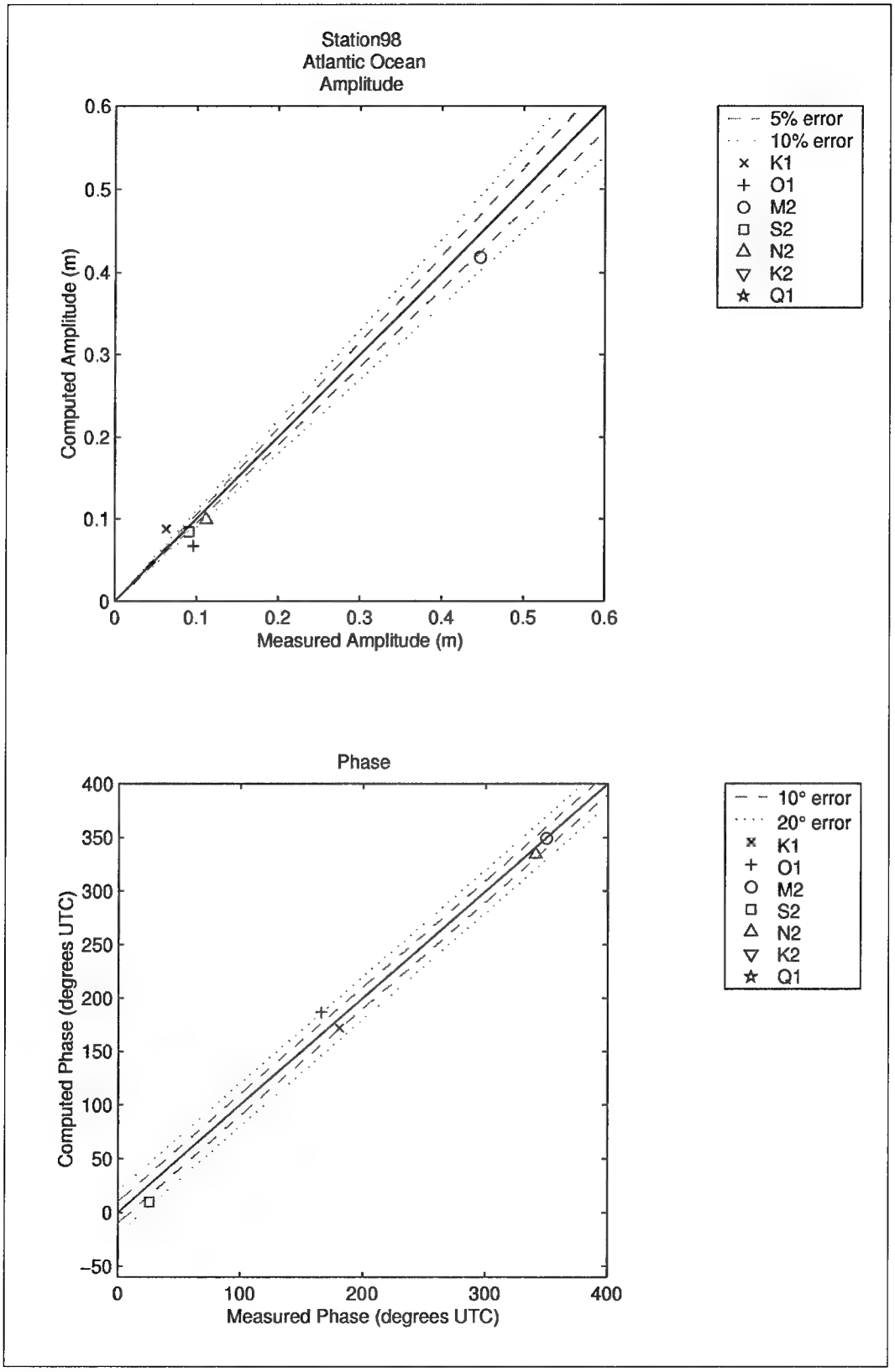

Figure 129. Computed vs. measured harmonic constituents at sta 98

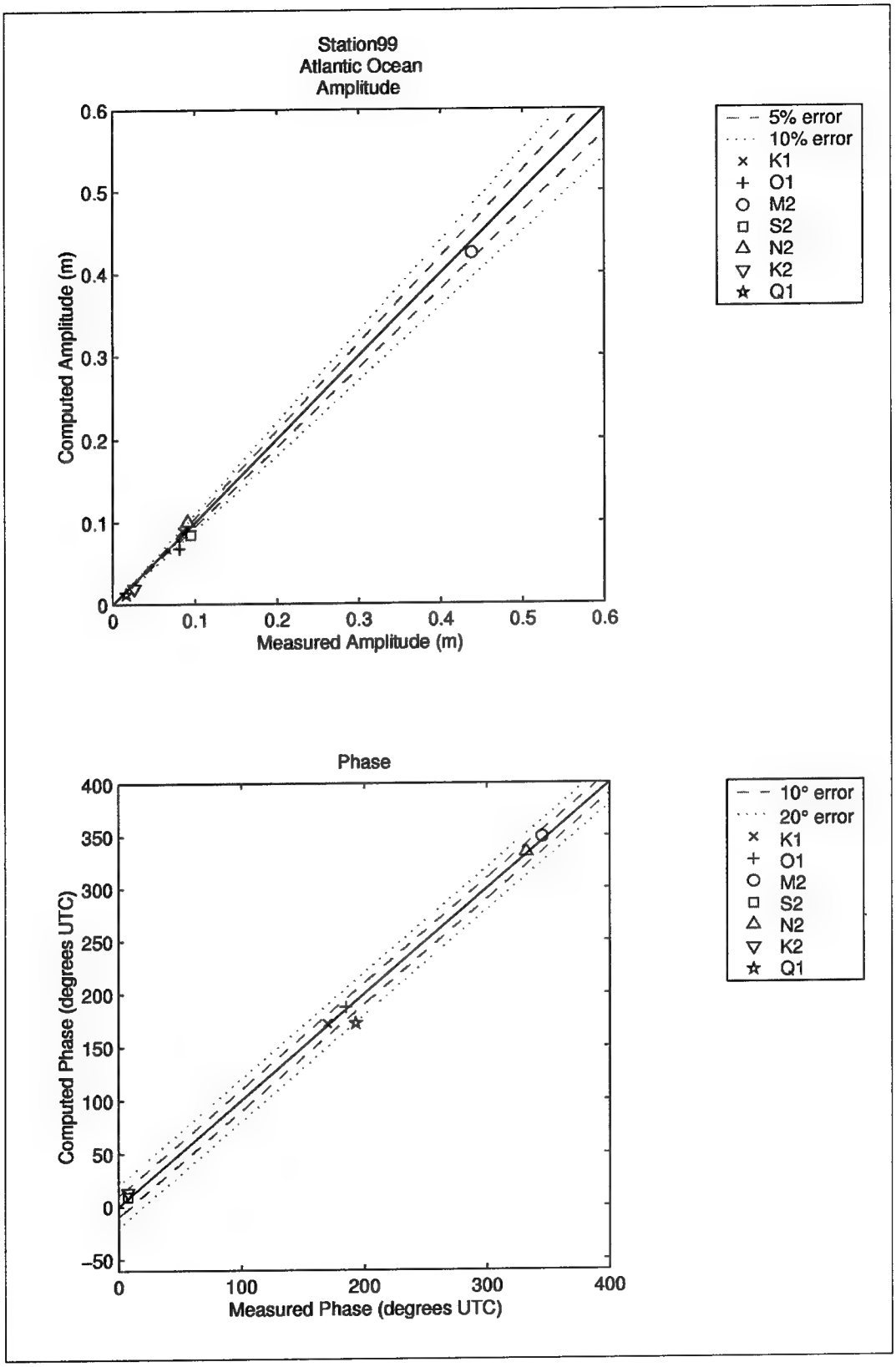

Figure 130. Computed vs. measured harmonic constituents at sta 99

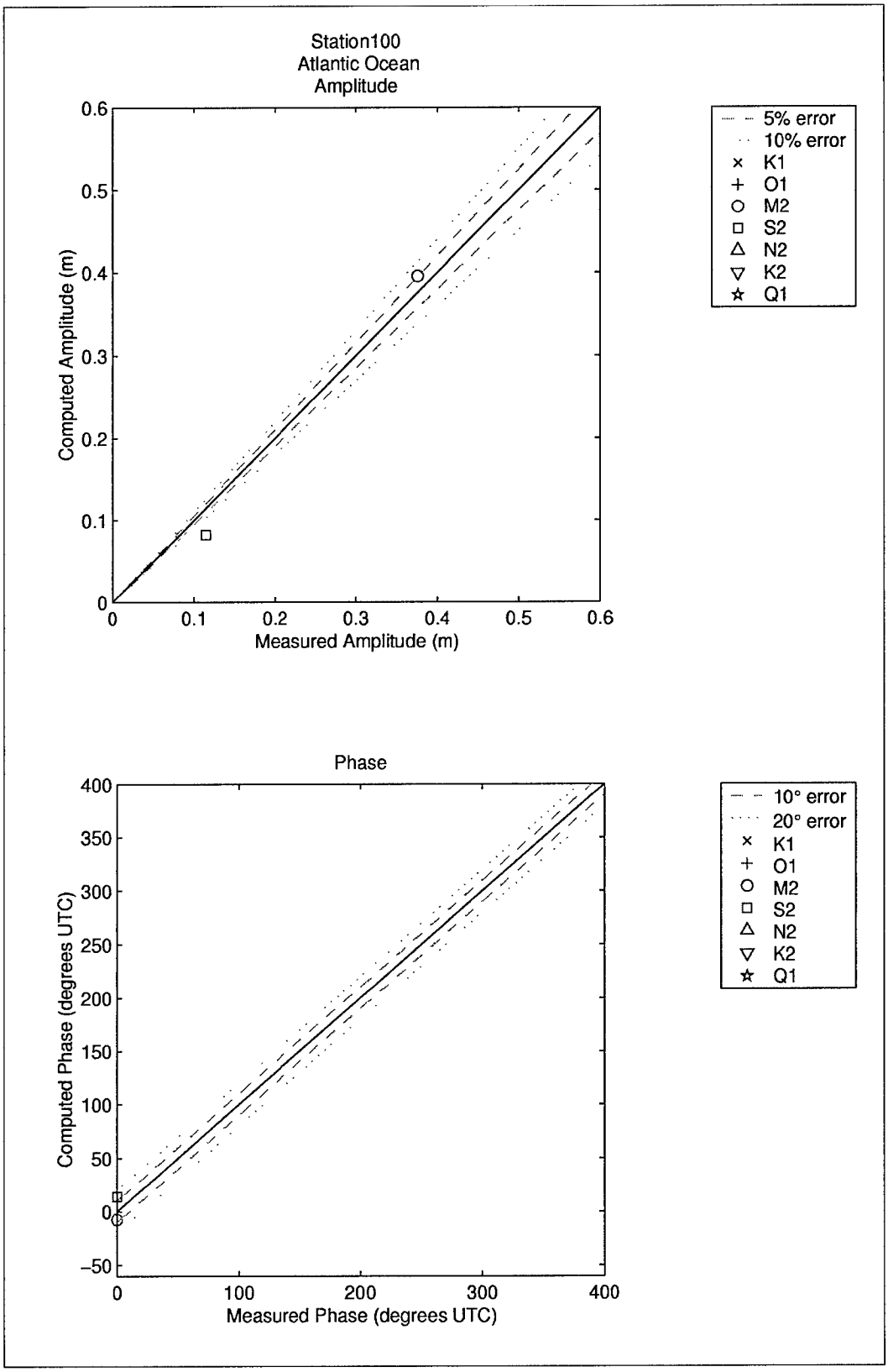

Figure 131. Computed vs. measured harmonic constituents at sta 100

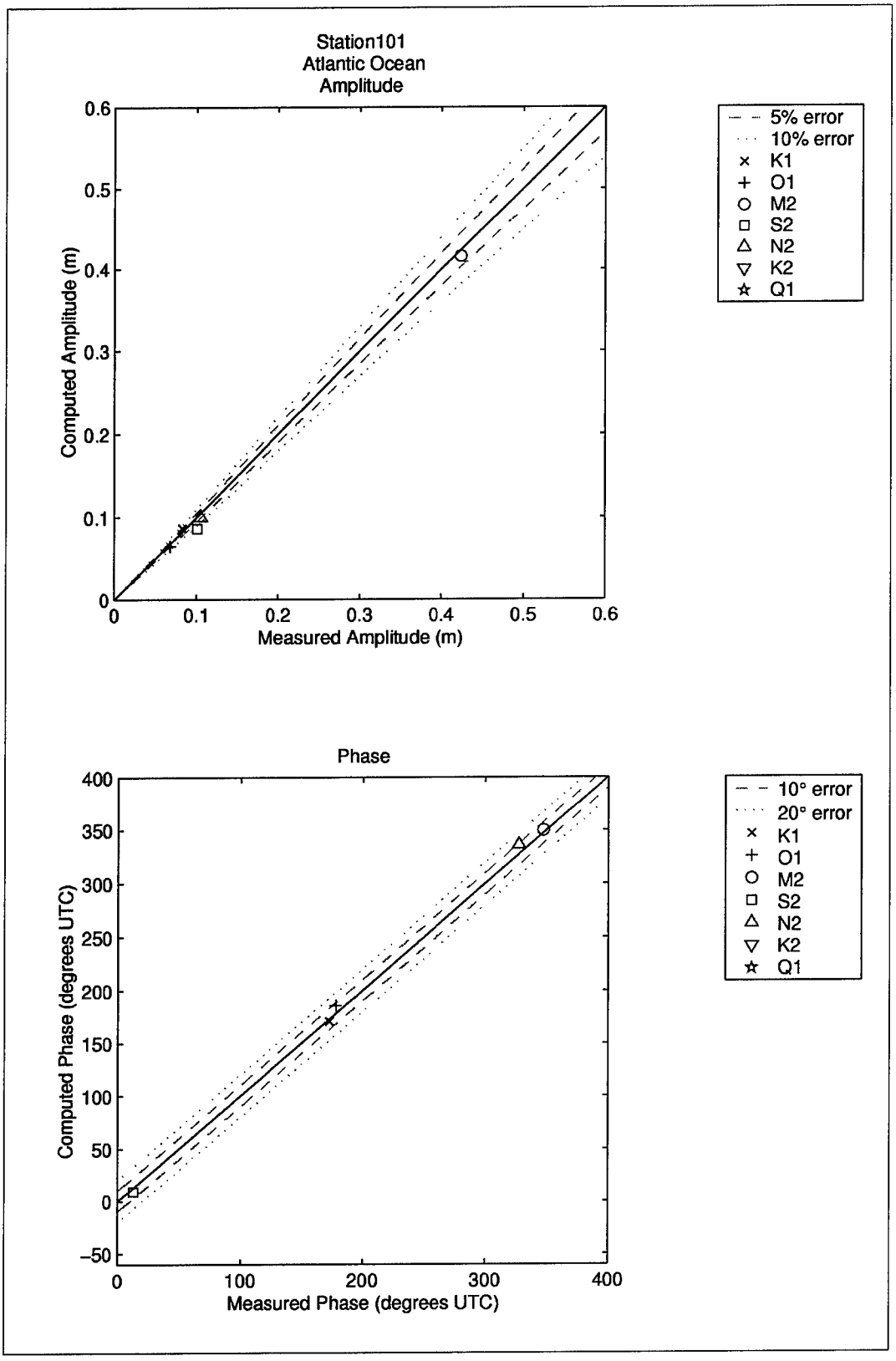

Figure 132. Computed vs. measured harmonic constituents at sta 101

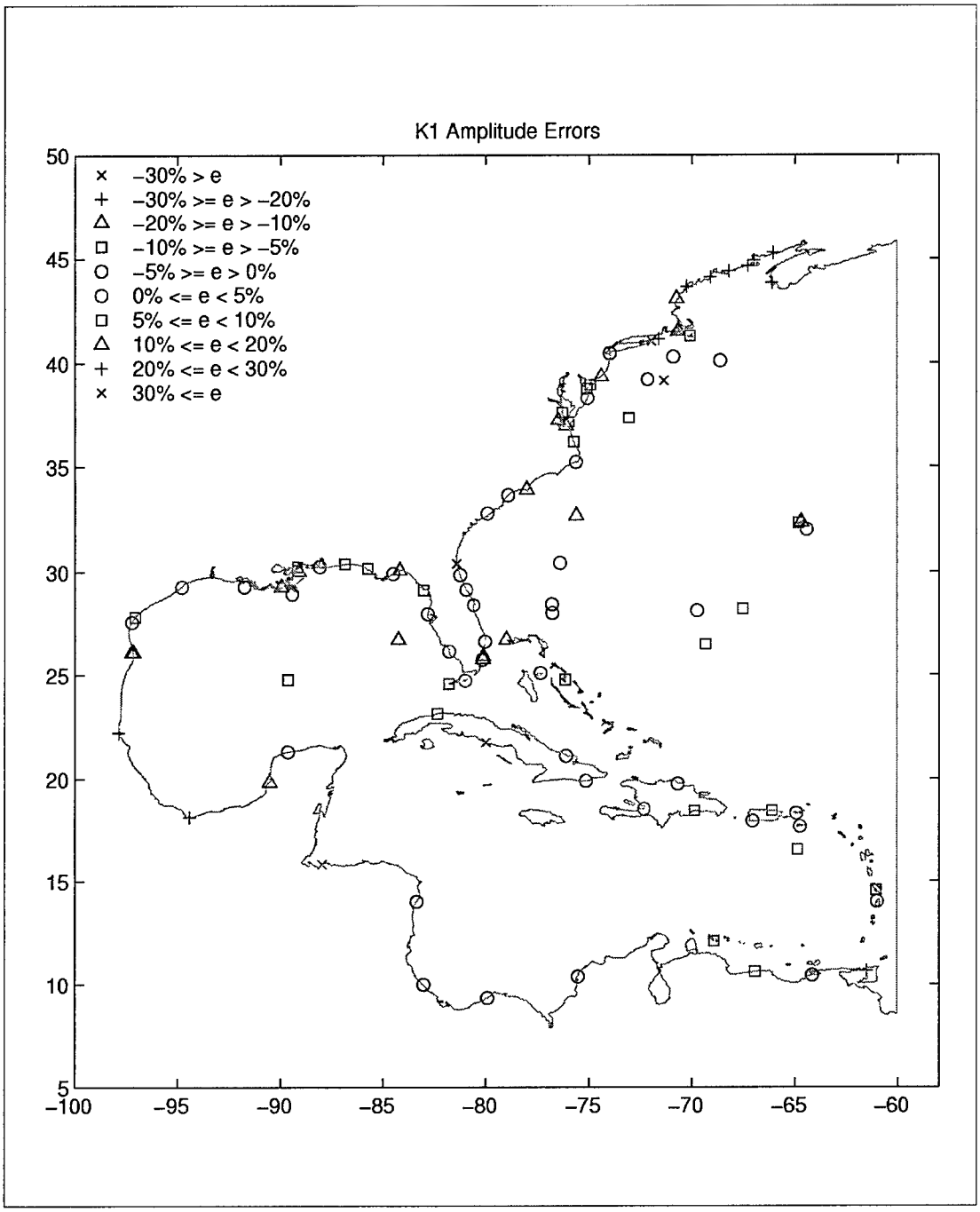

Figure 133. Distribution of K_1 amplitude error at stations

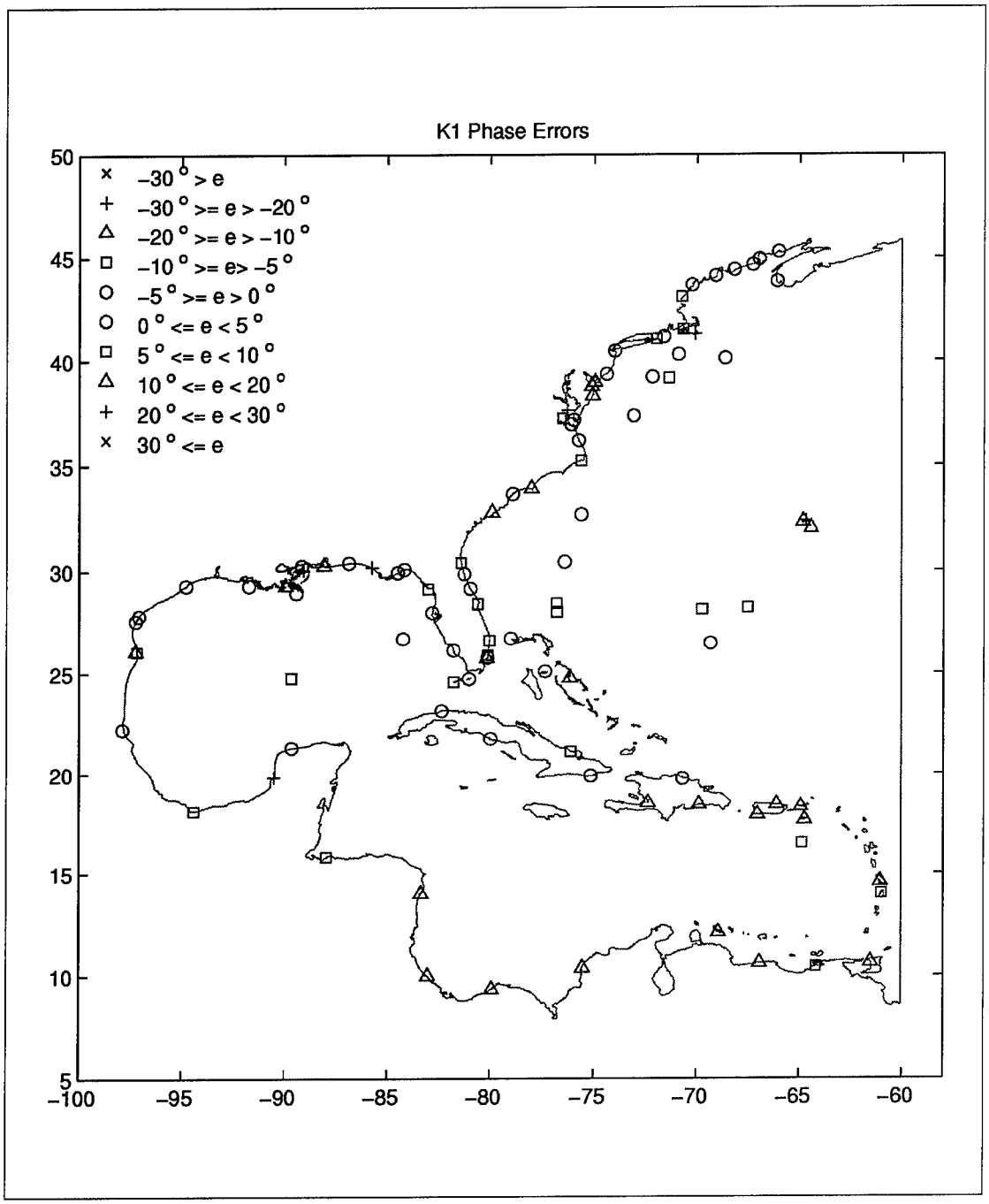

Figure 134. Distribution of K_1 phase errors at station

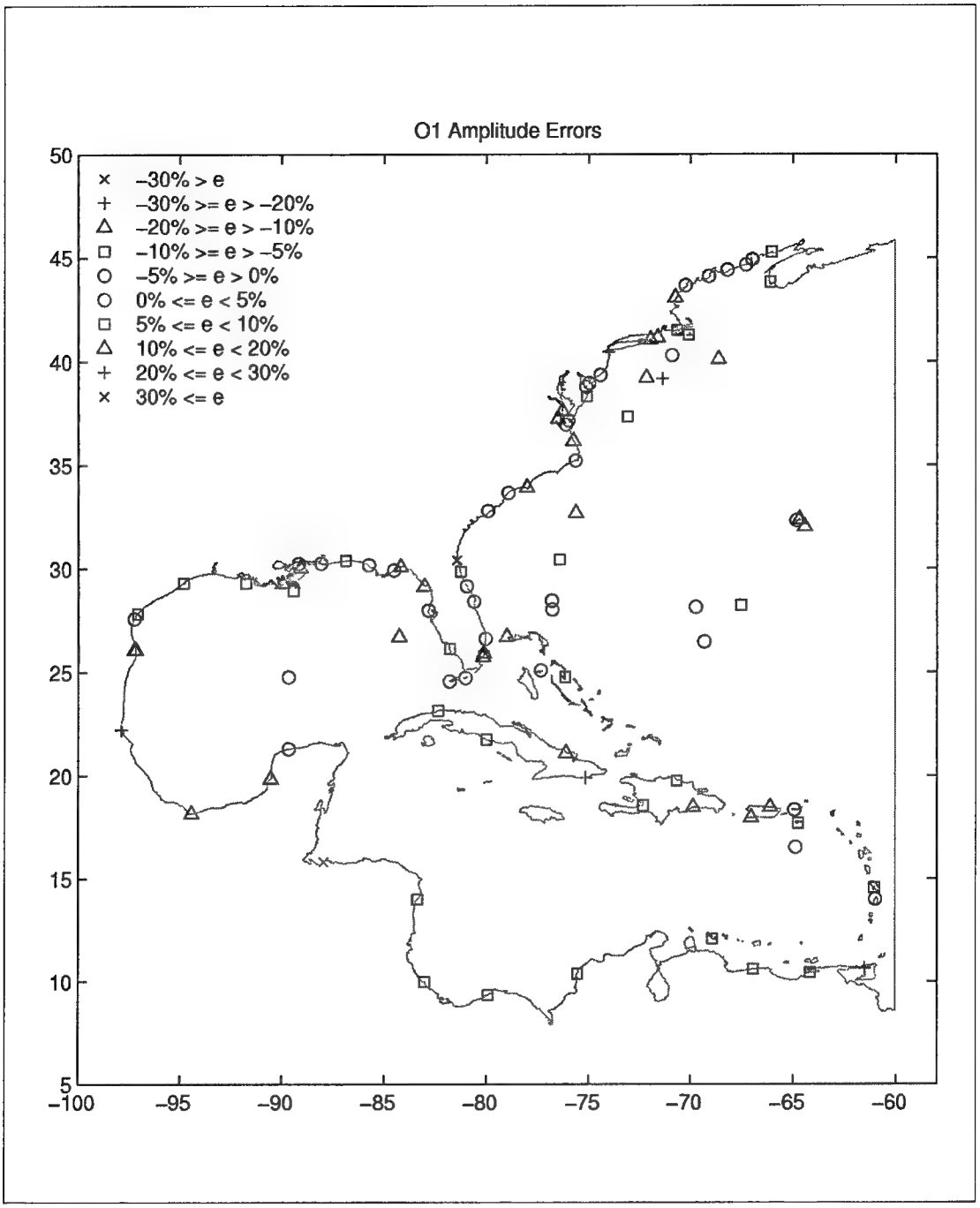

Figure 135. Distribution of O_1 amplitude errors at stations

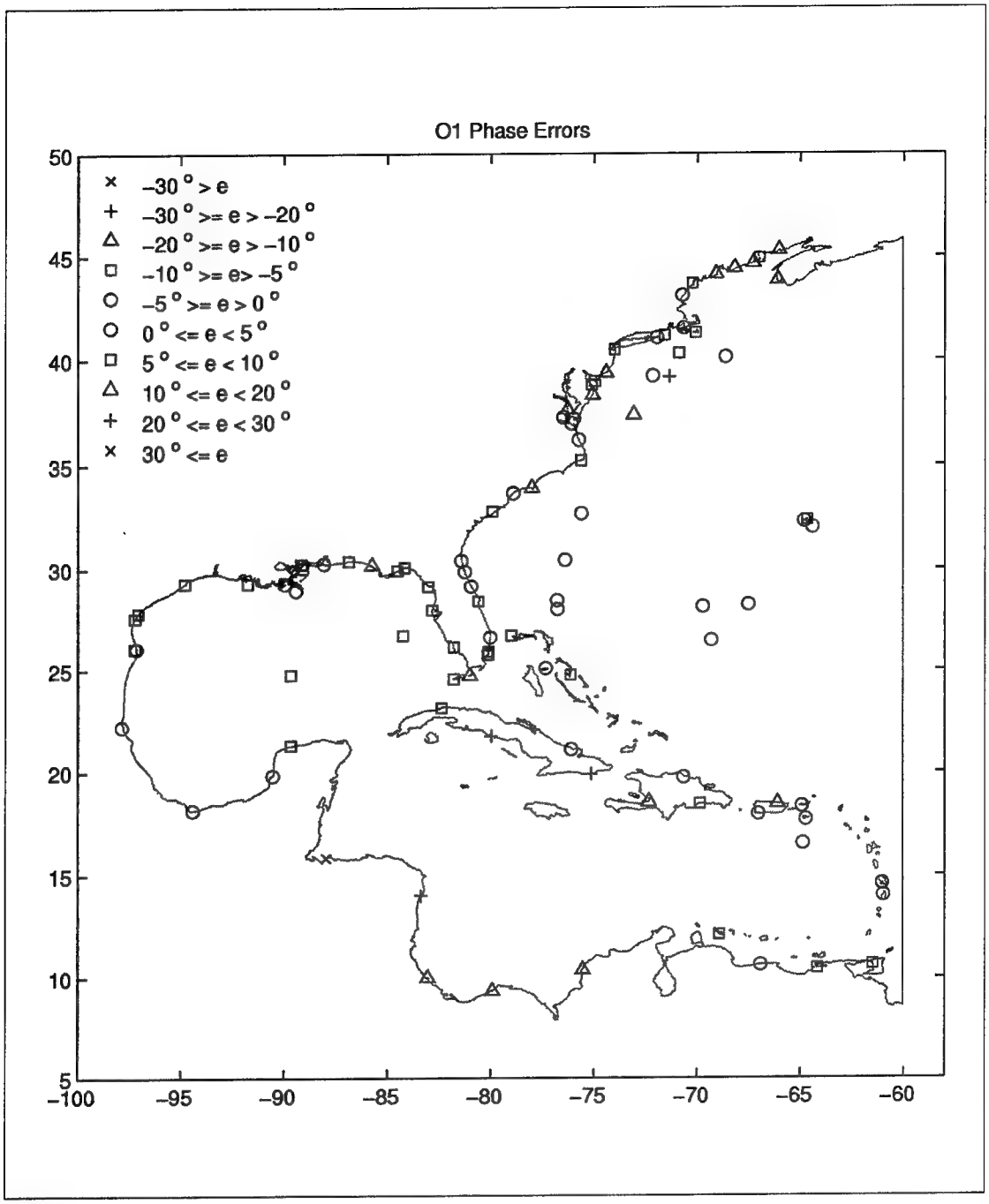

Figure 136. Distribution of O_1 phase errors at stations

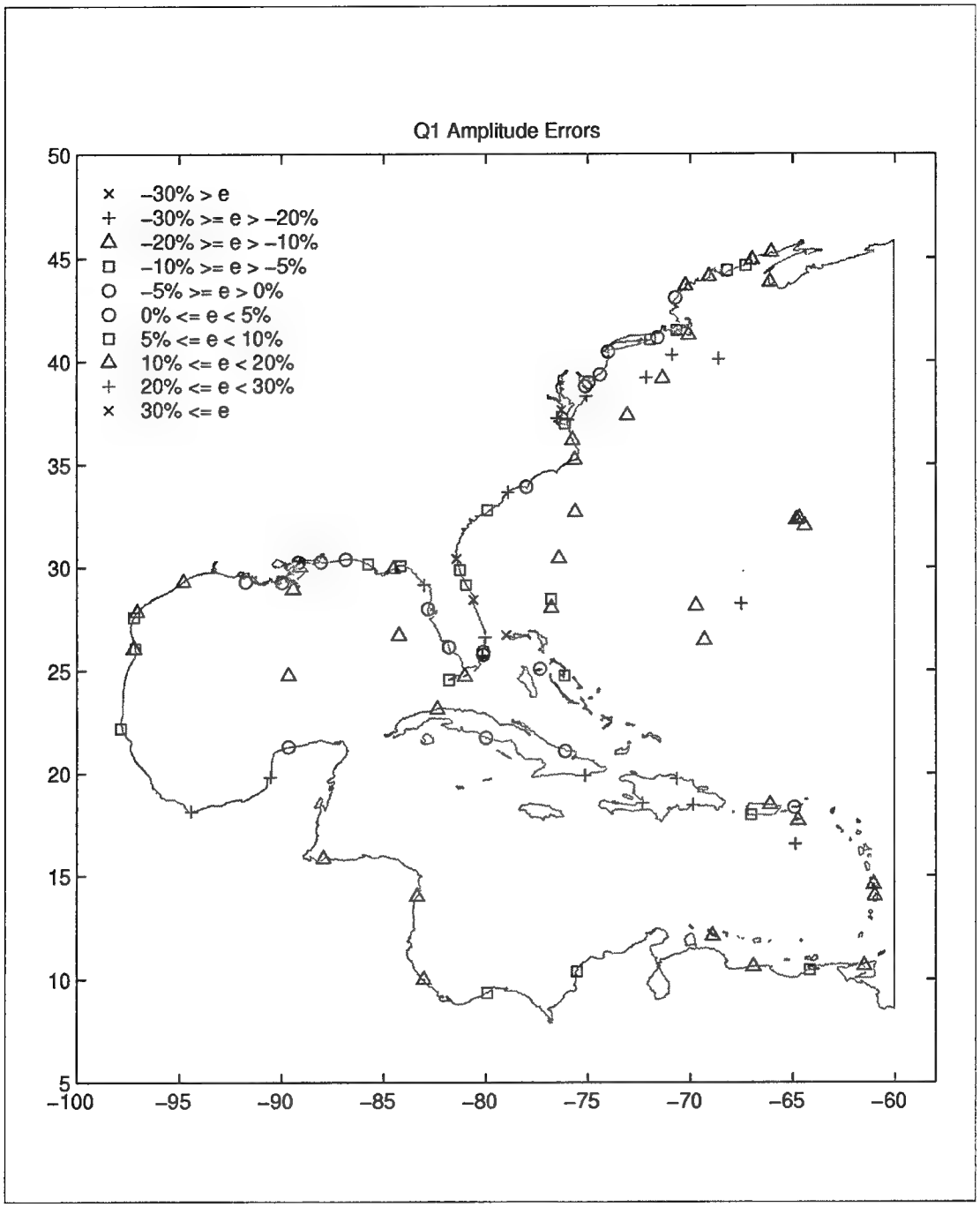

Figure 137. Distribution of Q_1 amplitude errors at stations

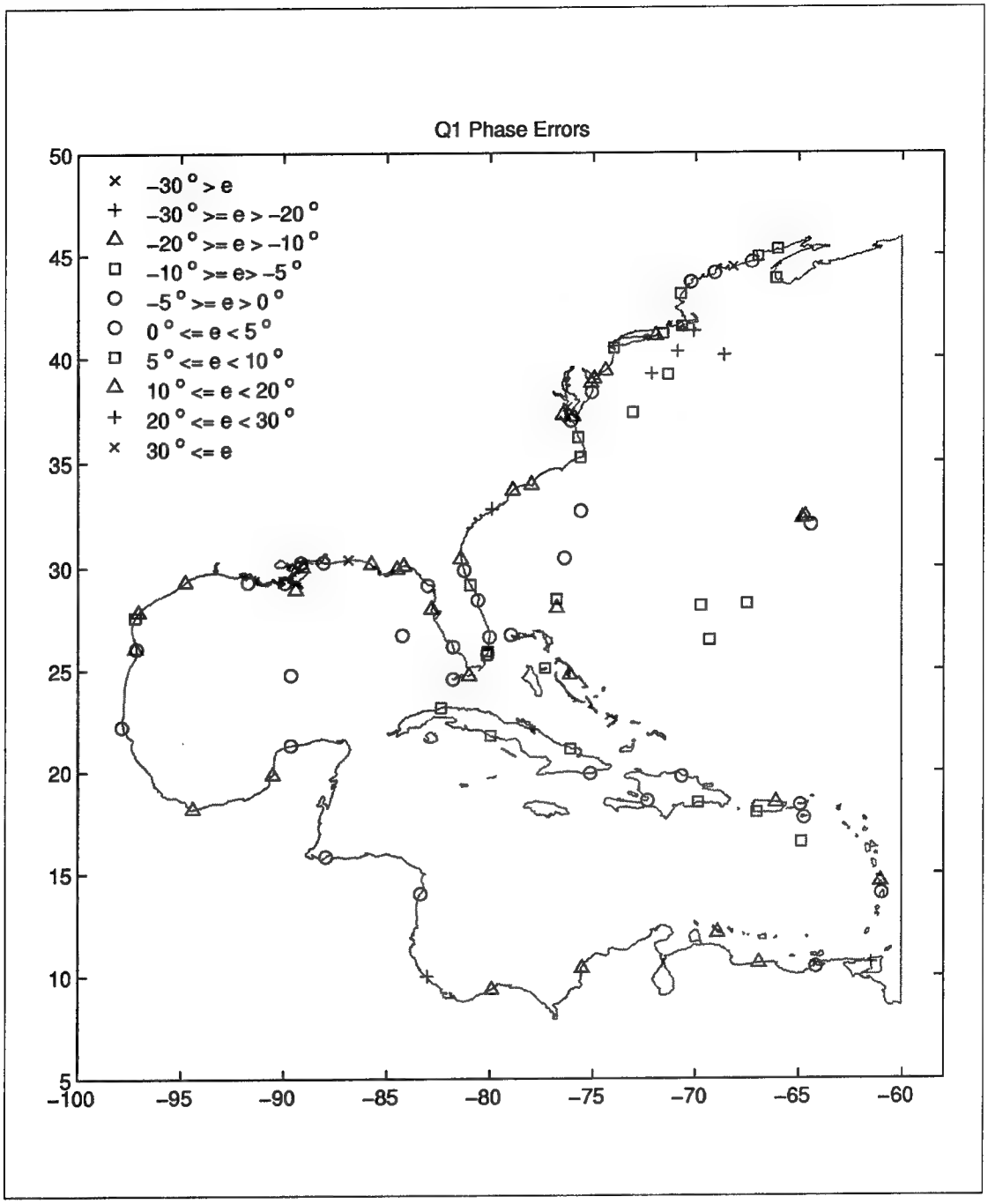

Figure 138. Distribution of Q_1 phase errors at stations

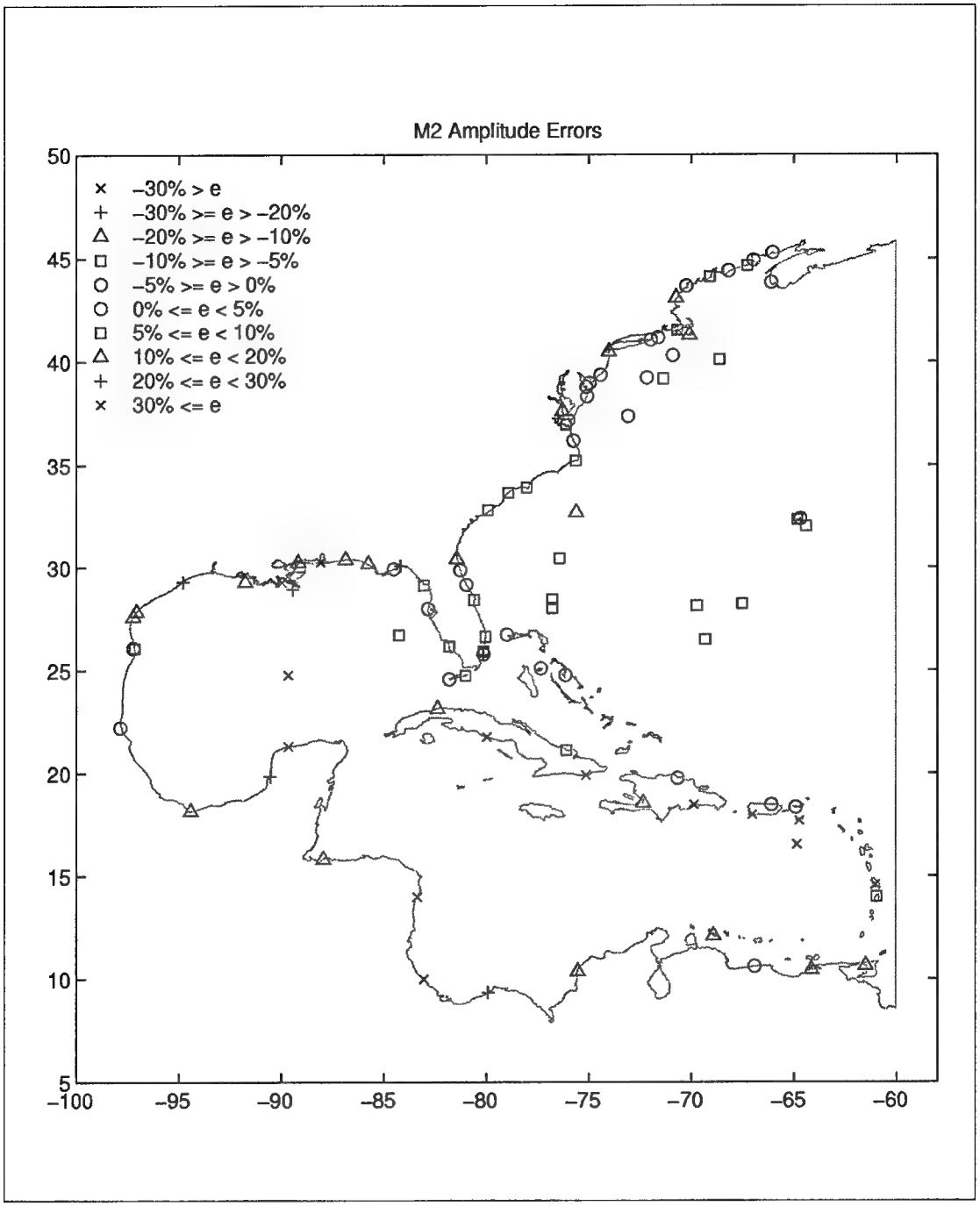

Figure 139. Distribution of M_2 amplitude errors at stations

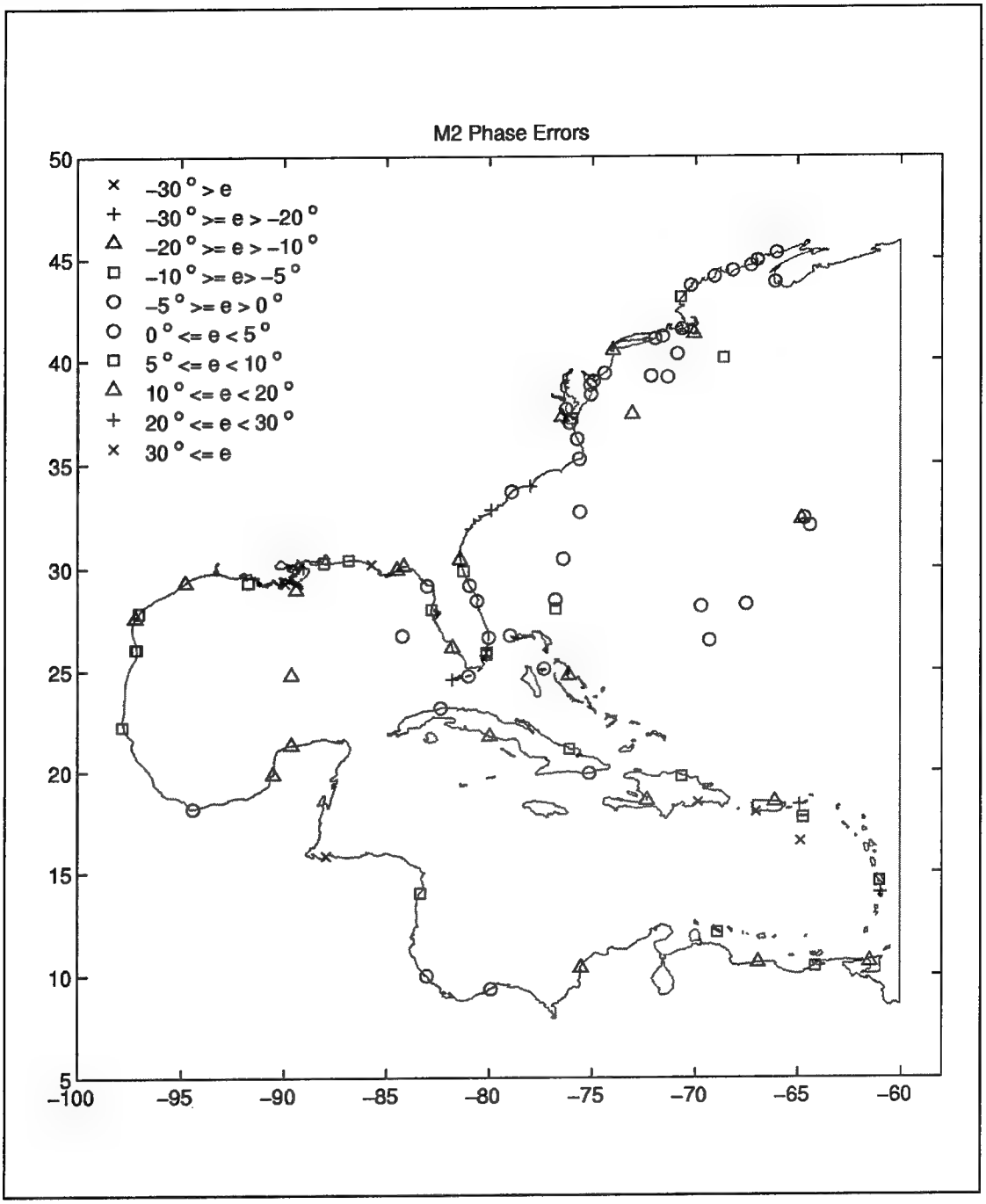

Figure 140. Distribution of M_2 phase errors at stations

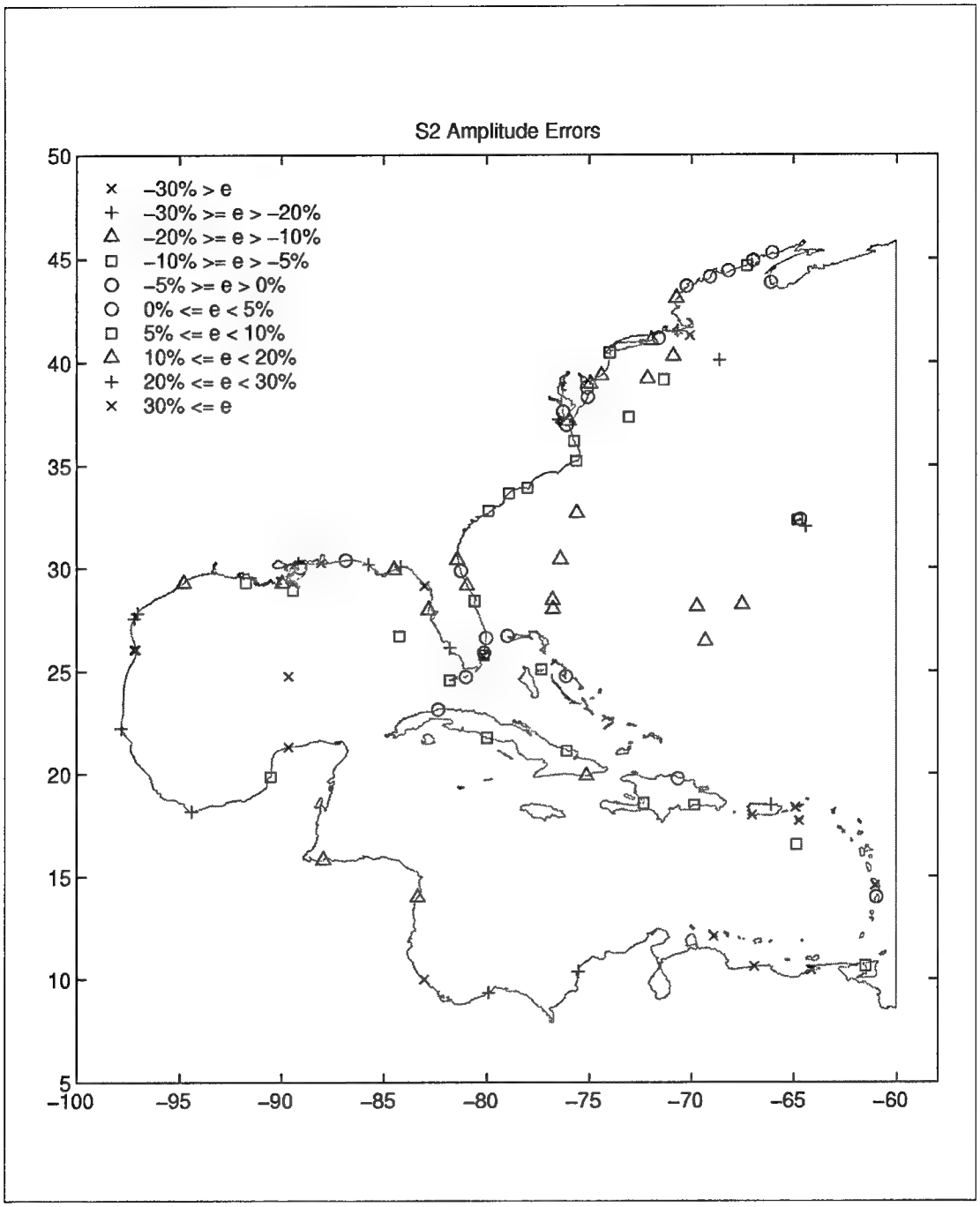

Figure 141. Distribution of S_2 amplitude errors at stations

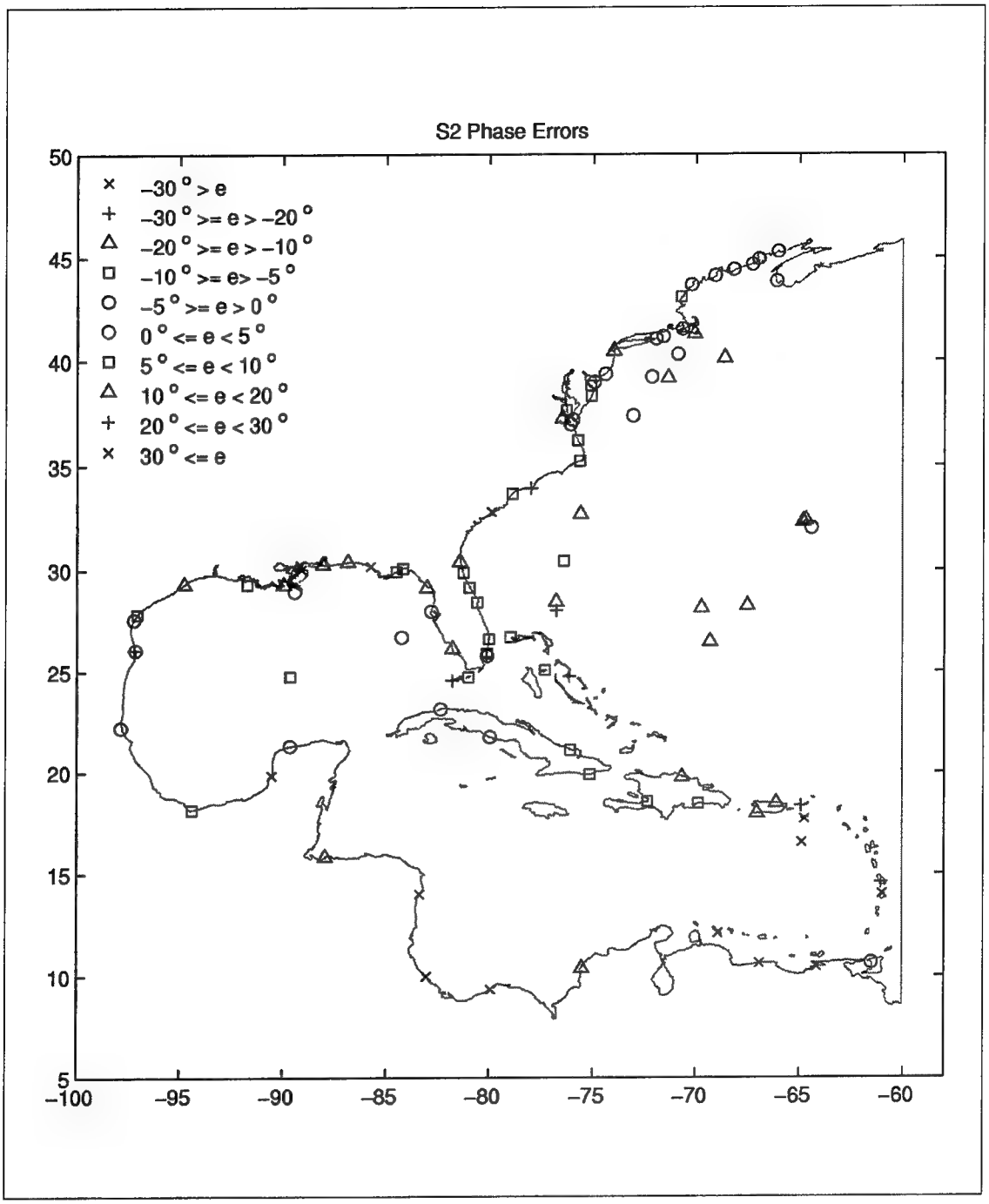

Figure 142. Distribution of S_2 phase errors at stations

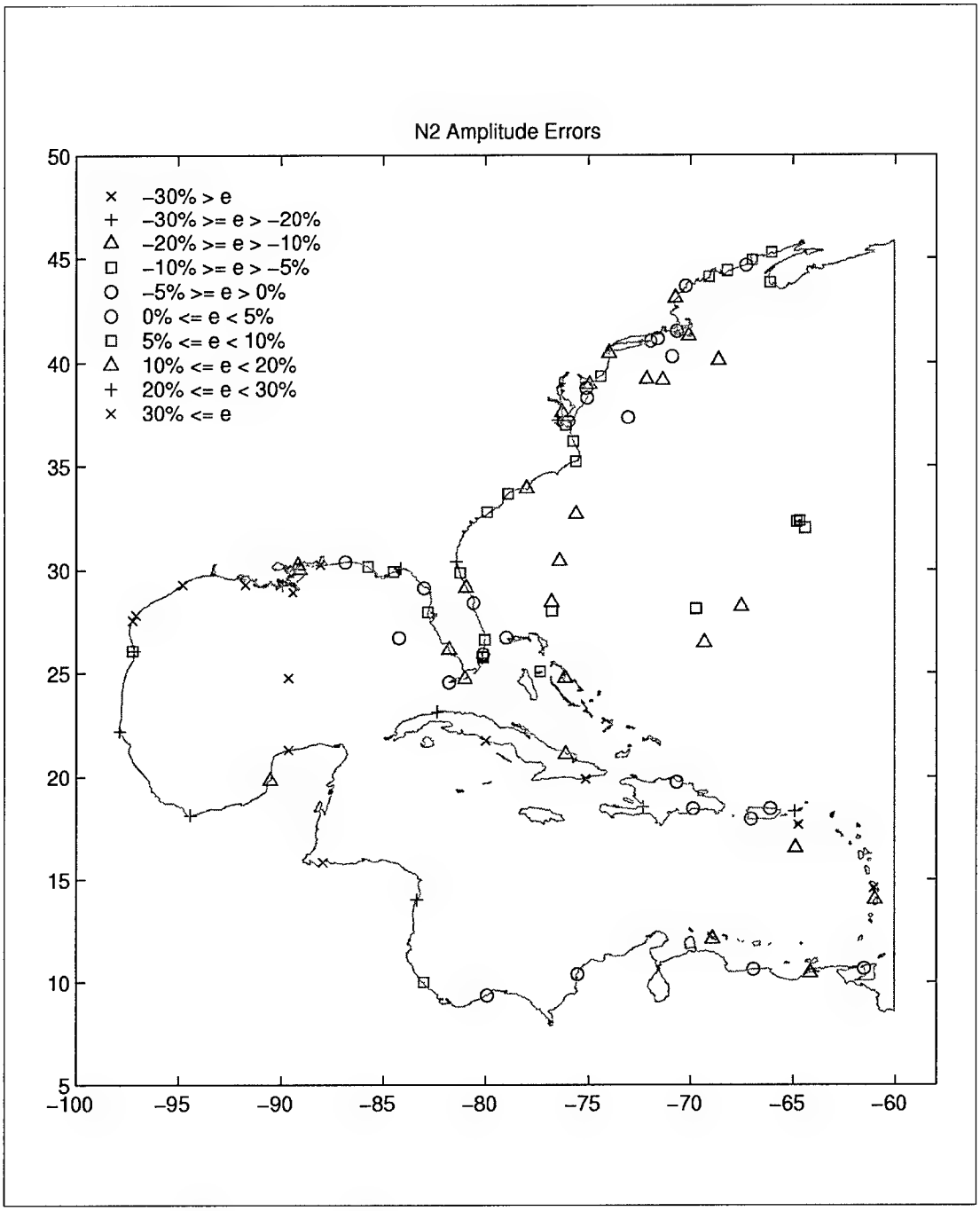

Figure 143. Distribution of N_2 amplitude errors at stations

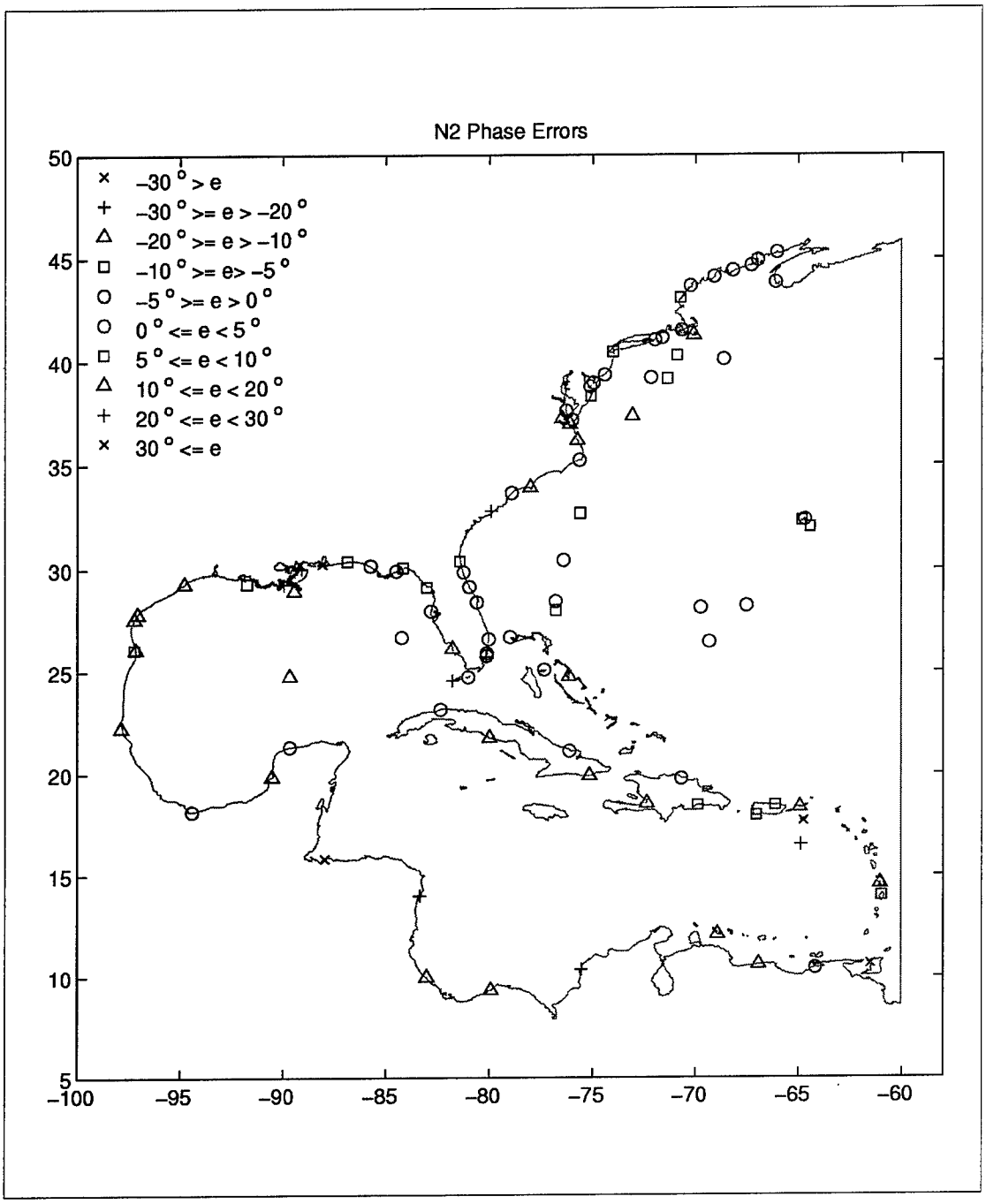

Figure 144. Distribution of N_2 phase errors at stations

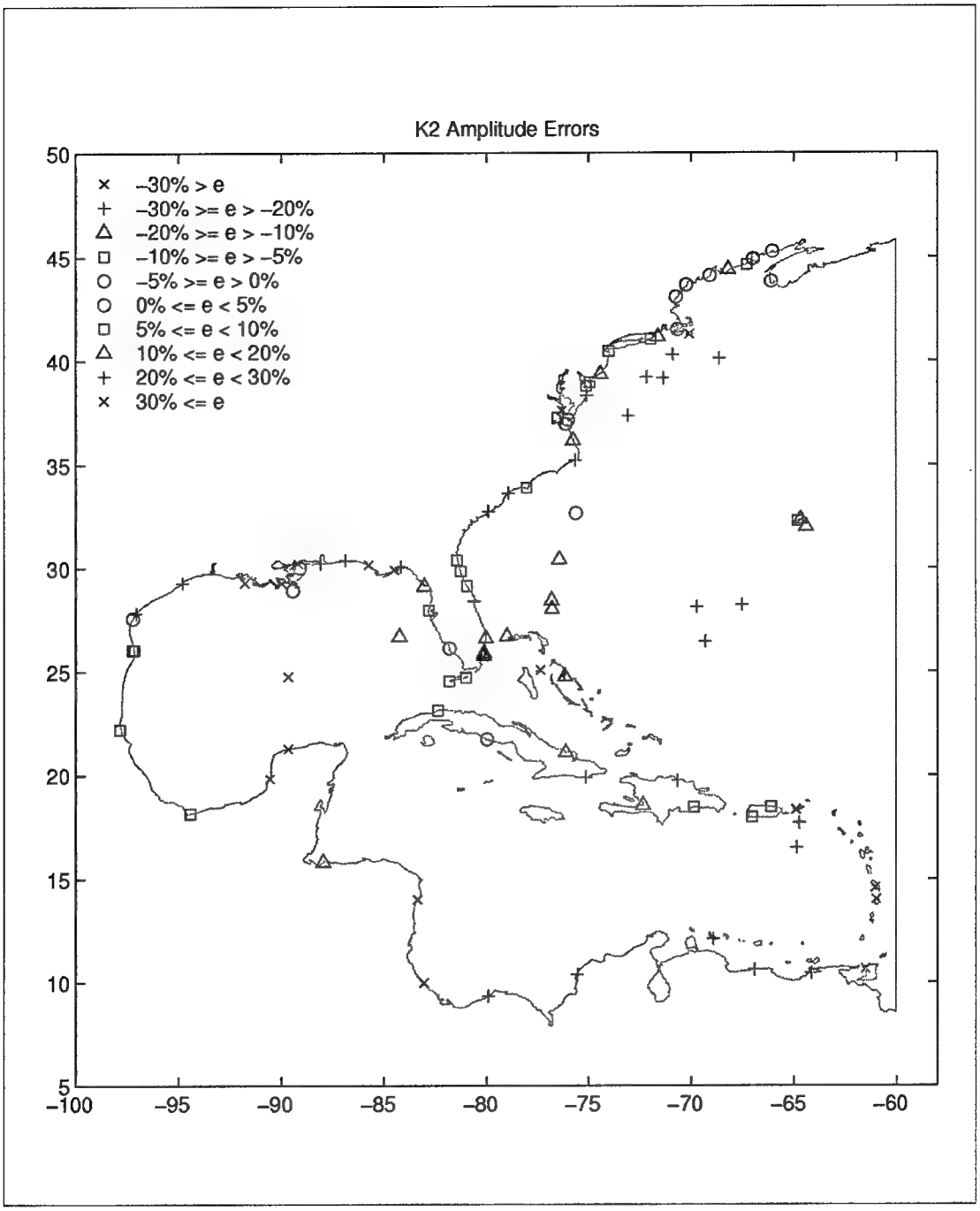

Figure 145. Distribution of K_2 amplitude errors at stations

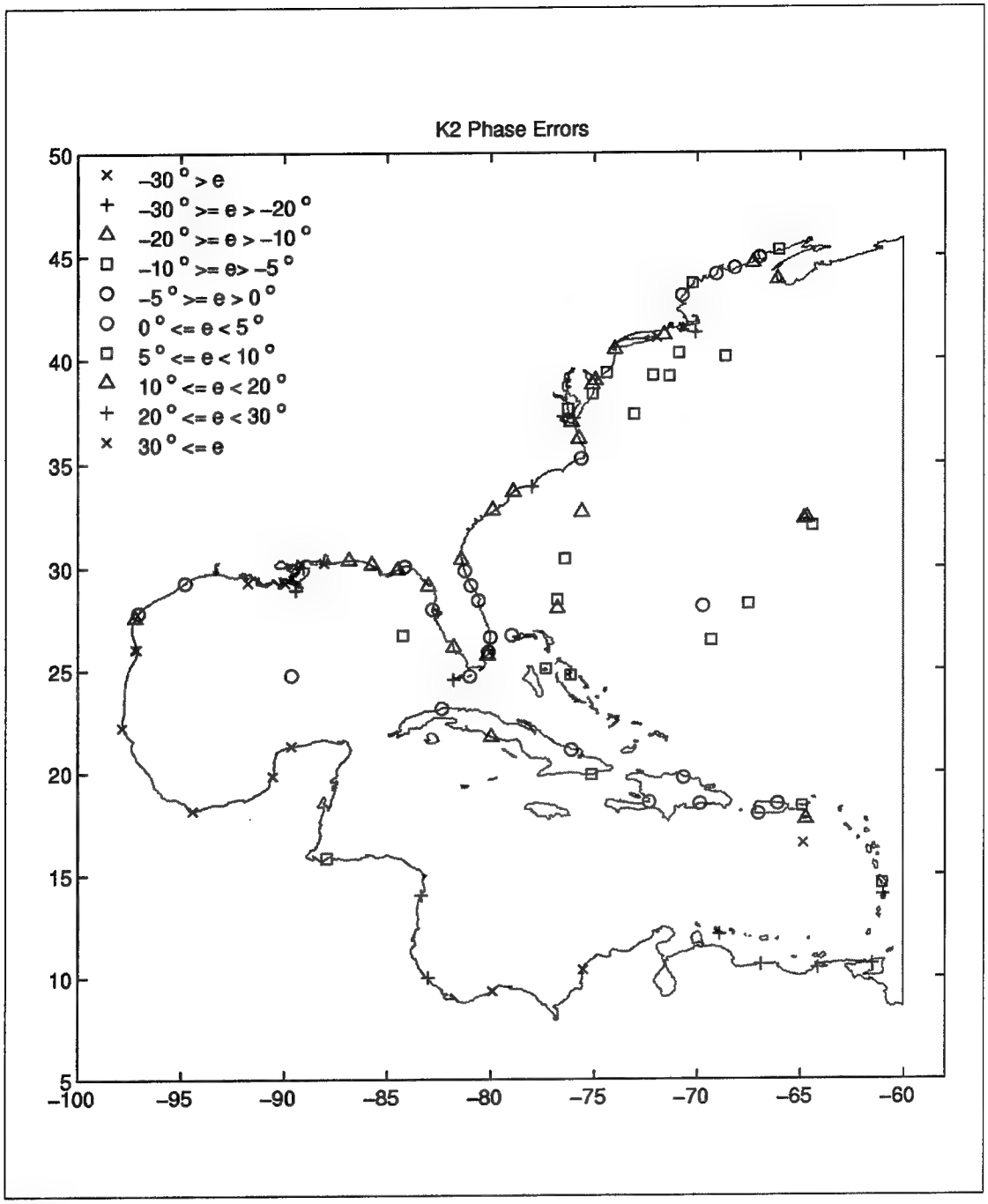

Figure 146. Distribution of K_2 phase errors at stations

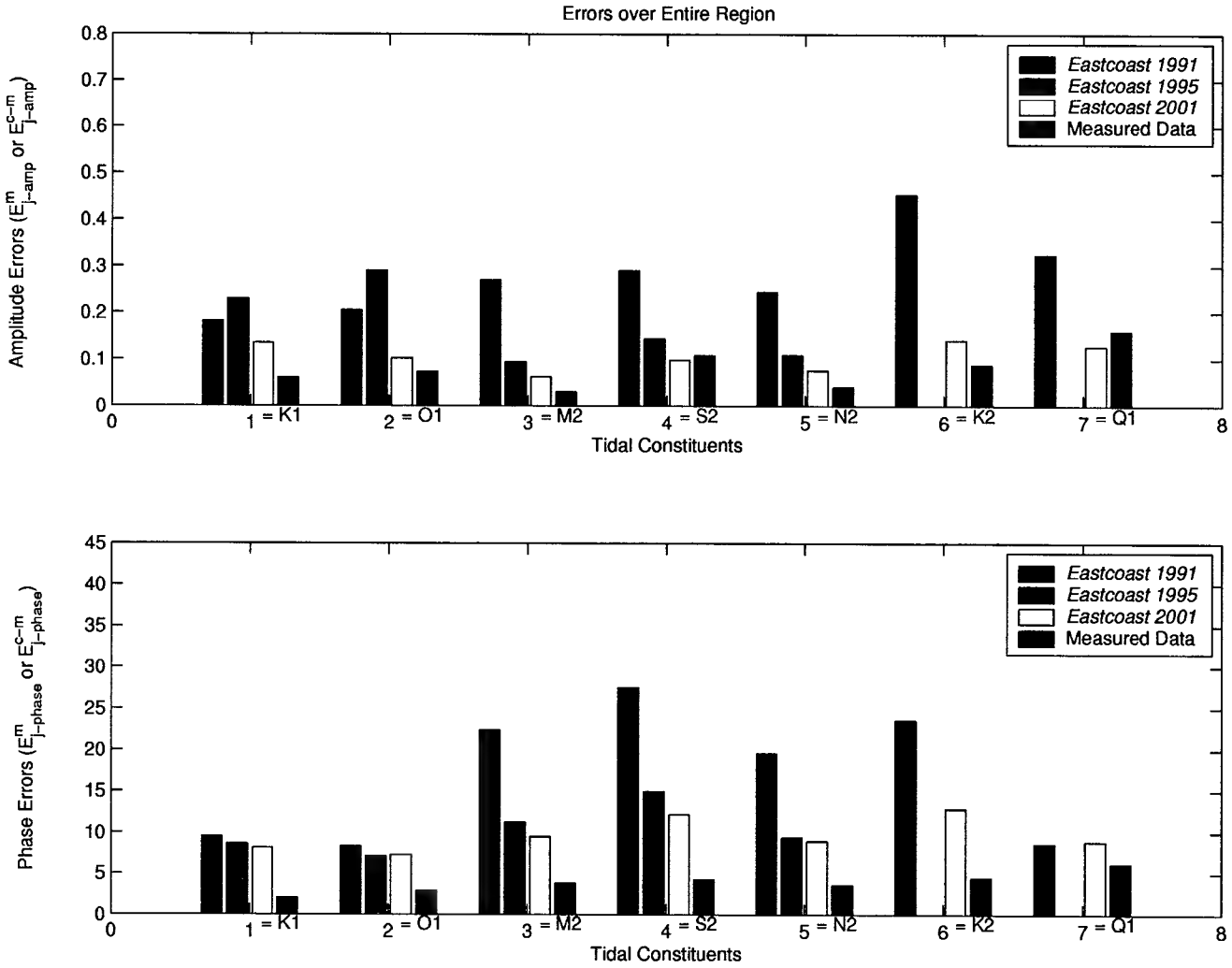

Figure 147. Harmonic constituent error comparison between databases over entire domain

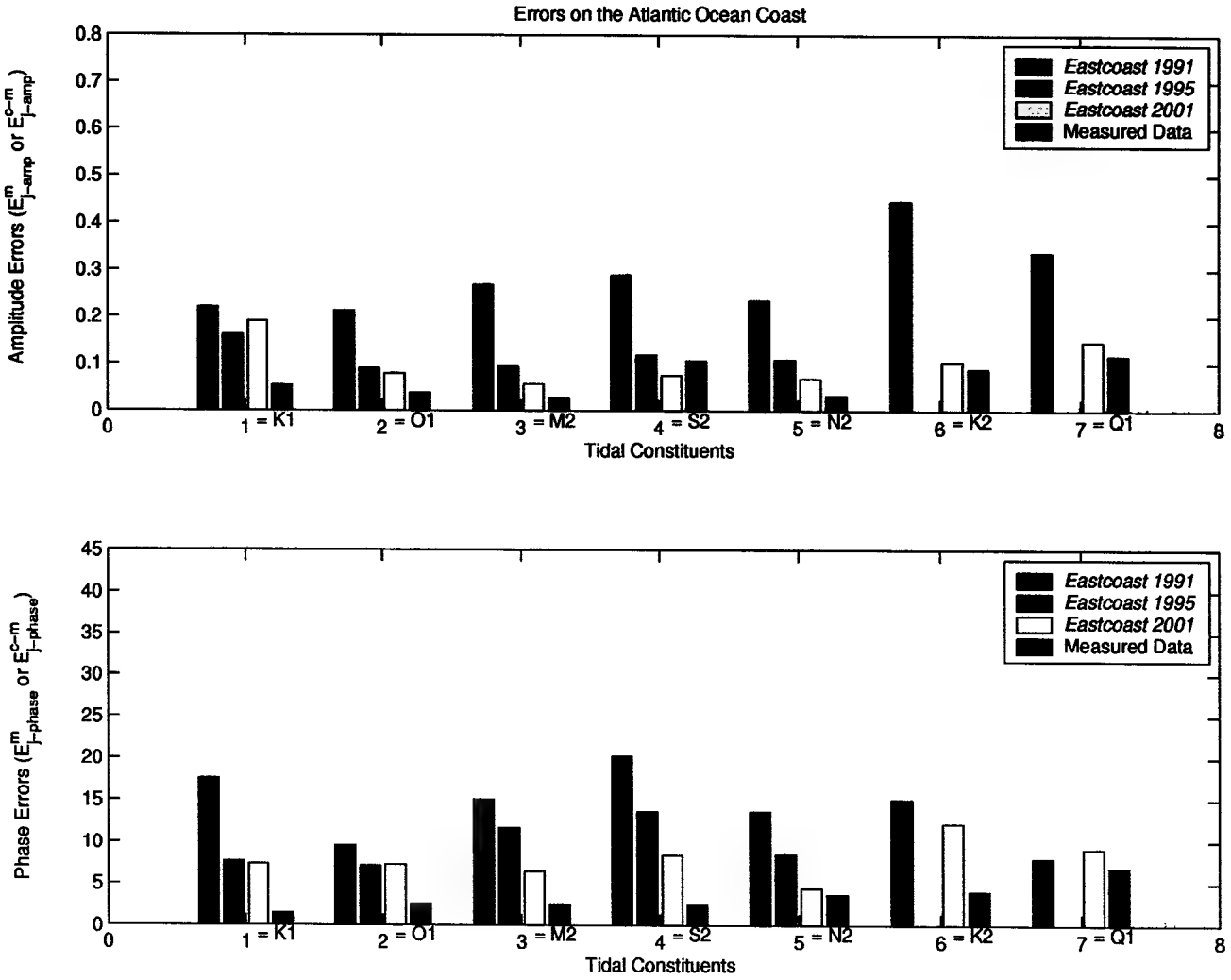

Figure 148. Harmonic constituent error comparison between databases for Atlantic Coast stations

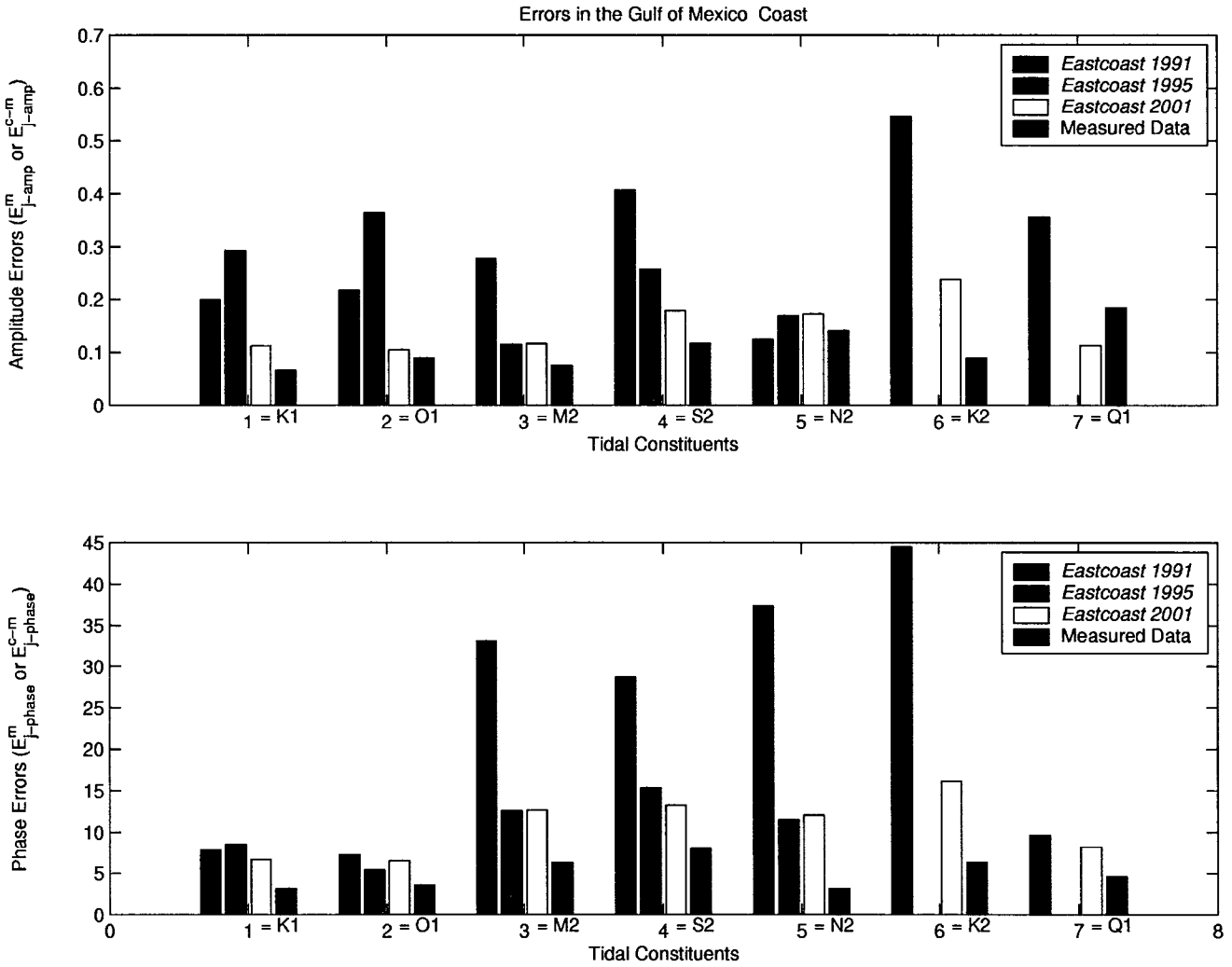

Figure 149. Harmonic constituent error comparison between databases for Gulf of Mexico stations

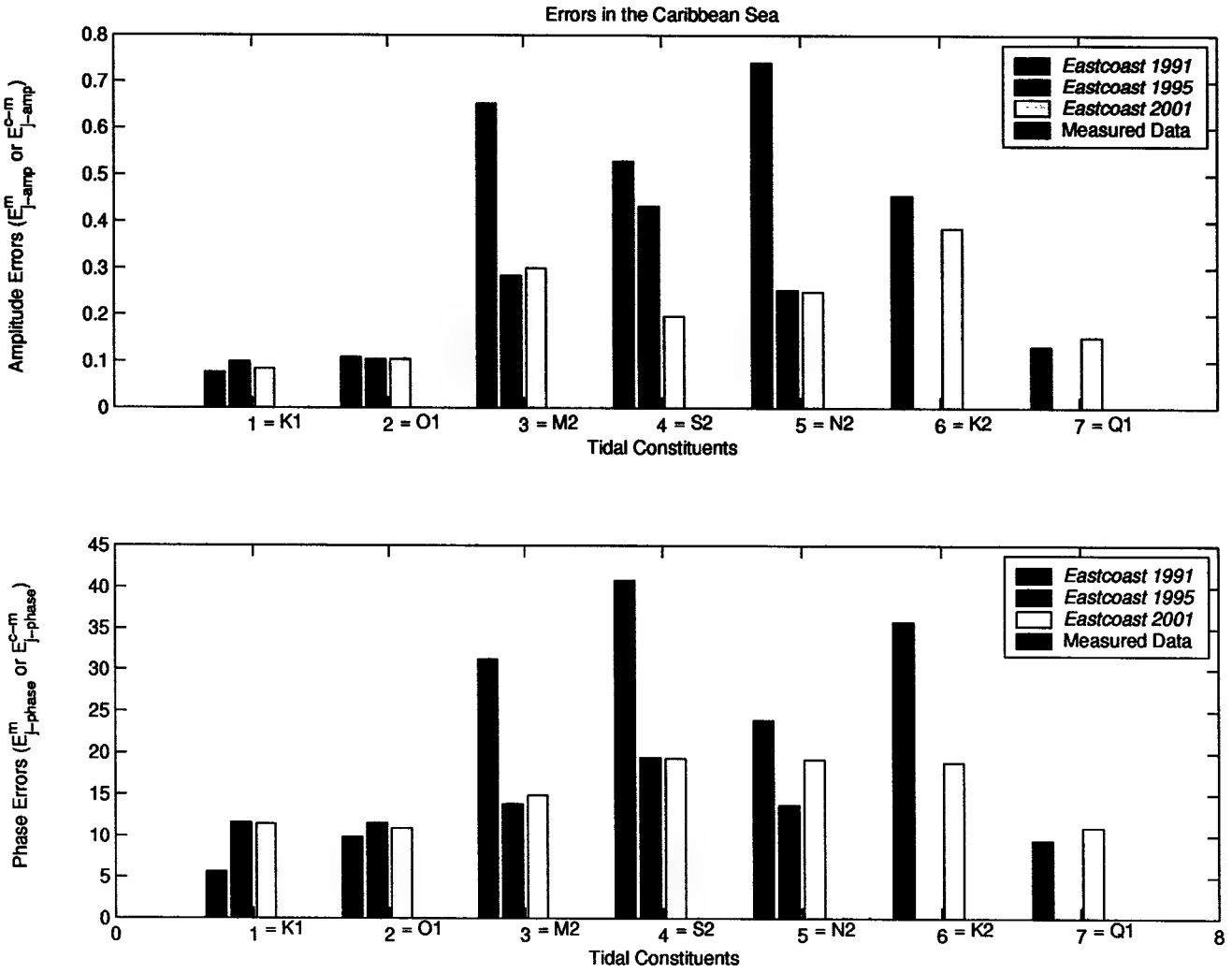

Figure 150. Harmonic constituent error comparison between databases for Caribbean Sea stations

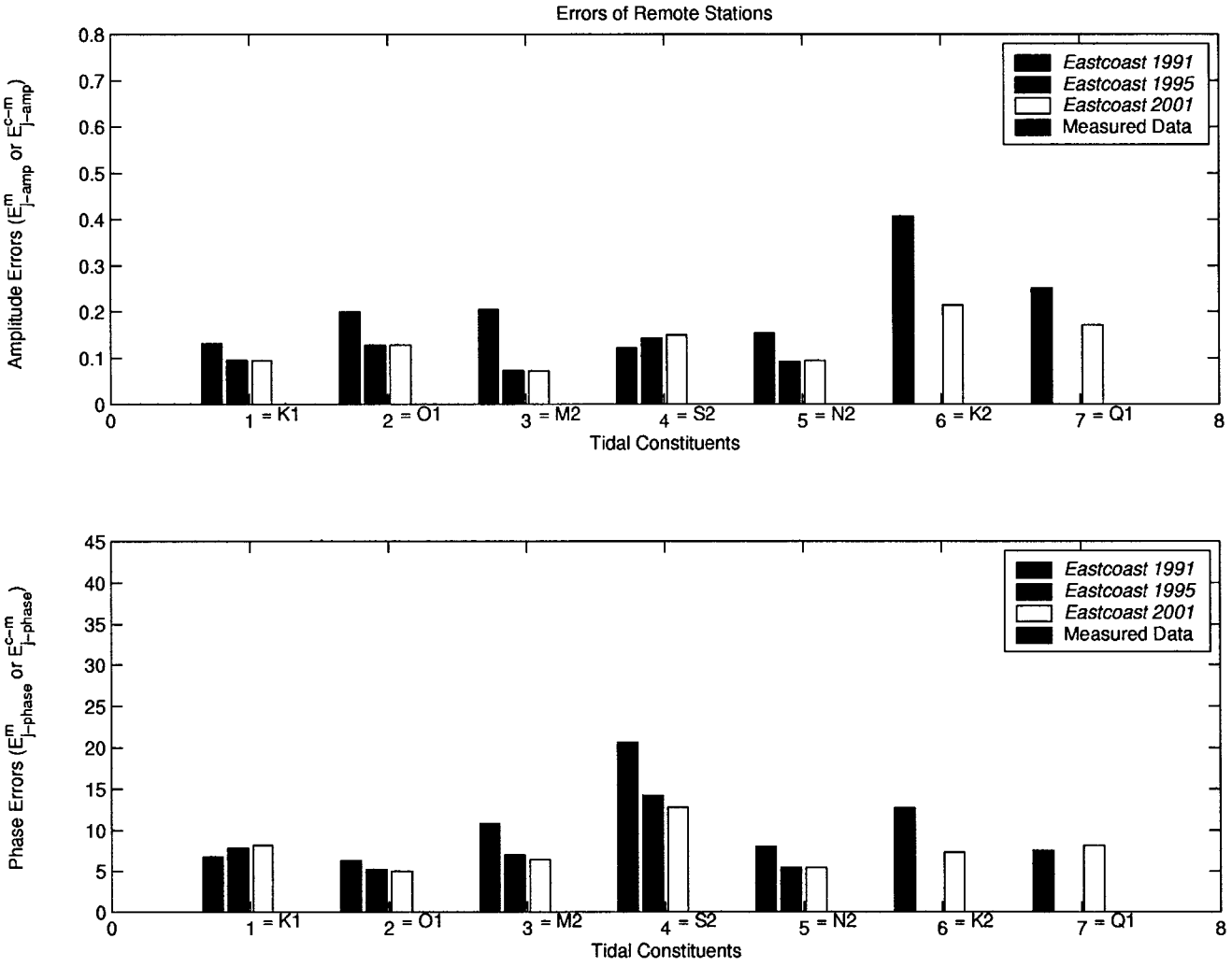

Figure 151. Harmonic constituent error comparison between databases for remote stations

Table 1
Tidal Potential Constants for Principal Tidal Constituents and Associated Effective Earth Elasticity Factor

Species, j	n	Constituent		T_{jn} (h)	C_{nj} (m)	α_{jn}
1	1	K_1	Luni-solar	23.934470	0.141565	0.736
	2	O_1	Principal lunar	25.819342	0.100514	0.695
	3	Q_1	Elliptical lunar	26.868357	0.019256	0.695
2	1	M_2	Principal lunar	12.420601	0.242334	0.693
	2	S_2	Principal solar	12.000000	0.112841	0.693
	3	N_2	Elliptical lunar	12.658348	0.046398	0.693
	4	K_2	Luni-solar	11.967235	0.030704	0.693

Table 2
Station Location and Data Source Information[1]

Station No.	Station Name	Lat (deg)	Long (deg)	Source	Sub-domain	Distance (miles)[3]	Width (miles)
1	Yarmouth, Nova Scotia	43.833333	-66.116667	IHO	Atlantic	2.78	1.00
2	St John, New Brunswick	45.266667	-66.050000	IHO	Atlantic	1.00	0.03
3	Eastport Passama-quoddy Bay, ME	44.903333	-66.985000	NOS	Atlantic	5.40	2.40
4	Cutler Naval Base, ME	44.641667	-67.296667	NOS	Atlantic	4.25	2.00
5	Bar Harbor, ME	44.400000	-68.200000	IHO[2]	Atlantic	5.50	4.11
6	Rockland, ME	44.105000	-69.101667	IHO[2]	Atlantic	4.00	5.00
7	Portland, ME	43.656667	-70.246667	NOS	Atlantic	3.30	0.56
8	Portsmouth, NH	43.080000	-70.741667	IHO	Atlantic	3.44	1.60
9	Woods Hole, MA	41.513333	-70.670000	IHO[2]	Atlantic	3.00	9.80
10	Nantucket Island, MA	41.286667	-70.095000	NOAA[2]	Atlantic	13.00	9.93
11	Block Island, RI	41.158333	-71.613333	NOS	Atlantic	--	--
12	Montauk, NY	41.050000	-71.966667	IHO[2]	Atlantic	15.60	13.30
13	Sandy Hook, NJ	40.468333	-74.011667	IHO[2]	Atlantic	4.00	5.30
14	Atlantic City, NJ	39.351667	-74.418333	IHO[2]	Atlantic	--	--
15	Cape May Ferry Terminal, NJ	38.968333	-74.960000	IHO[2]	Atlantic	3.00	10.80
16	Lewes, DE	38.781667	-75.120000	NOS	Atlantic	2.45	11.30
17	Kiptopeke, VA	37.166667	-75.988333	NOS	Atlantic	6.00	12.20
18	Windmill Point, VA	37.615000	-76.290000	NOS	Atlantic	--	--
19	Gloucester Point, VA	37.246667	-76.500000	NOS	Atlantic	7.00	2.23
20	Fishing Pier Ocean City, MD	38.323333	-75.085000	NOAA[2]	Atlantic	--	--
21	Chesapeake Bay, VA	36.966667	-76.113333	NOAA[2]	Atlantic	14.30	6.67
22	Duck Pier, NC	36.181667	-75.750000	NOAA[2]	Atlantic	--	--
23	Cape Hatteras Fishing Pier, NC	35.223333	-75.635000	NOS	Atlantic	--	--
24	Southport, NC	33.915000	-78.016667	IHO	Atlantic	3.03	1.20
25	Springmaid Pier, SC	33.655000	-78.918333	NOS	Atlantic	--	--
26	Charleston, SC	32.783333	-79.916667	IHO[2]	Atlantic	4.28	1.48

[1] Distance from open water and width of narrowest connection to open water are also listed.
[2] Sources were updated with current measured NOS data.
[3] To convert miles to kilometers, multiply number of miles by 1.609347.

Table 2 (Continued)

Station No.	Station Name	Lat (deg)	Long (deg)	Source	Sub-domain	Distance (miles)	Width (miles)
27	Mayport, FL	30.400000	-81.433333	IHO[2]	Atlantic	1.00	
28	St. Augustine Beach, FL	29.856667	-81.263333	NOS	Atlantic	--	0.44
29	Daytona Beach (ocean), FL	29.146667	-80.963333	NOS	Atlantic	--	--
30	Canaveral Harbor Entrance, FL	28.408333	-80.600000	NOS	Atlantic	0.85	--
31	Lake Worth Pier, FL	26.611667	-80.033333	NOS	Atlantic	--	0.10
32	Haulover Pier, North Miami Beach, FL	25.903333	-80.120000	NOS	Atlantic	--	--
33	Miami Harbour, FL	25.768333	-80.130000	IHO[2]	Atlantic	2.10	--
34	Virginia Key, FL	25.731667	-80.161667	NOS	Atlantic	--	0.56
35	Key Colony Beach, FL	24.718333	-81.018333	NOS	GOM	--	--
36	Key West, FL	24.550000	-81.800000	IHO[2]	GOM	--	--
37	Naples, FL	26.133333	-81.800000	IHO[2]	GOM	3.60	--
38	Clearwater Beach, FL	27.976667	-82.831667	NOS	GOM	--	0.08
39	Cedar Key, FL	29.133333	-83.031667	IHO[2]	GOM	--	--
40	St Marks Light, FL	30.066667	-84.183333	IHO[2]	GOM	--	--
41	Turkey Point, FL	29.915000	-84.511667	NOS	GOM	--	--
42	Alligator Bayou, FL	30.166667	-85.750000	IHO	GOM	5.92	--
43	Navarre Beach, FL	30.376667	-86.865000	NOS	GOM	--	0.25
44	Dauphin Island, AL	30.250000	-88.075000	NOS	GOM	0.16	--
45	Cat Island, MS	30.233333	-89.166667	IHO	GOM	4.40	3.25
46	Gulfport Harbor, Miss. Sound, MS	30.026667	-89.081667	NOS	GOM	--	6.30
47	Southwest Pass, LA	28.931667	-89.428333	IHO[2]	GOM	--	--
48	Grand Isle, East Point, LA	29.263333	-89.956667	NOS	GOM	26.20	--
49	Point au Fer, LA	29.286667	-91.750000	IHO	GOM	--	11.80
50	Galveston Pleasure Pier, TX	29.2850	-94.7883	NOS	GOM	--	--
51	Port Aransas	27.825000	-97.058333	GOM	GOM	--	--
52	Corpus Christi, GOM, TX	27.5800	-97.2167	NOS	GOM	--	--

Table 2 (Continued)

Station No.	Station Name	Lat (deg)	Long (deg)	Source	Sub-domain	Distance (miles)	Width (miles)
53	Port Isabel, Laguna Madre, TX	26.0600	-97.2150	NOS	GOM	5.00	0.25
54	South Padre Island, TX	26.066667	-97.150000	IHO	GOM	--	--
55	Ciudad Madero, Mexico	22.216667	-97.858333	GOM	GOM	8.10	0.30
56	Coatzacoalcos, Mexico	18.148333	-94.411667	IHO	GOM	--	--
57	Campeche, Mexico	19.833333	-90.533333	IHO	GOM	--	--
58	Progreso Yucatan, Mexico	21.300000	-89.650000	IHO	GOM	--	--
59	Middle of GOM	24.766667	-89.650000	IHO	GOM	--	--
60	Florida Bank	26.700000	-84.250000	IHO	GOM	--	--
61	Puerto Cortes, Honduras	15.833333	-87.950000	IHO	Caribbean	--	--
62	Puerto Cabezas, Nicaragua	14.016667	-83.366667	IHO	Caribbean	--	--
63	Puerto Limon, Costa Rica	10.000000	-83.033333	IHO	Caribbean	--	--
64	Cristobal, Panama	9.350000	-79.916667	IHO	Caribbean	--	--
65	Cartagena, Colombia	10.383333	-75.533333	IHO	Caribbean	--	--
66	Curacao, Antilles	12.100000	-68.933333	IHO	Caribbean	--	--
67	La Guaira, Venezuela	10.616667	-66.933333	IHO	Caribbean	--	--
68	Cumana, Venezuela	10.450000	-64.166667	IHO	Caribbean	--	--
69	Port of Spain, Trinidad and Tobago	10.650000	-61.516667	IHO	Caribbean	--	--
70	Castries, St Lucia	14.016667	-61.000000	IHO	Caribbean	--	--
71	Fort-de-France, Martinique	14.583333	-61.050000	IHO	Caribbean	--	--
72	St Thomas, Virgin Islands	18.333333	-64.933333	IHO[2]	Remote	--	--
73	Lime Tree Bay, St. Croix, VI	17.696667	-64.753333	NOS	Caribbean	--	--
74	San Juan, La Puntilla, Puerto Rico	18.461667	-66.116667	NOS	Remote	--	--
75	Magueyes Island, Puerto Rico	17.966667	-67.050000	IHO[2]	Caribbean	--	--
76	Ciudad, Dominican Republic	18.466667	-69.883333	IHO	Caribbean	--	--

Table 2 (Concluded)

Station No.	Station Name	Lat (deg)	Long (deg)	Source	Sub-domain	Distance (miles)	Width (miles)
77	Puerto Plato, Dominican Republic	19.750000	-70.683333	IHO	Remote	--	--
78	Port-au-Prince, Haiti	18.550000	-72.350000	IHO	Caribbean	--	--
79	Guantanomo Bay, Cuba	19.900000	-75.150000	IHO	Caribbean	--	--
80	Gibara, Cuba	21.100000	-76.116667	IHO	Remote	--	--
81	Casilda, Cuba	21.750000	-79.983333	IHO	Caribbean	--	--
82	Havana, Cuba	23.133333	-82.366667	IHO	GOM	--	--
83	Settlement Point, Grand Bahamas	26.710000	-78.996667	NOS	Remote	--	--
84	Nassau, Bahamas	25.083333	-77.350000	IHO	Remote	--	--
85	Eleuthera,, Bahamas	24.766667	-76.150000	IHO	Remote	--	--
86	Ireland Island, Bermuda	32.316667	-64.833333	IHO	Remote	--	--
87	St Davids Islands, Bermuda	32.370000	-64.695000	IHO	Remote	--	--
88	East Caribbean Sea	16.533333	-64.883333	IHO	Caribbean	--	--
89	Atlantic Ocean	26.466667	-69.333333	IHO	Remote	--	--
90	Atlantic Ocean	28.016667	-76.783333	IHO	Remote	--	--
91	Atlantic Ocean	28.133333	-69.750000	IHO	Remote	--	--
92	Atlantic Ocean	28.233333	-67.533333	IHO	Remote	--	--
93	Atlantic Ocean	28.450000	-76.800000	IHO	Remote	--	--
94	Atlantic Ocean	30.433333	-76.416667	IHO	Remote	--	--
95	Atlantic Ocean near Bermuda	32.016667	-64.433333	IHO	Remote	--	--
96	Atlantic Ocean	32.683333	-75.616667	IHO	Remote	--	--
97	Atlantic Ocean	37.366667	-73.083333	IHO	Remote	--	--
98	Atlantic Ocean	39.166667	-71.366667	IHO	Remote	--	--
99	Atlantic Ocean	39.216667	-72.166667	IHO	Remote	--	--
100	Atlantic Ocean	40.116667	-68.633333	IHO	Remote	--	--
101	Atlantic Ocean	40.300000	-70.900000	IHO	Remote	--	--

Table 3
Station Measurement Data Amplitude and Phase Errors

Constituent	Entire Domain	Atlantic Coast	Gulf of Mexico
Amplitude Errors, E^m_{j-amp}			
K_1	0.06067	0.05376	0.06680
O_1	0.07279	0.03822	0.08943
M_2	0.03080	0.02689	0.07523
S_2	0.10818	0.10593	0.11682
N_2	0.03982	0.03191	0.14143
K_2	0.08872	0.08863	0.08904
Q_1	0.16063	0.11648	0.18465
Phase Errors, $E^m_{j-phase}$			
K_1	2.02619	1.48286	3.11286
O_1	2.89619	2.56786	3.55286
M_2	3.79857	2.54643	6.30286
S_2	4.25571	2.40500	7.95714
N_2	3.54316	3.69000	3.13200
K_2	4.50833	3.99643	6.30000
Q_1	6.15600	6.81714	4.61333

Table 4
***Eastcoast 2001* Domain and Regional Model to Measured Data Errors**

Constituent	Entire Domain	Atlantic Coast	Gulf of Mexico	Caribbean Sea	Remote
Amplitude Errors, E_{j-amp}^{c-m}					
K_1	0.13466	0.19027	0.11211	0.08436	0.09439
O_1	0.10185	0.07829	0.10418	0.10434	0.12846
M_2	0.06254	0.05642	0.11661	0.29994	0.07215
S_2	0.09830	0.07541	0.17817	0.19617	0.14962
N_2	0.07604	0.06831	0.17284	0.24851	0.09454
K_2	0.14084	0.10261	0.23881	0.38512	0.2133
Q_1	0.12809	0.14601	0.11321	0.15134	0.17057
Phase Errors, $E_{j-phase}^{c-m}$					
K_1	8.07753	7.35788	6.68833	11.45950	8.12995
O_1	7.21907	7.19371	6.49900	10.95522	4.98352
M_2	9.52856	6.45435	12.66427	14.89206	6.42923
S_2	12.16547	8.36515	13.30262	19.32892	12.78745
N_2	8.93081	4.45144	12.06543	19.22187	5.39919
K_2	12.89956	12.16353	16.14971	18.84900	7.25394
Q_1	8.91849	9.09721	8.19108	11.02400	8.10176

Table 5
Harmonic Constituent Error Comparison Between Databases Over Entire Domain

Constituent	Eastcoast 1991	Eastcoast 1995	Eastcoast 2001	Field Data
Amplitude Error, E^{c-m}_{j-amp}				
K_1	0.182	0.22954	0.13466	0.06067
O_1	0.205	0.29040	0.10185	0.07279
M_2	0.270	0.09458	0.06254	0.03080
S_2	0.290	0.14344	0.09830	0.10818
N_2	0.244	0.10933	0.07604	0.03982
K_2	0.453	--	0.14084	0.08872
Q_1	0.324	--	0.12809	0.16063
Phase Error, $E^{c-m}_{j-phase}$				
K_1	9.5	8.65914	8.07753	2.02619
O_1	8.3	7.05207	7.21907	2.89619
M_2	22.4	11.23465	9.52856	3.79857
S_2	27.5	14.97727	12.16547	4.25571
N_2	19.6	9.37738	8.93081	3.54316
K_2	23.6	--	12.89956	4.50833
Q_1	8.6	--	8.91849	6.15600

Table 6
Harmonic Constituent Error Comparison Between Databases for Atlantic Coast Stations

Constituent	Eastcoast 1991	Eastcoast 1995	Eastcoast 2001	Field Data
Amplitude Error, E^{c-m}_{j-amp}				
K_1	0.220	0.16161	0.19027	0.05376
O_1	0.212	0.08964	0.07829	0.03822
M_2	0.266	0.09368	0.05642	0.02689
S_2	0.288	0.11806	0.07541	0.10593
N_2	0.234	0.10760	0.06831	0.03191
K_2	0.444	--	0.10261	0.08863
Q_1	0.336	--	0.14601	0.11648
Phase Error, $E^{c-m}_{j-phase}$				
K_1	17.6	7.67785	7.35788	1.48286
O_1	9.5	7.08882	7.19371	2.56786
M_2	15.1	11.69432	6.45435	2.54643
S_2	20.2	13.62459	8.36515	2.40500
N_2	13.6	8.47306	4.45144	3.69000
K_2	15.0	--	12.16353	3.99643
Q_1	8.0	--	9.09721	6.81714

Table 7
Harmonic Constituent Error Comparison Between Databases for Gulf of Mexico Stations

Constituent	Eastcoast 1991	Eastcoast 1995	Eastcoast 2001	Field Data
Amplitude Error, E^{c-m}_{j-amp}				
K_1	0.199	0.29334	0.11211	0.06680
O_1	0.218	0.36409	0.10418	0.08943
M_2	0.278	0.11527	0.11661	0.07523
S_2	0.407	0.25725	0.17817	0.11682
N_2	0.124	0.16874	0.17284	0.14143
K_2	0.546	--	0.23881	0.08904
Q_1	0.356	--	0.11321	0.18465
Phase Error, $E^{c-m}_{j-phase}$				
K_1	7.8	8.54052	6.68833	3.11286
O_1	7.2	5.44144	6.49900	3.55286
M_2	33.1	12.58563	12.66427	6.30286
S_2	28.7	15.32892	13.30262	7.95714
N_2	37.4	11.50765	12.06543	3.13200
K_2	44.5	--	16.14971	6.30000
Q_1	9.6	--	8.19108	4.61333

Table 8
Harmonic Constituent Error Comparison Between Databases for Caribbean Sea Stations

Constituent	Eastcoast 1991	Eastcoast 1995	Eastcoast 2001	Field Data
Amplitude Error E^{m}_{j-amp}				
K_1	0.077	0.09958	0.08436	--
O_1	0.109	0.10424	0.10434	--
M_2	0.652	0.28459	0.29994	--
S_2	0.529	0.43228	0.19617	--
N_2	0.741	0.25292	0.24851	--
K_2	0.455	--	0.38512	--
Q_1	0.131	--	0.15134	--
Phase Error $E^{c-m}_{j-phase}$				
K_1	5.6	11.64000	11.45950	--
O_1	9.9	11.59033	10.95522	--
M_2	31.2	13.88613	14.89206	--
S_2	40.8	19.43108	19.32892	--
N_2	23.9	13.70664	19.22187	--
K_2	35.8	--	18.84900	--
Q_1	9.4	--	11.02400	--

Table 9
Harmonic Constituent Error Comparison Between Databases for Remote Stations

Constituent	Eastcoast 1991	Eastcoast 1995	Eastcoast 2001	Field Data
Amplitude Error, E_{j-amp}^{c-m}				
K_1	0.131	0.09534	0.09439	--
O_1	0.199	0.12786	0.12846	--
M_2	0.204	0.07325	0.07215	--
S_2	0.122	0.14263	0.14962	--
N_2	0.154	0.09219	0.09454	--
K_2	0.407	--	0.21330	--
Q_1	0.251	--	0.17057	--
Phase Error, $E_{j-phase}^{c-m}$				
K_1	6.7	7.84538	8.12995	--
O_1	6.3	5.17343	4.98352	--
M_2	10.8	6.93786	6.42923	--
S_2	20.6	14.22282	12.78745	--
N_2	8.0	5.43445	5.39919	--
K_2	12.7	--	7.25394	--
Q_1	7.5	--	8.10176	--

REPORT DOCUMENTATION PAGE

Form Approved
OMB No. 0704-0188

1. REPORT DATE *(DD-MM-YYYY)*	2. REPORT TYPE	3. DATES COVERED *(From - To)*
September 2002	Final report	

4. TITLE AND SUBTITLE

Eastcoast 2001, A Tidal Constituent Database for Western North Atlantic, Gulf of Mexico, and Caribbean Sea

5a. CONTRACT NUMBER

5b. GRANT NUMBER

5c. PROGRAM ELEMENT NUMBER

6. AUTHOR(S)

A. Y. Mukai, J. J. Westerink, R. A. Luettich, Jr., D. Mark

5d. PROJECT NUMBER

5e. TASK NUMBER

5f. WORK UNIT NUMBER

7. PERFORMING ORGANIZATION NAME(S) AND ADDRESS(ES)

See reverse.

8. PERFORMING ORGANIZATION REPORT NUMBER

ERDC/CHL TR-02-24

9. SPONSORING / MONITORING AGENCY NAME(S) AND ADDRESS(ES)

U.S. Army Corps of Engineers
Washington, DC 20314-1000

10. SPONSOR/MONITOR'S ACRONYM(S)

11. SPONSOR/MONITOR'S REPORT NUMBER(S)

12. DISTRIBUTION / AVAILABILITY STATEMENT

Approved for public release; distribution is unlimited.

13. SUPPLEMENTARY NOTES

14. ABSTRACT

The Eastcoast 2001 tidal constituent database described in this report was developed by the University of Notre Dame. The work was performed as an activity of the Inlet Modeling System (IMS) Work Unit, Coastal Inlets Research Program (CIRP), of Headquarters, U.S. Army Corps of Engineers (HQUSACE). This IMS research and development product was conducted under contract DACW 42-00-C-0006 with the U.S. Army Research and Development Center (ERDC), Coastal and Hydraulics Laboratory (CHL), Vicksburg, MS.

This report describes the development of the *Eastcoast 2001* database of computed tidal elevation and velocity constituents within the Western North Atlantic Tidal (WNAT) domain. The WNAT domain encompasses the Western North Atlantic Ocean, Gulf of Mexico, and Caribbean Sea. The computations are based on a strategically designed finite element grid and the coastal hydrodynamic circulation model, ADCIRC. The resulting *Eastcoast 2001* database defines the computed elevation and velocity amplitude and phase for the O_1, K_1, Q_1, M_2, S_2, N_2, and K_2 tidal constituents.

The *Eastcoast 2001* database is significantly more accurate than the previous *Eastcoast 1995* and *Eastcoast 1991* databases based on the following feature improvements: a) a new grid generation technique with better node placement and distribution, b) a significantly greater number of total nodes, c) a more accurate coastal boundary, and d) inclusion of more reliable bathymetric databases.

(Continued)

15. SUBJECT TERMS

See reverse.

16. SECURITY CLASSIFICATION OF:			17. LIMITATION OF ABSTRACT	18. NUMBER OF PAGES	19a. NAME OF RESPONSIBLE PERSON
a. REPORT	b. ABSTRACT	c. THIS PAGE			19b. TELEPHONE NUMBER *(include area code)*
UNCLASSIFIED	UNCLASSIFIED	UNCLASSIFIED		194	

7. (Concluded)

Department of Civil Engineering and Geological Sciences
University of Notre Dame
Notre Dame, IN 46556;

University of North Carolina at Chapel Hill
Institute of Marine Sciences
Morehead City, NC 28557;

Coastal and Hydraulics Laboratory
U.S. Army Engineer Research and Development Center
3909 Halls Ferry Road
Vicksburg, MS 39180-6199

14. (Concluded)

The new grid generation technique is the combination of two a priori mesh criteria a) the wavelength to grid size ratio and b) the topographic length scale criteria. This combination optimally and more accurately places grid nodes in areas where high resolution is needed. Error analysis of computed versus measured elevation amplitude and phase at 101 stations in addition to an assessment of measured data errors globally and locally quantifies the level of reliability of the computed constituents.

15. (Concluded)

ADCIRC
Atlantic Ocean
Caribbean Sea
Currents
Eastcoast 1991
Eastcoast 1995
Eastcoast 2001
Gulf of Mexico
Hydrodynamic circulation model
Tidal constituent
Tidal elevation